Structural aspects of systems with spin–orbit coupling

Tobias Fröhlich

Structural aspects of systems with spin–orbit coupling

Inaugural-Dissertation

zur

Erlangung des Doktorgrades

der Mathematisch-Naturwissenschaftlichen Fakultät

der Universität zu Köln

vorgelegt von

Tobias Fröhlich

aus Münster

Köln, 2020

Berichterstatter:	Prof. Dr. Markus Braden
	Prof. Dr. Thomas Lorenz
Vorsitzende der Prüfungskommision:	Prof. Dr. Petra Becker

Tag der mündlichen Prüfung: 2020-02-03

Contents

Introduction

Spin-orbit coupling gained great attention [1] in solid state physics after experimental results from 1983 [2, 3] were explained one year later [4] using the Rashba term [5]. Also the Kugel-Khomskii model [6] depends on spin-orbit coupling. Spin-orbit coupling plays an important role for the physics of many compounds investigated in the present work.

Pristine Bi_2Se_3 is a topological insulator [7]. Its band structure is characterized by strong spin-orbit coupling: The Hamiltonian contains terms that combine orbital states with the electronic spin [7]. This gives rise to a spin texture on the Fermi surface, where the spin depends on the orbital and on k [7]. In the present work, the doped compound $Cu_xBi_2Se_3$ is investigated. The doping induces charge carriers that give rise to topological superconductivity [8, 7].

The compounds $Ba_3CuSb_2O_9$ [9] and $Ba_3IrTi_2O_9$ [10] were proposed as spin-liquid candidates. The idea behind this is the Kitaev model [11], where the coupling of spins on a honeycomb lattice depends on the bond-direction between them. The realization of this model needs a system with spin-orbit coupling [12]. Related compounds of the form $Ba_3XIr_2O_9$ were investigated in this work.

The superexchange interaction derived by H. A. Kramers [13] and P. W. Anderson [14] was extended by T. Moriya [15] who added spin-orbit coupling. This results in an antisymmetric term that was introduced before by I. Dzyaloshinsky [16]. This so-called Dzyaloshinsky-Moriya interaction gives rise to weak ferromagnetism driven by magnetic ordering in multiferroic compounds like $(NH_4)_2[FeCl_5(H_2O)]$ as investigated in the present work.

After W. C. Röntgen published the discovery of X-rays in 1896 [17], M. von Laue reported the first X-ray diffraction experiment in 1914 [18]. This technique allows investigations of bulk crystal structures on the atomic scale. Several decades later, also neutron radiation was used for diffraction experiments. The neutron was discovered by J. Chadwick in 1932 [19]. The first neutron diffraction experiments were carried out in the 1940s in the context of the Manhattan Project. An overview of these early experiments is given in [20].

Since then, diffraction experiments have become an important tool for crystallography and solid-state physics. Despite the fact that polarized synchrotron radiation can be used for the investigation of magnetic structures (e.g. [21]), neutron diffraction is usually the first choice for this issue. For the determination of crystal structures, both neutron and X-ray diffraction can be used.

The geometry of crystal structures plays an important role for the understanding of inter-

atomic coupling mechanisms like in the Kitaev model [12] or for the Dzaloshinsky-Moriya interaction [15], as introduced above. In the present work, small distortions of crystal structures are studied by means of elastic X-ray and neutron diffraction techniques. Magnetic structures are investigated using neutron diffraction.

The work is structured as follows: The first chapters contain basics of theory and experiment. Chapter 1 gives an introduction to the mechanisms that are relevant for the physical properties of the investigated materials. In Chapter 2, concepts of diffraction are elucidated with the focus on neutron diffraction. While Chapter 2 is very general, Chapter 3 introduces the instruments used in the present work. The next chapters present and discuss the results of the work. In Chapter 4, the erythrosiderite-type compounds $(NH_4)_2[FeCl_5(H_2O)]$ (including the deuterated compound) and $Cs_2[FeCl_5(H_2O)]$ are treated. The former compound is multiferroic while the latter is magneto-electric. For both compounds, a structural and a magnetic phase transition are investigated. Chapter 5 deals with the compound $Cs_3Fe_2Br_9$, which is related to the erythrosiderite-type compounds. It exhibits a very rich phase diagram with a plethora of magnetic phases. For one of these phases, the magnetic structure is determined. Chapters 6 and 7 present structural investigations of the compounds $Ba_3XIr_2O_9$ with $X = \mathrm{In}, \mathrm{Nb}, \mathrm{Ce}$ and Ba_2XIrO_6 with $X = \mathrm{Ce}, \mathrm{Pr}$. Occupation disorder and breaking of symmetry are discussed. In Chapter 8, Cu doped Bi_2Se_3 is investigated. It focuses on the search for Cu atoms because it is still an open question which sites they occupy. Furthermore, structural distortions of this compound are discussed and an impurity phase is characterized.

1 Theory

This section gives a short overview of the theoretical concepts that are used in the context of the investigated compounds.

1.1 Band models and topology

1.1.1 Tight binding model

The tight binding model describes electronic wavefunctions in a periodic potential as linear combination of atomic orbitals. In the limit where all atoms are separated, there exists only one energy level for all the electrons, namely the energy of the atomic orbital ϵ_{atomic}. However, if the atoms are closer together, these atomic orbitals are no longer eigenstates of the Hamiltonian. The deviation from the limit where all atoms are seperated is expressed as the hopping term t, which equals zero if the atoms are separated and increases as the atoms approach each other. A finite value for t has the effect, that the eigenstates are no longer degenerate, but cover an energy interval, which is called band. If there are several non-degenerate orbitals for each atom, there exist several bands. If the hopping term t is large enough, these bands are broad and might overlap. If they do not overlap, the material exhibits a band gap [22].

1.1.2 Nearly free electron model

Another way of treating this problem is the nearly free electron model. Here, the description starts with a free electron gas and the periodic potential caused by the atoms is treated via perturbation theory. While the free electron gas has a dispersion that covers all energies above a minimum energy, the periodic potential makes band gaps open up at the Brillouin zone boundaries [22].

1.1.3 Comparison of the two models

The tight binding model and the nearly free electron model result in very similar dispersions: In the vicinity of momentum $\boldsymbol{k} = \mathbf{0}$ and at the Brillouin zone, the dispersion relation is parabolic. In both cases, band gaps appear or might be avoided by overlapping bands.

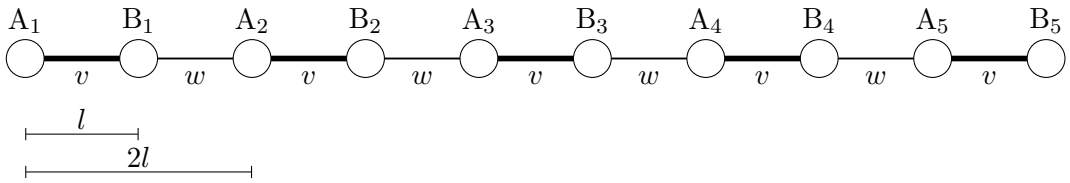

Figure 1.1: Su-Schrieffer-Heeger model for $2N$ atoms with $N = 5$. The atoms are alternatingly spaced with a distance of $l+\delta$ and $l-\delta$. Between them, there are alternating hopping amplitudes v and w. In the general case, the unit cell has length $2l$.

1.1.4 Topological insulators

Topological insulators of dimension 3 (2, 1) exhibit an insulating topological band structure in the bulk and conducting states at the surface (edge, ends) [23]. This concept is rather old and for simple cases well understood. Perhaps the simplest model with a topological band structure is the Su-Schrieffer-Heeger model [24]: It describes the band structure of polyacetylene, which is in principle a one-dimensional chain of C atoms, which are bound by alternating single and double bounds. This results in staggered hopping amplitudes, as shown in Figure 1.1. $2N$ atoms with distance l are alternatingly coupled with hopping amplitudes v and w. A detailed derivation of the electronic bands can be found in [25].

For $v = w \neq 0$, the chain is conducting with parabolic bands and the band gap is closed at the edges of the Brillouin zone. For $v = 1$ and $w = 0$, the electronic wave functions are localized and the bands are flat with a band gap [25].Assuming periodic boundary conditions, this case is physically equivalent to $v = 0$ and $w = 1$. However, the equations look very different: The eigen energy of states with different wave vectors k can be identified with the magnitude of the vector on the circle with center $v + 0\mathrm{i}$ and radius w in the complex plane. Depending on the parameters v and w, this loop might enclose the origin or not. The number of times the loop winds around the origin (in this case 0 or 1) is called winding number and is characteristic for the topology of the system. Systems with different winding numbers are called adiabatically distinct: They cannot be transformed into each other by an adiabatic deformation[1]. For experimental and technological purposes, it is important that the system cannot change between states with different topology by small perturbations like thermal activation. An intuitively accessible explanation in the case of the Su-Schrieffer-Heeger model is that it is not possible to flip the coupling parameters one by one using a small energy, but instead all of them must be flipped at once. This protects topological states against e.g. thermal activation. The topologically non-trivial band structures of topological insulators lead to the effect that there must be gapless states at interfaces with topologically trivial materials [23].

The compound Bi_2Se_3, which is of importance for the present work, has a band structure that exhibits two orbitals which can be ascribed to the two symmetrically not equivalent Se positions. The Hamiltonian contains a strong spin-orbit-coupling term [7] so that the

[1]For a definition of "adiabatic deformation" cf. [25]

spin orientation at the Fermi surface depends on the wave vector and the orbital. States in different orbitals with the same wave vector have opposite spin direction [7].

1.1.5 Topological superconductors

Topological superconductors are adiabatically distinct from conventional superconductors that exhibit a topologically trivial band structure [7]. In general, two classes of topological superconductors are distinguished: For "weak topological superconductors" it is sufficient to exhibit a topologically non-trivial band structure. If additionally the gap is fully open, the superconductivity is called "strong" [7]. There are several ways for realizing a topological superconductor. A material is said to show "intrinsic topological superconductivity" if the pristine sample is topologically superconducting. So far, there are not many candidates for this and only superfluid ^{3}He is a verified intrinsic topological superconductor [26]. Other materials are topological insulators or topological semimetals and become superconducting when high pressure is applied [26]. Recently, a further method was discovered that turns topological semimetals into superconductors by applying a hard point contact. The physics of these so called "tip-induced superconductors" is not well understood yet [26]. Furthermore, there are many different setups in order to induce topological superconductivity by arranging materials in artificial structures. With some of these approaches, superconductivity can be tuned by a voltage in a structure similar to a field-effect transistor. Others use the proximity effect in order to induce topological superconductivity at interfaces between different materials [26]. A further possibility is doping of topological insulators or topological crystalline insulators. Since in this work, the compound $Cu_xBi_2Se_3$ is investigated, the next paragraph pays closer attention to doping induced topological superconductivity in topological insulators.

As stated above, a topological insulator has an insulating band structure in the bulk where the topology of the bands is non-trivial. By doping the material appropriately, it is possible to induce charge carriers that are at the Fermi surface [7]. The pristine material exhibits a spin texture due to strong spin-orbit coupling: The spin of an electron depends on the wave number and this dependence is different for different orbitals [7]. This results in two possibilities for forming Cooper pairs. If cooper-pairs consist of electrons in the same orbital, these electrons will have opposite spin and form a spin singlet state. If the electrons of a Cooper pair come from different orbitals, they have parallel spins and form a spin triplet state. The way the electrons couple and form Cooper pairs is predicted by the form of the pair potential Δ. Let P be the inversion operator, then the pair potential is called even if $P\Delta P^t = \Delta$ and odd if $P\Delta P^t = -\Delta$. Possible coupling mechanisms can be categorized by the parity of the pair potential and the multiplet of the spins. In the case of $Cu_xBi_2Se_3$, four combinations are possible. Calculations revealed that an odd-parity spin-triplet state is realized.

1.2 Frustrated systems

When it is not possible to satisfy all competing forces in a system simultaneously, the system is called frustrated [27]. Some possible states for such a system are presented in this section.

1.2.1 Classical spin liquid

A spin liquid is a system of spins which are frustrated and fluctuate classically [27]. The simplest example for a frustrated system consists of three $S = 1/2$ Ising spins which are placed at the corners of an equilateral triangle and which are coupled antiferromagnetically [27]. The system is frustrated because not all three spins can be pairwise oriented in opposite direction. At first glance it seems obvious that frustration can occur only in antiferromagnetically coupled systems because for ferromagnetic coupling all forces can be satisfied by orienting all spins in the same direction. However, when the spins exhibit Ising anisotropy, frustration is also possible for ferromagnetically coupled spins. This is the case in $Ho_2Ti_2O_7$ [28] with strong easy-axis anisotropy, which is the first realization of a spin ice material [27]. Both the system investigated in [29] and spin ice are classical spin liquids.

1.2.2 Quantum spin liquid

A quantum spin liquid state is a state where the entropy at low energy is released by quantum effects [30]. There are two models for describing such an effect in certain systems: The resonant valence bond state and the Kitaev model.

The resonant valence bond state describes a system in which spin dimers fluctuate. If the interactions between spins in a lattice is antiferromagnetic, it is possible that in the the ground state the spins couple to ordered singlet dimers. An example for such a material is $SrCu_2(BO_3)_2$ [31]. Since every singlet has the total spin quantum number $J = 0$, the ground state is not magnetic [27]. Such a system is called valence bond solid. It is also possible that the system fluctuates between different dimer configurations. The state of the system is then a linear combination of wave functions that correspond to these dimer configurations [32]. This is called resonant valence bond state and realizes a quantum spin liquid. The word ”resonant” stems from the pictorial image that the system is resonating between the different configurations [32]. The resonant valence bond state is not exactly solved [30]. It is predicted for a triangular antiferromagnet, however next-nearest-neighbor interactions are supposed to destroy this state [32].

Another kind of quantum spin liquid is the Kitaev model. It consists of a honeycomb lattice of $S = 1/2$ spins where each spin couples to three nearest neighbors. The coupling between each pair of neighbored spins is ferromagnetic and possesses a strong Ising anisotropy which depends on the spatial orientation of the connecting line of these spins [11][30]. The model is solved exactly in a formalism which represents spins by Majorana

operators [11].

While classical spin liquids occur for large spin quantum numbers, quantum spin liquids are expected for systems with $S = 1/2$ because there is no energy barrier [27]. To the knowledge of the author, no such material could be unambiguously identified so far. The difficulty in searching for such materials experimentally lies in the fact that it is not characterized by a single experiment. There are rather indirect hints, which however do not exclude other explanations. One indication for a quantum spin liquid is the absence of magnetic ordering down to low temperatures despite a strong magnetic interaction. A measure for this is the frustration parameter $f = |\Theta_{\mathrm{CW}}|/T_{\mathrm{c}}$, where Θ_{CW} is the Curie-Weiss temperature determined from the temperature dependent susceptibility and T_{c} is the temperature at which magnetic ordering sets in. For quantum spin liquids, a frustration parameter of at least 100 is expected [27]. Using muon spin resonance or nuclear magnetic resonance experiments, also disordered magnetic moments can be detected, which must be absent in quantum spin liquids. By specific heat or thermal transport measurement or by neutron scattering experiments, excitations can be detected which are characteristic for quantum spin liquids. A candidate was $Ba_3CuSb_2O_9$ [9], which exhibits single- and double-octahedrons. The single octahedrons are occupied by Sb while one site of the the double octahedrons is occupied by Sb and the other site by Cu. The occupation is nearly ordered [9], so that effectively a triangular lattice of Cu^{2+} ions in isolated octahedrons is formed [9]. The $3d$ electrons of Cu^{2+} were expected to form a quantum spin liquid. However, later it turned out to be rather a random singlet state than a quantum spin orbital liquid [33]. Crystallizing with a very similar structure, $Ba_3TiIr_2O_9$ was proposed to be a quantum spin liquid [10]. Instead of $3d$ electrons, Ir^{4+} exhibits $5d$ electrons.

1.2.3 Quantum spin-orbital liquid

If the spin and orbital degrees of freedom in a compound are coupled, the Kugel-Khomskii model [6] is used. The basis states for a site are the pairs of a spin and an orbital state [34]. These combinations are called colors, so that e.g. two orbitals and two spin states give four different colors. This formalism is applied to Mott insulators [34]. If the spins in the formalism of quantum spin liquids are replaced by colors, this state is called quantum spin-orbital liquid [34].

Candidates for such a state are $LaTiO_3$ [35], $FeCs_2S_4$ [36]. The crystal structure of $LaTiO_3$ consists of corner-sharing TiO_6 octahedrons [37], while $FeCs_2S_4$ consists of isolated FeS_4 tetrahedrons [38].

The compound $Ba_3ZnIr_2O_9$ exhibits a crystal structure similar to that of the previously mentioned $Ba_3CuSb_2O_9$, but both sites of the double octahedrons are occupied by Ir^{5+} ions with only 5 % disorder [39]. The magnetic moment of an Ir^{5+} ion is expected to be $J = 0$ due to spin orbit coupling [39]. However, a small momentum remains [39], which is supposed to form a quantum spin-orbital liquid [39].

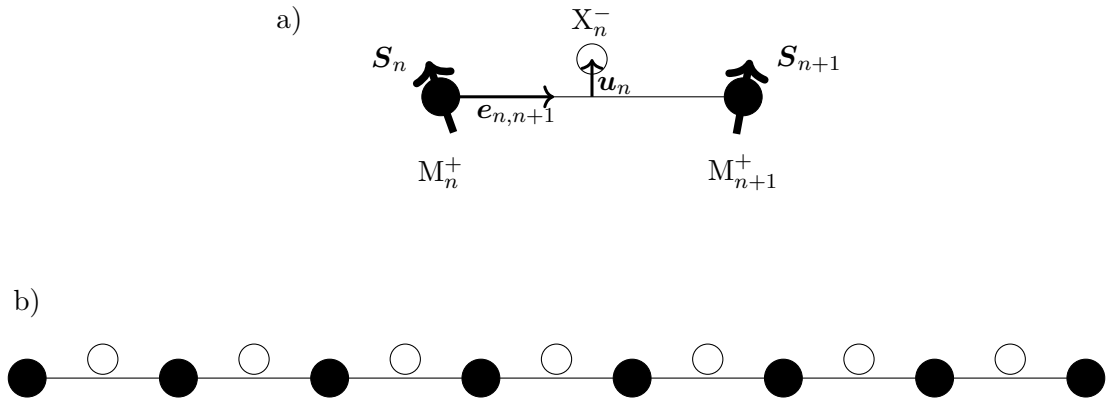

Figure 1.2: Dzyaloshinskii-Moriya interaction. a) A non-magnetic negatively charged ion X_n^- is placed between two positively charged magnetic ions M_n^+ and M_{n+1}^+ with magnetic moments $\boldsymbol{S}_n$ and $\boldsymbol{S}_{n+1}$, respectively. The negatively charged ion X_n^- can be shifted along the displacement vector $\boldsymbol{u}_n$. The total energy depends on this displacement. The vector $\boldsymbol{e}_{n,n+1}$ is the unit vector with the direction of the connecting line from M_n^+ to M_{n+1}^+. b) It can be shown that in the case of a spin cycloide the total energy is minimized when all X^- ions are shifted in the same direction, resulting in a non-zero polarization.

1.3 Dzyaloshinskii-Moriya interaction

In 1960, T. Moriya [15] developed an explanation for weak ferrimagnetism in $\alpha - Fe_2O_3$, $MnCO_3$ and CrF_3 based on symmetry arguments by I. Dzyaloshinskii [16] in 1957. This model uses an antisymmetric magnetic contribution to the Hamiltonian. In 2006, this so called Dzyaloshinskii-Moriya interaction was used to explain the strong coupling between ferroelectricity and antiferromagnetism in $R\mathrm{MnO_3}$ ($R = \mathrm{Gd, Tb, Dy}$) [40].

The modell is based on an alternating chain of positively charged magnetic ions M^+ and negatively charged non-magnetic ions X^-, as depicted in Figure 1.2a. The negatively charged ion X_n^- is allowed to shift away from the connecting line of the magnetic ions by a displacement vector $\boldsymbol{u}_n$. The magnetic ions carry magnetic moments $\boldsymbol{S}_n$ and $\boldsymbol{S}_{n+1}$, respectively.

Dependent on the orientation of the magnetic moments $\boldsymbol{S}_n, \boldsymbol{S}_{n+1}$ and the displacement vector $\boldsymbol{u}_n$, antisymmetric contribution to the Hamiltonian can be written as

$$H_{\mathrm{DM}} = \sum_n \boldsymbol{D}_{n,n+1} \cdot (\boldsymbol{S}_n \times \boldsymbol{S}_{n+1}) \quad , \tag{1.1}$$

where the Dzyaloshinskii vector $\boldsymbol{D}_{n,n+1}$ can be written as

$$\boldsymbol{D}_{n,n+1} = \gamma(\boldsymbol{u}_n \times \boldsymbol{e}_{n,n+1}) \tag{1.2}$$

with the unit vector $\boldsymbol{e}_{n,n+1}$ along the connecting line from M_n^+ to M_{n+1}^+ and a constant of proportionality γ [40, 41].

Furthermore, since in the antiferromagnetic phase, the ion X_n^- is shifted away from its equilibrium position of the paramagnetic phase, we have to take into account an elastic energy $H_{\mathrm{el}} = \sum_n \kappa/2|\boldsymbol{u}_n|^2$ with stiffness $\kappa > 0$ [40]. Thus, the total energy can be written as

$$\begin{aligned} H &= H_{\mathrm{DM}} + H_{\mathrm{el}} && (1.3)\\ &= \sum_n \left(\boldsymbol{D}_{n,n+1} \cdot (\boldsymbol{S}_n \times \boldsymbol{S}_{n+1}) + \frac{\kappa}{2}|\boldsymbol{u}_n|^2 \right) && (1.4)\\ &= \sum_n \left(\gamma(\boldsymbol{u}_n \times \boldsymbol{e}_{n,n+1}) \cdot (\boldsymbol{S}_n \times \boldsymbol{S}_{n+1}) + \frac{\kappa}{2}|\boldsymbol{u}_n|^2 \right) && (1.5)\\ &= \sum_n \left(\gamma \boldsymbol{u}_n \cdot (\boldsymbol{e}_{n,n+1} \times (\boldsymbol{S}_n \times \boldsymbol{S}_{n+1})) + \frac{\kappa}{2}|\boldsymbol{u}_n|^2 \right) \quad . && (1.6) \end{aligned}$$

We use a Cartesian coordinate system and differentiate with respect to the coordinates $(\boldsymbol{u}_n)_i$ for $i \in \{1, 2, 3\}$:

$$\frac{\partial H}{\partial (\boldsymbol{u}_n)_i} = \gamma(\boldsymbol{e}_{n,n+1} \times (\boldsymbol{S}_n \times \boldsymbol{S}_{n+1}))_i + \kappa(\boldsymbol{u}_n)_i \tag{1.7}$$

The equilibrium condition $\partial H/\partial(\boldsymbol{u}_n)_i = 0$ implies $(\boldsymbol{u}_n)_i = -\gamma/\kappa(\boldsymbol{e}_{n,n+1} \times (\boldsymbol{S}_n \times \boldsymbol{S}_{n+1}))_i$ and thus

$$\boldsymbol{u}_n \propto \boldsymbol{e}_{n,n+1} \times (\boldsymbol{S}_n \times \boldsymbol{S}_{n+1}) \quad . \tag{1.8}$$

Let us now analyze this result for some exemplary magnetic structures. For a ferromagnetic or a collinear antiferromagnetic structure, the cross product $\boldsymbol{S}_n \times \boldsymbol{S}_{n+1}$ is zero, thus no effect occurs. For a spiral magnetic structure, neighbored magnetic moments are canted by a certain angle, so the cross product is non-zero. Let us furthermore assume, all magnetic moments are oriented within a common plane A and can be described by a propagation vector $\boldsymbol{q}$. We consider two cases: If the propagation vector $\boldsymbol{q}$ is orthogonal to the plane A, we have a helical structure. The cross product is non-zero only for $\boldsymbol{e}_{n,n+1} \parallel \boldsymbol{q}$. But $\boldsymbol{S}_n \times \boldsymbol{S}_{n+1} \parallel \boldsymbol{e}_{n,n+1}$, so $\boldsymbol{e}_{n,n+1} \times (\boldsymbol{S}_n \times \boldsymbol{S}_{n+1}) = 0$. Thus, a helical structure does not induce a shift of the X^- ions neither. The second case is a cycloidal structure where $\boldsymbol{q}$ lies within the plane A. In this case, $\boldsymbol{S}_n \times \boldsymbol{S}_{n+1} \perp \boldsymbol{e}_{n,n+1}$, so $\boldsymbol{u}_n$ is non-zero. Furthermore, the angle between two neighbored magnetic moments with sites along the $\boldsymbol{q}$ direction is the same. This implies that all X^- ions are shifted in the same direction, resulting in a non-zero polarization. The polarization is perpendicular to $\boldsymbol{q}$ and lies within the plane A, see Figure 1.2b.

We have seen, that Dzyaloshinskii-Moriya interaction induces a polarization for cycloidal magnetic structures. This is a type II magneto-electric multiferroic effect.

2 Fundamental principles of diffraction

2.1 Group theory

Basic concepts of group theory like the definition of a group, coset decomposition or homomorphisms can be found in many text books like e.g. [42]. The application to crystallographic symmetry groups is described in [43], [44] and [45]. In [46], symmetry groups are considered in the context of quantum mechanics.

Representation theory is introduced [47] or alternatively in [42]. Note that the terms "projective representation" [44] and "loaded representation" [48] are used synonymously.

A recipe for the construction of any irreducible representation of a space group is given in [44]. A more general mathematical derivation of this can be found in [49].

Space groups with its representation theory do not cover cases where magnetic moments are included. For this purpose, magnetic space groups are needed and instead of representations one deals with corepresentations. The reason for this is that symmetry elements are quantum mechanical operators that can be unitary or anti-unitary. In [50] this is discussed in detail. The construction of corepresentations of magnetic space groups is derived in [46] and useful formulas for practical calculations can be found in [48]. Ibidem, also a draft about the application of corepresentation theory for the analysis of magnetic structures is given.

2.2 Scattering of neutrons by matter

2.2.1 Scattering of neutrons by nuclei

The scatter process of neutrons on a nucleus is a nuclear process. It consists of elastic scattering and nuclear reactions. A part of the elastic scattering is coherent so that it can be exploited for crystallographic investigations as Bragg reflections. All other processes absorb a neutron or scatter in an incoherent way and thus give not rise to Bragg reflections. They have to be taken into account for absorption and extinction correction.

The following interactions of neutrons with nuclei take place:

- Potential scattering

  - elastic potential scattering
  - inelastic scattering
  - resonant absorption
- spin dependent scattering
- magnetic scattering by the nuclear moment

The mechanisms for inelastic scattering are direct processes and processes which contain a compound nucleus [51]. Inelastic scattering does not occur for thermal neutrons[1]. Magnetic scattering by the magnetic moment of the nucleus is very small and in many cases neglectable.

2.2.1.1 Potential scattering

The term "potential scattering" is not consistently used in literature. Some authors (i.e. [52]) use it for the part of the scattering with an $A^{1/3}$ dependence, where A is the mass number of the nucleus. Other authors (i.e. [53]) label a quantity by "potential scattering" which shows a complicated isotope dependence. An explanation for this inconsistency is that there are different models that use different potentials and explain the experimental data more or less precisely. In this text, the term is used for the part of the nuclear scattering that does not depend on the spins or the magnetic moments of the neutron and the nucleus.

The potential scattering of a neutron on a nucleus is described by a central potential acting on a plane wave. The plane wave can be developed by a series using partial wave expansion: Every summand is a spherical wave (Bessel function) multiplied with a term that depends on the scattering angle (Legendre polynomial) [51]. The summands are numerated by the order $0 \leq l < \infty$. The zeroth order ($l = 0$) is a purely spherical wave without scattering angle dependence. Fortunately, below a neutron energy of about 20 MeV, only the $l = 0$ term must be taken into account [51]. This can be explained by the fact that the nucleus is small compared to the neutron wavelength. Using this approximation, the problem can be described one-dimensional. A basic quantum mechanical calculation yields the result that the scattered wave possesses the same wave length[2] as the incoming wave and a phase shift δ that depends on the potential. An attractive square-well potential shifts the scattered wave towards the origin ($\delta > 0$), whereas a repulsive square-well potential shifts the scattered wave away from the origin ($\delta < 0$) [51]. For more complicated potentials, this must not be true [54].

It has been found that for neutron energies below 20 MeV, the scattering process does

[1] We talk about nuclear processes which are not to be confused with inelastic neutron scattering where the neutron interacts with phonons of a crystal.

[2] Formally, the two particles are described as one particle with reduced mass. In this calculation, the wave length does not change. When the neutron is scattered at a free nucleus, the wavelength of the neutron in the two-particle description can change.

not depend on the details of the potential, but instead can be described by two parameters: The scattering length a and the effective range r_e. They determine the phase shift δ by the equation $k\cot(\delta) = -1/a + 1/2 r_\mathrm{e} k^2$ which is called the "Effective Range Approximation" [55][56]. The sign conventions may vary in literature.

For very low energies, the Effective Range Approximation can be further simplified to $k\cot(\delta) = -1/a$ or even $k\delta = -a$ [51]. This is the case for neutron diffraction used in solid state physics, so we can deal with this approximation and describe the elastic scattering process solely by the scattering length a.

If the scattered current density is evaluated from the wave function, one yields for the scattering cross section $\sigma = \pi/k^2 \left|1 - \mathrm{e}^{\mathrm{i}2\delta}\right|^2$. For a real scattering length, this can be simplified to $\sigma = 4\pi/k^2 \sin(\delta)^2$ [51]. Using the approximation $k\delta = -1/a$, one gets $\sigma = 4\pi a^2$.

The phase shift δ gives for the scattered wave a factor $\mathrm{e}^{2\mathrm{i}\delta}$. Often in literature, the scattering length is given as a complex quantity [57][56]. A non-zero imaginary part of the scattering length is equivalent to a non-zero imaginary part of the phase shift, thus reducing the amplitude of the scattered wave because the factor $\mathrm{e}^{2\mathrm{i}\delta}$ not only changes the phase but also the amplitude. This can be illustrated by an opaque glass sphere that scatters light, which is why in nuclear physics this model is called the "optical model" [51]. This absorption is called "resonant absorption" because it happens when the energy of the neutron is suitable to form a compound nucleus. Physically, this is neutron capture. One might think that this resonant absorption is strongly wavelength-dependent. However, the energy that has to be considered is not only the kinetic energy of the neutron, but also the energy that is gained by the capture. For thermal neutrons, this energy is much higher than the kinetic energy, so we do not see resonant peaks.

Using a non-real scattering length a (including absorption processes in the imaginary part) the calculation becomes more complicated. The elastic scattering cross section amounts to $\pi/k^2 \left|1 - \mathrm{e}^{\mathrm{i}2\delta}\right|^2$ and the absorption cross section to $\pi/k^2 \left(1 - \left|\mathrm{e}^{\mathrm{i}2\delta}\right|^2\right)$, so that the total scattering cross section is $2\pi/k^2 \left(1 - \mathrm{Re}\left(\mathrm{e}^{\mathrm{i}2\delta}\right)\right)$ [51]. For low energies, one gets a scattering cross section of approximately $4\pi|a|^2$ and an absorption cross section of approximately $4\pi\mathrm{Im}(a)/k$ [56]. This is often called the $1/v$ law where $v \propto k$ is the velocity of the neutron.

The scattering process of a neutron by a free nucleus differs from that by a bound nucleus. A scattering process with two free particles of masses m_1 and m_2 is described in the center-of-mass frame as a one-particle scattering process by a central potential using the reduced mass $m_1 m_2/(m_1+m_2)$. In contrast to that, if the particle is kept fixed, its frame and the mass of the other particle are used. Neutron scattering by a nucleus in a crystal corresponds to the latter case[3]. The free scattering length a of a neutron scattering by a free nucleus with atomic mass number A and the bound scattering length b of the same nucleus bound in a crystal relate to each other by $b = (A+1)/A\ a$ [56]. For neutron diffraction with crystals, the bound scattering length b must be used.

[3] As long as inelastic scattering (in the sense of interaction with phonons) is neglected.

This scattering is not only dependent on the element, but also on the isotope.

2.2.1.2 Spin dependence of nuclear scattering

Nuclear forces are strongly spin-dependent [51]. The nuclear scattering of a neutron depends on the orientation of the spins of the neutron and of the nucleus. The system of a nucleus with spin I and a neutron with spin 1/2 can exhibit the total quantum numbers $I + 1/2$ and $I - 1/2$ if $I > 0$. For $I = 0$, only the total quantum number 1/2 is possible. For $I > 0$, the two different states have different bound scattering length b^+ for total spin $I + 1/2$ and b^- for total spin $I - 1/2$. Since each spin state has the same probability, the probability for total spin $I + 1/2$ is $(I + 1)/(2I + 1)$, and the probability for total spin $I - 1/2$ is $I/(2I + 1)$. In the next paragraph, we will use these probabilities in order to derive mean values that are used to describe diffraction experiments.

2.2.1.3 Coherent and incoherent scattering

Because isotopes and nuclear spins are not ordered in most cases, the scattered neutron waves interfere coherently on the common parts and incoherently on the deviations. A detailed derivation of this effect is done in [58]. The derivation given here is strongly simplified but follows the ideas of that publication that are relevant for this work.

Consider a crystal that consists of a very large number of N unit cells. Each unit cell contains J atoms $1 \leq j \leq J$. Different isotopes randomly occupy the lattice sites. Often, all isotopes of one lattice site will belong to the same element, but the following calculation works also for lattice sites shared by different elements.

For a given distribution of isotopes on the lattice sites, consider an ensemble. The crystals of this ensemble differ in the orientation of the nuclear spins. The orientations of the spins of different lattice sites are independent from each other. We will name this ensemble "spin ensemble". The crystals of the spin ensemble contain the same occupation by isotopes but differ in spin orientations.

Consider an ensemble of spin ensembles: The spin ensembles differ in the distribution of the isotopes on the lattice sites. The occupations of different sites are independent from each other. We will call this ensemble of spin ensembles "isotope ensemble".

We enumerate the isotope ensembles by $1 \leq \gamma \leq \Gamma$. We enumerate the spin ensembles (of the isotope ensemble γ) by $1 \leq \xi \leq \Xi(\gamma)$. The atom of isotope ensemble γ and spin ensemble ξ in unit cell n on site j has the bound scattering length $b_{nj}^{\gamma\xi}$. Independent on the ensembles, the atom in unit cell n on site j has the position r_{nj}.

According to [58], we use different symbols for averaging over the different ensembles,

$$\begin{aligned} \text{average over isotope ensembles:} \quad \langle x \rangle \quad &:= \quad \tfrac{1}{\Gamma} \sum_{\gamma=1}^{\Gamma} x(\gamma) \\ \text{average over spin ensembles:} \quad \{y(\gamma)\} \quad &:= \quad \tfrac{1}{\Xi(\gamma)} \sum_{\xi=1}^{\Xi(\gamma)} y(\gamma,\xi) \quad , \end{aligned} \tag{2.1}$$

where $x(\gamma)$ is a quantity that depends on the isotope ensemble and $y(\gamma, \xi)$ is a quantity that depends on both ensembles.

The partial scattering cross section in dependence of wave vector $\vec{k}$ for a given isotope and spin ensemble (γ, ξ) is given by[4]:

$$\begin{aligned} \frac{\mathrm{d}\sigma}{\mathrm{d}\Omega}(\vec{k},\gamma,\xi) &= \left| \sum_{nj} b_{nj}^{\gamma\xi} \, \mathrm{e}^{\mathrm{i}2\pi\vec{k}\cdot\vec{r}_{nj}} \right|^2 \\ &= \sum_{njn'j'} b_{nj}^{\gamma\xi} \, \overline{b}_{n'j'}^{\gamma\xi} \, \mathrm{e}^{\mathrm{i}2\pi\vec{k}\cdot(\vec{r}_{nj}-\vec{r}_{n'j'})} \quad , \end{aligned}$$

where the limits of the sums are $1 \leq n, n' \leq N$ and $1 \leq j, j' \leq J$.

We are interested on the average over the ensembles:

[4]The scattering lengths are allowed to be complex. This is justified, because the formalism does not change if the interfering waves have attenuated amplitudes

$$
\begin{aligned}
\left\langle \left\{ \frac{\mathrm{d}\sigma}{\mathrm{d}\Omega}(\vec{k}) \right\} \right\rangle &= \left\langle \left\{ \sum_{njn'j'} b_{nj}\, \overline{b}_{n'j'}\ \mathrm{e}^{\mathrm{i}2\pi\vec{k}\cdot(\vec{r}_{nj}-\vec{r}_{n'j'})} \right\} \right\rangle \\
&\overset{(1)}{=} \left\langle \sum_{njn'j'} \left\{ b_{nj}\, \overline{b}_{n'j'} \right\}\ \mathrm{e}^{\mathrm{i}2\pi\vec{k}\cdot(\vec{r}_{nj}-\vec{r}_{n'j'})} \right\rangle \\
&\overset{(2)}{=} \left\langle \sum_{njn'j'} \{b_{nj}\} \left\{ \overline{b}_{n'j'} \right\}\ \mathrm{e}^{\mathrm{i}2\pi\vec{k}\cdot(\vec{r}_{nj}-\vec{r}_{n'j'})} + \sum_{nj} \left(\left\{ |b_{nj}|^2 \right\} - |\{b_{nj}\}|^2 \right) \right\rangle \\
&\overset{(3)}{=} \sum_{njn'j'} \left\langle \{b_{nj}\} \left\{ \overline{b}_{n'j'} \right\} \right\rangle\ \mathrm{e}^{\mathrm{i}2\pi\vec{k}\cdot(\vec{r}_{nj}-\vec{r}_{n'j'})} + \sum_{nj} \left(\left\langle \left\{ |b_{nj}|^2 \right\} \right\rangle - \left\langle |\{b_{nj}\}|^2 \right\rangle \right) \\
&\overset{(4)}{=} \sum_{njn'j'} \langle \{b_{nj}\} \rangle \left\langle \left\{ \overline{b}_{n'j'} \right\} \right\rangle\ \mathrm{e}^{\mathrm{i}2\pi\vec{k}\cdot(\vec{r}_{nj}-\vec{r}_{n'j'})} \\
&\qquad + \sum_{nj} \left(\left\langle \left\{ |b_{nj}|^2 \right\} \right\rangle - \left\langle |\{b_{nj}\}|^2 \right\rangle + \left\langle |\{b_{nj}\}|^2 \right\rangle - |\langle \{b_{nj}\} \rangle|^2 \right) \\
&= \sum_{njn'j'} \langle \{b_{nj}\} \rangle \left\langle \left\{ \overline{b}_{n'j'} \right\} \right\rangle\ \mathrm{e}^{\mathrm{i}2\pi\vec{k}\cdot(\vec{r}_{nj}-\vec{r}_{n'j'})} + \sum_{nj} \left(\left\langle \left\{ |b_{nj}|^2 \right\} \right\rangle - |\langle \{b_{nj}\} \rangle|^2 \right) \\
&= \frac{\mathrm{d}\sigma^{\mathrm{coh}}}{\mathrm{d}\Omega}(\vec{k}) + \frac{\mathrm{d}\sigma^{\mathrm{inc}}}{\mathrm{d}\Omega}
\end{aligned}
$$

In steps (1) and (3), we used linearity of the average. In steps (2) and (4) we added terms because for $(n, j) = (n', j')$, the scattering lengths are not independent. The two components of the partial scattering cross section are called coherent and incoherent partial scattering cross sections (the subscript n can be ommited for the averaged values because it does not depend on the cell):

$$
\begin{aligned}
\frac{\mathrm{d}\sigma^{\mathrm{coh}}}{\mathrm{d}\Omega}(\vec{k}) &= \sum_{njn'j'} \langle \{b_j\} \rangle \left\langle \left\{ \overline{b}_{j'} \right\} \right\rangle\ \mathrm{e}^{\mathrm{i}2\pi\vec{k}\cdot(\vec{r}_{nj}-\vec{r}_{n'j'})} \\
\frac{\mathrm{d}\sigma^{\mathrm{inc}}}{\mathrm{d}\Omega} &= \sum_{nj} \left(\left\langle \left\{ |b_j|^2 \right\} \right\rangle - |\langle \{b_j\} \rangle|^2 \right)
\end{aligned}
\tag{2.2}
$$

The coherent part depends on the wave vector $\vec{k}$ and gives rise to Bragg reflections. The incoherent part does not depend on the structure or on $\vec{k}$ and gives rise to background.

The mean values can be computed as the average over the ensembles using Equation 2.1, where the choice of n is arbitrary:

$$\begin{aligned}\langle\{b_j\}\rangle = \langle\{b_{nj}\}\rangle &= \frac{1}{\Gamma}\sum_{\gamma=1}^{\Gamma}\frac{1}{\Xi(\gamma)}\sum_{\xi=1}^{\Xi(\gamma)} b_{nj}^{\gamma\xi} \\ \left\langle\left\{|b_j|^2\right\}\right\rangle = \left\langle\left\{|b_{nj}|^2\right\}\right\rangle &= \frac{1}{\Gamma}\sum_{\gamma=1}^{\Gamma}\frac{1}{\Xi(\gamma)}\sum_{\xi=1}^{\Xi(\gamma)} \left|b_{nj}^{\gamma\xi}\right|^2\end{aligned} \tag{2.3}$$

If for each lattice site j, the isotope distribution is known, we can easily calculate the averages. Let $c_{j,i}$ be the concentration of isotope i on lattice site j, such that $\sum_i c_{j,i} = 1$ for all sites j. The probabilities for the nuclear spin orientation are given in the previous chapter and depend on the spin quantum number I_i of the isotope i. We thus yield the well known formula [54]:

$$\begin{aligned}\langle\{b_j\}\rangle &= \sum_i \frac{c_{j,i}}{2I_i+1}\left((I_i+1)b_i^+ + I_i b_i^-\right) \\ \left\langle\left\{|b_j|^2\right\}\right\rangle &= \sum_i \frac{c_{j,i}}{2I_i+1}\left((I_i+1)\left|b_i^+\right|^2 + I_i\left|b_i^-\right|^2\right)\end{aligned}$$

The ensembles were defined in the way that this equations are consistent with Equations 2.3.

Additionally, it is possible to define scattering cross sections for coherent and incoherent scattering by a site j in the following way [54]:

$$\begin{aligned}\sigma_j^{\text{coh}} &= 4\pi\left|\langle\{b_j\}\rangle\right|^2 \\ \sigma_j^{\text{inc}} &= 4\pi\left(\left\langle\left\{|b_j|^2\right\}\right\rangle - \left|\langle\{b_j\}\rangle\right|^2\right)\end{aligned} \tag{2.4}$$

It is possible to define coherent and incoherent scattering lengths b^{coh} and b^{inc}. They are constructed such that Equation 2.4 reads like

$$\begin{aligned}\sigma^{\text{coh}} &= 4\pi\left|b^{\text{coh}}\right|^2 \\ \sigma^{\text{inc}} &= 4\pi\left|b^{\text{inc}}\right|^2 \quad .\end{aligned}$$

For a single isotope with spin I and spin-dependent scattering length b^+, b^-, we can calculate them:

$$
\begin{aligned}
\left|b^{\mathrm{coh}}\right|^2 &= \left|\langle\{b\}\rangle\right|^2 = \left|\frac{1}{2I+1}\left((I+1)b^+ + Ib^-\right)\right|^2 \\
\left|b^{\mathrm{inc}}\right|^2 &= \left\langle\left\{|b|^2\right\}\right\rangle - \left|\langle\{b\}\rangle\right|^2 \\
&= \frac{I+1}{2I+1}\left|b^+\right|^2 + \frac{I}{2I+1}\left|b^-\right|^2 - \left|\frac{1}{2I+1}\left((I+1)b^+ - Ib^-\right)\right|^2 \\
&= \frac{I(I+1)}{(2I+1)^2}\left|b^+ - b^-\right|^2
\end{aligned}
$$

Since b^{coh} and b^{inc} do not have any physical meaning, we can choose the phases arbitrarily and define [56]:

$$
\begin{aligned}
b^{\mathrm{coh}} &= \frac{1}{2I+1}\left((I+1)b^+ + Ib^-\right) \\
b^{\mathrm{inc}} &= \frac{\sqrt{I(I+1)}}{2I+1}\left(b^+ - b^-\right)
\end{aligned}
$$

2.2.2 Scattering of neutrons at electrons

There are the following interactions between a neutron at the electrons of an atom:

- Electrostatic interactions
- Magnetic scattering

2.2.2.1 Electromagnetic scattering

The neutron does not carry any electric charge[5], so electrostatic interactions are small. However, the neutron is electrically polarizable, so the scattering of neutrons at the electrons has a small electrostatic contribution [57]. This effect is smaller than 0.5 % of the nuclear interactions [57] and depends on the scattering vector because the electron density of an atom has extensions on the length scale of the neutron wave length. For crystallographic or magnetic investigations like in this work, it can be neglected.

2.2.2.2 Magnetic scattering

Neutrons scatter at the magnetic moments of unpaired electrons. The scattering lengths are similar to those of nuclear scattering [60]. It derives from electromagnetic interactions

[5] Measurements in 2018 have found an electric charge compatible with zero in the order of magnitude 10^{-23} electron charges [59].

of the magnetic moment $\vec{\mu}_\mathrm{n}$ of the neutron with the magnetic field $\vec{H}$ caused by the unpaired electrons of the sample, so that the energy of the neutron at position $\vec{r}$ reads as follows [61]:

$$V_\mathrm{M}(\vec{r}) = -\vec{\mu}_\mathrm{n} \cdot \vec{H}(\vec{r})$$

However, for calculating the scattering amplitude, it is sufficient to know the magnetic moment density distribution. If some atom has magnetic moment $\vec{S}$ and the density distribution $\vec{r} \mapsto d(\vec{r})$, then the moment density is

$$\vec{M}(\vec{r}) = \vec{S}\, d_j(\vec{r}) \quad .$$

Because the moment density distribution varies on the length scale which is comparable of the neutron wave length, the scattering length depends on the scattering vector. This will later be taken into account by the form factor $f_j(\vec{k})$ in Equation 2.5 in section 2.3.2. For practical use, these form factors are tabulated in section 4.4.5 of [57] for different ions. Furthermore, only the component of the magnetic moment perpendicular to the scattering vector takes effect. This will be considered in Equation 2.6 in this work.

2.3 Neutron diffraction

Neutrons interact with a crystal in two different ways: With the nuclei and with the magnetic moments of unpaired electrons. The interaction with the magnetic moment of the nuclei is very small and can be neglected in this work.

In this section, the following symbols are used for the distinct spaces: $\mathbb{P}$ is the affine space of spatial positions. $\mathbb{V}$ is the spatial vector space of differences of positions. $\mathbb{A}$ is the vector space of axial vectors like magnetic moments. $\mathbb{V}^*$ is the reciprocal space, so that a dot product $\cdot : \mathbb{V}^* \times \mathbb{V} \to \mathbb{R} : (\vec{k}, \vec{v}) \mapsto \vec{k} \cdot \vec{v}$ is defined. As usual, $\mathbb{R}$ is the field of real numbers and $\mathbb{C}$ is the field of complex numbers.

2.3.1 Nuclear neutron diffraction

Usual, the energy of neutrons does not suffice to excite a nucleus, so nuclear scattering can be considered elastic. Since nuclear forces are of short range compared to the wavelength of the neutron, we can describe the scattering density by δ functions [61]:

$$N : \mathbb{P} \to \mathbb{R} : \vec{O}_a + \vec{r} \mapsto \sum_{\vec{p} \in \mathcal{P}} \sum_{j \in \mathcal{J}} b_j \delta(\vec{r} - \vec{r}_j - \vec{p})$$

$\mathcal{P} = \{n_1\vec{a}_1 + n_2\vec{a}_2 + n_3\vec{a}_3 \mid (n_1, n_2, n_3) \in \mathbb{Z}^3\} \subset \mathbb{V}$ is the position of the unit cells with respect to the origin $\vec{O}_a$ using the basis vectors $(\vec{a}_1, \vec{a}_2, \vec{a}_3) \in \mathbb{V}^3$ of a unit cell a. The set

$\mathcal{J}$ contains all atoms within the zeroth unit cell, und $\vec{r}_j \in \mathbb{V}$ is the position of the atom $j \in \mathcal{J}$ with respect to the origin $\vec{O}_a$. b_j is the scattering length of atom $j \in \mathcal{J}$, which does not depend on the wave vector.

Diffraction processes can be described with the aid of the Fourier transform of the scattering density. In order to yield finite values, we carry out the integration over some subset $V \subset \mathbb{V}$ of the direct space and normalize by its volume. The limit of this volume covering the whole space $\mathbb{V}$ yields the normalized Fourier transform ($|V|$ is the volume of V):

$$N^* : \mathbb{V}^* \to \mathbb{C} : \vec{k} \mapsto \lim_{V \to \mathbb{V}} \frac{1}{|V|} \int_V N(\vec{O}_a + \vec{r}) \mathrm{e}^{2\pi \mathrm{i} \vec{k} \cdot \vec{r}} \mathrm{d}\vec{r}$$

The scattering amplitude a_N of one unit cell at a scattering vector $\vec{k} \in \mathcal{T}^* = \{h\vec{a}^1 + k\vec{a}^2 + l\vec{a}^3 \mid (h,k,l) \in \mathbb{Z}^3\} \subset \mathbb{V}^*$ is identical with the Fourier transform N^* of the scattering density N:

$$a_N : \mathbb{V}^* \to \mathbb{C} : \vec{k} \mapsto a_N(\vec{k}) = N^*(\vec{k}) = \begin{cases} \frac{1}{V_a} \sum\limits_{j \in \mathcal{J}} b_j \mathrm{e}^{2\pi \mathrm{i} \vec{k} \cdot \vec{r}_j} & \text{for } \vec{k} \in \mathcal{T}^* \\ 0 & \text{otherwise} \end{cases}$$

V_a is the volume of the unit cell spanned by the basis vectors $\vec{a}_1, \vec{a}_2, \vec{a}_3$. Equation 2.3.1 is (apart from the factor $1/V_a$) the well known structure that is derived in any text book about solid state physics e.g. in [61] or [62] for neutron diffraction and in [63] for X-ray diffraction.

2.3.2 Magnetic neutron diffraction

Magnetic neutron diffraction arises from the interaction of the magnetic moment of the neutron with the magnetic moment density of unpaired electrons in the crystal.

We start with a quite general description of a magnetic structure. A magnetic structure is the moment density, i.e. a function from the affine space of positions to the vector space of axial vectors

$$\vec{M} : \mathbb{P} \mapsto \mathbb{A} : \vec{O}_a + \vec{r} \mapsto \sum_{j \in \mathcal{J}, \vec{p} \in \mathcal{P}} \vec{S}_{j,\vec{p}}\, d_j(\vec{r} - \vec{r}_j - \vec{p}) \quad ,$$

where $\mathcal{J}$ is the set of magnetic atoms in a unit cell. The unit cell axes (coordinate system a) are $\vec{a}_1, \vec{a}_2, \vec{a}_3 \in \mathbb{V}$ with origin $\vec{O}_a \in \mathbb{P}$. The set $\mathcal{P} = \{n_1\vec{a}_1 + n_2\vec{a}_2 + n_3\vec{a}_3 \mid (n_1, n_2, n_3) \in \mathbb{Z}^3\} \subset \mathbb{V}$ contains the positions of the unit cells relative to the origin of the coordinate system and $\vec{r}_j \in \mathbb{V}$ is the difference of the j-th atom in any unit cell from the position of this unit cell. The function $d_j : \mathbb{V} \to \mathbb{R}$ describes the moment density of the j-th atom and $\vec{S}_{j,\vec{p}} \in \mathbb{A}$ is the magnetic moment of the j-th atom in the unit cell at position $\vec{O}_a + \vec{p}$.

2.3.2.1 Fourier transform of a magnetic structure

In this section, we derive the magnetic structure factor for commensurate and incommensurate magnetic structures. Commensurate magnetic structures can be seen as special cases of incommensurate magnetic structures with propagation vector zero, so we can use one description for both cases. The derivation is adapted from [54] and [61].

So far, every single atom can have any magnetic moment. However, we want to describe ordered magnetic structures by a set $\mathcal{K}$ of propagation vectors $\vec{K} \in \mathbb{V}^*$. In the following, we write the magnetic moments as row vectors with respect to the coordinate system a defined by our choice of unit cell:

$$\vec{S}_{j,\vec{p}} = \sum_{\vec{K}\in\mathcal{K}} \mathrm{e}^{-2\pi\mathrm{i}\vec{K}\cdot\vec{p}}\vec{S}_j(\vec{K}) \quad \text{for} \quad j \in \mathcal{J}, \vec{p} \in \mathcal{P}$$

The quantities $\vec{S}_j(\vec{K}) \in \mathbb{A} + \mathrm{i}\mathbb{A}$ are called fourier coefficients and their number is only $|\mathcal{J}| \cdot |\mathcal{K}|$ instead of infinitely many $\vec{S}_{j,\vec{p}}$. In order to obtain real axial vectors $\vec{S}_{j,\vec{p}} \in \mathbb{A}$, we assert for all $\vec{K} \in \mathbb{V}^*$ the equivalence $\vec{K} \in \mathcal{K} \Leftrightarrow -\vec{K} \in \mathcal{K}$ and for all $\vec{K} \in \mathcal{K}$ the condition $\vec{S}_j(-\vec{K}) = \overline{\vec{S}_j(\vec{K})}$.

For the calculation of the magnetic structure factor, we use a rational approximation for the propagation vectors: Let $N_1, N_2, N_3 \in \mathbb{N}$ be natural numbers and for all $\vec{K} \in \mathcal{K}$ let $m_1^{\vec{K}}, m_2^{\vec{K}}, m_3^{\vec{K}} \in \mathbb{Z}$ be integers, such that with respect to our basis

$$\boldsymbol{K}(a) = (K(a)^1, K(a)^2, K(a)^3) \approx \left(\frac{m_1^{\vec{K}}}{N_1}, \frac{m_2^{\vec{K}}}{N_2}, \frac{m_3^{\vec{K}}}{N_3}\right)$$

is an approximation to the propagation vectors.

We use another coordinate system b with the basis vectors $(\vec{b}_1, \vec{b}_2, \vec{b}_3) = (N_1\vec{a}_1, N_2\vec{a}_2, N_3\vec{a}_3)$ and with the same origin $\vec{O}_b = \vec{O}_a$. The approximated magnetic structure is periodic with respect to the large unit cell defined by the coordinate system b, and the propagation vectors in this basis have the entries $\boldsymbol{K}(b) = (K(b)_1, K(b)_2, K(b)_3) = (m_1^{\vec{K}}, m_2^{\vec{K}}, m_3^{\vec{K}}) \in \mathbb{Z}^3$.

We will calculate the structure factor of the large unit cell b. Most of the reflections will be extinct, but a few will remain. These are the magnetic reflections which belong to the propagation vectors.

For the structure factor $\vec{M}^*$ we only need the atoms within the zeroth large unit cell b. For this, we define the set $\mathcal{Q} = \{n_1\vec{a}_1 + n_2\vec{a}_2 + n_3\vec{a}_3 \mid n_1, n_2, n_3 \in \mathbb{Z}, 0 \le n_1 < N_1, 0 \le n_2 < N_2, 0 \le n_3 < N_3\} \subset \mathcal{P}$. Reflections occur only for scattering vectors $\vec{k}$ which are integer with respect to the basis b, i.e. $\boldsymbol{k}(b) = (k(b)_1, k(b)_2, k(b)_3) \in \mathbb{Z}^3$.

$$\begin{aligned}
\vec{M}^*(\vec{k}) &= \frac{1}{V_b}\int\limits_{\mathbb{V}} \sum_{j\in\mathcal{J}}\sum_{\vec{p}\in\mathcal{Q}} \vec{S}_{j,\vec{p}}\, d_j(\vec{r}-\vec{r}_j-\vec{p})\mathrm{e}^{2\pi\mathrm{i}\vec{k}\cdot\vec{r}}\mathrm{d}\vec{r} \\
&= \frac{1}{V_b}\int\limits_{\mathbb{V}} \sum_{j\in\mathcal{J}}\sum_{\vec{p}\in\mathcal{Q}}\sum_{\vec{K}\in\mathcal{K}} \mathrm{e}^{-2\pi\mathrm{i}\vec{K}\cdot\vec{p}}\vec{S}_j(\vec{K})\, d_j(\vec{r}-\vec{r}_j-\vec{p})\mathrm{e}^{2\pi\mathrm{i}\vec{k}\cdot\vec{r}}\mathrm{d}\vec{r} \\
&= \frac{1}{V_b}\sum_{\vec{K}\in\mathcal{K}}\sum_{\vec{p}\in\mathcal{Q}} \mathrm{e}^{-2\pi\mathrm{i}\vec{K}\cdot\vec{p}}\sum_{j\in\mathcal{J}}\vec{S}_j(\vec{K})\int\limits_{\mathbb{V}} d_j(\vec{r}-\vec{r}_j-\vec{p})\mathrm{e}^{2\pi\mathrm{i}\vec{k}\cdot\vec{r}}\mathrm{d}\vec{r} \\
&= \frac{1}{V_b}\sum_{\vec{K}\in\mathcal{K}}\sum_{\vec{p}\in\mathcal{Q}} \mathrm{e}^{-2\pi\mathrm{i}\vec{K}\cdot\vec{p}}\sum_{j\in\mathcal{J}}\vec{S}_j(\vec{K})\int\limits_{\mathbb{V}} d_j(\vec{r})\mathrm{e}^{2\pi\mathrm{i}\vec{k}\cdot(\vec{r}+\vec{r}_j+\vec{p})}\mathrm{d}\vec{r} \\
&= \frac{1}{V_b}\sum_{\vec{K}\in\mathcal{K}}\sum_{\vec{p}\in\mathcal{Q}} \mathrm{e}^{-2\pi\mathrm{i}(\vec{K}+\vec{k})\cdot\vec{p}}\sum_{j\in\mathcal{J}}\vec{S}_j(\vec{K})\mathrm{e}^{2\pi\mathrm{i}\vec{k}\cdot\vec{r}_j}\int\limits_{\mathbb{V}} d_j(\vec{r})\mathrm{e}^{2\pi\mathrm{i}\vec{k}\cdot\vec{r}}\mathrm{d}\vec{r} \\
&= \frac{1}{V_b}\sum_{\vec{K}\in\mathcal{K}}\sum_{\vec{p}\in\mathcal{Q}} \mathrm{e}^{-2\pi\mathrm{i}(\vec{K}+\vec{k})\cdot\vec{p}}\vec{h}_{\vec{K}}(\vec{k})
\end{aligned}$$

For the last equality, for brevity, we introduced the new quantity

$$\vec{h}_{\vec{K}}(\vec{k}) = \sum_{j\in\mathcal{J}}\vec{S}_j(\vec{K})\mathrm{e}^{2\pi\mathrm{i}\vec{k}\cdot\vec{r}_j}\int\limits_{\mathbb{V}} d_j(\vec{r})\mathrm{e}^{2\pi\mathrm{i}\vec{k}\cdot\vec{r}}\mathrm{d}\vec{r}\ \ .$$

For a further simplification, we write the scalar product $(\vec{K}+\vec{k})\cdot\vec{p}$ in components with respect to the coordinate system b, the numbers x, y, z are integers.

$$\begin{aligned}
\vec{M}^*(\vec{k}) &= \frac{1}{V_b}\sum_{\vec{K}\in\mathcal{K}}\sum_{\vec{p}\in\mathcal{Q}} \vec{h}_{\vec{K}}(\vec{k})\mathrm{e}^{-2\pi\mathrm{i}(\vec{K}+\vec{k})\cdot\vec{p}} \\
&= \frac{1}{V_b}\sum_{\vec{K}\in\mathcal{K}} \vec{h}_{\vec{K}}(\vec{k}) \sum_{\substack{0\le x<N_1\\0\le y<N_2\\0\le z<N_3}} \mathrm{e}^{2\pi\mathrm{i}\left((K(b)_1+k(b)_1)\frac{x}{N_1}+(K(b)_2+k(b)_2)\frac{y}{N_2}+(K(b)_3+k(b)_3)\frac{z}{N_3}\right)} \\
&= \frac{1}{V_b}\sum_{\vec{K}\in\mathcal{K}} \vec{h}_{\vec{K}}(\vec{k}) \left(\sum_{0\le x<N_1} \mathrm{e}^{-2\pi\mathrm{i}(K(b)_1+k(b)_1)\frac{x}{N_1}}\right) \\
&\left(\sum_{0\le y<n_2} \mathrm{e}^{-2\pi\mathrm{i}(K(b)_2+k(b)_2)\frac{y}{N_2}}\right)\left(\sum_{0\le z<N_3} \mathrm{e}^{-2\pi\mathrm{i}(K(b)_3+k(b)_3)\frac{z}{N_3}}\right)
\end{aligned}$$

It is a well known fact that for $n \ge 2$ the n-th roots of unity add up to zero. Without proof it is intuitively clear (though a bit fiddly) that for $n \ge 2$ the sum $\sum_{j=0}^{n-1}\mathrm{e}^{2\pi\mathrm{i}mj/n}$ equals n if $m \in n\mathbb{Z}$ and zero otherwise.

For the structure factor this means:

$$\vec{M}^*(\vec{k}) = \frac{1}{V_b} \sum_{\vec{K} \in \mathcal{K}} \left(\vec{h}_{\vec{K}}(\vec{k}) \begin{cases} N_1 N_2 N_3 & \begin{smallmatrix} \text{if } K(b)_1 + k(b)_1 \in N_1\mathbb{Z} \\ \text{and } K(b)_2 + k(b)_2 \in N_2\mathbb{Z} \\ \text{and } K(b)_3 + k(b)_3 \in N_3\mathbb{Z} \end{smallmatrix} \\ 0 & \text{otherwise} \end{cases} \right)$$

The unit cell a is smaller than unit cell b by the relation $V_b = N_1 N_2 N_3 V_a$. So we can normalize to our small unit cell:

$$\vec{M}^*(\vec{k})(a) = \frac{1}{V_a} \sum_{\substack{\vec{K} \in \mathcal{K} \text{ with} \\ \boldsymbol{K}(a) + \boldsymbol{k}(a) \in \mathbb{Z}^3}} \sum_{j \in \mathcal{J}} \vec{S}_j(\vec{K}) f_j(\vec{k}) \mathrm{e}^{2\pi \mathrm{i} \vec{k} \cdot \vec{r}_j} \quad , \tag{2.5}$$

where

$$f_j(\vec{k}) = \int_{\mathbb{V}} d_j(\vec{r}) \mathrm{e}^{2\pi \mathrm{i} \vec{k} \cdot \vec{r}} \mathrm{d}\vec{r}$$

is the form factor of the j-th atom (if necessary, including the Debye-Waller factor).

2.3.2.2 Scattering amplitude

In the magnetic case, only the component of the value of the Fourier transform perpendicular to the scattering vector gives rise to scattering [61]:

$$\vec{M}^*_\perp(\vec{k}) = \vec{M}^*(\vec{k}) - \left(\frac{\vec{k}}{|\vec{k}|} \cdot \vec{M}^*(\vec{k}) \right) \frac{\vec{k}}{|\vec{k}|} \tag{2.6}$$

Since this is a quantum mechanical process, we describe the perpendicular component of the Fourier transform $\vec{M}^*_\perp(\vec{k})$ of the magnetic moment density and the spin $\vec{s}_{\text{in}}$ and $\vec{s}_{\text{out}}$ of the incoming and outgoing neutron in the basis of the Pauli matrices [62],

$$\sigma_0 = \begin{pmatrix} 1 & 0 \\ 0 & 1 \end{pmatrix}, \sigma_1 = \begin{pmatrix} 0 & 1 \\ 1 & 0 \end{pmatrix}, \sigma_2 = \begin{pmatrix} 0 & -\mathrm{i} \\ \mathrm{i} & 0 \end{pmatrix}, \sigma_3 = \begin{pmatrix} 1 & 0 \\ 0 & -1 \end{pmatrix},$$

so that we can write with respect to a basis $\vec{e}_1, \vec{e}_2, \vec{e}_3$, where $\vec{e}_3$ is the quantization axis and the basis is orthonormal [62]:

$$\begin{aligned}\vec{M}_\perp^*(\vec{k}) &= M_\perp^1(\vec{k})\vec{e}_1 + M_\perp^2(\vec{k})\vec{e}_2 + M_\perp^3(\vec{k})\vec{e}_3 \\ &\hat{=} M_\perp^1(\vec{k})\sigma_1 + M_\perp^2(\vec{k})\sigma_2 + M_\perp^3(\vec{k})\sigma_3 \\ &= \begin{pmatrix} M_\perp^3(\vec{k}) & M_\perp^1(\vec{k}) - \mathrm{i}M_\perp^2(\vec{k}) \\ M_\perp^1(\vec{k}) + \mathrm{i}M_\perp^2(\vec{k}) & -M_\perp^3(\vec{k}) \end{pmatrix}\end{aligned}$$

For the components of $\vec{M}_\perp^*(\vec{k})$ we omit the $*$ for the sake of readability. The nuclear scattering does not change the spin of the neutron, so we can describe it as a scalar [62]:

$$N^*(\vec{k}) \hat{=} \begin{pmatrix} N^*(\vec{k}) & 0 \\ 0 & N^*(\vec{k}) \end{pmatrix}$$

The scattering amplitude taking into account nuclear scattering and magnetic scattering (by the electron shells), can thus be written as [62]:

$$\begin{aligned}a(\vec{k}) &\hat{=} \begin{pmatrix} N^*(\vec{k}) & 0 \\ 0 & N^*(\vec{k}) \end{pmatrix} + p \begin{pmatrix} M_\perp^3(\vec{k}) & M_\perp^1(\vec{k}) - \mathrm{i}M_\perp^2(\vec{k}) \\ M_\perp^1(\vec{k}) + \mathrm{i}M_\perp^2(\vec{k}) & -M_\perp^3(\vec{k}) \end{pmatrix} \\ &= \begin{pmatrix} N^*(\vec{k}) + pM_\perp^3(\vec{k}) & pM_\perp^1(\vec{k}) - \mathrm{i}pM_\perp^2(\vec{k}) \\ pM_\perp^1(\vec{k}) + \mathrm{i}pM_\perp^2(\vec{k}) & N^*(\vec{k}) - pM_\perp^3(\vec{k}) \end{pmatrix} \\ &= A(\vec{k})\end{aligned}$$

The factor $p = 0.2696 \cdot 10^{-12}\,\mathrm{cm}/\mu_\mathrm{B}$ (where μ_B is the Bohr magneton) relates a magnetic moment to a scattering length [61].

The quantity $a(\vec{k})$ is a quantum mechanical operator and we wrote it as $A(\vec{k})$ in the basis given by the quantization axis. If $|\mathrm{in}\rangle$ and $|\mathrm{out}\rangle$ are the spin states of the incoming and outgoing neutron, we can calculate the probability of this scattering process by the square of the absolute value $\left|\langle \mathrm{out}|a(\vec{k})|\mathrm{in}\rangle\right|^2$ of the matrix element.

For the scope of this work it is sufficient to consider only one quantization axis, so that we can restrict the incoming and outgoing neutron spin states to

$$|\uparrow\rangle \hat{=} \begin{pmatrix} 1 \\ 0 \end{pmatrix} \text{ and } |\downarrow\rangle \hat{=} \begin{pmatrix} 0 \\ 1 \end{pmatrix} \quad .$$

We now get four different matrix elements [61]:

$$\begin{aligned}
\langle\uparrow|a(\vec{k})|\uparrow\rangle &= \begin{pmatrix}1 & 0\end{pmatrix} A(\vec{k}) \begin{pmatrix}1\\0\end{pmatrix} = N^*(\vec{k}) + pM^3_\perp(\vec{k}) \\
\langle\downarrow|a(\vec{k})|\downarrow\rangle &= \begin{pmatrix}0 & 1\end{pmatrix} A(\vec{k}) \begin{pmatrix}0\\1\end{pmatrix} = N^*(\vec{k}) - pM^3_\perp(\vec{k}) \\
\langle\downarrow|a(\vec{k})|\uparrow\rangle &= \begin{pmatrix}0 & 1\end{pmatrix} A(\vec{k}) \begin{pmatrix}1\\0\end{pmatrix} = pM^1_\perp(\vec{k}) + \mathrm{i}pM^2_\perp(\vec{k}) \\
\langle\uparrow|a(\vec{k})|\downarrow\rangle &= \begin{pmatrix}1 & 0\end{pmatrix} A(\vec{k}) \begin{pmatrix}0\\1\end{pmatrix} = pM^1_\perp(\vec{k}) - \mathrm{i}pM^2_\perp(\vec{k})
\end{aligned} \tag{2.7}$$

2.3.3 Unpolarized neutron diffraction

If the incoming neutron beam is not polarized, half of the incoming neutrons are in spin state $|\uparrow\rangle$ and the other half are in state $|\downarrow\rangle$. If furthermore the outgoing neutron beam is not analysed with respect to the spin, all neutrons are detected. This means, that the four probabilities are weighted by 1/2 and added. The probabilities are the squares of the absolute values of the matrix elements in equations 2.7 (the vinculum denotes complex conjugate) [62] :

$$\begin{aligned}
&\frac{1}{2}\left|\langle\uparrow|a(\vec{k})|\uparrow\rangle\right|^2 + \frac{1}{2}\left|\langle\downarrow|a(\vec{k})|\downarrow\rangle\right|^2 + \frac{1}{2}\left|\langle\downarrow|a(\vec{k})|\uparrow\rangle\right|^2 + \frac{1}{2}\left|\langle\uparrow|a(\vec{k})|\downarrow\rangle\right|^2 \\
=&\frac{1}{2}\Big((N^*(\vec{k}) + pM^3_\perp(\vec{k}))(\overline{N}^*(\vec{k}) + p\overline{M}^3_\perp(\vec{k})) \\
&+ (N^*(\vec{k}) - pM^3_\perp(\vec{k}))(\overline{N}^*(\vec{k}) - p\overline{M}^3_\perp(\vec{k})) \\
&+ (pM^1_\perp(\vec{k}) + \mathrm{i}pM^2_\perp(\vec{k}))(p\overline{M}^1_\perp(\vec{k}) - \mathrm{i}p\overline{M}^2_\perp(\vec{k})) \\
&+ (pM^1_\perp(\vec{k}) - \mathrm{i}pM^2_\perp(\vec{k}))(p\overline{M}^1_\perp(\vec{k}) + \mathrm{i}p\overline{M}^2_\perp(\vec{k}))\Big) \\
=&\left|N^*(\vec{k})\right|^2 + p^2\left(\left|M^1_\perp(\vec{k})\right|^2 + \left|M^2_\perp(\vec{k})\right|^2 + \left|M^3_\perp(\vec{k})\right|^2\right) \\
\overset{(1)}{=}&\left|N^*(\vec{k})\right|^2 + \left|p\vec{M}^*_\perp(\vec{k})\right|^2 \\
\overset{(2)}{=}&\left|F_{\mathrm{N}}(\vec{k})\right|^2 + \left|\vec{F}_{\mathrm{M}}(\vec{k})\right|^2
\end{aligned}$$

For equality (1), we use that the basis we have identified with the pauli matrices is

orthonormal. For equality (2), we have defined the nuclear structure factor F_N and the magnetic structure factor F_M as follows:

$$\begin{aligned} F_\mathrm{N}(\vec{k}) &:= N^*(\vec{k}) \\ \vec{F}_\mathrm{M}(\vec{k}) &:= p\vec{M}^*_\perp(\vec{k}) \end{aligned}$$

2.3.4 Polarized neutron diffraction

For many neutron diffraction experiments, polarized neutrons are used. The spin of the neutrons in the incoming beam are polarized along a certain direction, and the spin of the neutrons in the outgoing beam is analyzed in a further direction.

In the simplest case, both directions are parallel or antiparallel. This type of experiment is called uniaxial polarization analysis. It was first carried out in 1969 by Moon et al. [64].

Two decades later, in 1989, Tasset carried out a a neutron diffraction experiment that coniders all possible orientations of the polarizations of the incoming and the outgoing beam [65]. This type of experiment is called spherical polarization analysis.

In the following paragraph, uniaxial polarization analysis is explained, focusing on the special cases that are relevant for the present work.

2.3.4.1 Uniaxial polarization analysis

A uniaxial polarization analysis neutron scattering experiment consists of the neutron source with monochromator, a polarizer, the sample, an analyser and the detector. (The analyser is technically also a polarizer, but we use the word "analyser" in order to distinguish between the two polarizers.)

We want to measure the squares of the absolute values of the four matrix elements in equations 2.7, which we call "intensities":

$$\begin{aligned} I^{\uparrow\uparrow}(\vec{k}) &= \left|\langle\uparrow|a(\vec{k})|\uparrow\rangle\right|^2 \\ I^{\downarrow\downarrow}(\vec{k}) &= \left|\langle\downarrow|a(\vec{k})|\downarrow\rangle\right|^2 \\ I^{\uparrow\downarrow}(\vec{k}) &= \left|\langle\downarrow|a(\vec{k})|\uparrow\rangle\right|^2 \\ I^{\downarrow\uparrow}(\vec{k}) &= \left|\langle\uparrow|a(\vec{k})|\downarrow\rangle\right|^2 \end{aligned} \tag{2.8}$$

(In the following, we omit the $\vec{k}$ dependence for sake of readability.) The idea is, to orient the polarizer and the analyzer in the way that only neutrons of the desired incoming and

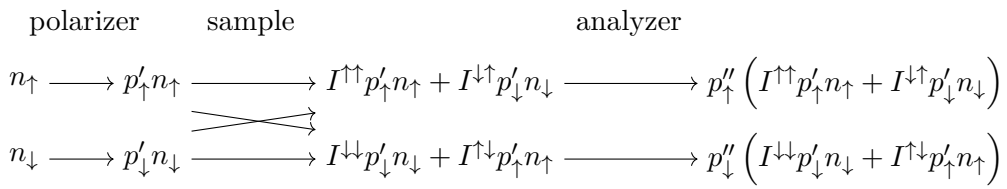

Figure 2.1: Schematic sketch of a uniaxial polarization analysis neutron scattering experiment. The neutrons pass the polarizer, the sample, and the analyser. The upper row denotes the number of neutrons with spin up, and the lower row the number of neutrons with spin down.

outgoing spin directions can pass. The problem is, that the polarizer and the analyzer are not ideal, so that also neutrons with the wrong spin direction can pass: At the end of the day, the detector detects the neutrons with any spin that "survived" the path through the polarizer, the scattering process at the sample in the according direction, and the analyser. Four different combinations of polarizer and analyzer oriented up or down can be measured: $\uparrow\uparrow, \downarrow\downarrow, \uparrow\downarrow, \downarrow\uparrow$, where the first digit represents the orientation of the polarizer and the second digit the orientation of the analyser. These combinations are called "channels", while the first two are called "non-spin-flip channels" (NSF) and the second two are called "spin-flip channels" (SF). We call the number of detected neutrons for the four cases $C^{\uparrow\uparrow}, C^{\downarrow\downarrow}, C^{\downarrow\uparrow}, C^{\uparrow\downarrow}$. If the polarizer and analyser were ideal, the channels would equal the intensities: $C^{\uparrow\uparrow} = I^{\uparrow\uparrow}, C^{\downarrow\downarrow} = I^{\downarrow\downarrow}, C^{\uparrow\downarrow} = I^{\uparrow\downarrow}, C^{\downarrow\uparrow} = I^{\downarrow\uparrow}$. For real polarizers and analyzers, these values differ, but the intensities can be calculated from the channels as shown in the following considerations. The derivation of Equation 2.15 is adapted from [66].

The number of neutrons measured for the four channels can be calculated straight forward by considering the probability that a neutron "survives" the stages of the experimental setup. This is schematically shown in Figure 2.1. The upper row contains the number of neutrons with spin up, and the lower row contains the number of neutrons with spin down. On the left hand side, $n_\uparrow$ neutrons with spin up and $n_\downarrow$ neutrons with spin down are emitted by the monochromator. Usually, n neutrons will be emitted, where $n_\uparrow = n_\downarrow = \frac{1}{2}n$. Following the arrows, the neutrons pass the polarizer. The probability that a neutron with spin up passes the polarizer is $p'_\uparrow$, and for a neutron with spin down it is $p'_\downarrow$. Behind the polarizer, we have $p'_\uparrow n_\uparrow$ neutrons with spin up and $p'_\downarrow n_\downarrow$ neutrons with spin down. Some of these neutrons are scatted by the sample in the direction specified by the scattering vector $\vec{k}$, while some of them change their spin direction. The probabilities for these are given by the intensities in equations 2.8. In the considered outgoing beam, there are $I^{\uparrow\uparrow} p'_\uparrow n_\uparrow + I^{\downarrow\uparrow} p'_\downarrow n_\downarrow$ neutrons with spin up and $I^{\downarrow\downarrow} p'_\downarrow n_\downarrow + I^{\uparrow\downarrow} p'_\uparrow n_\uparrow$ neutrons with spin down. The neutrons with spin up pass the analyzer with probability $p''_\uparrow$ and the neutrons with spin down with probability $p''_\downarrow$. The detector counts all of them, so we measure

$$p''_\uparrow I^{\uparrow\uparrow} p'_\uparrow n_\uparrow + p''_\uparrow I^{\downarrow\uparrow} p'_\downarrow n_\downarrow + p''_\downarrow I^{\downarrow\downarrow} p'_\downarrow n_\downarrow + p''_\downarrow I^{\uparrow\downarrow} p'_\uparrow n_\uparrow \tag{2.9}$$

neutrons.

polarizer	analyser	probabilities	number of neutrons detected for this channel
$\uparrow$	$\uparrow$	$p'_\uparrow = r'$ $p'_\downarrow = w'$ $p''_\uparrow = r''$ $p''_\downarrow = w''$	$C^{\uparrow\uparrow} =$ $r''I^{\uparrow\uparrow}r'n_\uparrow + r''I^{\downarrow\uparrow}w'n_\downarrow + w''I^{\downarrow\downarrow}w'n_\downarrow + w''I^{\uparrow\downarrow}r'n_\uparrow$
$\downarrow$	$\downarrow$	$p'_\uparrow = w'$ $p'_\downarrow = r'$ $p''_\uparrow = w''$ $p''_\downarrow = r''$	$C^{\downarrow\downarrow} =$ $w''I^{\uparrow\uparrow}w'n_\uparrow + w''I^{\downarrow\uparrow}r'n_\downarrow + r''I^{\downarrow\downarrow}r'n_\downarrow + r''I^{\uparrow\downarrow}w'n_\uparrow$
$\uparrow$	$\downarrow$	$p'_\uparrow = r'$ $p'_\downarrow = w'$ $p''_\uparrow = w''$ $p''_\downarrow = r''$	$C^{\uparrow\downarrow} =$ $w''I^{\uparrow\uparrow}r'n_\uparrow + w''I^{\downarrow\uparrow}w'n_\downarrow + r''I^{\downarrow\downarrow}w'n_\downarrow + r''I^{\uparrow\downarrow}r'n_\uparrow$
$\downarrow$	$\uparrow$	$p'_\uparrow = w'$ $p'_\downarrow = r'$ $p''_\uparrow = r''$ $p''_\downarrow = w''$	$C^{\downarrow\uparrow} =$ $r''I^{\uparrow\uparrow}w'n_\uparrow + r''I^{\downarrow\uparrow}r'n_\downarrow + w''I^{\downarrow\downarrow}r'n_\downarrow + w''I^{\uparrow\downarrow}w'n_\uparrow$

Table 2.1: The number of neutrons in the four channels can be calculated by term 2.9 by substituting the probabilities.

The polarizer is not ideal, so the probability for a neutron with the desired spin direction to pass the polarizer is r', and with wrong spin direction the probability to pass is w', with $0 < w' < r' < 1$. Analogously, r'' and w'' for the analyzer are defined. The number of neutrons in the four channels can now be calculated by substituting the probability variables $p'_\uparrow, p'_\downarrow, p''_\uparrow, p''_\downarrow$ in equation 2.9 by the probabilities r', w', r'', w'' as shown in table 2.1.

This can be written in matrix form as follows:

$$\begin{pmatrix} C^{\uparrow\uparrow} \\ C^{\uparrow\downarrow} \\ C^{\downarrow\uparrow} \\ C^{\downarrow\downarrow} \end{pmatrix} = \begin{pmatrix} r''r' & w''r' & r''w' & w''w' \\ w''r' & r''r' & w''w' & r''w' \\ r''w' & w''w' & r''r' & w''r' \\ w''w' & r''w' & w''r' & r''r' \end{pmatrix} \begin{pmatrix} I^{\uparrow\uparrow}n_\uparrow \\ I^{\uparrow\downarrow}n_\uparrow \\ I^{\downarrow\uparrow}n_\downarrow \\ I^{\downarrow\downarrow}n_\downarrow \end{pmatrix}$$

The flipping ratios of the polarizer and the analyzer are defined as $R' = r'/w'$ and $R'' = r''/w''$, respectively [67]. Substituting this, we get:

$$\begin{pmatrix} C^{\uparrow\uparrow} \\ C^{\uparrow\downarrow} \\ C^{\downarrow\uparrow} \\ C^{\downarrow\downarrow} \end{pmatrix} = \begin{pmatrix} R''R' & R' & R'' & 1 \\ R' & R''R' & 1 & R'' \\ R'' & 1 & R''R' & R' \\ 1 & R'' & R' & R''R' \end{pmatrix} \begin{pmatrix} I^{\uparrow\uparrow} n_\uparrow \\ I^{\uparrow\downarrow} n_\uparrow \\ I^{\downarrow\uparrow} n_\downarrow \\ I^{\downarrow\downarrow} n_\downarrow \end{pmatrix} w''w' \tag{2.10}$$

Special case: Purely magnetic reflections of non-chiral magnetic structure or purely nuclear reflections Equation 2.10 can be drastically simplified for two cases.

First, we consider the case that a purely magnetic reflection of a non-chiral magnetic structure is considered. Since the reflection is purely magnetic, we can assume $N^*(\vec{k}) = 0$ and non-chirality means that $\boldsymbol{M}^*_\perp$ is parallel to its complex conjugate $\overline{\boldsymbol{M}}^*_\perp$ [62]. The second condition means that it is possible to choose some factor $\alpha \in \mathbb{R}$, such that $\alpha M^1_\perp = \overline{M}^1_\perp$, $\alpha M^2_\perp = \overline{M}^2_\perp$ and $\alpha M^3_\perp = \overline{M}^3_\perp$. This means that $M^1_\perp \overline{M}^2_\perp - \overline{M}^1_\perp M^2_\perp = 0$. Thus, equation 2.7 substituted into equation 2.8 can be simplified in the following way:

$$\begin{aligned} I^{\uparrow\uparrow}(\vec{k}) &= p^2 |M_\perp(\vec{k})^3|^2 \\ I^{\downarrow\downarrow}(\vec{k}) &= p^2 |M_\perp(\vec{k})^3|^2 \\ I^{\uparrow\downarrow}(\vec{k}) &= p^2 |M_\perp(\vec{k})^1|^2 + p^2 |M_\perp(\vec{k})^2|^2 \\ I^{\downarrow\uparrow}(\vec{k}) &= p^2 |M_\perp(\vec{k})^1|^2 + p^2 |M_\perp(\vec{k})^2|^2 \end{aligned}$$

Even more simple is the case, where a purely nuclear reflection is considered: In this case, $I^{\uparrow\uparrow}(\vec{k}) = I^{\downarrow\downarrow} = |N^*(\vec{k})|^2$ and $I^{\uparrow\downarrow}(\vec{k}) = I^{\downarrow\uparrow}(\vec{k}) = 0$.

In both cases, we have $I^{\uparrow\uparrow} = I^{\downarrow\downarrow}$ and $I^{\uparrow\downarrow} = I^{\downarrow\uparrow}$. Furthermore, we assume that $n_\uparrow = n_\downarrow$. Now we can write equation 2.10 as

$$\begin{pmatrix} C^{\uparrow\uparrow} \\ C^{\downarrow\uparrow} \\ C^{\uparrow\uparrow} \\ C^{\downarrow\uparrow} \end{pmatrix} = \begin{pmatrix} R''R' & R' & 1 & R'' \\ R' & R''R' & R'' & 1 \\ 1 & R'' & R''R' & R' \\ R'' & 1 & R' & R''R' \end{pmatrix} \begin{pmatrix} I^{\uparrow\uparrow} n_\uparrow \\ I^{\downarrow\uparrow} n_\uparrow \\ I^{\uparrow\uparrow} n_\uparrow \\ I^{\downarrow\uparrow} n_\uparrow \end{pmatrix} w''w' \quad ,$$

which is redundant and can be further simplified as

$$\begin{pmatrix} C^{\uparrow\uparrow} \\ C^{\downarrow\uparrow} \end{pmatrix} = \begin{pmatrix} R''R'+1 & R''+R' \\ R''+R' & R''R'+1 \end{pmatrix} \begin{pmatrix} I^{\uparrow\uparrow} \\ I^{\downarrow\uparrow} \end{pmatrix} w''w'n_\uparrow$$
$$= \begin{pmatrix} r''r'+w''w' & r''w'+r'w'' \\ r''w'+r'w'' & r''r'+w''w' \end{pmatrix} \begin{pmatrix} I^{\uparrow\uparrow} \\ I^{\downarrow\uparrow} \end{pmatrix} n_\uparrow \quad .$$

We can invert the matrix to solve the equation for $I^{\uparrow\uparrow}$ and $I^{\downarrow\uparrow}$:

$$\begin{pmatrix} I^{\uparrow\uparrow} \\ I^{\downarrow\uparrow} \end{pmatrix} = \frac{1}{(r''r'+w''w')^2-(r''w'+r'w'')^2} \begin{pmatrix} r''r'+w''w' & -r''w'-r'w'' \\ -r''w'-r'w'' & r''r'+w''w' \end{pmatrix} \begin{pmatrix} C^{\uparrow\uparrow} \\ C^{\downarrow\uparrow} \end{pmatrix} \frac{1}{n_\uparrow} \tag{2.11}$$

$$= \frac{r''w'+r'w''}{(r''r'+w''w')^2-(r''w'+r'w'')^2} \begin{pmatrix} \frac{r''r'+w''w'}{r''w'+r'w''} & -1 \\ -1 & \frac{r''r'+w''w'}{r''w'+r'w''} \end{pmatrix} \begin{pmatrix} C^{\uparrow\uparrow} \\ C^{\downarrow\uparrow} \end{pmatrix} \frac{1}{n_\uparrow} \tag{2.12}$$

$$= \frac{1}{r''w'+r'w''} \frac{1}{\left(\frac{r''r'+w''w'}{r''w'+r'w''}\right)^2-1} \begin{pmatrix} \frac{r''r'+w''w'}{r''w'+r'w''} & -1 \\ -1 & \frac{r''r'+w''w'}{r''w'+r'w''} \end{pmatrix} \begin{pmatrix} C^{\uparrow\uparrow} \\ C^{\downarrow\uparrow} \end{pmatrix} \frac{1}{n_\uparrow} \tag{2.13}$$

$$= \frac{1}{w} \frac{1}{R^2-1} \begin{pmatrix} R & -1 \\ -1 & R \end{pmatrix} \begin{pmatrix} C^{\uparrow\uparrow} \\ C^{\downarrow\uparrow} \end{pmatrix} \frac{1}{n_\uparrow} \tag{2.14}$$

In the last step we used the substitution

$$\begin{aligned} r &:= r''r'+w''w' \\ w &:= r''w'+w''r' \\ R &:= \frac{r}{w} = \frac{r''r'+w''w'}{r'w'+w''r'} = \frac{R''R'+1}{R''+R'} \quad . \end{aligned}$$

Writing th 2.11 in the form of two equations, we get [66]:

$$\begin{aligned} I^{\uparrow\uparrow} &= \frac{1}{n_\uparrow} \frac{1}{w} \frac{R-1}{R^2-1} \left(C^{\uparrow\uparrow} + \frac{1}{R-1} \left(C^{\uparrow\uparrow} - C^{\uparrow\downarrow} \right) \right) \\ I^{\downarrow\uparrow} &= \frac{1}{n_\uparrow} \frac{1}{w} \frac{R-1}{R^2-1} \left(C^{\downarrow\uparrow} + \frac{1}{R-1} \left(C^{\downarrow\uparrow} - C^{\uparrow\uparrow} \right) \right) \quad . \end{aligned} \tag{2.15}$$

This gives a great experimental simplification in the cases considered: We do not need to know the flipping ratios R' of the polarizer and R'' of the analyser. Instead, it suffices to determine the overall flipping ratio R. This can be determined by measuring the non-spin-flip channel $C^{\uparrow\uparrow}$ and the spin-flip channel $C^{\downarrow\uparrow}$ of a purely magnetic reflection. Since we know that $I^{\downarrow\uparrow} = 0$ and using equation 2.15, we can determine the overall flipping ratio $R = C^{\uparrow\uparrow}/C^{\downarrow\uparrow}$.

2.4 Structural refinements

2.4.1 The algorithm used in refinement software

This work mainly deals with structural refinements of crystal structures that are roughly known and only small deviations are investigated. This issue differs from structural solutions where the crystal structure of a totally unknown compound is determined. For the latter case, techniques can be used that calculated Fourier maps from the measured intensities – first with only small-angle reflections and a rough spatial resolution and then subsequently increase the number of reflections to higher angles and improve the resolution of the electron density map [68]. The former case (refinements of principally known crystal structures) will be addressed in this section.

The principle behind refinements is that a model is varied until it best fits to observed data. In this case, the model is a crystal structure, i.e. atomic positions and atomic displacement parameters (ADPs). There are different possibilities to choose the quantity that is used as observed data [68]: The intensity I^{obs} of reflections measured in a diffraction experiment can be used. Alternatively, the absolute value of the structure factor can be used, where the sign is inherited from the intensity ($F^{\mathrm{obs}} = \mathrm{sign}(I^{\mathrm{obs}}) \cdot \sqrt{I^{\mathrm{obs}}}$). A third alternative is the quantity $(F^{\mathrm{obs}})^2$ which differs from I^{obs} in the cases where negative intensities were recorded due to background subtraction. Apart from technical details and problems with corrupted data, the choice does not seem to have any serious influence on the result [68]. Whatever quantity is chosen, it will be called Y^{obs} in the following. The model allows to predict the same quantity Y^{cal}. The refinement minimizes the difference between the observed and calculated values Y^{obs} and Y^{cal}. An overview of the algorithm that subsequently reduces this difference is given in [68]. The difference between the observed and calculated values is called "minimization function" M and can be defined in different ways. The program JANA2006, used in this work, chooses [69] the least-squares method with

$$M = \sum_{\text{all reflections } (h\,k\,l)} w_{(h\,k\,l)} \left(Y^{\mathrm{obs}}_{(h\,k\,l)} - Y^{\mathrm{cal}}_{(h\,k\,l)} \right)^2$$

which is a weighted sum of deviation squares [68]. By default, the considered quantity is $Y = F$ and the weights are chosen as $w_{(h\,k\,l)} = 1/\sigma \left(F^{\mathrm{obs}}_{(h\,k\,l)} \right)^2$ where $\sigma \left(F^{\mathrm{obs}}_{(h\,k\,l)} \right)$ is

the error of the observed structure factor[6]. In this work, these default choices are not changed.

2.4.2 *R* values and goodness of fit

2.4.2.1 The internal *R* value

Before a structural refinement is carried out, intensities of reflections that are equivalent with respect to the point group are averaged. Let $\{h\,k\,l\}$ be the set of all reflections that are equivalent to $(h\,k\,l)$. We denote the number of measured equivalent reflections by $|\{h\,k\,l\}|$. The average value is

$$\overline{I}_{\{h\,k\,l\}} = \frac{1}{|\{h\,k\,l\}|} \sum_{(h'\,k'\,l')\in\{h\,k\,l\}} I_{(h'\,k'\,l')} \quad .$$

The internal R value $R(\mathrm{int})$ is defined as [70][71]

$$R(\mathrm{int}) = \frac{\sum\limits_{\{h\,k\,l\}} \sum\limits_{(h'\,k'\,l')\in\{h\,k\,l\}} \left| I_{(h'\,k'\,l')} - \overline{I}_{\{h\,k\,l\}} \right|}{\sum\limits_{\{h\,k\,l\}} \sum\limits_{(h'\,k'\,l')\in\{h\,k\,l\}} I_{(h'\,k'\,l')}} \quad .$$

For an ideal experiment and correct point group, the $R(\mathrm{int})$ value woud be zero. Deviations can be attributed to statistical errors, systematical errors or a wrong point group. From the knowledge of the author, good single-crystal X-ray diffraction data after absorption correction yield $R(\mathrm{int})$ values not much greater than 5 %. Also with $R(\mathrm{int}) \approx 10\,\%$, however, useful refinements might be possible. Often this quantity is named $R^2(\mathrm{int})$ or $R2(\mathrm{int})$ in order to imply that the intensity (i.e. F^2) was used in the calculation.

There is an alternative to the internal R value [71]:

$$R(\mathrm{meas}) = \frac{\sum\limits_{\{h\,k\,l\}} \sqrt{\frac{|\{h\,k\,l\}|}{|\{h\,k\,l\}|-1}} \sum\limits_{(h'\,k'\,l')\in\{h\,k\,l\}} \left| I_{(h'\,k'\,l')} - \overline{I}_{\{h\,k\,l\}} \right|}{\sum\limits_{\{h\,k\,l\}} \sum\limits_{(h'\,k'\,l')\in\{h\,k\,l\}} I_{(h'\,k'\,l')}} \quad .$$

The quantity $R(\mathrm{meas})$ has the advantage that the quality of data collections with few reflections is not overestimated. Despite that, usually the less meaningful $R(\mathrm{int})$ is used.

[6] This can be checked in the output file with ending "ref".

2.4.2.2 The *R* values of the refinement

After the structural refinement converged, R values can be calculated that compare the model to the measured data. This is done by the following formula [70]:

$$R = \frac{\sum\limits_{\text{all reflections } (h\,k\,l)} \left| F^{\text{obs}}_{(h\,k\,l)} - F^{\text{cal}}_{(h\,k\,l)} \right|}{\sum\limits_{\text{all reflections } (h\,k\,l)} F^{\text{obs}}_{(h\,k\,l)}}$$

The software JANA2006 [69] calculates four variations of this quantity: R(obs) only considers the observed reflections, while R(all) takes into account all of them. A reflection is said to be observed, if the intensity exceeds a threshold (by default 3 times its error). The value wR(obs) and wR(all) use a weighted sum of the observed resp. all reflections. Good refinements should not yield R values much greater than 3 %.

Alternatively, the R values can be calculated using the intensities. In this case, they are often labeled R^2(obs) etc. Such values are expected to be much greater than the ones calculated from structure factors. A further difference is that strong reflections get more weight in the sum if intensity is used.

2.4.2.3 The goodness of fit

The χ^2 test allows to detect a bad fit [72]. For structural refinements, this value is defined as [68]

$$\chi^2 = \sum_{\text{all reflections } (h\,k\,l)} w_{(h\,k\,l)} \left(Y^{\text{obs}}_{(h\,k\,l)} - Y^{\text{cal}}_{(h\,k\,l)} \right)^2 \quad , \tag{2.16}$$

where $w_{(h\,k\,l)} = 1/\sigma^2_{(h\,k\,l)}$ is the inverse of the squared error on the quantity $Y^{\text{obs}}_{(h\,k\,l)}$. For possible choices of Y cf. Section 2.4.1. The value for χ^2 is expected to be the number of degrees of freedom, i.e. $n - m$ for n reflections and m parameters [72]

Closely related is the goodness of fit, denoted by S or GoF. It is defined as [68]

$$\text{GoF} = \sqrt{\frac{\chi^2}{n-m}}$$

and thus expected to amount to 1. If the goodness of fit is much greater than 1, the model might be wrong or the experimental errors are larger than assumed. A goodness of fit much smaller than 1 is an indication for a pessimistic error estimation [68].

2.4.3 The physical meaning of structural results

Structural refinements must always be considered in the context of research. The models used in refinements have many degrees of freedom and often different models yield similarly good R values. It can easily happen that artifacts of the measurements are interpreted as structural features. For example anisotropic atomic displacement parameters (ADPs) are prone to compensate small inaccuracies which always occur in real experiments. Though, it might be necessary to include anisotropic ADPs in the model because otherwise other parameters might compensate the missing degrees of freedom. Therefore, a structural solution must be compared with results of other experimental methods. It is common experience that refinements of small structural distortions on their own are usually not reliable in a scientific sense. Distortions of the metric can be determined by evaluating peak positions in powder diffraction data. Polarized microscopy is very sensible for the determination of monoclinic distortions. Local distortions can be verified by means of spectroscopy. There are also some tests which give indications for the reasonableness of a structural solution. These tests can increase the reliability. Some of these concepts are presented in this section.

2.4.3.1 Bond-valence sum

The concept of bond-valence sums allows the prediction of crystal structures on the basis of empirically found parameters from known structures. It is used in this work for deciding whether a structural refinement is plausible or not. The parameters can be found in [73] which base on previous results in [74].

A bond valence can be attributed to each bond between neighbored atoms with the following condition: The sum of all bond valences of the bonds an atom is involved in equals the valence of this atom [73]:

$$\sum_j v_{ij} = V_i$$

Here, i is a fixed cation with valence V_i, j runs over all of its neighbors, and v_{ij} is the bond valence of the bond between the cation i and the anion j [74]. Each bond valence is predicted by the empirical expression [73] [74]

$$v_{ij} = \mathrm{e}^{(R_{ij}-d_{ij})/b} \quad ,$$

where $b = 0.37\,\text{Å}$ is approximately constant for all pairs of elements [74], d_{ij} is the distance between the cation i and the anion j, and R_{ij} is the bond-valence parameter that depends on the pair of elements. An exhaustive listing of bond-valence parameters can be found in [73].

In this work, bond-valence sums are used in order to carry out a check for credibility of structural refinements.

2.4.3.2 Goldschmidt tolerance factor

Crystals with the same chemical formula can have isomorph crystal structures, depending on the relative sizes of their compounds. In the case of structures with stoichiometry $A^{2+}B^{4+}X_3^{2-}$, the crystal structure can be of perovskite type. It was phenomenologically found [75] that the perovskite type appears if the Goldschmidt tolerance factor

$$t_{\mathrm{G}} = \frac{r_{\mathrm{A}} + r_{\mathrm{X}}}{\sqrt{2}(r_{\mathrm{B}} + r_{\mathrm{X}})} \quad ,$$

where r_{A}, r_{B} and r_{X} are the radii of the ions A^{2+}, B^{4+} and X^{2-}, respectively, lies between 0.8 and 1. If the Goldschmidt tolerance factor t_{G} is smaller, the crystal structure is distorted.

For the computation of t_{G} is is important to use the correct valences and coordination numbers of the ions.

3 Instruments

3.1 X-ray diffraction instruments

3.1.1 Bruker AXS Kappa APEX II

Single-crystal X-ray diffraction experiments in this work were carried out on a Bruker AXS Kappa APEX II diffractometer, which is a four-circle single-crystal X-ray diffractometer produced by Bruker AXS Inc.

An X-ray tube with a Mo anode is used to generate MoK_α radiation with a wavelength of $\lambda = 0.710730\,\text{Å}$, neglecting the $K_{\alpha1} - K_{\alpha2}$ splitting [76]. A tunable graphite crystal is used as monochromator [76]. The monochromatic beam is sent through a collimator in a horizontal direction. The X-ray tube is usually operated with an acceleration voltage of 50 kV and a current of 30 mA. In order to avoid the $\lambda/2$ effect, where radiation with half the nominal wavelength is produced and gives rise to reflections which can be confused with superstructure reflections, for some measurements a lower acceleration voltage is used. The wavelength that must be avoided is $\lambda/2 = 0.355365\,\text{Å}$, which corresponds to an acceleration voltage of $hc/(\lambda/2) = 34.96\,\text{kV}$, where h is the Planck constant and c the velocity of light in vacuum. Thus, in cases where the $\lambda/2$ effect shall be avoided, an acceleration voltage of 30 kV is a good choice.

The goniometer contains three motors for the orientation of the sample. The ω axis is oriented vertically, and thus orthogonal to the direction of the incoming beam. The ω motor moves the κ axis around the ω axis. The κ axis is tilted approximately 55° away from the vertical direction[1]. The κ motor moves the ϕ axis around the κ axis. The ϕ motor rotates the sample about the ϕ axis. This setup is equivalent to the Eulerian cradle, whereas the χ axis of the latter is replaced by the κ axis. Both setups are explained in [63]. The κ geometry has the advantage that it does not use a χ circle that shields the incoming or outgoing beam in some directions and impedes the access of the sample from the top, which can be necessary for low- or high-temperature measurements.

A video microscope is used for centering the sample in the pivot point of the ω, κ and ϕ rotation. It is possible to record images of the sample which allows for creating a polytope-shaped model of the sample for absorption correction.

A CCD detector with 512×512 pixels is used for the collection of reflections. The detector is mounted on an arm which can rotate around the vertical 2θ axis. Additionally, the detector can move radially in order to change the sample-detector distance. Typically, a

[1] This value is measured. To the knowledge of the author, this angle is not given in the manual [76].

distance of 60 mm is used for the collection of a huge number of reflections for structural refinement. The detector is cooled down to −40°C.

The procedure of an experiment (collection of reflections for structural refinements or observation of chosen reflections) is controlled by the software APEX2 suite [76]. This software also undertakes the preprocessing of the collected data, i.e. integration of reflection intensities and absorption correction. Absorption correction can be done by an algorithm that reconstructs a model of the sample geometry from redundant reflections, called "Multiscan Absorption Correction". Alternatively, it is possible to use the model for the sample shape determined from the images of the microscope camera as mentioned above, which is called "Numerical Absorption Correction (from Face indices)". The latter algorithm yields more reliable values for atomic displacement parameters (ADP) in the refinement.

Low-temperature measurements are possible by the use of an Oxford Cryosystems N-Helix [77] combined with a Coolstar Cryodrive 3.0 [78] which are both produced by Oxford Cryosystems Ltd. The Cryodrive cools down helium gas in a closed cycle to the desired temperature. The N-Helix uses this gas to cool nitrogen (above 90 K) or helium (below 90 K), which is then blown at the sample in the form of an open gas stream. The N-Helix exhibits a vacuum for thermal insulation. To prevent icing at the sample, the cold stream is shielded by a shroud of dry gas at room temperature [77]. This technology works insufficiently, so that the icing at the sample is not prevented effectively. After a period between a few minutes and one hour (depending on the position of the goniometer), the sample is covered with ice and must be defrosted manually by a stream of air at room temperature or above. This makes low-temperature data collection for structural refinements very costly in terms of labor.

The optimal shape of a sample for single-crystal X-ray diffraction is a sphere because this minimizes artifacts due to absorption. For some materials, it is possible to prepare a spherical sample using an air driven sphere grinder as described in [79]. This "Bond grinder" consists of a cylindrical cavity in a metal block. Air is blown with moderate pressure through a hole in the side of the cavity approximately in tangential direction. The air can leave the cavity through a hole in the middle of the upper end cap. The cylinder wall is covered with abrasive paper. Small pieces of the sample material are moved by the air stream tangentially along the cylinder wall. The exit hole is covered with very fine gaze to prevent a loss of the samples. The samples lose some of their material when they roll along the abrasive paper. After usually several hours, the samples have a spherical shape and a suitable size for single-crystal X-ray diffraction. It is useful to control the air flow by means of a rotameter in order to obtain reproducible parameters. Every few hours the grinder has to be opened to supervise the size of the samples under the microscope. The probability that a sample is lost during the grinding process is very high, so often many attempts have to be made. There is also an improved setup, where the samples are filtered through a gaze of appropriate mesh size, so that the grinding process automatically stops when the sample has the desired size [80]. This was used e.g. by O. Schumann [81]. For many materials, grinding is not possibile. The crystal must be hard enough and must not cleave. Often, crystals with cubic structure are good candidates.

3.1.2 D5000

3.1.2.1 Experimental setup

The D5000 is a powder X-ray diffractometer in Bragg-Brentano geometry as explained in Section 3.1.2.2. The history of the experimental setup dates back to the 1990s, where originally a diffractometer of type D500 by Siemens was used [82]. Usually, it is used with an X-ray tube that produces CuK_α radiation. The detector is a position-sensitive proportional counter [82]. In 1998, it was considered to replace the proportional counter by a diode array, but it was decided to keep the proportional counter because the diode array must be cooled in order to reduce noise [83].

Alternatively, a room temperature setup or a cryostat can be used for the sample environment. In 1991, temperature dependent measurements were automated by B. H. Freitag [82]. Those days, the user interface was written in Turbo Pascal [82]. In 1998, C. Huhnt replaced the diffractometer of type D500 was by one of type D5000 (Siemens) [83]. In this context, the Turbo Pascal programm was modified [83]. In 2005, M. Haider replaced the Turbo-Pascal program by a LabView program [84]. Furthermore, a new multichannel analyzer was installed in order to increase the angular resolution [84]. For temperature dependent scans, a cryostat is used which operates by evaporation of liquid helium. A heater is necessary because the temperature reacts too slowly to a change of the helium flow, so that a control by the helium valve alone is not possible. Two approaches were realized for the temperature control: On the one hand a fuzzy controller and on the other hand two coupled PID controllers [84]. Usually, the PID solution is in use: A first PID controller regulates the temperature by controlling the heating power. A second PID controller regulates the temperature and the heating power by controlling the helium flow [84]. In this work, the Schumix cryostat was used, which was installed by H. Ulbrich, who also constructed a sample stick for this cryostat in 2009 [85]. The cryostat covers a nominal temperature range from 4 K to 325 K [85]. However, temperatures below approx. 7 K are usually not possible.

Although the D5000 is a powder diffractometer, for some cases it is necessary to carry out single-crystal diffraction using this instrument. It turned out that the room temperature setup is sufficiently well aligned so that a sample with well-defined faces can be simply mounted to record rocking curves. Unfortunately, the sample orientation in the cryostat is less precise. For powder diffraction this is no problem, but single crystal diffraction needs a better orientation of the sample. In this work, a goniometer was fixed to the sample stick so that the χ angle can be controlled within a few degrees. For every change of χ, the sample stick has to be removed from the cryostat. This resulted in slightly different θ positions of the sample, because of clearance of the seal. Thus, after every single change of χ, the θ position must be readjusted. The feature for carrying out θ scans is not working in the LabView program, so that the adjustment of θ must be realized by a series of 2θ scans with varying θ position. Often, several hours are necessary to localize a Bragg reflection of a single-crystal.

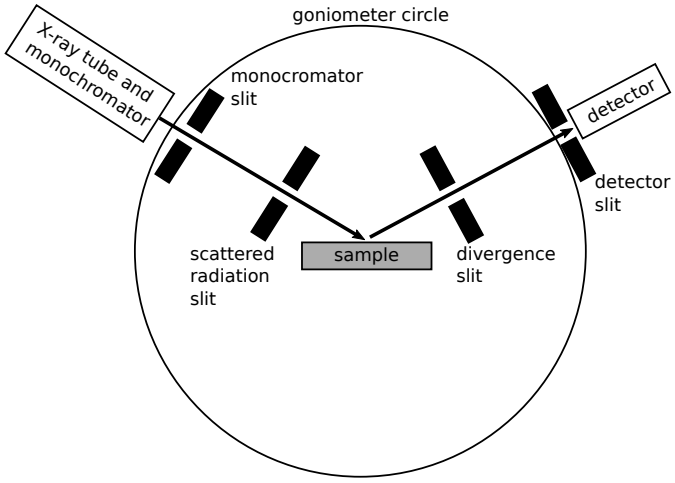

Figure 3.1: Bragg-Brentano geometry for powder diffraction.

3.1.2.2 Powder diffraction

Bragg-Brentano geometry The Bragg-Brentano geometry for powder diffraction uses monochromatic X-ray radiation which is diffracted by the surface of a flat sample (Figure 3.1). The detector is usually a point detector which is moved on a circular path around the sample, thus scanning the detector angle 2θ in fine steps much smaller than the typical reflection width. The sample is rotated with half speed compared to the detector such that the incident and the reflected beam always confine the Bragg angle θ with regard to the sample surface. The focus of the X-ray tube and the focus of the detector must have the same distance from the sample [86]. If the intensities of reflections shall be analyzed, it is important that the sample face is larger than the illuminated surface, because the illuminated surface depends on the Bragg angle θ [86].

A correct determination of the detector angle 2θ of a reflection requires the sample surface to be placed in the centre of the goniometer circle, wherein a displacement of S in direction of the sample surface normal leads to a shift of the measured Bragg angle of $S\cos\theta/R$, wherein R is the distance between the sample and X-ray tube focus or detector focus [86].

Reflection profile A real powder diffraction experiment produces reflections with a non-zero width and a certain peak profile when the number of counts is plotted against the detector angle 2θ. The measured intensity is then [87]

$$I(2\theta) = A \cdot \underbrace{((P_{\text{radiation}} \otimes P_{\text{instrument}}) \otimes P_{\text{sample}})}_{P_{\text{reflection}}}(2\theta) + B \quad ,$$

wherein A is the height of the reflection, B the background. The profile functions for the spectral distribution of the radiation $P_{\text{radiation}}$, for instrumental effects $P_{\text{instrument}}$ and for sample effects P_{sample} are convoluted ($\otimes$) in order to obtain the peak profile function $P_{\text{reflection}}$.

The instrument profile function is mainly a Gaussian function and the main part of the sample profile function is of Lorentzian type. However, the sample profile function can exhibit Gaussian parts, as we will see in the next sections.

The Gaussian function can be written as

$$G(2\theta) = \frac{2\sqrt{\ln(2)}}{\Gamma_{\text{G}}} \cdot \exp\left(\frac{-4\ln(2)}{\Gamma_{\text{G}}^2} \cdot (2\theta - 2\theta_0)^2\right) \quad , \tag{3.1}$$

wherein 2θ is the detector angle, $2\theta_0$ is the position of the reflection, and Γ_{G} is the width of the Gaussian function.

The Lorentzian function can be written as

$$L(2\theta) = \frac{2}{\pi} \frac{\Gamma_{\text{L}}}{\Gamma_{\text{L}}^2 + 4(2\theta - 2\theta_0)^2} \quad , \tag{3.2}$$

wherein 2θ and $2\theta_0$ are defined as above and Γ_{L} is the width of the Lorentzian function.

The reflection profile $P_{\text{reflection}}$, as introduced in equation 3.1.2.2, is essentially a Voigt function, i.e. a convolution of a Gaussian and a Lorentzian function:

$$P_{\text{reflection}}(2\theta) = (G \otimes L)(2\theta) \quad .$$

The Gaussian function has the width Γ_{G} and the Lorentzian function has the width Γ_{L}, which both depend on several geometric and physical quantities. An overview is given in Fig. 3.2.

Radiation profile function The X-ray or neutron source emits a spectrum which contains several wavelengths. That gives rise to the radiation profile function [87].

Instrument profile function The instrument profile function can be described in detail by a convolution of profiles arising from six effects: The projected focal spot profile, varying displacements of different parts of the specimen surface, axial divergence specimen transparency, the receiving slit and misalignment [63]. The main contribution can be described by a Gaussian function (Equation 3.1) [87].

The width Γ_{G} of the Gaussian part of the instrument profile function depends on the Bragg angle θ in the following way [88]:

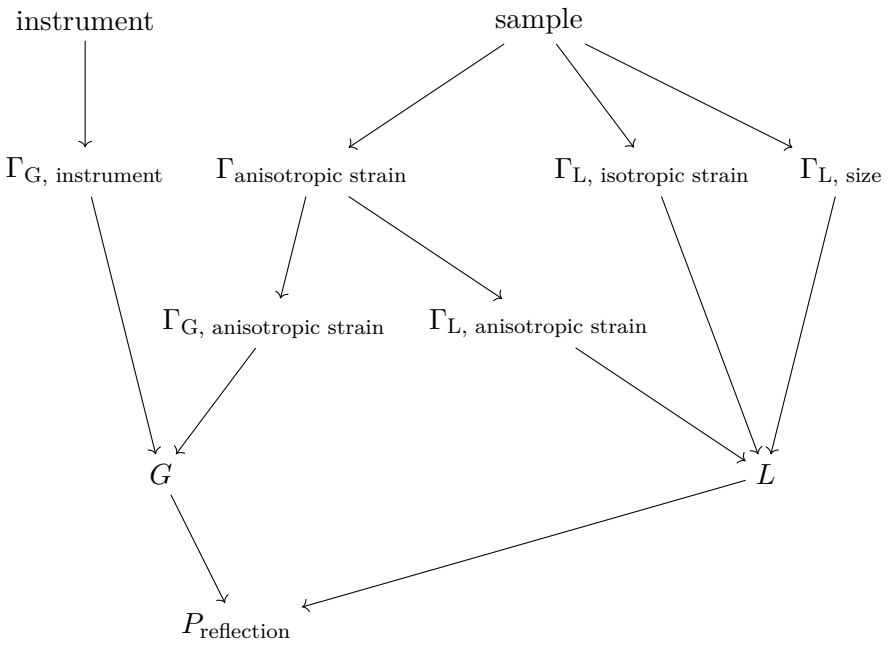

Figure 3.2: The reflection profile $P_{\text{reflection}}$ depends on several geometric and physical properties of the instrument and the sample. G is a Gaussian function, L a Lorentzian function and $\Gamma_{\dots}$ are peak widths.

$$\Gamma_{\text{G, instrument}} = \sqrt{U\tan(\theta)^2 + V\tan(\theta) + W}$$

This equation is known as the Caglioti formula [89]. The parameters U, V, W are determined in the refinement. Theoretically, they depend on the instrument only, but for a good refinement they should be refined for each measurement.

Because the detector has a finite height in the direction of the 2θ-axis and the powder rings bend away from $2\theta = 90°$, the peaks become asymmetric. This effect is called axial divergence [63],[87].

Sample profile function Interference yields sharp reflections if the number of scattering points is large. However, for very small crystallites, the finite number of unit cells gives rise to a broadening of the reflections. This is called size effect and gives rise to a Lorentz type broadening with a width $\Gamma_{\text{L, size}}$ described by the Scherrer formula [90]

$$\Gamma_{\text{L, size}} = \frac{K\lambda}{L\cos(\theta)} = Y\frac{1}{\cos(\theta)} \quad ,$$

wherein K is a shape dependent factor with $K = 2\sqrt{\frac{\ln(2)}{\pi}}$ for cube shaped crystallites, λ is the wavelength of the X-ray radiation, L the size of the crystallites and θ the Bragg angle. For a refinement, usually the parameter Y is used.

Furthermore, mechanical strain influences the lattice parameters, which can give rise to a further broadening of the reflection. If the strain is isotropically distributed, the width of the Gaussian function can be described as [91]

$$\Gamma_{\text{L, isotropic strain}} = X \tan(\theta) \quad ,$$

wherein the parameter X is used for refinement.

If the strain is anisotropically distributed, the broadening of the reflection does not have a simple dependence on the Bragg angle. For this case, there exist a model [91], wherein for all six lattice parameters (e.g. lattice constants a, b, c and angles α, β, γ or alternatively any six independent components of the metric tensor) a statistical Gaussian contribution is assumed. In this formalism, M_{hkl} is the inverse square of a reciprocal lattice vector $(h\,k\,l)$. Dependent on the miller indices $(h\,k\,l)$ and the statistical distribution of lattice constants, the variance $\sigma^2(M_{hkl})$ contributes to the peak width as the anisotropic broadening [91]

$$\Gamma_{\text{anisotropic strain}}(hkl) = \sqrt{\sigma^2(M_{hkl})}\tan(\theta)/M_{hkl} \quad ,$$

wherein θ is the Bragg angle. The formalism is mathematically justified for the Gaussian broadening of the peak profile, but not for the Lorentzian broadening. Nevertheless, the common procedure is to split the anisotropic strain into a Gaussian and a Lorentzian part using a weighting factor $0 \leq \zeta \leq 1$:

$$\begin{aligned} \Gamma_{\text{G, anisotropic strain}}(hkl) &= (1-\zeta)\Gamma_{\text{anisotropic strain}}(hkl) \\ \Gamma_{\text{L, anisotropic strain}}(hkl) &= \zeta\Gamma_{\text{anisotropic strain}}(hkl) \quad . \end{aligned}$$

The pseudo-Voigt function Since the Voigt function 3.1.2.2 is numerically quite expensive due to the convolution, usually an approximation named pseudo Voigt function pV is used. This is a linear combination of a Gaussian function and a Lorentzian function.

Let us consider the case that we want to approximate the Voigt function

$$V(x) = (G \otimes L)(x)$$

with Lorentzian width Γ_{L} and Gaussian width Γ_{G}.

Our approximation is

$$pV(2\theta) = (1-\eta)G'(2\theta) + \eta L'(2\theta)$$

with Lorentzian width Γ'_{L} and Gaussian width Γ'_{G} and a weighting $0 \leq \eta \leq 1$. Furthermore we assume in our approximation model $\Gamma'_{\text{G}} = \Gamma'_{\text{L}} =: \Gamma$. This approximation is

worst in the case, where the widths of our original functions G and L are the same, thus $\Gamma_G = \Gamma_L$, and even in this worst case the maximal deviation is less then 1 % [92].

It should be emphasized that the weighting η is not related to any peak heights of the original functions G and L, but rather to the widths Γ_G and Γ_L. Wherein the Voigt function is parametrized by Γ_G and Γ_L, the pseudo Voigt function is parametrized by η and Γ. Indeed, it is possible to calculate one set of parameters from the others as shown in [88]. The inverse map can be found in the FullProf manual [93].

3.2 Neutron diffraction instruments

3.2.1 6T2

6T2 is a thermal neutron four-circle diffractometer with lifting counter, located at Laboratoire Léon Brillouin [94]. It is placed at the thermal source 6T and uses a Cu (2 2 0) monochromator and an Er filter for the wave length 0.90 Å. Alternatively, a pyrolytic graphite (0 0 2) monochromator with a PG filter can be used for wave length of 1.55 Å or 2.35 Å. A ^{3}He single detector and a 2D detector are available. oFor experiments with a cryostat, like in this work, a three-circle configuration with lifting counter is used.

3.2.2 5C2

The hot neutron four-circle diffractometer 5C2 is located at the hot source 5C2 at the Laboratoire Léon Brillouin [95]. It is equipped with a centric Eulerian cradle by Stoe. Either a Cu (2 2 0) monochromator with an Er filter can be used for a wave length of 0.830 Å or a $Ge_{1-x}Si_x$ (3 1 1) monochromator for a wave length of 1.106 Å. Point detectors operating with ^{3}He or BF_3 are available. Low and high temperatures between 5 K and 1 400 K can be reached using a cryostat or a furnace.

3.2.3 HEiDi

The single crystal diffractometer HEiDi is is located at the Forschungsneutronenquelle FRMII of the Heinz Maier Leibnitz Zentrum in Munich. It is attached to the hot neutron source SR-9b, which provides neutrons with wavelengths between 0.55 Å and 1.2 Å [96]. At a wavelength of 1.17 Å, the neutron flux amounts to $1.4 \cdot 10^7\,\mathrm{cm^{-2}s^{-1}}$. It can be alternatively equipped with a closed cycle cryostat ranging from 2 K to room temperature, a mirror furnace ranging from room temperature to 1 500 K, a micro furnace ranging from room temperature to 500 K or a uniaxial pressure cell.

3.2.4 D9

The hot neutron four-circle diffractometer D9 is located at the reactor of Institute Laue-Langevin. Due to the hot neutron source, it is possible to access short wavelengths: The wavelength is variable between 0.35 Å and 0.85 Å [97] using a Cu(2 2 0) monochromator in transmission geometry. Pin holes with diameters from few mm to more than 1 cm are available to adjust the area of the incoming beam to the size of the sample in order to reduce the background signal.

The area detector, operating with sets of wires in a mixture of ^{3}He and C_3H_8 gas contains 32×32 pixels of size 2 mm × 2 mm [98]. Since the sample-detector distance amounts to 49 cm, the detector covers an angle of $8° \times 8°$ [97]. This area detector thus covers only a small angular range. It is used as a point detector, collecting one reflection per shut, with the advantage that the surrounding regions can be masked out afterwards. A further advantage is a reduction of measuring time, because each image contains background signal that can be used for the background correction [98]. However, the greatest advantage comes into play for twinned crystals or incommensurate structures, where overlapping reflections appear [98]. The reason for the choice of the size and number of pixels is the following: On the Institut Laue-Langevin, a typical sample-detector distance amounts to roughly half a meter. Since most crystals have lattice constants of at least 4 Å, assuming a wavelength of 1 Å, a coverage of 8° is sufficient to collect the reciprocal space between two reflections. On the other hand, the pixel size of 2 mm is smaller than most samples, so even for a perfectly parallel aligned beam, smaller pixels would not reveal further information [98].

Formerly, the instrument was controlled by the command-line sequencer MAD, which was replaced by the sequencer NOMAD. The guide [97] is still written for the the old MAD, however most of the commands have not changed. For the determination of the UB matrix and integration of the reflections, the program racer [99] is used. It is capable to deal with various shapes of reflections. It is further able to mask out parts of the reciprocal space, which are corrupted by neighbored reflections. The process of integration can be visualized by the program fly.

3.2.5 D3

D3 is a polarized hot-neutron beam facility located at the hot neutron source of the Institut Laue-Langevin [100]. It uses polarizing monochromators ($Co_{92}Fe_8$ and Heusler[101] Cu_2MnAl) for wave length between 0.25 Å and 0.84 Å. Spin analysis is realized by a ^{3}He spin filter. For low magnetic fields up to 0.6 T, an Orange cryostat [102] inside a CRYOPAD [65] is used, which allows temperatures from room temperature down to 1.4 K. For higher fields up to 10 T, a cryomagnet with dilution insert (down to 0.04 K can be used. The high-field setup allows for uniaxial polarization analysis and with the low-field setup even three-dimensional polarization analysis is possible [103].

3.3 Further instruments

3.3.1 DiMoS

The DiMoS was set up by S. Holbein [104] (in those days called "Experimental setup for dielectric measurements"), and later improved by J. Stein [105] (where the name "DiMoS" ("Dielectric Measurement on Single Crystals") appears for the first time. It is able to measure pyrocurrents and surface charges of polar single crystals at temperatures down to a few Kelvin. From the beginning, the DiMoS was constructed with the prospect to move to the research reactor FRMII in Munich [104] and is going to be integrated in the instrument KOMPASS [105]. Details about the devices (model and producer) can be found in [104].

The DiMoS is able to access temperatures down to a few Kelvin using a cold-head cryocooler which operates by compression of He gas inside a metal tube[104]. The sample is cooled via thermal conductivity to the metal tube. In order to avoid convection, the sample environment is evacuated [104]. The cold head and the wires for electric contact are made of metals with weak thermal conductivity [104]. A tube around the sample is kept at a low temperature in order to reduce thermal exchange via radiation [104]. The cryocooler cannot be controlled in order to stabilize a desired temperature, so the temperature control is realized via an electric heater [104].

For the electric measurements, two parallel surfaces of the sample are metalized and placed between copper contacts. This system is a capacitor were the sample plays the role of the dielectric medium. In general two kinds of measurements are possible [104]: The pyrocurrent can be measured by an Ampere meter or the surface charges can be measured using a Sawyer-Tower circuit [106]. Furthermore, the polarity of the dielectric sample can be switched by applying a high voltage of several kV. All three functionalities are realized in one circuit [104].

Additionally to safety precautions in order to prevent personal damage, the sensitive and expensive electrometer must be protected from the high voltage in the case of malfunction. Personal safety is guaranteed by the "safety box" that is already existent in the original setup by S. Holbein [104]. Later, J. Stein in cooperation with K. Lehmann added an active overvoltage protection in order to protect the electrometer and the temperature controller from damage [105].

Data acquisition is realized by a LabView script [104]. J. Stein improved the functionalities in the way that complex measurements can be controlled by an EMC script [105].

4 Erythrosiderite-type compounds

4.1 The family of erythrosiderite-type compounds

The family of Erythrosiderite-type compounds covers compounds with the chemical formula $A_2[FeX_5(H_2O)]$, wherein A is an alkali metal or an ammonium ion and X is Cl or Br. The structural parameters of some erythrosiderite-type compounds are listed in Table 4.1. At low temperature, the magnetic moments of the Fe ions order antiferromagnetically. Additionally, the compound $(NH_4)_2[FeCl_5(H_2O)]$ is multiferroic.

4.1.1 Crystal structures of erythrosiderite-type compounds

Most erythrosiderite-type compounds exhibit space group *Pnma* (Nr. 62) and can (apart from rather small deviations) be attained from each other by replacing the A or X. Figure 4.1(a) shows $K_2[FeCl_5(H_2O)]$ in an exemplary way. This compound and $Rb_2[FeCl_5(H_2O)]$, $Rb_2[FeBr_5(H_2O)]$ and $(NH_4)_2[FeCl_5(H_2O)]$ are isostructural if in the latter case the NH_4 molecule is considered as a single atom [107, 108, 112, 109]. The crystal structure of these compounds consists of $[FeX_5(H_2O)]$ octahedrons which are arranged as zig-zag chains along the b direction. The octahedrons within a chain are connected by $O-H-X$ bonds. The space between the zig-zag chains is occupied by the A atom or molecule. The crystal structure of $Cs_2[FeCl_5(H_2O)]$ differs from the crystal structure of the other erythrosiderite-type compounds. It crystallizes in space group *Cmcm* (Nr. 63). As depicted in Figure 4.1(b), the crystal structure resembles the crystal structures of the other erythrosiderite-type compounds but exhibits crucial differences: The zig-zag chain of $[FeCl_5(H_2O)]$ octahedrons is arranged in c direction rather than b direction. In Figure 4.1, for easy comparison, the orientations are chosen such that in both cases the zig-zag chains run vertically. At room temperature, $Cs_2[FeCl_5(H_2O)]$ exhibits structural disorder regarding the $O-H-Cl$ bonds connecting the $[FeCl_5(H_2O)]$ octahedrons: Since the distances from an O position to the positions of two Cl atoms in a neighbored octahedron are equal, both $O-H-Cl$ bonds are statistically equivalently realized.

The compounds $(NH_4)_2[FeCl_5(H_2O)]$ and $Cs_2[FeCl_5(H_2O)]$ exhibit structural phase transitions at around 80 K and 160 K, respectively, which are investigated in this work [113][114].

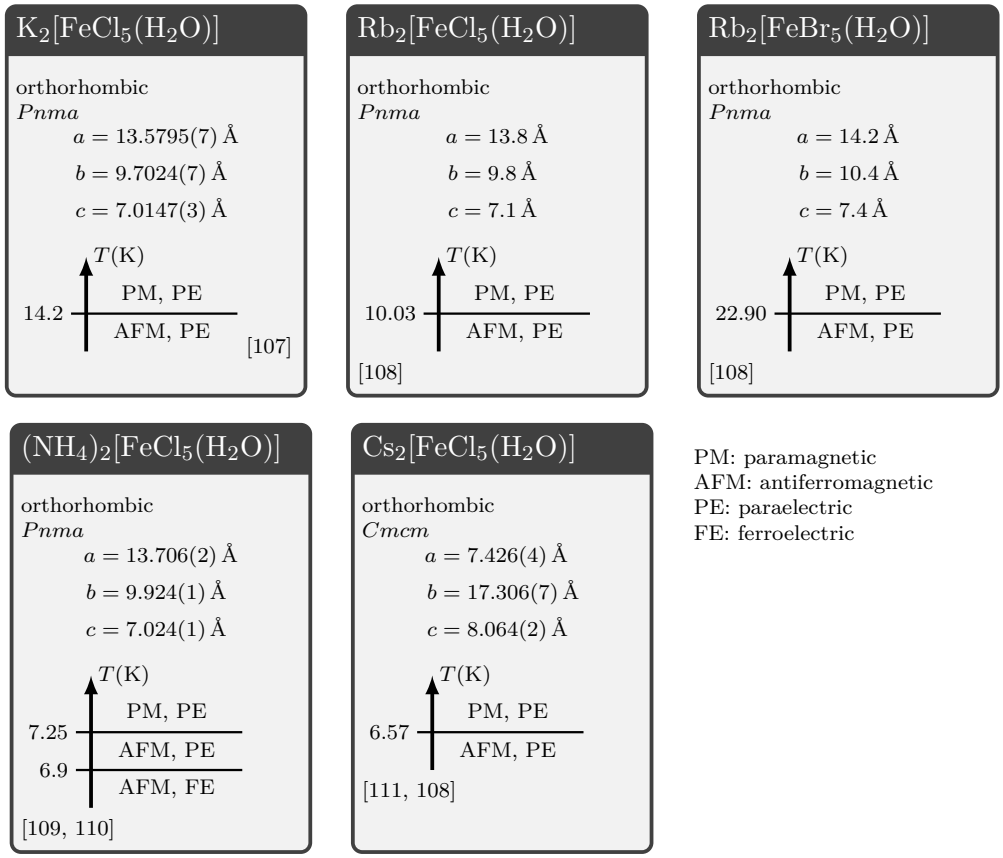

Table 4.1: Structural parameters and transition temperatures of erythrosiderite-type compounds. $(NH_4)_2[FeCl_5(H_2O)]$ is the only multiferroic erythrosiderite-type compound and $Cs_2[FeCl_5(H_2O)]$ differs regarding the crystal structure. The cell parameters of $Cs_2[FeCl_5(H_2O)]$ were determined at 273 K, all other cell parameters at room temperature. The transition temperature of $K_2[FeCl_5(H_2O)]$ was determined for a deuterated sample.

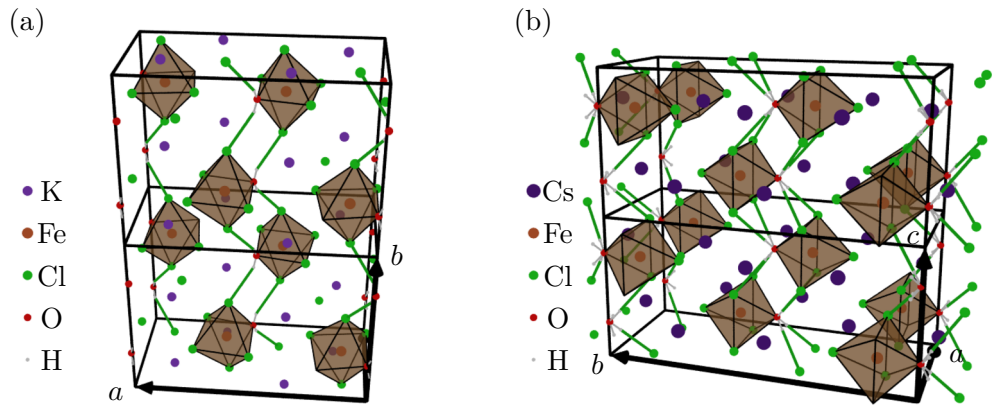

Figure 4.1: Room temperature crystal structures of erythrosiderite-type compounds. In both figures, the O – Cl bonds are drawn as green lines. These bonds form zig-zag chains in b respectively c direction. In this direction, two unit cells are drawn. (a) Room temperature crystal structure of $K_2[FeCl_5(H_2O)]$, according to [107] (deuterated compound). (b) Room temperature crystal structure of $Cs_2[FeCl_5(H_2O)]$, determined by X-ray diffraction. H atoms are schematically drawn using the H – Cl distance from [111]. Note that, at room temperature, two possible H – Cl bonds with different H positions are possible, which results in a disordered structure.

4.1.2 Magnetic and ferroelectric properties of erythrosiderite-type compounds

Recently, it was discovered that the compounds $K_2[FeCl_5(H_2O)]$, $Rb_2[FeCl_5(H_2O)]$ and $Cs_2[FeCl_5(H_2O)]$ are magneto-electric [115] and the compound $(NH_4)_2[FeCl_5(H_2O)]$ is even multiferroic [110].

The compounds $K_2[FeCl_5(H_2O)]$, $Rb_2[FeCl_5(H_2O)]$, $Rb_2[FeBr_5(H_2O)]$ and $Cs_2[FeCl_5(H_2O)]$ exhibit a phase transition at 14.2 K [107], 10.03 K [108], 22.90 K [108] and 6.57 K [108], respectively, from a paramagnetic phase to an antiferromagnetic phase. In both phases, the compounds are paraelectric. In contrast to that, $(NH_4)_2[FeCl_5(H_2O)]$ exhibits a phase transition at 7.25 K and a further phase transition at 6.9 K [110] which was already reported in [116]. During the phase transition at 7.25 K, the sample changes from a paramagnetic and paraelectric state to an antiferromagnetic state but still remains paraelectric. The phase transition at 6.9 K induces ferroelectricity that is strongly coupled to the magnetization, so that the compound is multiferroic below this temperature. For low magnetic fields, the electric polarization lies within the ab plane, close to the a direction. Increasing the magnetic field reveals a complex phase diagram [110]. The magnetic structures of these two phases is investigated by neutron diffraction in [117]: The antiferromagnetic paraelectric intermediate phase can be attributed to an incommensurate spin density wave with a propagation vector (0 0 0.23) where the magnetic moments are aligned along the a axis. The multiferroic phase can be described by a cycloidal spin state with the same propagation vector and the moments lying roughly in the ac plane. The cycloidal state exhibits a lattice modulation associated to the cycloidal order [117].

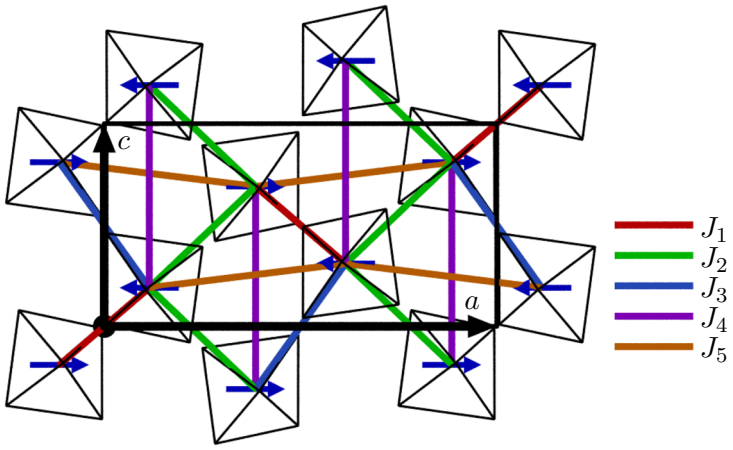

Figure 4.2: Magnetic structure of of $K_2[FeCl_5(H_2O)]$ and $Rb_2[FeCl_5(H_2O)]$ from [107]. The atoms are not shown for clarity, the magnetic moments are drawn as blue arrows at the Fe sites, in the centre of the $[FeCl_5(H_2O)]$ octahedrons. The magnetic interactions $J_1, \ldots, J_5$ are investigated in [119] for $K_2[FeCl_5(H_2O)]$. The plot uses structural data from [107]. The figure is adapted from [119].

The magnetic structures of $K_2[FeCl_5(H_2O)]$ and $Rb_2[FeCl_5(H_2O)]$ are well investigated and found to be identical [107]. The magnetic structure of these two compounds is shown in Figure 4.2. The surprisingly high transition temperatures (Table 4.1) can be ascribed to a high spin density delocalization towards the ligand atoms [112]. Magnetic interactions between the Fe ions have been investigated experimentally and by ab-initio calculations. A strongly simplified model for $Rb_2[FeCl_5(H_2O)]$ is used in [118], where only two interactions are taken into account: One interaction J_z between neighbored Fe ions within one zig-zag chain, and an interaction J_{xy} which is a mean of all interactions between different zig-zag chains. This model reflects the fact, that the system is at the crossover between a one- and a three-dimensional Heisenberg magnet. In the paramagnetic phase, the temperature is so high that the weak interaction J_{xy} has no effect, and the system can be described as a one-dimensional Heisenberg magnet with only one interaction J_z. Below the transition temperature of 10 K, in the antiferromagnetic phase, also J_{xy} must be taken into account, so the system is a three-dimensional Heisenberg magnet [118]. A more detailed model for $K_2[FeCl_5(H_2O)]$ and $Rb_2[FeBr_5(H_2O)]$ is investigated in [119]. The strong interaction J_1 along the zig-zag chains and further interactions $J_2, \ldots, J_5$ are taken into account, as illustrated in figure 4.2.

The magnetic easy axis of $K_2[FeCl_5(H_2O)]$, $Rb_2[FeCl_5(H_2O)]$ and $Cs_2[FeCl_5(H_2O)]$ is the a axis while $(NH_4)_2[FeCl_5(H_2O)]$ has the easy plane ac. However, since the crystal structure of $Cs_2[FeCl_5(H_2O)]$ differs from the others, a comparison of the magnetic easy axes and planes should be done with respect to the orientation of the zig-zag plane, as depicted in Figure 4.3. The centres of the octahedrons of a zig-zag chain approximately lie within a common plane. The easy axis of $Cs_2[FeCl_5(H_2O)]$ is oriented perpendicular to this plane. In contrast to this, for $K_2[FeCl_5(H_2O)]$ and $Rb_2[FeCl_5(H_2O)]$, the easy axis has a component within this plane. Furthermore, the easy plane of $(NH_4)_2[FeCl_5(H_2O)]$ is spanned by these two directions. Since $(NH_4)_2[FeCl_5(H_2O)]$ is the only multiferroic

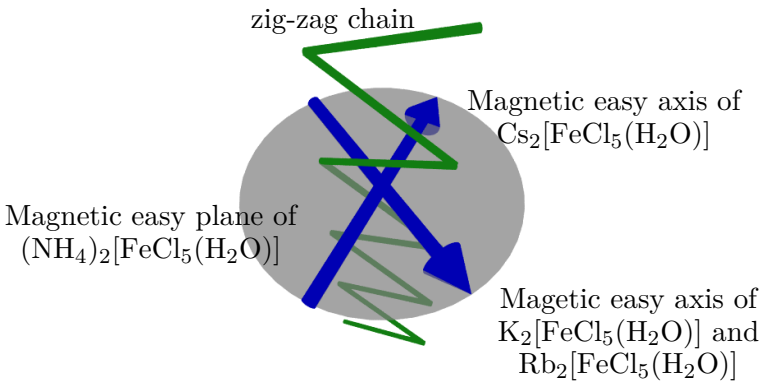

Figure 4.3: Schematic comparison of the orientation of the magnetic easy axes or planes of different erythrosiderite-type materials with respect to the zig-zag chain. The magnetic easy axis of $K_2[FeCl_5(H_2O)]$ and $Rb_2[FeCl_5(H_2O)]$ and the magnetic easy axis of $Cs_2[FeCl_5(H_2O)]$ span the magnetic easy plane of $(NH_4)_2[FeCl_5(H_2O)]$.

compound of this kind, it seems natural that the multiferroicity can be explained by the Dzyaloshinskii-Moriya effect introduced in section 1.3, wherein the magnetic moments lie in the easy plane and form a cycloidal structure with a propagation vector lying in the same plane. The spontaneous electric polarization was found to be aligned nearly in a direction and the magnetic easy plane is the ac plane [110], so according to this model, the propagation vector should be expected to have a large component in c direction. Indeed, this was recently confirmed by neutron diffraction [113].

4.2 $(NH_4)_2[FeCl_5(H_2O)]$ and $(ND_4)_2[FeCl_5(D_2O)]$

4.2.1 Sample characterization and experimental setup

Single crystals of $(NH_4)_2[FeCl_5(H_2O)]$ and $(ND_4)_2[FeCl_5(D_2O)]$ were grown from aqueous solution by L. Bohatý[120].

A box-shaped $(NH_4)_2[FeCl_5(H_2O)]$ sample (LB004-S002) of dimensions 1.5 mm in a direction, 3.5 mm in b direction and 4 mm in c direction as shown in Figure 4.4(a) was cut from a large single crystal for neutron diffraction on 6T2 as described in Section 3.2.1. The sample was glued to an aluminum sample holder with the (0 1 0) direction along the ω axis of the goniometer. The sample was placed inside a cryostat and temperature scans were carried out in the range 1.6 K to 8 K in order to investigate the antiferromagnetic and ferroelectric phase transitions using a wave length of 2.42 Å. The (0 0 0.77) reflection was measured with fixed sample and detector positions over this temperature interval. For the (0 0 1.24) reflection, ω scans were carried out in the same temperature range.

An as-grown single crystal of the deuterated compound $(ND_4)_2[FeCl_5(D_2O)]$ with a mass of (40 ± 2) mg (LB021-S014) was investigated by neutron diffraction on the single crystal neutron diffractometer HEiDi (cf. 3.2.3). The sample is shown in Figure 4.4(b), the

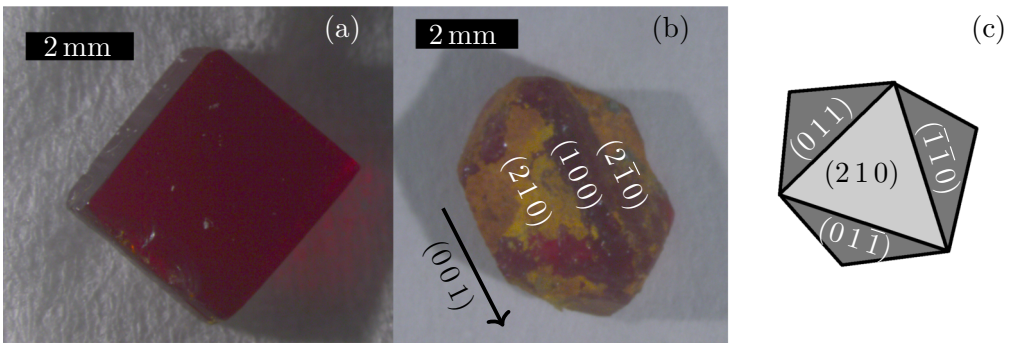

Figure 4.4: (a) $(NH_4)_2[FeCl_5(H_2O)]$ sample LB004-S002 used for single crystal neutron diffraction on 6T2. (b) The as-grown $(ND_4)_2[FeCl_5(D_2O)]$ sample LB021-S014 used for single crystal neutron diffraction on HEiDi. (c) Schematic drawing of the top-view of another typical morphology of as-grown crystals of this compound.

photo was taken after the experiment. The sample was wrapped in aluminum foil which was glued to the sample holder in a way that the (0 0 1) direction was parallel to the ϕ axis. In Figure 4.4(b) it can be seen that its surface corroded during a few weeks. The morphology of this sample is typical for as-grown samples of this compound: At one side, a roof-like shape is visible which consists of two large faces (2 1 0) and (2 $\bar{1}$ 0) and a more or less pronounced narrow face (1 0 0) like a roof ridge. The face indices of this sample were not verified, but are suggested by the investigation of several similar as-grown crystals of this compound via single crystal X-ray diffraction on APEX. Figure 4.4(c) shows another typical morphology of as-grown crystals of this compound. In both cases, the back-side of the crystal usually does not show pronounced faces, which probably can be attributed to the fact that the crystals touched the glass container during the growth process.

On HEiDi, the sample LB021-S014 was placed in a closed cycle cryostat and temperatures of 100 K and 10 K were chosen. Both temperatures are in the paramagnetic state and the structural transition [113] lies between them. At 100 K, reflections in the range $7° < 2\theta < 80°$ were collected with a wavelength of 1.170 Å and reflections in the range $49° < 2\theta < 80°$ were collected with a wavelength of 0.793 Å. At 10 K, reflections in the range $8° < 2\theta < 90°$ were collected with a wavelength of 1.170 Å and reflections in the range $45° < 2\theta < 66°$ were collected with a wavelength of 0.793 Å. In total, 3 335 reflections were collected at 100 K and 5 204 at 10 K. Furthermore, a temperature scan of the (0 4 0) reflection was carried out in the temperature range between 10 K and 100 K.

4.2.2 Results and discussion

4.2.2.1 Magnetic phase transitions

The incommensurate magnetic reflection (0 0 0.77) was measured during cooling and heating the sample over the phase transition with fixed sample and detector position. The result of the measurement during cooling is shown in Figure 4.5. At 7.699(12) K,

the reflection arises. The value was determined by fitting a power law of the form

$$\frac{\text{Counts}}{\text{Monitor}} = \begin{cases} b + a(T_\text{c} - T)^{2\beta} & \text{if } T \leq T_\text{c} \\ b & \text{if } T > T_\text{c} \end{cases},$$

where the transition temperature T_c, the amplitude a, the background b and the critical exponent β are varied during the fit procedure. The fit yields the above mentioned T_c and an exponent of $\beta = 0.197(17)$.

The measured temperature might strongly deviate from the real temperature due to the experimental setting. This is visible for measurements of another compound at the same instrument (cf. Figure 5.9).

The phase transition can be attributed to the inset of long-range magnetic order when the sample enters the antiferromagnetic, paraelectric phase. Between 6 K and 7 K, the the bending of the curve changes sign. The derivative has a maximum at this temperature, as shown as green line in figure 4.5. This cannot be explained by the second phase transition where the sample changes its magnetic structure from the incommensurate spin density wave to a cycloidal structure, as reported in [117]: The temperature difference between the two features is too large (note that the experimental setting provides reliable temperature differences as long as the temperature scan parameters are unaltered, cf. Figure 5.9).

No sudden change of the intensity is visible when the cycloidal magnetic structure is entered. This can be explained by the fact that only the c components of the magnetic moments change, which are parallel to the scattering vector of the (0 0 0.77) reflection.

The inset of Figure 4.5 shows a comparison with a measurement carried out during heating. Far away from the phase transition, the intensities are very similar. However, in the vicinity of the phase transition, the reflection exhibits higher intensity during the heating cycle. This might be an hysteresis effect or a problem with the temperature measurement.

Also the incommensurate magnetic reflection (0 0 1.24) could be detected via single crystal neutron diffraction, as shown in Figure 4.6(a). The reflection is clearly visible below the magnetic phase transition at 7.699(12) K and disappears above.

Gaussian distributions were fitted to the reflections, except for the two highest temperatures, where the reflection is not visible any more. Figure 4.6(b) shows the intensity of this reflection at different temperatures. The right arrow indicates the transition temperature from the paramagnetic to the antiferromagnetic phase as determined in Figure 4.5. This is also the temperature at which this reflection disappears.

The left arrow in Figure 4.6(b) shows the expected transition temperature from the paraelectric to the ferroelectric phase, assuming that it is 0.5 K below the other phase transition as stated in [117]. Again, no sudden change is visible since the reflection is in c direction while only the z components of the Fourier coefficients change during

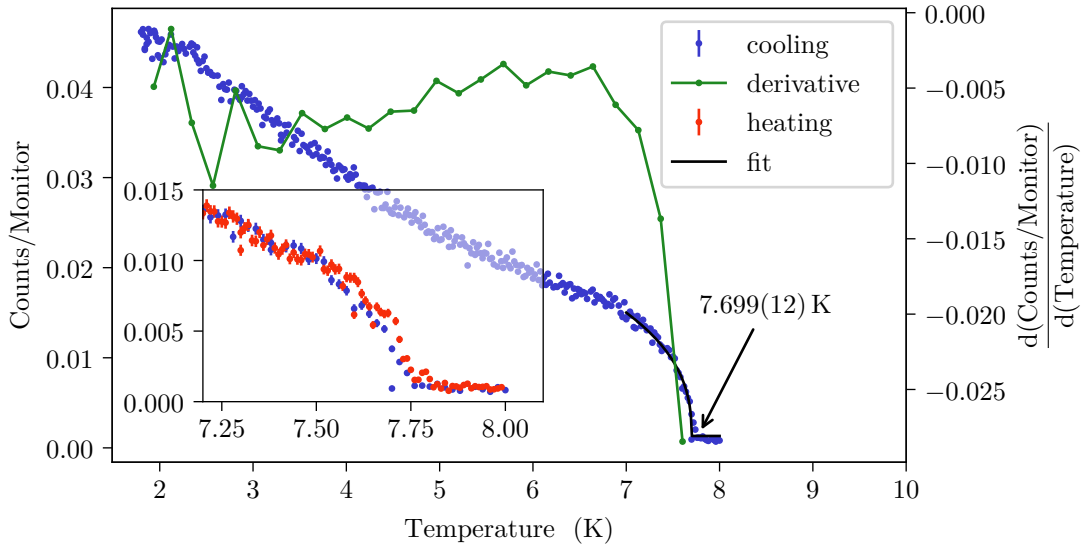

Figure 4.5: Temperature scan of the magnetic (0 0 0.77) reflection during a cooling cyle (blue). A fit (black curve) was carried out to determine the transition temperature. The position of the inflection point is visible in the first derivative (green). Inset: A comparison with a measurement during heating (red) reveals that around the phase transition the intensities are higher during heating.

the phase transition from the spin-density magnetic structure to the cycloidal structure. The amplitude shows a small feature at this temperature which can be attributed to the ferroelectric phase transition.

The position and width of the (0 0 1.24) reflection are displayed in Figure 4.6(c) and (d). The reflection shifts to higher l values when the temperature decreases, the peak width stays rather constant.

4.2.2.2 Structural phase transition

Figure 4.7(a) shows a temperature-dependent ω scan of the (0 4 0) reflection of a deuterated sample, measured on HEiDi. The reflection splits at 79(2) K. This value was determined by fitting a double Gauss function to the reflection. The splitting – i.e. the difference of the positions of the two Gauss functions – is plotted in Figure 4.7(b). The splitting indicates a symmetry reduction to a monoclinic or triclinic space group where different twins are slightly misaligned. Furthermore, Figure 4.7(b) shows that the intensity of the reflection is drastically enhanced below the phase transition. This can be explained by a reduced extinction due to the misaligned twins.

A structural phase transition might be accompanied by a loss of symmetries which give rise to selection rules in the high-symmetry phase. The parent space group of $(ND_4)_2[FeCl_5(D_2O)]$ is *Pnma*, so selection rules can be attributed to two glide planes

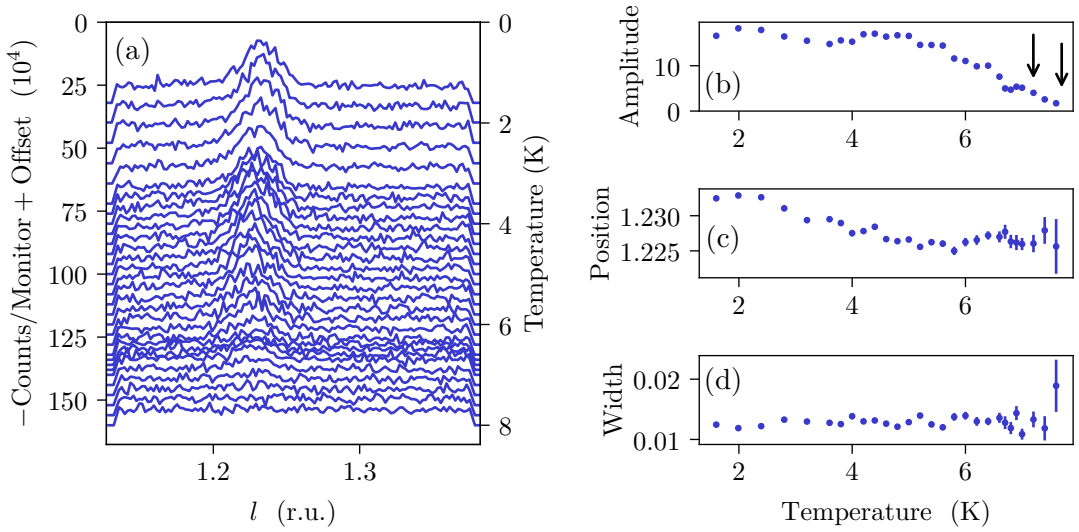

Figure 4.6: (a) Temperature-dependent scans of the magnetic (0 0 1.24) reflection along the reciprocal coordinate l. (b) Amplitude (10^4 counts/monitor) determined by fitting a Gaussian distribution to the reflection. The right and left arrows indicate the transition temperature from the paramagnetic to the antiferromagnetic phase and from the paraelectric to the ferroelectric phase, respectively. The upper temperature was determined in Figure 4.5 and the lower temperature is expected to be 0.5 K below [117]. (c)-(d) Position and width (relative reciprocal units) determined by these fits.

and three screw axes, as shown in the left column of Table 4.2. Rodriguez et al. [113] claim that the low temperature phase has space group $P2_1/a$. If this is true, we should see superstructure reflections at 10 K which appear because some of the symmetries are broken, as shown in the right column of Table 4.2. All selection rules except $00l \;:\; l = 2n$ were investigated since $(0\,0\,l)$ reflections could not be reached with our instrumental setup. In the low temperature phase, the glide plane n $(0, \frac{1}{2}, \frac{1}{2})$ $\frac{1}{4}, y, z$ and the screw axis 2 $(0, \frac{1}{2}, 0)$ $0, y, 0$ are broken, as can be seen in Figure 4.8. Figure 4.9 shows that the glide plane a $x, y, \frac{1}{4}$ and the screw axis 2 $(\frac{1}{2}, 0, 0)$ $x, \frac{1}{4}, \frac{1}{4}$ remain in the low temperature phase. This is in accordance with the symmetry reduction to $P2_1/a$ as reported in [113]. Notice that the broken screw axis 2 $(\frac{1}{2}, 0, 0)$ $x, \frac{1}{4}, \frac{1}{4}$ cannot lead to reflections $(h\,0\,0)$ with odd h because they are also forbidden by the glide plane a $x, y, \frac{1}{4}$. This is, why we cannot definitely exclude space group $P2_1/m$ on the basis of this selection rule analysis. Also the absence of reflections of the form $(h\,k\,0)$ with odd h is not a strict knock-out criterion, because they could just be below the detection level. This is why we will try a refinement in space group $P2_1/m$ as well. Space group $P2_1/n$ can be ruled out because we observed reflections $(0\,k\,0)$ with odd k and $(0\,k\,l)$ with odd $k + l$. These reflections cannot be explained by multiple scattering because they are not observed at 100 K, where the mosaicity is lower compared to 10 K, as we have shown in Figure 4.7.

Structural refinements were carried out for the 100 K data in space group $Pnma$ and for the 10 K data in space groups $Pnma$, $P2_1/a$, $P2_1/m$ and Pa. Space group Pa was tested because there are hints for polarization as discussed later.

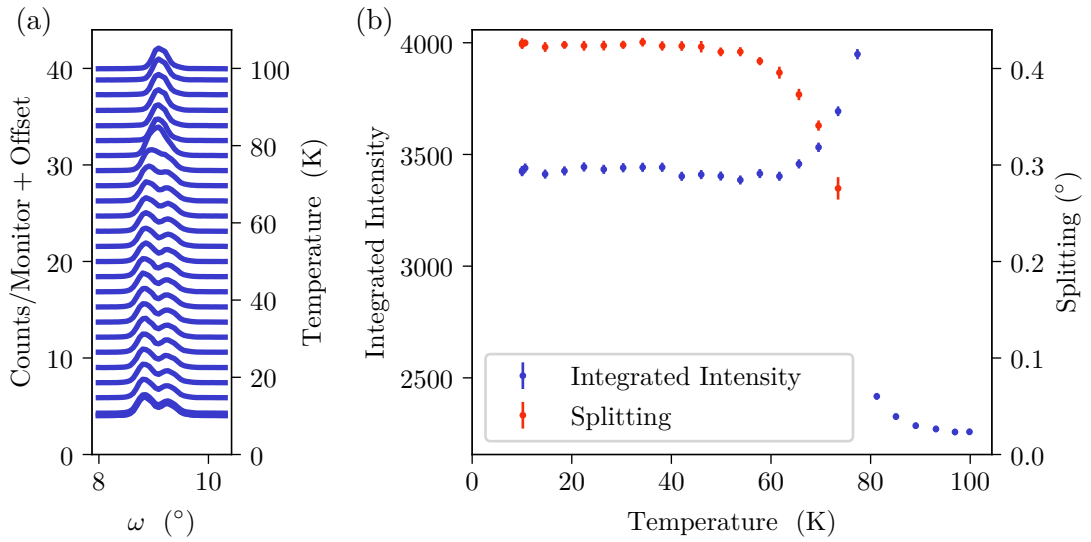

Figure 4.7: Temperature-dependent ω scan of the (0 4 0) reflection in $(ND_4)_2[FeCl_5(H_2O)]$ by single crystal neutron diffraction on HEiDi. (a) The reflection splits below the phase transition. (b) At the phase transition, the reflection increases in intensity and the splitting angle at 10 K is 0.417(5)°. The phase transition temperature can be determined to amount (79 ± 2) K. Adapted from [121].

$P\frac{2_1}{n}\frac{2_1}{m}\frac{2_1}{a}$		Γ_2^+	Γ_3^+	Γ_4^+	forbidden reflection observed
symmetry element	selection rule	$P11\frac{2_1}{a}$	$P\frac{2_1}{n}11$	$P1\frac{2_1}{m}1$	
1		✓	✓	✓	
2 $(0,0,\frac{1}{2})$ $\frac{1}{4},0,z$	$00l$: $l=2n$	✓	–	–	
2 $(\frac{1}{2},0,0)$ $x,\frac{1}{4},\frac{1}{4}$	$h00$: $h=2n$	–	–	✓	no
2 $(0,\frac{1}{2},0)$ $0,y,0$	$0k0$: $k=2n$	–	✓	–	yes
$\bar{1}$ $0,0,0$		✓	✓	✓	
a $x,y,\frac{1}{4}$	$hk0$: $h=2n$	✓	–	–	no
m $x,\frac{1}{4},z$		–	–	✓	
n $(0,\frac{1}{2},\frac{1}{2})$ $\frac{1}{4},y,z$	$0kl$: $k+l=2n$	–	✓	–	yes

Table 4.2: Two glide planes and three screw axes in space group *Pnma* give rise to selection rules. A check mark "✓" in the columns of the subgroups indicates that the corresponding symmetry class is also an element of the subgroup, a dash "–" means that it is not an element. The last column summarizes the experimental observation of reflections that are forbidden in space group *Pnma*. The selection rule $00l$: $l=2n$ could not be investigated for experimental reasons (cf. text).

(a)

Forbidden by glide plane n $(0, \frac{1}{2}, \frac{1}{2})$ $\frac{1}{4}, y, z$:

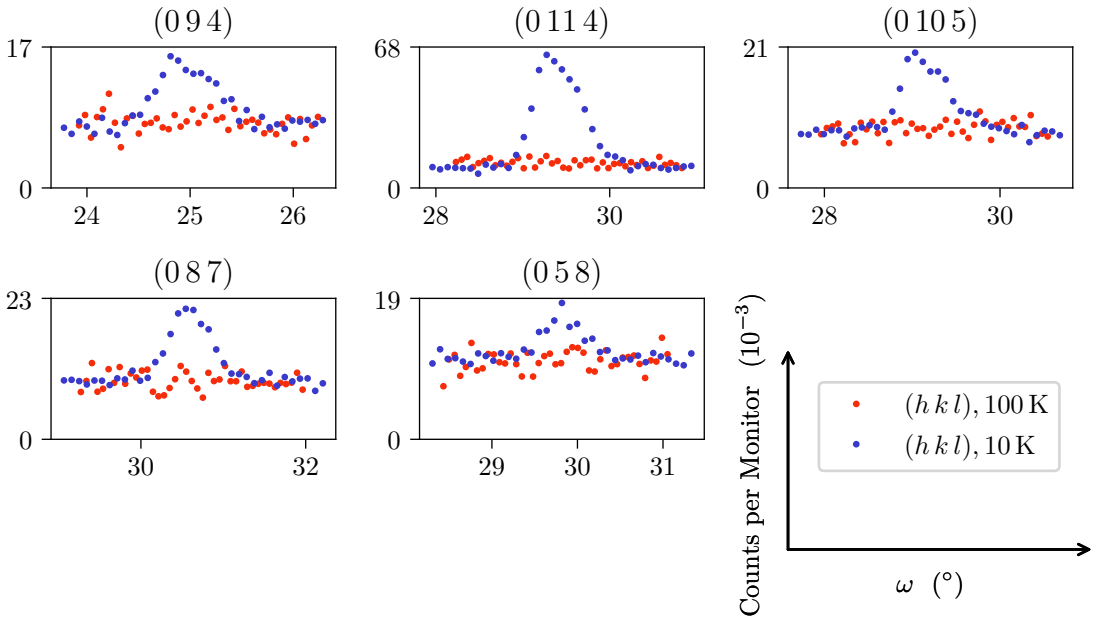

(b)

Forbidden by screw axis 2 $(0, \frac{1}{2}, 0)$ $0, y, 0$:

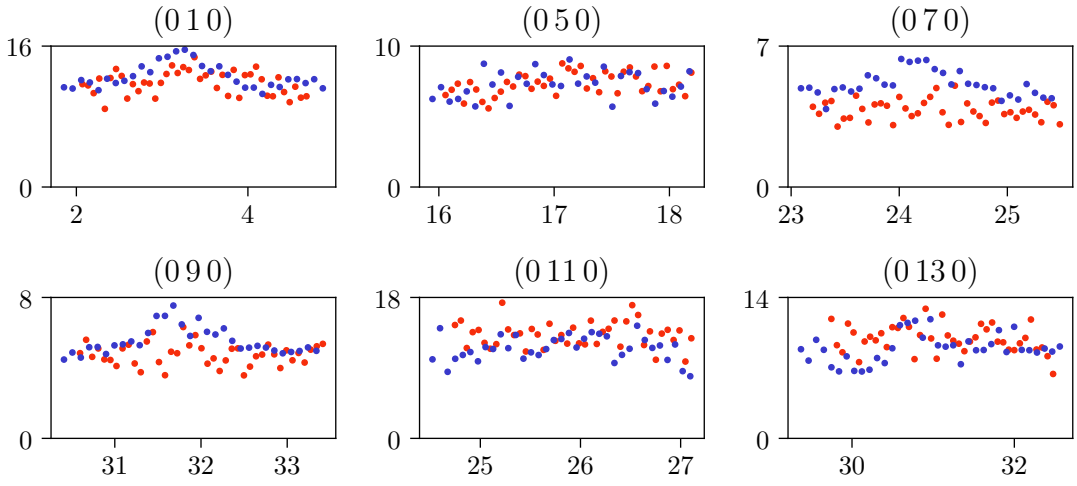

Figure 4.8: Single crystal neutron diffraction ω scans of $(ND_4)_2[FeCl_5(D_2O)]$ at 100 K (red) and 10 K (blue). The reflections are forbidden by glide plane n or the screw axis in y direction. It can be seen that at low temperature, both symmetry elements are broken.

(a)

Forbidden by glide plane a $x, y, \frac{1}{4}$:

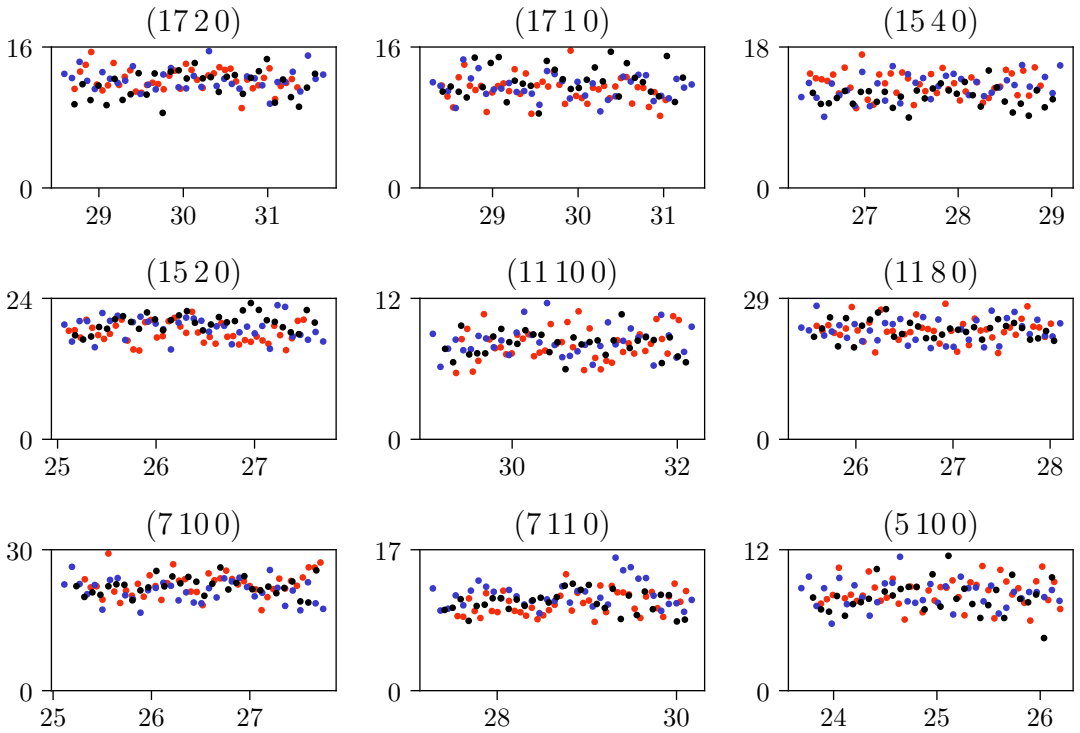

(b)

Forbidden by screw axis 2 $(\frac{1}{2}, 0, 0)$ $x, \frac{1}{4}, \frac{1}{4}$:

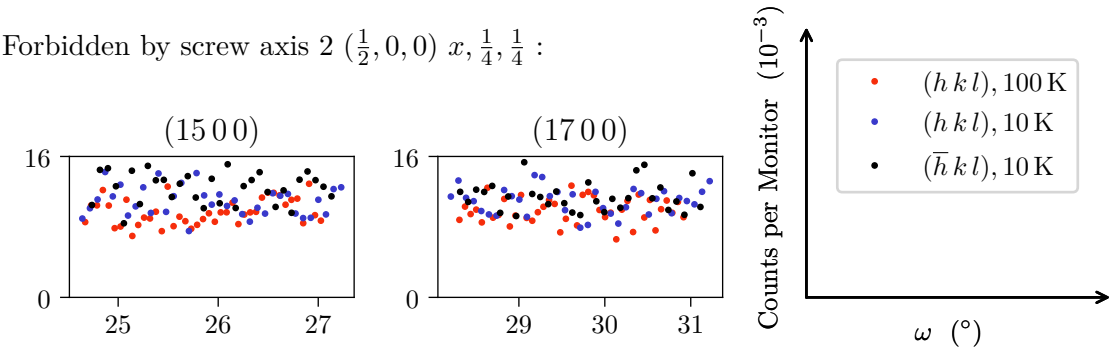

Figure 4.9: Single crystal neutron diffraction ω scans of $(ND_4)_2[FeCl_5(D_2O)]$ at 100 K (red) and 10 K (blue and black). The reflections are forbidden by glide plane a or the screw axis in x direction. It can be seen that at low temperature, both symmetry elements remain.

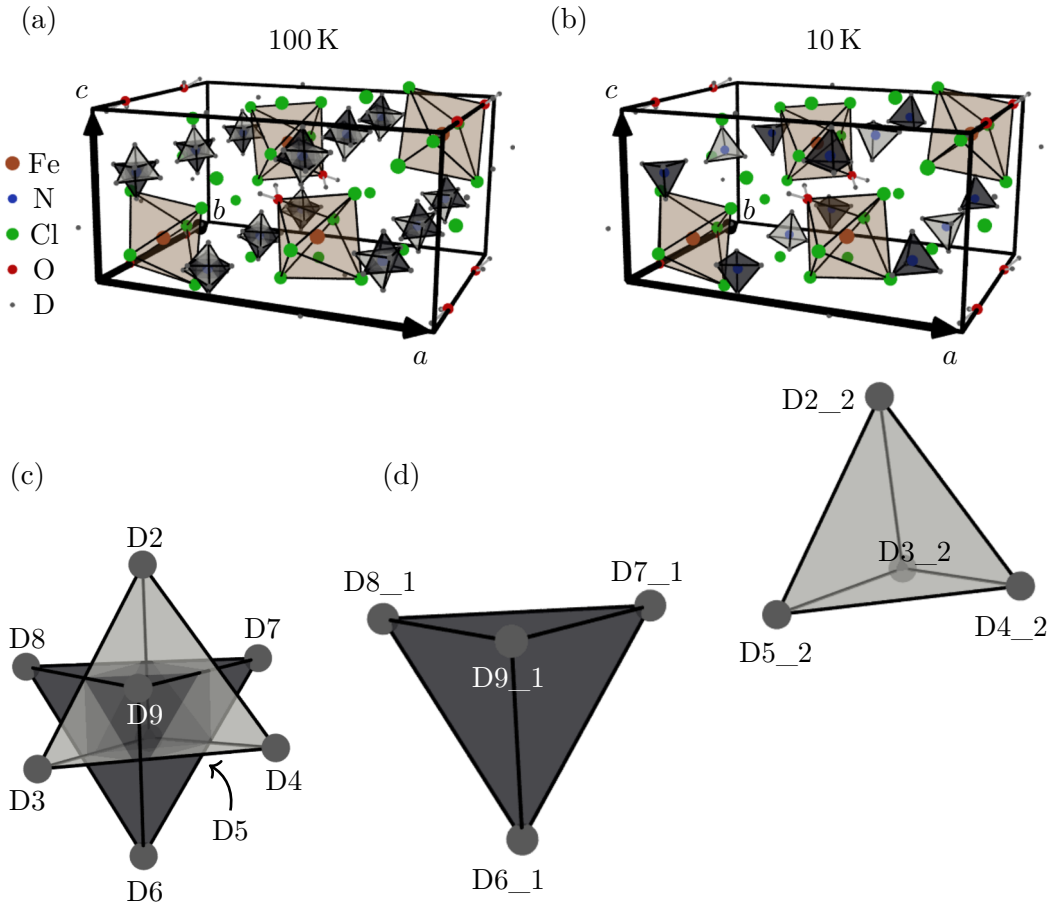

Figure 4.10: Crystal structure of $(ND_4)_2[FeCl_5(D_2O)]$ at 100 K above the structural phase transition (a) and below at 10 K (b). At high temperature, the ND_4 molecules are disordered and occupy both orientations. Symmetrically equivalent $[ND_4]$ tetrahedrons are displayed in the same color (light/dark). (c) Positions and labels of the D atoms in the disordered $[ND_4]$ tetrahedrons in space group *Pnma*. (d) Positions and labels of the D atoms in the ordered $[ND_4]$ tetrahedrons in space group $P2_1/a$.

The ADPs of the D atoms of the [ND_4] molecules are constrained in a way that D atoms which are located at opposite corners (e.g. D2 and D6 or D2_2 and D6_1 in Figure 4.10(c) and (d)) have the same ADPs. The ADPs of the Fe atom are refined isotropically, all other atoms have harmonic ADPs. The occupancies of the [ND_4] tetrahedrons are refined with the constraint that D atoms of the same tetrahedron have the same occupancy. Furthermore, the occupancies of two intersecting tetrahedrons shall add up to 1.

The refinement of the crystal structure at 100 K works well with space group *Pnma*, yielding R values of R(obs) = 4.33 %, wR(obs) = 5.08 %, R(all) = 7.52 %, wR(all) = 5.25 %. The structural parameters are listed in Table A.1 and the crystal structure is shown in Figure 4.10(a). All D positions are occupied approximately equally, i.e. the atoms D2 ... D5 have an occupancy of 0.4387(16) and the atoms D6 ... D9 have an occupancy of 0.6513(16). Physically this means that the two possible orientations of an ND_4 molecule are both occupied with approximately the same probability.

This picture drastically changes at 10 K. A refinement with space group *Pnma* yields bad R values of R(obs) = 14.45 %, wR(obs) = 23.51 %, R(all) = 15.78 %, wR(all) = 23.54 %. The structural parameters are listed in Table A.2. However, a reduction of the symmetry to space group $P2_1/a$ drastically improves the R values to R(obs) = 3.47 %, wR(obs) = 4.30 %, R(all) = 5.45 %, wR(all) = 4.41 %. The structural parameters are listed in Table A.3. In $P2_1/a$, the tetrahedron positions split so that some tetrahedrons can have different occupancies while they were equivalent in space group *Pnma*. Indeed, the tetrahedrons displayed in Figure 4.10(b) have occupancies near 1, while the other tetrahedrons are not occupied. The exact occupancies of the D positions as displayed in Figure 4.10(d) are 0.953(3) for D2_2 ... D5_2 and 0.047(3) for D6_2 ... D9_2 which build two intersecting tetrahedrons. The other pair of intersecting tetrahedrons is D6_1 ... D9_1 with an occupancy of 0.955(2) and D2_1 ... D5_1 with an occupancy of 0.045(2). Because the positional parameters of all D atoms are refined, the refinement yields physically not meaningful positions for atoms D2_1 ... D5_1 and D6_2 ... D9_2 which however does not reduce the quality of the refinement since these positions are nearly not occupied.

The refinement in space group $P2_1/m$ yields bad R values of R(obs) = 13.91 %, wR(obs) = 18.11 %, R(all) = 19.39 %, wR(all) = 18.30 %. This can be explained by the fact that the occupancies of the [ND_4] tetrahedrons are close to 0.5, so that the correct ordering of the occupancy cannot be described in this space group. The structural parameters are listed in Tables A.4 and A.5.

Since substitution of ammonium molecules by K causes pyroelectric polarization [121], a refinement in the polar space group Pa (Nr. 7) was carried out. The occupancy was not refined, instead the occupancies of the D atoms which had a high occupancy from the refinement in space group $P2_1/a$ were set to 1 and the other D atoms were omitted. The ADPs were constrained similar to the refinement in space group $P2_1/a$. By this symmetry reduction, the R values improve to R(obs) = 3.03 %, wR(obs) = 3.49 %, R(all) = 4.42 % and wR(all) = 3.59 %. The structural parameters are listed in Tables A.6 and A.7. Space group Pa allows polarization in a and b direction. Using the

nominal charges $(N^{3-}D_4^{1+})_2[Fe^{3+}Cl_5^{1-}(D_2^{1+}O^{2-})]$, the structural data of the refinement yield a polarization in a direction of $P_a = 0.00123(8)\,\mathrm{C/m^2}$ and in b direction of $P_b = 0.00024(13)\,\mathrm{C/m^2}$. This polarization would be several orders of magnitudes higher and had a different direction compared to the polarization determined by integration of the pyrocurrent or magnetocurrent [121]. The polarization determined by diffraction seems to have no physical meaning. This means that the improvement of the R values in space group Pa compared to space group $P2_1/a$ is not caused by a better description but rather by the larger number of parameters. Within the precision of the measurement, a symmetry reduction to space group Pa is not visible.

4.2.3 Conclusion

The magnetic phase transition could be determined to occur at 7.699(12) K. The ferroelectric phase transition is visible in diffraction data of the investigated $(0\,0\,l)$ reflection. The deflection point in the intensity of the (0 0 0.77) reflection cannot be attributed to this ferroelectric phase transition.

The symmetry reduction to space group $P2_1/a$ according to [113] could be verified by an investigation of selection rules in combination with structural refinements. A further symmetry reduction to the polar space group Pa yields too high values for the polarization compared to existing pyroelectric measurements, so that such a symmetry reduction could not be verified within the precision of the data.

4.3 $Cs_2[FeCl_5(H_2O)]$

Most investigations of the compound $Cs_2[FeCl_5(H_2O)]$ that are presented in this work are also published in [122].

4.3.1 Crystal growth and experimental setup

Large single crystals of $Cs_2[FeCl_5(H_2O)]$ were grown by L. Bohatý [120]rom aqueous solution. The solution consisted of two parts CsCl and one part $FeCl_3$, and a surplus of hydrochloric acid was used. The crystals were grown at a constant temperature of 323 K by slow evaporation of the solvent. Also attempts with temperature decrease were carried out, however the constant temperature yields the best results. After $10-12$ weeks, crystals of sizes up to $15 \times 20 \times 25\,\mathrm{mm^3}$ were obtained. The material is optically clear and the morphological faces well-developed. They could be used for the orientation of the crystals. Such a crystal is depicted in Figure 4.11(a).

For pyroelectric measurements, a plate-like sample of 0.88 mm thickness in (0 1 0) direction and with an area of $4.4 \times 4.0\,\mathrm{mm^2}$ was prepared. The DiMoS setup 3.3.1 was used to measure the pyroelectric charge. The sample was cooled in an applied electric field and during the subsequent heating cycles, the pyroelectric charge was measured. A

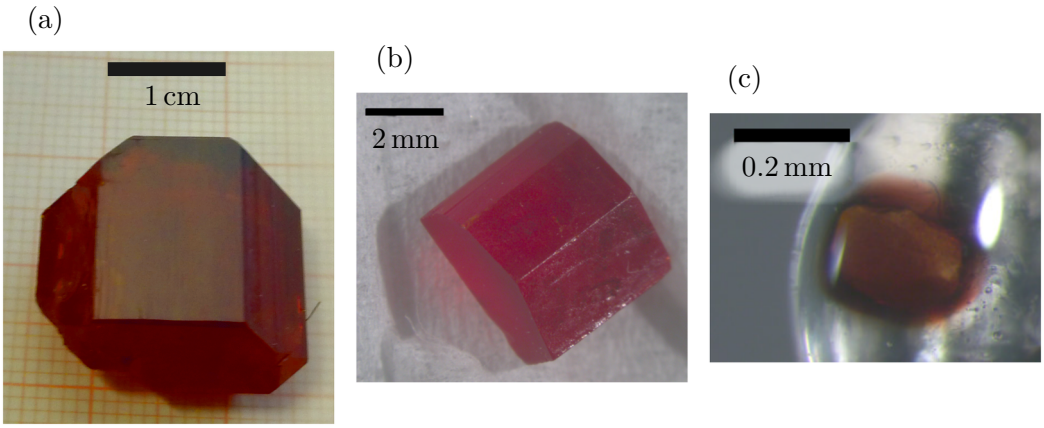

Figure 4.11: Crystals of the compound $Cs_2[FeCl_5(H_2O)]$. (a) As-grown crystal. (b) Sample LB007-S002 for neutron diffraction. (c) Sample LB008-S003 for X-ray diffraction used for structural refinements.

temperature rate of $3 - 5\,\mathrm{K/min}$ was used and two different fields of $0.568\,\mathrm{kV/mm}$ and $1.705\,\mathrm{kV/mm}$ with opposite sign were applied.

A single-crystal sample of $5 \times 5 \times 2\,\mathrm{mm}^3$, as depicted in Figure 4.11(b), was used for neutron diffraction experiments at the thermal neutron four-circle diffractometer 6T2 with lifting counter 3.2.1. An orientation with the b axis vertical to the scattering plane was chosen. Low temperatures were accessed by means of a ^{4}He cryostat and a wavelength of $0.9\,\text{Å}$ was used. The temperature dependence of a magnetic and a structural superstructure reflection was investigated. For structural refinements, sets of reflections were collected at $1.6\,\mathrm{K}$ and at $10\,\mathrm{K}$ which are below and above the Néel temperature, respectively.

Two different X-ray diffraction experiments were carried out. The D5000 3.1.2 was used to investigate the splitting of a reflection due to the structural phase transition. For this, a plate-like single-crystal with an area of $18\,\mathrm{mm}^2$ perpendicular to the $[0\,\overline{2}\,1]$ direction was prepared. A helium flow cryostat was used for low temperatures. A small sample, depicted in Figure 4.11(c) was prepared by evaporating a small amount of solution for a few minutes. The small as-grown crystallite could be used for single-crystal X-ray diffraction without further preparation. Single-crystal X-ray diffraction was carried out on a Bruker AXS Kappa APEX II four-circle diffractometer in combination with an Oxford Cryosystems N-HeliX for low temperaturs, as described in Section 3.1.1. At room temperature and at $100\,\mathrm{K}$, several thousand reflections were collected. A temperature dependent scan of the $(\overline{6}\,7\,\overline{5/2})$ reflection was carried out in the temperature range from $100\,\mathrm{K}$ to $200\,\mathrm{K}$.

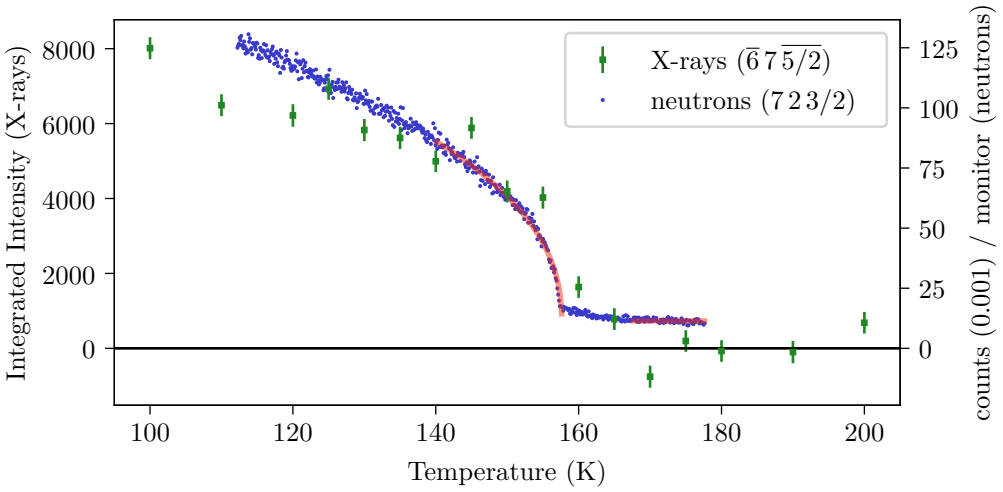

Figure 4.12: Intensities measured by neutron-diffraction (blue) of the (7 2 3/2) reflection and by X-rays (green) of the ($\overline{3}\,7\,\overline{5/2}$) reflection. The phase transition is clearly visible and can be determined by a power-law fit (red) to (157.6 ± 0.1) K.

4.3.2 Results and discussion

4.3.2.1 Structural phase transition

In 1987, a structural phase transition at 151.5 ± 0.5 K was detected via Mössbauer spectroscopy [114]. The single-crystal diffraction data of our samples, both with X-rays and with neutrons, show super-structure reflections arising below a comparable temperature. Figure 4.12 shows the ($\overline{6}\,7\,\overline{5/2}$) reflection investigated by X-ray diffraction and the ($7\,2\,3/2$) reflection by neutron diffraction at different temperatures. A power-law fit of the form $b + A \cdot (T_S - T)^{2\beta}$ was applied to the neutron diffraction data. The background b and the scaling factor A do not contain physically relevant information. The transition temperature T_K could be determined to 157.6 ± 0.1 K and the critical exponent β amounts to 0.220 ± 0.002. The error on the transition temperature was estimated since the fit yields an error which is much smaller than the precision of the experimental setup. The transition temperature is roughly the same as in [114] taking into account that different samples were investigated which might differ in impurity concentration or other defects. The critical exponent of 0.220 is an indication for non-mean-field behavior. The shape of the temperature dependence indicates a second order transition.

In the following we assume that the structural transition is continuous. In this case, it can be associated to a single phonon mode. The possible low-temperature space groups can be looked up in [123]. Since we know that the unit cell is doubled in c direction, the only possible space groups are the ones listed in Table 4.3.

In the following, we write the Miller indexes of the respective subgroup with primes and

mode	monoclinic, centrosymmetric	orthorhombic, polar	monoclinic, polar
Z_1	$C2/m$	$Amm2$	Cm
Z_2	$C2/c$	$Ama2$	Cc
T_1	$C2/m$	$Imm2$	Cm
T_2	$C2/c$	$Ima2$	Cc

Table 4.3: Possible isotropy subgroups for the low-temperature crystal structure according to the modes in agreement with the superstructure reflections [123].

the Miller indexes in the setting of space group $Cmcm$ without primes. Subgroup $C2/m$ acoording to mode Z_1 and subgroup $C2/c$ according to mode Z_2 have the selection rule $h'+k' \in 2\mathbb{Z}$. In both cases, the transformation is $(h', k', l') = (k, h, -2l)$. This gives the selection rule $h+k \in 2\mathbb{Z}$ with the condition $l \in \frac{1}{2}\mathbb{Z}$. Subgroup $Amm2$ according to mode Z_1 and subgroup $Ama2$ according to mode Z_2 exhibit the selection rule $k'+l' \in 2\mathbb{Z}$ and the transformation in both cases is $(h', k', l') = (2l, h, k)$. This also yields the selection rule $h+k \in 2\mathbb{Z}$ and $l \in \frac{1}{2}\mathbb{Z}$ in the setting of space group $Cmcm$. Subgroup $C2/m$ according to mode T_1 and subgroup $C2/c$ according to mode T_2 obey the selection rule $h'+k' \in 2\mathbb{Z}$ and the transformation is $(h', k', l') = (-k+2l, h, k)$. Thus, the selection rule written in the setting of $Cmcm$ is $2\mathbb{Z} \ni h'+k' = -k+2l+h$ which is equivalent to $h+k \in 2\mathbb{Z}$ for $l \in \mathbb{Z}$ and $h+k \in 2\mathbb{Z}+1$ for $l \in \mathbb{Z}+\frac{1}{2}$. Subgroup $Imm2$ according to mode T_1 has the selection rule $h'+k'+l' \in 2\mathbb{Z}$ and the transformation reads $(h', k', l') = (-h, 2l, k)$. This gives the selection rule $2\mathbb{Z} \ni h'+k'+l' = -h+2l+k$ which is equivalent to $h+k \in 2\mathbb{Z}$ for $l \in \mathbb{Z}$ and $h+k \in 2\mathbb{Z}+1$ for $l \in \mathbb{Z}+\frac{1}{2}$. Subgroup $Ima2$ according to mode T_2 has the selection rule $h'+k'+l' \in 2\mathbb{Z}$ and the transformation $(h', k', l') = (2l, h, k)$. The selection rule in the setting of $Cmcm$ thus reads $2\mathbb{Z} \ni h'+k'+l' = 2l+h+k$ which is equivalent to $h+k \in 2\mathbb{Z}$ for $l \in \mathbb{Z}$ and $h+k \in 2\mathbb{Z}+1$ for $l \in \mathbb{Z}+\frac{1}{2}$. The space groups Cm or Cc have the same setting as the respective space groups $C2/m$ or $C2/c$ of the same mode. The selection rules of the former do not differ from the ones of the latter.

We can summarize these considerations in the way that the subgroups of the modes Z_1 and Z_2 have only reflections with even $h+k$ independent on the l that might be integer or half-integer. In contrast to that, the subgroups of the modes T_1 and T_2 have reflections with integer l only for even $h+k$ while the superstructure reflections with half-integer l occur only for odd $h+k$.

Figure 4.13 shows histograms of super-structure reflections (with half-integer l) separately for the reflections with even resp. odd $h+k$. The distribution of the intensity divided by its error $I/\sigma(I)$ of superstructure reflections with even $h+k$ is centered around zero. In contrast to that, the superstructure reflections with odd $h+k$ show statistically significant non-zero intensities. According to the considerations above, all subgroups that belong to the modes Z_1 or Z_2 can be ruled out. This means that the

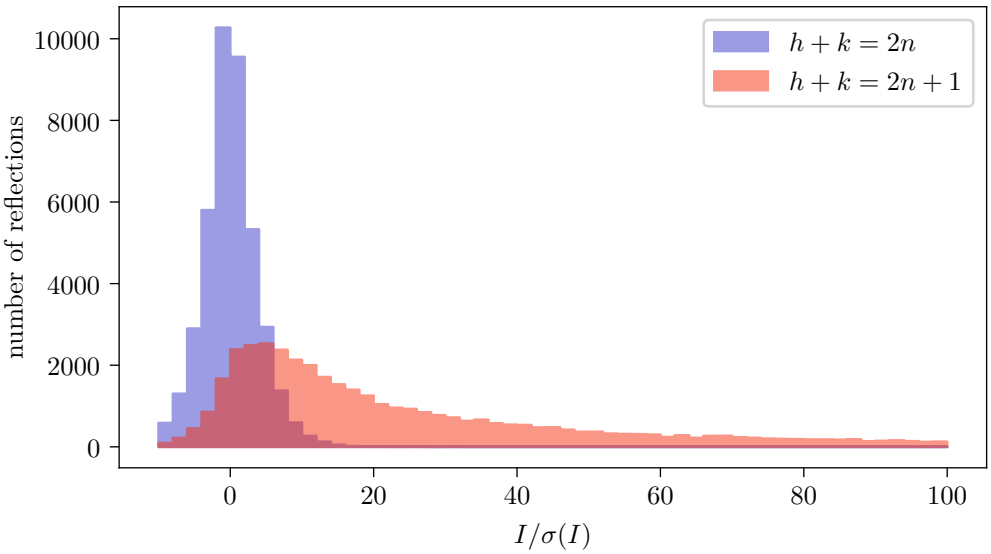

Figure 4.13: Histograms of the intensities divided by its error $I/\sigma(I)$ of reflections (h, k, l) with half-integer l with respect to the $Cmcm$ setting. The intensities of reflections with even $h+k$ are compatible with zero intensity, while the reflections with odd $h + k$ show significant intensities.

possible subgroups can be restricted to those of the modes T_1 and T_2.

Table 4.3 shows that the subgroups differ also in the fact that some of them are monoclinic while others are orthorhombic and some of them are centrosymmetric while others are polar. This results in different physical properties which are discussed in the next few paragraphs.

A measurement of the polarization allows to distinguish between the polar space groups $Imm2$, $Ima2$, Cm and Cc and the centrosymmetric space groups $C2/m$ and $C2/c$ of the modes T_1 and T_2. For all polar subgroups, the polarization is expected to appear along the b direction of the $Cmcm$ setting. The pyrocurrent is shown in Figure 4.14. Although the experimental setup is very sensitive, no signal is visible at the phase transition. Even multiferroic materials, which have a relatively weak ferroelectric polarization compared to ferroelectric materials, typically show a ferroelectric polarization in the order of a few hundred $\mu C/m^2$ [124]. Due to the high precision of the measurement, we can rule out a breaking of the inversion symmetry during the phase transition at $(157.6 \pm 0.1)\,\mathrm{K}$. As upper bound for the ferroelectric polarization, $0.5\,\mu\mathrm{C/m^2}$ should be a reasonable value. The upper panel of Figure 4.14 shows a slope in the integrated charge. This corresponds to the non-zero current shown in the upper panel. This can be explained by several artifacts which are possible: It might be the Seebeck effect which is induced by temperature gradients. Corrosion of the contact surfaces could lead to ion exchange. Also the triboelectric effect, which causes a constant drift of the operational amplifier, is a possible explanation.

The possible monoclinic subgroups have the unique axis along a with respect to the

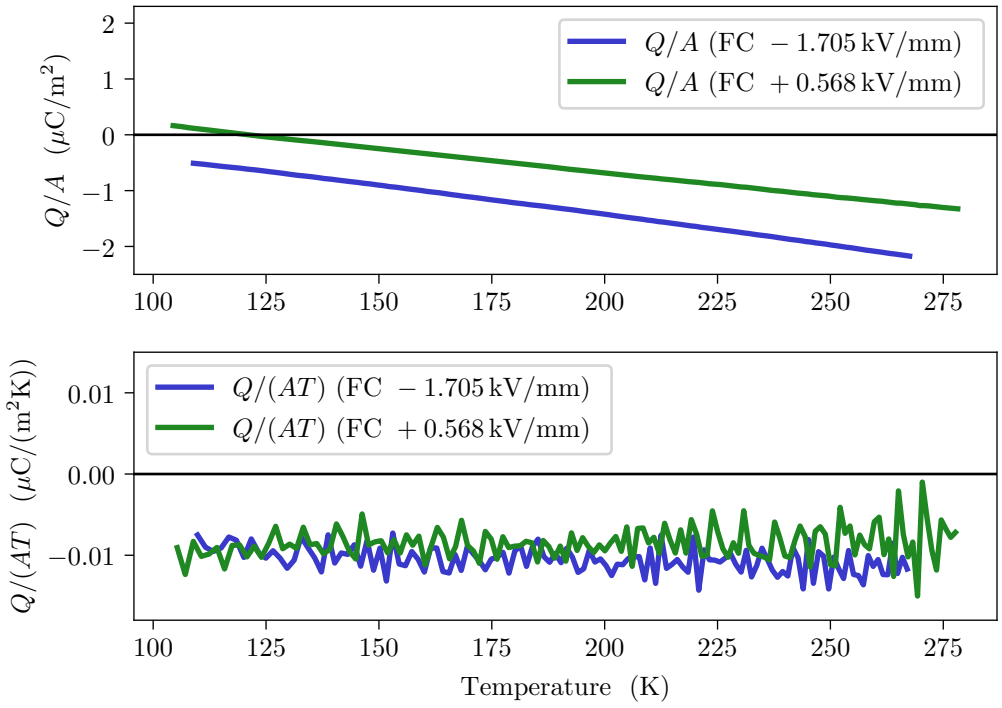

Figure 4.14: Integrated pyro charge divided by the sample area (upper panel) and the pyro current (lower panel) in b direction with respect to the $Cmcm$ setting. During cooling, an electric field was applied to the sample and the measurement was carried out during the heating cycle.

Cmcm setting. From this, it can be concluded that for example reflections of the form $(0\,k\,l)$ with $k \neq 0 \neq l$ are expected to show a monoclinic splitting. $(0\,2\bar{l}\,l)$ scanes of the $(0\,\bar{8}\,4)$ reflection at different temperatures are shown in Figure 4.15(a). Temperatures above the structural phase transition are indicated by a red color, while scans below the phase transition are plotted in blue. At high temperatures, the α_1/α_2 splitting of the CuK_α radiation is clearly visible. At lower temperatures, this splitting disappears. This is a clear indication for a broadening of the reflection, and thus for a monoclinic space group at low temperatures. Figures 4.15(b)-(d) show the results of pseudo-Voigt fits. The profile function for the fit contains two pseudo-Voigt functions, one for the α_1 and α_2 radiation, respectively. The intensity ratio is fixed to $I(\alpha_2)/I(\alpha_1) = 0.515$ and the positions of the two peaks are constrained by the known values for the energies $E_{\alpha_1} = 8.048\,\text{keV}$ and $E_{\alpha_2} = 8.028\,\text{keV}$ [125]. The Lorentz fraction of the pseudo Voigt functions is fixed to $\eta = 0.4$. In Figure 4.15(d), the change of the peak width is clearly visible. The fit of a step function with the step position fixed to the transition temperature shows that the peak is broadened from 0.108° to 0.146°. From this, the monoclinic angle can be determined in the following way: We assume that the peak width due to the instrument and sample imperfections amounts to $\Gamma_{Profile} = 0.108°$. The total peak width also includes the monoclinic splitting, such that $\Gamma^2 = \Gamma^2_{Profile} + \Gamma^2_{monoclinic}$. The latter summand can be calculated for different values of the metric angle $\alpha = 90° + \delta$ by a comparison of the Bragg angles $\theta_{(0\,8\,4)}$ and $\theta_{(0\,\bar{8}\,4)}$ of the reflections $(0\,8\,4)$ and $(0\,\bar{8}\,4)$. For an orthorhombic crystal, these two Bragg angles equal, but their difference increases with δ. The peak width caused by the monoclinic splitting is $\Gamma_{monoclinic} = |2\theta_{(0\,8\,4)} - 2\theta_{(0\,\bar{8}\,4)}|$. Using the known lattice constants, for different possible values of δ, the total peak width Γ is calculated and in a graphical way the value for δ that corresponds to $\Gamma = 0.146°$ is read of. The deviations from the orthorhombic metric turns out to amount to $\delta = 0.08°$.

We have seen that the low-temperature crystal structure is centrosymmetric and monoclinic, so the possible subgroups can be restricted to $C2/m$ of mode T_1 and $C2/c$ of mode T_2. The R values of the refinements are listed in Table 4.4. Also refinements in the space groups $Imm2$ and $Ima2$ are carried out. Notice that the R values of subgroups belonging to the same mode are very similar, while the refinement in space group $C2/c$ yields much better R values compared to $C2/m$. Taking into account that the crystal structure is monoclinic and non-polar, we can conclude that $C2/c$ is the correct space group for the crystal structure of $Cs_2[FeCl_5(H_2O)]$ below the structural phase transition at 157.6 K.

For a better understanding of the structural distortion, it is useful to describe the low-temperature crystal structure in the non-standard setting $I2/c$ instead of $C2/c$. The basis transformation from the *Cmcm* setting to the $I2/c$ setting is

$$(\boldsymbol{a}, \boldsymbol{b}, \boldsymbol{c})_{I2/c} = (\boldsymbol{b}, \boldsymbol{a}, -2\boldsymbol{c})_{Cmcm} \quad .$$

The transformation from the standard setting $C2/c$ to $I2/c$ is

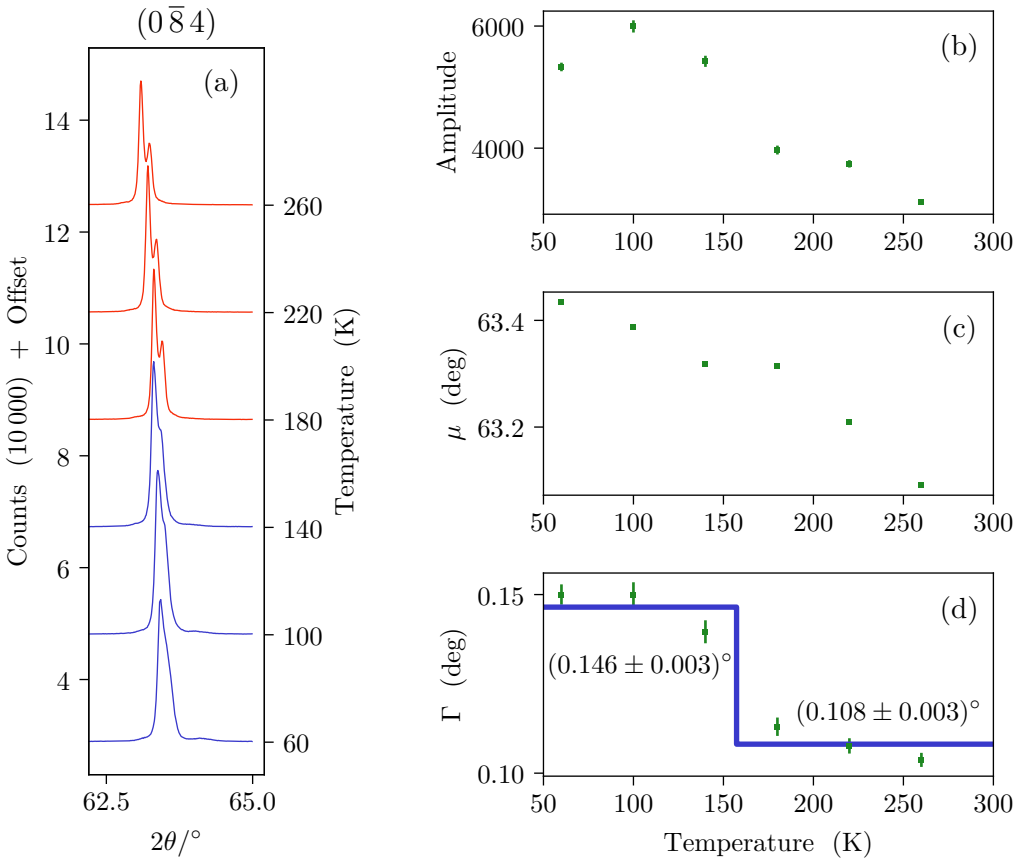

Figure 4.15: (a) Temperature dependent $(0\,2\bar{l}\,l)$ scans of the $(0\,\overline{8}\,4)$ reflection. (b)-(d) Aplitude, position and peak width at different temperatures, determined by pseudo-Voigt fits. A step function is fitted to the temperature-dependent peak width in (d) in order to estimate the monoclinic angle in the low-temperature phase.

mode	monoclinic	orthorhombic
	$C2/m$	$Imm2$
	$R(\text{obs}) = 4.21\,\%$	$R(\text{obs}) = 4.30\,\%$
T_1	$wR(\text{obs}) = 5.96\,\%$	$wR(\text{obs}) = 5.89\,\%$
	$R(\text{all}) = 6.16\,\%$	$R(\text{all}) = 6.49\,\%$
	$wR(\text{all}) = 6.21\,\%$	$wR(\text{all}) = 6.16\,\%$
	$C2/c$	$Ima2$
	$R(\text{obs}) = 3.17\,\%$	$R(\text{obs}) = 3.13\,\%$
T_2	$wR(\text{obs}) = 3.94\,\%$	$wR(\text{obs}) = 3.95\,\%$
	$R(\text{all}) = 4.75\,\%$	$R(\text{all}) = 5.04\,\%$
	$wR(\text{all}) = 4.19\,\%$	$wR(\text{all}) = 4.25\,\%$

Table 4.4: R values of the refinements carried out several isotropy subgroups of $Cmcm$.

$$(\boldsymbol{a}, \boldsymbol{b}, \boldsymbol{c})_{I2/c} = (\boldsymbol{c}, \boldsymbol{b}, -\boldsymbol{a} - \boldsymbol{c})_{C2/c} \quad ,$$

preceded by an origin shift to $(-1/4, -1/4, -1/2)^{\mathrm{T}}_{C2/c}$.

The refinement in space group $C2/c$ uses isotropic atomic displacement parameters (ADPs) for the atoms Fe1_1 and Cl1_1 and anisotropic ADPs for all other atoms. The ADPs of the other Cl atoms (Cl2_1, Cl2_2, Cl2_3 and Cl2_4) are constrained in a way that opposing atoms have the same ADPs and neighbored atoms have ADPs rotated about 90° around the a axis. The result of the refinements of the high-temperature data (in space group $Cmcm$) and of the low-temperature data (in the non-standard setting $I2/c$ of space group $C2/c$) are shown in Table A.8. The low-temperature refinement also takes into account a twinning law of the form $(h\,\overline{k}\,\overline{l})_{I2/c}$, wherein the second twin covers a volume fraction of 0.2. This means that despite the small size of the sample, ferroelastic domains arise at the structural phase transition. It is important to keep that twinning in mind when measurements on larger crystals are interpreted.

Note that the ADPs at room-temperature are quite large: The U_{iso} in the order of magnitude $0.025\,\text{Å}^2$ correspond to displacements in the order of $0.1\,\text{Å}$ which can only be explained by strong disorder at room-temperature. The largest displacement is U_{11} of the O atom which is in agreement with the recent publication [126] on the deuterated compound $Cs_2[FeCl_5(D_2O)]$. This large ADP at high temperature corresponds to the shift of the O atom at low temperature.

Figure 4.16 shows the low-temperature crystal structure with space group $C2/c$. The

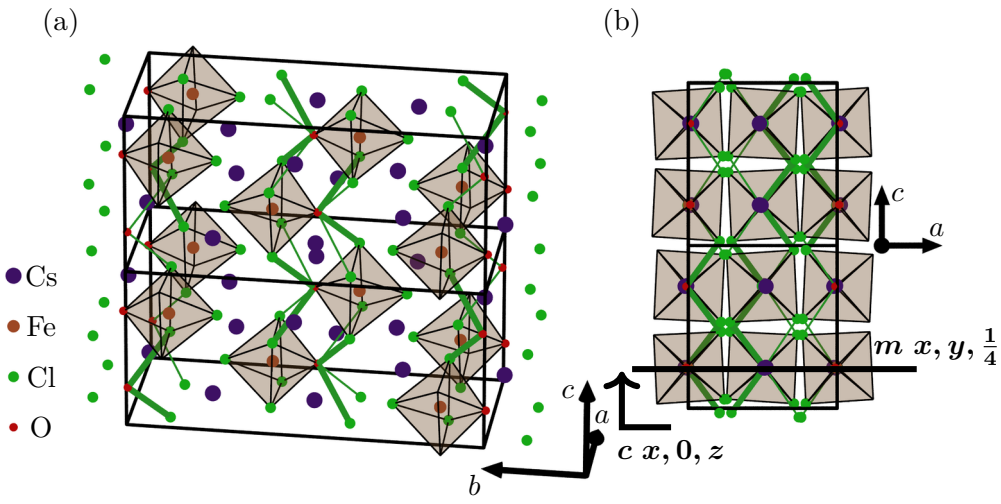

Figure 4.16: Low-temperature crystal structure of $Cs_2[FeCl_5(H_2O)]$. The axes refer to the *Cmcm* setting of the high-temperature crystal structure. (a) Oblique projection. (b) View along *b*. The short O − Cl distances are displayed by thick green lines while the long ones are displayed by thin green lines. The mirror plane $m\ x, y, \frac{1}{4}$ and the glide plane $c\ x, 0, z$ are broken at low temperature.

axes refer to the *Cmcm* setting, the unit cell is twice as large in *c* direction. While in the high-temperature phase, the hydrogen bonds are disordered, so that two symmetrically equivalent bonds exist, in the low-temperature phase only one of them is realized (thick green lines in Figure 4.16). The O − Cl distances split into short ones of length 3.328(8) Å resp. 3.300(8) Å and long distances of 3.460(7) Å resp. 3.499(8) Å. The high-temperature structure exhibits distance of 3.4205(14) Å for all O − Cl bonds. The distortion furthermore leads to a tilting of the octahedrons around the *a* axis of the *Cmcm* setting about 3.4(4)° as depicted in Figure 4.16(b). The sign of the tilting order can be explained by the O − H − Cl bonds: The short O − Cl distances contain the H atom so that the hydrogen-bond length fits to the geometry of the water molecule. Since such a water molecule connects two next-nearest-neighbor octahedrons seperated by the lattice constant *c*, these octahedrons must rotate in opposite direction, resulting in a doubling of the *c* axis.

4.3.2.2 Magnetic phase transition

The (0 0 1) reflection in the *Cmcm* setting is forbidden in *Cmcm* and it is also weak in the low-temperature space group $I2/c$. However, using neutron diffraction, this reflection appears at the magnetic phase transition as shown in Figure 4.17. A fit similar to that one in Figure 4.12 was applied for the determination of the exact transition temperature. The transition temperature[1] amounts to (6.35 ± 0.05) K and the critical exponent is $\beta = 0.2890(2)$, which is expected for a three-dimensional Heisenberg model.

[1]The error of the fit amounts to 0.002 K, while the experimental precision of the temperature should be estimated to 0.05 K.

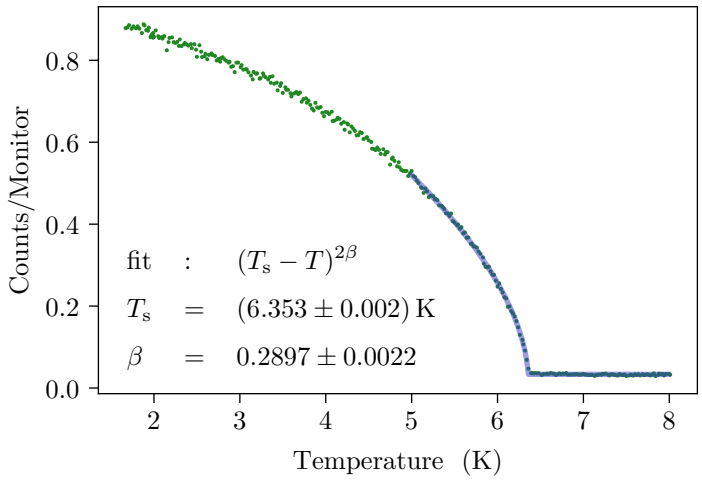

Figure 4.17: Neutron-diffraction temperature-scan of the (0 0 1) reflection (green). The reflection appears at a temperature of 6.35 K. The error 0.002 K of the fit (blue) is smaller than the precision of the temperature setup.

Since the structural deviation from space group $Cmcm$ is small, it can be neglected for the magnetic analysis. The occurrence of the (0 0 1) reflection shows that the propagation vector is $\boldsymbol{k} = \mathbf{0}$ and the magnetic moments are aligned perpendicular to c. In [115], it was found that below the Néel temperature T_N, the magnetic susceptibility along the a direction is suppressed, which is is good agreement with our observation of the (0 0 1) reflection. The symmetry analysis carried out by the program BasIreps of the Fullprof Suite [127] is shown in Table 4.5.

Since we know that the magnetic moments are oriented perpendicular to c and the crystal structure is antiferromagnetic, we can restrict the possible irreducible representations to Γ_2 and Γ_4. The refinements of the magnetic structure were carried out in the following way: The intensity differences of the measurements of the paramagnetic phase at 10 K and of the antiferromagnetic phase at 1.6 K were calculated so that only the magnetic contribution remains. Because of the magnetic form factor and the big errors which occur for the intensity differences, only reflections with $2\theta < 30°$ we used for the refinements. 116 reflections remained. Additionally to the magnetic refinements, a structural refinement using the data at 10 K was carried out. This yields R values of $R(F^2) = 13.1\,\%$ and $wR(F^2) = 16.1\,\%$. These R values are good enough for the determination of a reliable overall scaling factor, the structural data are not used in the further analysis. The scaling factor is used in order to determine the magnitude of the magnetic moments. The magnetic refinements according to Γ_2 and Γ_4 yield $\chi^2 = 37$ and $\chi^2 = 1.7$ respectively. The R values for Γ_2 amount to $R(F^2) = 62.9\,\%$ and $wR(F^2) = 68.6\,\%$ and for Γ_4 they amount to $R(F^2) = 28.8\,\%$ and $wR(F^2) = 14.9\,\%$. Thus, the magnetic refinements clearly show that the magnetic structure can be described according to Γ_4, where the magnetic moments are aligned along the a axis and have a magnitude of $4.10(3)\,\mu_B$. The susceptibility data [115] determined the magnetic moment to $5.92\,\mu_B$

	$0, y, \frac{1}{4}$	$0, \overline{y}, \frac{3}{4}$
Γ_2	$0, v, 0$	$0, \overline{v}, 0$
Γ_3	$0, 0, w$	$0, 0, w$
Γ_4	$u, 0, 0$	$\overline{u}, 0, 0$
Γ_5	$0, v, 0$	$0, v, 0$
Γ_7	$u, 0, 0$	$u, 0, 0$
Γ_8	$0, 0, w$	$0, 0, \overline{w}$

Table 4.5: Irreducible representations that describe the possible magnetic structures according to the propagation vector $\boldsymbol{k} = \mathbf{0}$. The magnetic Fe ions are located at $0, y, \frac{1}{4}$ and $0, \overline{y}, \frac{3}{4}$. The entries of the table describe the orientations of the magnetic moments. Generated by BasIreps of the FullProf Suite [127].

and the expected value of a spin-5/2 magnetic moment is $5\,\mu_B$. One possible explanation for the smaller magnetic moment is that fluctuations appear. Furthermore, it must be taken into account that a part of the moments is transferred to ligands. This lowers the effective form factor in contrast to the model used in the refinement, where the magnetic moments are distributed only over the Fe atoms. The magnetic point group is mmm' and the magnetic structure corresponds to Shubnikov group $Cmcm'$, which is consistent with [115]. The magnetic structure is displayed in Figure 4.18.

4.3.3 Conclusion and comparison to existing results

It could be shown that $Cs_2[FeCl_5(H_2O)]$ undergoes a structural phase transition at $(157.6 \pm 0.1)\,K$. This phase transition can be identified with the one found in [114]. The investigation in this work shows that the c axis is doubled and the symmetry reduces from space group $Cmcm$ to space group $I2/c$ with a monoclinic angle that deviates roughly 0.08° from 90°. The structural distortion can be attributed to an ordering of the hydrogen bonds, which are statistically realized in the high-temperature structure. A 3.4(4)° rotation of the $[FeCl_5(H_2O)]$ octahedrons around the b axis takes place during the structural phase transition. The monoclinic distortion is visible as broadening of a Bragg reflection so that orthorhombic subgroups can be ruled out. Also polar subgroups are not possible because pyroelectric measurements do not show any pyrocharge. The room temperature lattice parameters found in this work deviate from the ones published by Fabelo et al. [126] for $Cs_2[FeCl_5(D_2O)]$, while the atomic positions and the ADPs are in agreement. The differences in the lattice parameters can be explained by the fact that Fabelo et al. used the deuterated compound. In the latter publication, the low-temperature crystal structure was determined at 20 K in contrast to 100 K as in the present work. This explains differences in the structural data at low temperature. A qualitative comparison shows that the distortion is of the same kind. The tilting of the $[FeCl_5(D_2O)]$ octahedrons in [126] amounts to 3.73(3)° in contrast to 3.4(4)° for the

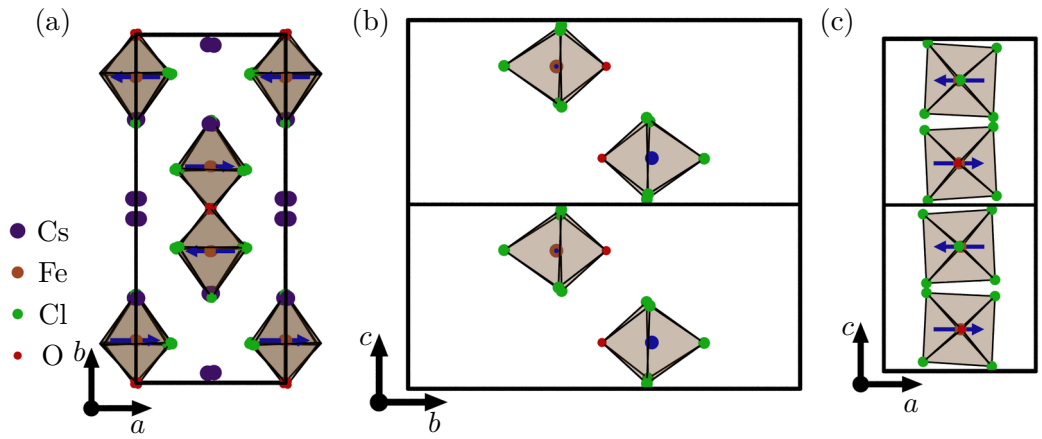

Figure 4.18: Magnetic structure of $Cs_2[FeCl_5(H_2O)]$. The axis refer to the *Cmcm* setting of the high-temperature crystal structure. (a) View along *c*. (b) View along *a*. (c) View along *b*. In (b) and (c) only one zig-zig chain of $[FeCl_5(H_2O)]$ octahedrons is displayed for the sake of clarity.

$[FeCl_5(H_2O)]$ octahedrons in the present work.

The magnetic structure with Shubnikov group *Cmcm′*, proposed by Ackermann et al. [115], could be verified by neutron diffraction. The structural distortion can be neglected for the description of the magnetic structure because no significant α_{32} or α_{23} coefficients could be measured [115]. The magnetic structure published by Fabelo et al. [126] is in agreement with our result. Also in the former publication, the magnetic moment is lower than expected and amounts to $4.39\,\mu_B$.

5 $Cs_3Fe_2Br_9$

The compound $Cs_3Fe_2Br_9$ was first published by Wei et al. in [128], where small crystals on the mm scale were produced. They are described as having a black color. Wei et al. discovered this compound in the context of photovoltaic applications and focus their work on opto-electronic properties. In contrast to this, we obtained $Cs_3Fe_2Br_9$ as a by-product of the research in the field of erythrosiderite-type compounds and are interested in magnetic properties.

5.1 Phase diagram

The compound $Cs_3Fe_2Br_9$ exhibits a very rich phase diagram. Figure 5.1 shows the phase diagram of this compound with the magnetic field aligned along the c axis [129]. At high temperature, the sample is in the paramagnetic phase P0. At zero-field, there are two transitions between 13 K and 14 K, below which the sample is in the antiferromagnetic phase P1. Between these two transition temperatures, the antiferromagnetic phase P2 exists in a narrow region which is much broader at higher fields around 10 T. Seven further phases could be detected, which partially exist only at very high fields up to nearly 40 T. This work focuses on the magnetic structures of the phases P1, P2 and P3.

5.2 Sample characterization and experimental setup

Single crystals of $Cs_3Fe_2Br_9$ were grown from non-stoichiometric aqueous solution by L. Bohatý [120] The growth method differs from that used by Wei et al. [128]. Particularly, Wei et al. used a hydrothermal process at $160°C$, while our samples were grown at room temperature during all processes. The crystal used for neutron diffraction experiments in this work was a by-product of the growth of $Cs_2[FeBr_5(H_2O)]$. It exhibits a very dark red color and a shiny surface. The surface corrodes when exposed to air for many weeks. This process can be prevented by an oil film. Carefully wiping the corroded surface with propanol restores the shiny surface.

A first structural determination by X-ray diffraction was done by I. Cisarova [130]. The crystal structure exhibits the hexagonal space group $P6_3/mmc$ (No. 194) with lattice constants $a = b = 7.5258(5)$ Å and $c = 18.5638(12)$ Å. The atomic positions are given in table 5.1. The measurement was carried out at 150 K. The lattice constants are larger compared to those published by Wei et al. at this temperature [128].

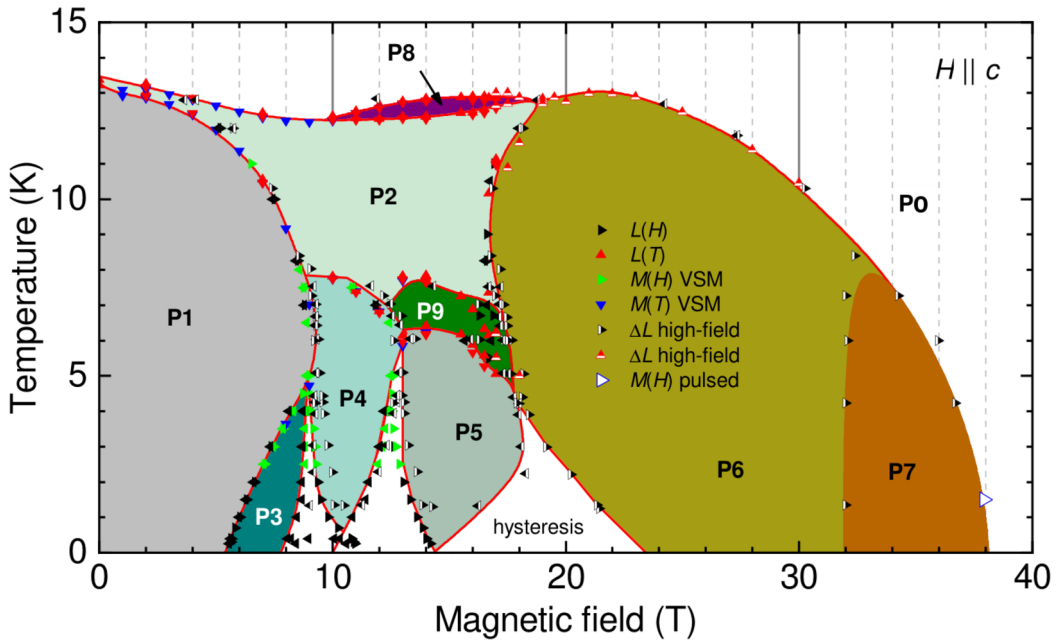

Figure 5.1: Phase diagram of $Cs_3Fe_2Br_9$ with the magnetic field aligned along the c direction [129]. The phase diagram was determined by measurements of the following quantities: Magnetostriction $L(H)$; thermal expansion $L(T)$; magnetisation in dependence of the magnetic field $M(H)$ and the temperature $M(T)$, measured with a vibrating sample magnetometer (VSM) or in a pulsed high-field (pulsed), ΔL is magnetostriction in high magnetic field. The high field measurements were measured during a short field pulse which can dissipate energy so that the temperature might be corrupted. From D. Brüning [129].

	x	y	z
Cs01	0	0	1/4
Cs02	1/3	2/3	0.41776(4)
Br03	0.51243(8)	$2x$	1/4
Br04	$2y$	0.17217(6)	0.41242(4)
Fe05	2/3	1/3	0.34667(9)

Table 5.1: Structure determination of $Cs_3Fe_2Br_9$ by I. Cisarova [130].

Neutron diffraction experiments were carried out on HEiDi (FRM II) and 6T2 (LLB) (cf. Sections 3.2.3 and 3.2.1) using the crystal LB025-S001 which has a mass of 48.680(14) mg and thus a volume of 10.85 mm^3. The shape of the sample is roughly a prism with an irregular hexagonal base, as shown in Figure 5.2(a). The base faces are cut along the [0 0 1] directions and the other faces are naturally grown along the [1 0 0] and equivalent directions with respect to the hexagonal space group $P6_3/mmc$. For the measurement on HEiDi, the sample was wrapped in aluminum foil which was glued to the sample stick with two-component glue (Figure 5.2(b)). For the measurement on 6T2, the sample was tied to an aluminum plate with aluminum wire (Figure 5.2(c)). Both methods have the advantage that the chemically sensitive sample is not in contact with glue.

On HEiDi, the sample LB025-S001 was cooled using a He cryostat with no field applied. As primary optics, an Er filter, 16 mm tube with elongation and no collimation was used. The secondary optics consisted of a 25 mm tube and a $15 \times 25\ mm^2$ rectangular slit. The collection was carried out using a point detector. Temperature dependent scans of some magnetic superstructure reflections were carried out with a wavelength of 1.171 Å during heating. A search for superstructure reflections of the form $(0\,0\,l)$ was carried out at 2.5 K with a wavelength of 1.171 Å. Nuclear reflections were collected using the wavelengths 1.171 Å and 0.795 Å. Magnetic reflections were collected with the wavelength 1.171 Å. Corrupted reflections were culled manually, so the following numbers refer to the remaining reflections: For the structural refinement, 1291 reflections were collected at 15 K (649 of which are unique with respect to space group $P6_3/mmc$ and 282 unique reflections were observed) and 1109 reflections were collected at 2.5 K (350 of which are unique with respect to space group $P6_3/mmc$ and 272 unique reflections were observed). For the magnetic refinement, 336 magnetic reflections were collected at 2.5 K (310 of which belong to different Friedel pairs and 94 of which were observed).

On 6T2, the sample was placed in a magnetic coil that can provide magnetic fields up to approximately 7 T with a Variable Temperature Insert operating with liquid He. Temperature- and field-dependent scans of some reflections were carried out using a point detector. The collection of reflections for refinement was done with a 2D detector in order to cover a large number of reflections in a relatively short time. A wavelength of 2.432 Å was chosen. 55 magnetic reflections were collected (51 of which belong to different Friedel pairs and all of them are observed) at a temperature of 12.5 K and a magnetic field of 6 T. The investigation of phase P2 (section 5.3.2.2) was carried out with sample LB025-S001, while for the investigation of phase P3 (section 5.3.2.3) the sample LB026-S003 was used. The positions of the reflections vary systematically due to a bend sample stick, so that a precise determination of the Miller indices of the superstructure reflections is not possible.

5.3 Results and discussion

The following considerations use several different choices for the unit cell. The relations between the a and b axes is given in figure 5.3 while the c axis is unchanged. The basis transformations are given in Equation 5.1.

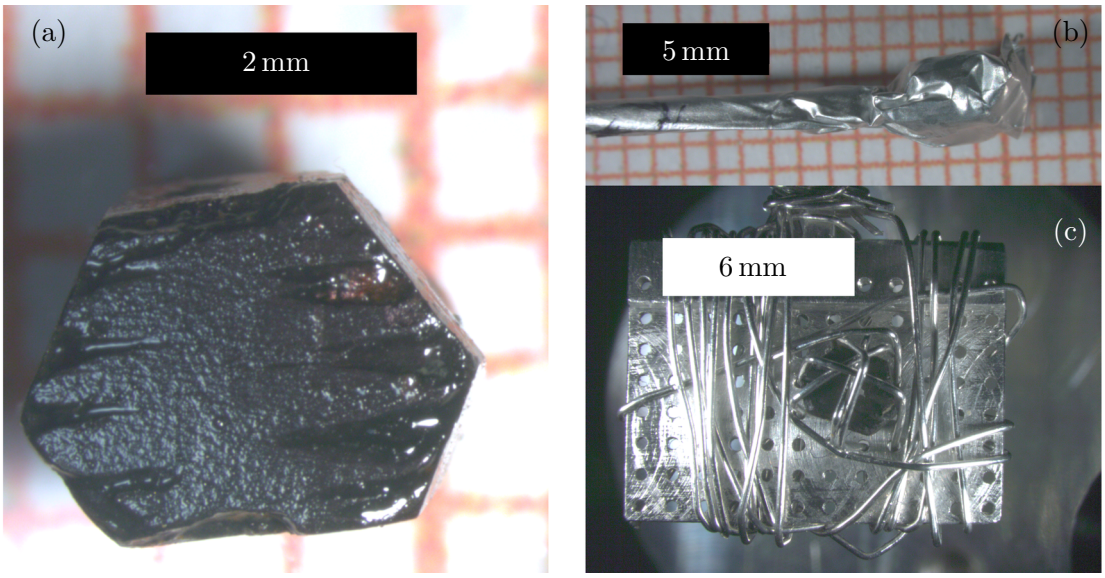

Figure 5.2: $Cs_3Fe_2Br_9$ sample LB025-S001 used for neutron diffraction measurements. (a) The sample has roughly the shape of an irregular hexagonal prism. (b) For the measurement on HEiDi, the sample was wrapped in aluminum foil. (c) For the measurement on 6T2, the sample was tied with aluminum wire.

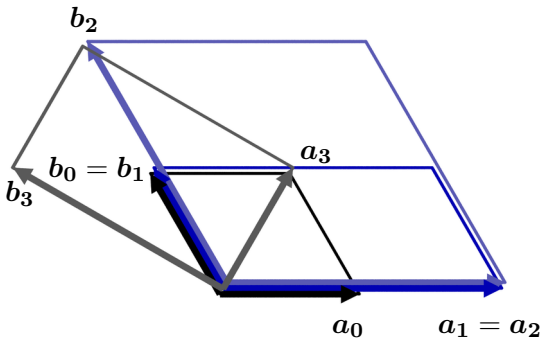

Figure 5.3: Different cell choices used in this chapter. $\boldsymbol{a_0}$ and $\boldsymbol{b_0}$ are used to describe the crystallographic unit cell. $\boldsymbol{a_1}$ and $\boldsymbol{b_1}$ describe the unit cell for the zero-field magnetic structure in phase P1, however the refinement is carried out in the cell defined by $\boldsymbol{a_2}$ and $\boldsymbol{b_2}$ for practical reasons. The cell defined by $\boldsymbol{a_3}$ and $\boldsymbol{b_3}$ describes the low-temperature crystallographic structure with space group *Cmcm*. The transformations are given in Equation 5.1.

$$
\begin{aligned}
\boldsymbol{a_1} &= 2\boldsymbol{a_0} & \boldsymbol{a_2} &= 2\boldsymbol{a_0} \\
\boldsymbol{b_1} &= \boldsymbol{b_0} & \boldsymbol{b_2} &= 2\boldsymbol{b_0} \\
\boldsymbol{c_1} &= \boldsymbol{c_0} & \boldsymbol{c_2} &= \boldsymbol{c_0}
\end{aligned}
\tag{5.1}
$$

$$
\begin{aligned}
\boldsymbol{a_3} &= \boldsymbol{a_0} + \boldsymbol{b_0} \\
\boldsymbol{b_3} &= -\boldsymbol{a_0} + \boldsymbol{b_0} \\
\boldsymbol{c_3} &= \boldsymbol{c_0}
\end{aligned}
$$

5.3.1 Investigation of the crystal structure

The results of the structure determination with neutron diffraction on HEiDi are shown in Table 5.2 for 15 K and in Table 5.3 for 2.5 K. At both temperatures, the positions deviate from the structure determined by Ivana Cisarova (cf. Table 5.1) only after three significant figures. The largest deviations can be found in the x and y coordinates of the Br atoms. It is worth mentioning that the structure determinations by Ivana Cisarova and in this work differ both in temperature (150 K / 15 K resp. 2.5 K) and in the type of probe (X-ray / neutron). Thus it is clear that small deviations can be expected. More interesting is a comparison of the crystal structure at 15 K and at 2.5 K. The R values are much better at 2.5 K, but this can be referred to the fact that at 2.5 K the number of unique reflections was much smaller compared to 15 K. The atomic positions are consistent within one standard deviation. Most atomic displacement parameters (ADPs) behave as expected: At 2.5 K, they are smaller compared to 15 K. There are few exception from this rule: U_{11}, U_{22} and U_{12} of the Fe atom is slightly bigger at the lower temperature. However, the difference is well below one standard deviation, so it might not have any physical meaning.

Wei et al. [128] base their theoretical predictions about the magnetic couplings on DFT calculations. These include a refinement of the metric and atomic positions (cf. supplemental of [128]). The lattice parameters of the DFT calculation are 2 % (a and b axis) resp. 1 % (c axis) smaller than those determined by us via single crystal neutron diffraction, which is not conspicuous because single crystal diffraction is not suitable for a precise determination of the metric. However, huge differences occur in the geometry of the $[Fe_2Br_9]$ double-octahedrons: The $Fe-Fe$ distance determined by neutron diffraction is 3.5834(22) Å, while the DFT calculation predicts only 3.0018 Å. Also the bonding angle of the $Fe-Br-Fe$ super exchange coupling deviates drastically, namely 82.94(5)° determined by neutron diffraction and 76.48° for the DFT. We will see later that these differences can explain that the magnetic couplings predicted by Wei et al. are not in accordance with the magnetic structures determined in this work. The geometry of the double-octahedron in the crystal structure predicted by Wei et al. via DFT calculations has rather a close similarity to the compound $Cs_3Cr_2Br_9$, which exhibits a $Cr-Cr$ distance of 3.194(34) Å and a $Cr-Br-Cr$ angle of 75.5(7)° [131].

The magnetic structure is antiferromagnetic and in the next section we will see that the

	x	y	z
Cs01	0	0	1/4
Cs02	1/3	2/3	0.41779(13)
Br03	0.51173(16)	0.0235(3)	1/4
Br04	0.34273(19)	0.17137(10)	0.41275(5)
Fe05	2/3	1/3	0.34658(9)

R_{obs}	$= 3.71\,\%$
wR_{obs}	$= 4.05\,\%$
R_{all}	$= 16.03\,\%$
wR_{all}	$= 4.85\,\%$

	U_{ani}(Å^2)	U_{11}(Å^2)	U_{22}(Å^2)	U_{33}(Å^2)	U_{12}(Å^2)	U_{13}(Å^2)	U_{23}(Å^2)
Cs01	0.0049(11)	0.0030(12)	0.0030(12)	0.009(2)	0.0015(6)	0	0
Cs02	0.0068(7)	0.0060(9)	0.0060(9)	0.0084(12)	0.0030(4)	0	0
Br03	0.0061(6)	0.0047(6)	0.0063(9)	0.0079(8)	0.0032(5)	0	0
Br04	0.0066(4)	0.0046(7)	0.0056(5)	0.0091(5)	0.0023(3)	-0.0005(7)	-0.0002(3)
Fe05	0.0049(4)	0.0038(5)	0.0038(5)	0.0073(6)	0.0019(3)	0	0

Table 5.2: Refinement of the crystal structure of $Cs_3Fe_2Br_9$ at 15 K using single crystal neutron diffraction data collected on HEiDi. The refinement was carried out for space group $P6_3/mmc$.

	x	y	z
Cs01	0	0	1/4
Cs02	1/3	2/3	0.41798(8)
Br03	0.51178(11)	0.0236(2)	1/4
Br04	0.34287(13)	0.17143(7)	0.41277(4)
Fe05	2/3	1/3	0.34660(6)

R_{obs}	$= 2.44\,\%$
wR_{obs}	$= 2.15\,\%$
R_{all}	$= 4.67\,\%$
wR_{all}	$= 2.44\,\%$

	U_{ani}(Å^2)	U_{11}(Å^2)	U_{22}(Å^2)	U_{33}(Å^2)	U_{12}(Å^2)	U_{13}(Å^2)	U_{23}(Å^2)
Cs01	0.0040(7)	0.0026(8)	0.0026(8)	0.0067(14)	0.0013(4)	0	0
Cs02	0.0052(5)	0.0045(6)	0.0045(6)	0.0067(8)	0.0022(3)	0	0
Br03	0.0052(4)	0.0044(4)	0.0046(7)	0.0067(5)	0.0023(3)	0	0
Br04	0.0054(3)	0.0043(5)	0.0050(3)	0.0066(3)	0.0022(2)	0.0000(5)	0.0000(2)
Fe05	0.0044(3)	0.0041(4)	0.0041(4)	0.0049(4)	0.00203(18)	0	0

Table 5.3: Refinement of the crystal structure of $Cs_3Fe_2Br_9$ at 2.5 K using single crystal neutron diffraction data collected on HEiDi. The refinement was carried out for space group $P6_3/mmc$.

antiferromagnetic ordering takes place within the *ab* plane. This is why the three-fold symmetric axis in $P6_3/mmc$ must be broken and we end up in the orthorhombic space group $Cmcm$ (No. 63). The transformation between these space groups is not trivial. Since the group-subgroup relation is translationengleich but in $Cmcm$, a C centered cell is chosen so that the unit cell is twice as large. The group-subgroup relation is given in Figure 5.4. The first column describes space group $P6_3/mmc$ as usual in the cell with axes $\boldsymbol{a_0}, \boldsymbol{b_0}, \boldsymbol{c_0}$. The second column uses the same setting, but the three-fold symmetry is broken. This space group is $Cmcm$, but an unconventional cell choice is used. The third column describes space group $Cmcm$ in the conventional setting using the axes $\boldsymbol{a_3}, \boldsymbol{b_3}, \boldsymbol{c_3}$. Note, that this cell is twice as big, so the additional translation is restored by the C centering (cf. Figure 5.3). This is why the number of cosets in the middle column is 8, but in the right column it is 16. In order to follow the positions of the atoms when the symmetry is reduced, Fig. 5.5 shows a Bärnighausen diagramm [132]. From the multiplicities it is easy to see that a unit cell with axes $\boldsymbol{a_3}, \boldsymbol{b_3}, \boldsymbol{c_3}$ contains twice as much atoms compared to a unit cell with axes $\boldsymbol{a_0}, \boldsymbol{b_0}, \boldsymbol{c_0}$. The group-subgroup relation is translationengleich and its index in this case is $[P6_3/mmc : Cmcm] = 3$.

In order to search for a breaking of the three-fold symmetry, the following procedure was applied: The crystal structure was refined in space group $P6_3/mmc$ using the axes $\boldsymbol{a_0}, \boldsymbol{b_0}, \boldsymbol{c_0}$. Then the structure was transformed to space group $Cmcm$ with axes $\boldsymbol{a_3}, \boldsymbol{b_3}, \boldsymbol{c_3}$. Two refinements in space group $Cmcm$ were carried out: One with the atomic positions and ADPs kept fixed, and one refining them. The R values of these two refinements can be compared in order to check whether a significant improvement could be achieved by the lower symmetry. The results are shown in Table 5.4. In this case, the refinement in $Cmcm$ yields non-positive definite ADPs when all degrees of freedom are refined. That is why isotropic ADPs are applied and the ADPs of the Br atoms are constrained to be identical. This explains why the R values of space group $P6_3/mmc$ in Table 5.4 are higher than in Tables 5.2 and 5.3. No significant improvement of the refinement could be achieved by the breaking of the three-fold symmetry. Especially, the improvement is not better for 2.5 K below the magnetic phase transition compared to 15 K above. This is not unusual because structural distortions induced by a magnetic phase transition are often very small and below the resolution of a diffraction experiment.

5.3.2 Investigation of the magnetic structure

5.3.2.1 Phase P1

Figure 5.6 shows a cut through the reciprocal space along the plane with $l = 0$ in phase P1 at 2.5 K. Superstructure reflections are clearly visible at $\left(\frac{3}{2}\,0\,0\right)$, $\left(1\,\bar{\frac{1}{2}}\,0\right)$ and $\left(\frac{1}{2}\,\frac{1}{2}\,0\right)$. The origin of the powder rings is unknown. We will later see that the superstructure reflections can be explained by the propagation vector $\left(\frac{1}{2}\,0\,0\right)$.

The superstructure reflections indeed appear at the transition temperature to the antiferromagnetic phase as shown by the temperature-dependent scans of the reflections $\left(\frac{3}{2}\,0\,0\right)$ and $\left(\frac{1}{2}\,\frac{1}{2}\,0\right)$ in Figure 5.7(a). From these scans, the transition temperature can

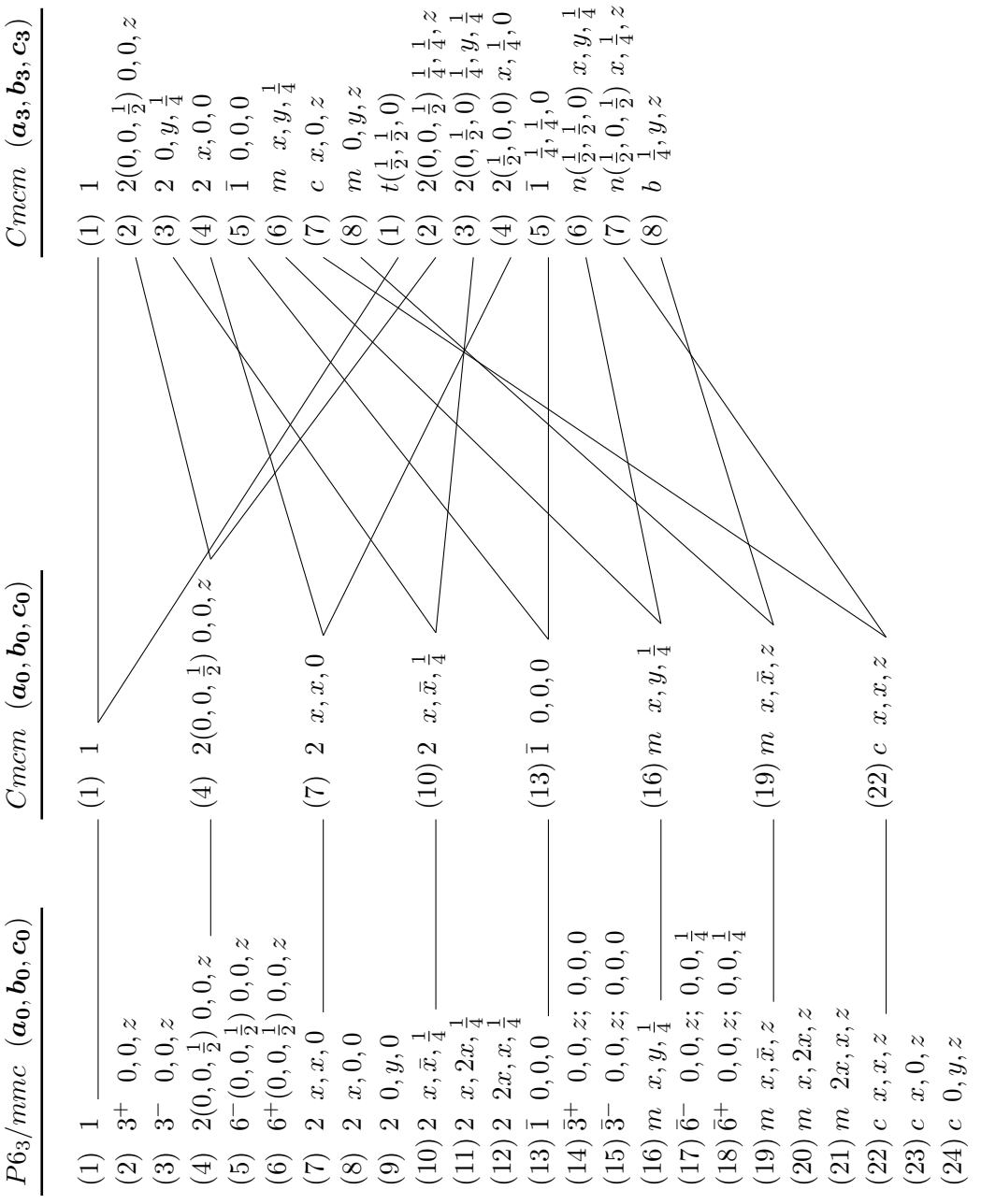

Figure 5.4: Group-subgroup relation between the space groups $P6_3/mmc$ and $Cmcm$ that is expected for the phase transition of $Cs_3Fe_2Br_9$. The middle column describes the space group $Cmcm$ in the cell $\boldsymbol{a_0}, \boldsymbol{b_0}, \boldsymbol{c_0}$ in which conventionally space group $P6_3/mmc$ is described.

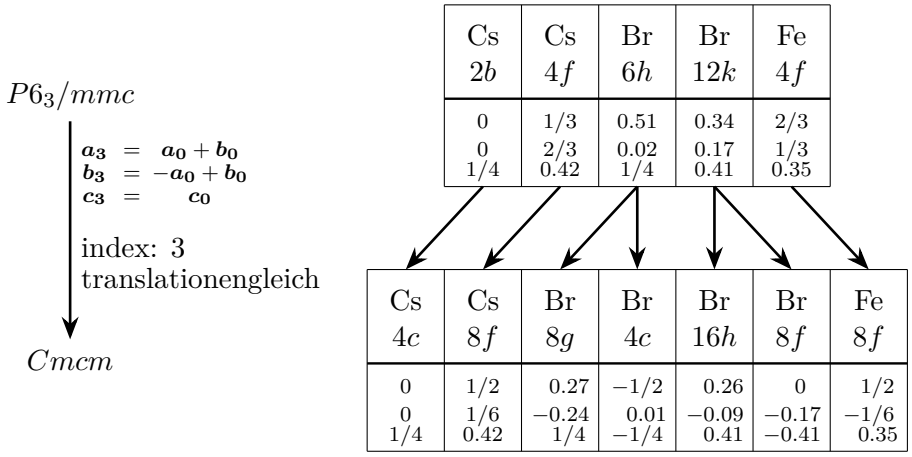

Figure 5.5: A Bärnighausen diagram (cf. [132]) shows how the crystal structure of $Cs_3Fe_2Br_9$ is described in the space groups $P6_3/mmc$ and $Cmcm$.

		$P6_3/mmc$	$Cmcm$ (fixed)	$Cmcm$ (refined)
15 K	R(obs)	4.16 %	4.52 %	4.32 %
	wR(obs)	4.62 %	4.74 %	4.07 %
	R(all)	16.30 %	17.79 %	17.67 %
	wR(all)	5.33 %	5.64 %	4.86 %
2.5 K	R(obs)	2.76 %	3.35 %	3.26 %
	wR(obs)	2.48 %	3.53 %	3.43 %
	R(all)	4.97 %	6.15 %	5.97 %
	wR(all)	2.74 %	3.81 %	3.63 %

Table 5.4: The refinement of the neutron diffraction data of $Cs_3Fe_2Br_9$ at 15 K and 2.5 K in the orthorhombic space group $Cmcm$ does not yield significantly better results compared to $P6_3/mmc$.

be determined to be $(13.5 \pm 0.5)\,\mathrm{K}$. Large peak widths above the phase transition are physically meaningless and originate from bad fits due to the low amplitudes. However, also below the phase transition the peak width increases when the phase transition is approached. This can be explained by an incomplete long-range ordering. Parts of the volume might already be in the paramagnetic phase P0 or in the intermediate antiferromagnetic phase P2 which will be investigated in section 5.3.2.2.

Half-integer reflections (with respect to the crystallographic cell) were investigated in l direction, i.e. reflections with $h = k = 0$. Scans of such reflections are shown in Figure 5.7(b). All of these reflections are absent, which is an indication for an alignment of the magnetic moments along the c direction.

A symmetry analysis was carried out using the program BasIreps of the FullProf suite [127]. In space group $P6_3/mmc$, the propagation vector $\left(\frac{1}{2}\,0\,0\right)$ with a magnetic moment at the Fe position $\left(\frac{2}{3}, \frac{1}{3}, 0.35\right)$ allows eight irreducible representations $\Gamma_1, \ldots, \Gamma_8$, as shown in Table 5.5. The parameters u and v for the magnetic moment can be chosen arbitrarily. In Table 5.5, all atoms in the magnetic unit cell with axes $\boldsymbol{a_1}, \boldsymbol{b_1}, \boldsymbol{c_1}$ are given (cf. Figure 5.3 and Equation 5.1). Due to the propagation vector $\left(\frac{1}{2}\,0\,0\right)$ (in the crystallographic unit cell with axes $\boldsymbol{a_0}, \boldsymbol{b_0}, \boldsymbol{c_0}$), a translation along $\boldsymbol{a_0} = \frac{1}{2}\boldsymbol{a_1}$ leads to a phase shift of π, i.e. a factor -1 for the magnetic moment. Since we know that the magnetic moments are aligned along the c axis, we can restrict the set of possible irreducible representations to $\Gamma_2, \Gamma_3, \Gamma_6, \Gamma_7$ and furthermore assume $u = 0$. It is clear that the sign of v does not change the magnetic structure but rather translates along $\boldsymbol{a_0}$.

The magnetic structures according to all four irreducible representations were refined using the software JANA [69]. The refinement was carried out in the unit cell with the axes $\boldsymbol{a_2}, \boldsymbol{b_2}, \boldsymbol{c_2}$ (cf. Figure 5.3 and Equation 5.1). This has the advantage that twinning by loss of the three-fold axis can be easily described by the following transformations for the Miller indeces: $h_{\mathrm{twin2}} = k_{\mathrm{twin1}}, k_{\mathrm{twin2}} = -h_{\mathrm{twin1}} - k_{\mathrm{twin1}}$ and $h_{\mathrm{twin3}} = -h_{\mathrm{twin1}} - k_{\mathrm{twin1}}, k_{\mathrm{twin3}} = h_{\mathrm{twin1}}$, while the index l remains unchanged. The magnetic moments were set to unity so that the amplitude information can be recovered from the scaling factors. This implies the constraint that all magnetic moments have the same amplitude.

Table 5.6 shows the resulting R values for the four possible magnetic structures. It is obvious that the magnetic structure according to the irreducible representation Γ_3 describes the measured intensities by far better than the other structures. The twins cover 39.27(70) %, 30.83(51) % and 29.89(48) %, respectively. The magnetic structure is depicted in Figure 5.8. The magnetic moments of the two Fe ions in one double-octahedron are aligned ferromagnetically. The nearest neighbours of a double-octahedron in the plane below and above in c direction are mainly aligned antiferromagnetically, i.e. four of them have the opposite orientation and two of them have the same orientation. The next-nearest neighbours in b direction are aligned ferromagnetically and in a and $a + b$ direction antiferromagnetically. By comparing the scale factors of the magnetic refinement and the nuclear refinement, the magnetic moment can be determined to amount $(3.97 \pm 0.02)\,\mu_\mathrm{B}$. This is slightly below the expected value of $5\,\mu_\mathrm{B}$ for an Fe^{3+} ion. Possible explanations for this are fluctuations or a spatial distribution of the magnetic

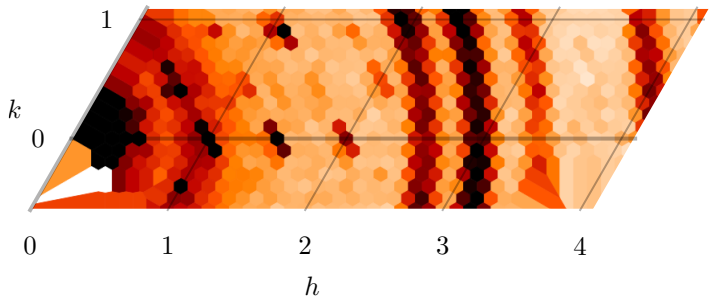

Figure 5.6: Superstructure reflections of $Cs_3Fe_2Br_9$ at 2.5 K without magnetic field. The plot shows the plane in reciprocal space with $l = 0$. The Miller indices refer to the crystallographic cell with axes $\boldsymbol{a_0}, \boldsymbol{b_0}, \boldsymbol{c_0}$. The magnetic superstructure reflections $\left(\frac{3}{2}\,0\,0\right)$, $\left(1\,\bar{\frac{1}{2}}\,0\right)$ and $\left(\frac{1}{2}\,\frac{1}{2}\,0\right)$ are clearly visible.

	x	y	z	Γ_1	Γ_2	Γ_3	Γ_4	Γ_5	Γ_6	Γ_7	Γ_8
Fe_1	$\frac{2}{3}$	$\frac{1}{3}$	0.35	$0\ \bar{u}\ 0$	$2u\ u\ v$	$2u\ u\ v$	$0\ \bar{u}\ 0$	$0\ \bar{u}\ 0$	$2u\ u\ v$	$2u\ u\ v$	$u\ \bar{u}\ 0$
Fe_2	$\frac{1}{3}$	$\frac{2}{3}$	0.85	$0\ \bar{u}\ 0$	$2u\ u\ \bar{v}$	$2u\ u\ \bar{v}$	$0\ \bar{u}\ 0$	$0\ u\ 0$	$2\bar{u}\ \bar{u}\ v$	$2\bar{u}\ \bar{u}\ v$	$0\ u\ 0$
Fe_3	$\frac{1}{3}$	$\frac{2}{3}$	0.65	$0\ u\ 0$	$2u\ u\ v$	$2\bar{u}\ \bar{u}\ \bar{v}$	$0\ \bar{u}\ 0$	$0\ u\ 0$	$2u\ u\ v$	$2\bar{u}\ \bar{u}\ \bar{v}$	$0\ \bar{u}\ 0$
Fe_4	$\frac{2}{3}$	$\frac{1}{3}$	0.15	$0\ u\ 0$	$2u\ u\ \bar{v}$	$2\bar{u}\ \bar{u}\ v$	$0\ \bar{u}\ 0$	$0\ \bar{u}\ 0$	$2\bar{u}\ \bar{u}\ v$	$2u\ u\ \bar{v}$	$0\ u\ 0$

Table 5.5: Irreducible representations that describe zero-field antiferromagnetic structures with propagation vector $\left(\frac{1}{2}\,0\,0\right)$, generated by the program BasIreps of the FullProf suite [127]. The positions are given with respect to the crystallographic cell with axes $\boldsymbol{a_0}, \boldsymbol{b_0}, \boldsymbol{c_0}$. The magnetic cell is twice as large and can be described with the axes $\boldsymbol{a_1}, \boldsymbol{b_1}, \boldsymbol{c_1}$ (cf. Figure 5.3 and Equation 5.1).

moment that is not covered by the model and yields a smaller form factor.

5.3.2.2 Phase P2

In order to ensure that the sample is in the correct phase, we carried out temperature dependent scans of the $(\bar{1}\,\frac{1}{2}\,0)$ reflection at different magnetic fields. At some temperature, the reflection disappears. The temperature exhibits a large systematic error which is dependent on the direction of the temperature scan (cooling/heating). So it was not sure whether the reflection disappears at entering phase P2 or phase P0. Figure 5.9 shows the transition points in the phase diagram determined in this way. The shape of the phase boundary line shows that we detected the phase boundary line between P1 and P2.

Figure 5.10 shows a section of the reciprocal space in phase P2. Superstructure reflections are clearly visible. They are close to the wave vectors $\left(\frac{1}{2}\,\frac{1}{4}\,0\right)$, $\left(\frac{1}{4}\,\frac{1}{2}\,0\right)$, $\left(\frac{3}{4}\,\frac{1}{2}\,0\right)$ and $\left(\frac{1}{2}\,\frac{3}{4}\,0\right)$ according to the axes $\boldsymbol{a_0}, \boldsymbol{b_0}, \boldsymbol{c_0}$ (cf. Figure 5.3 and Equation 5.1). The data collection was not very precise so that reflections of a Friedel pair, that should have the same intensity, in some cases differ by more than a factor of 2. Later Measurements by S.

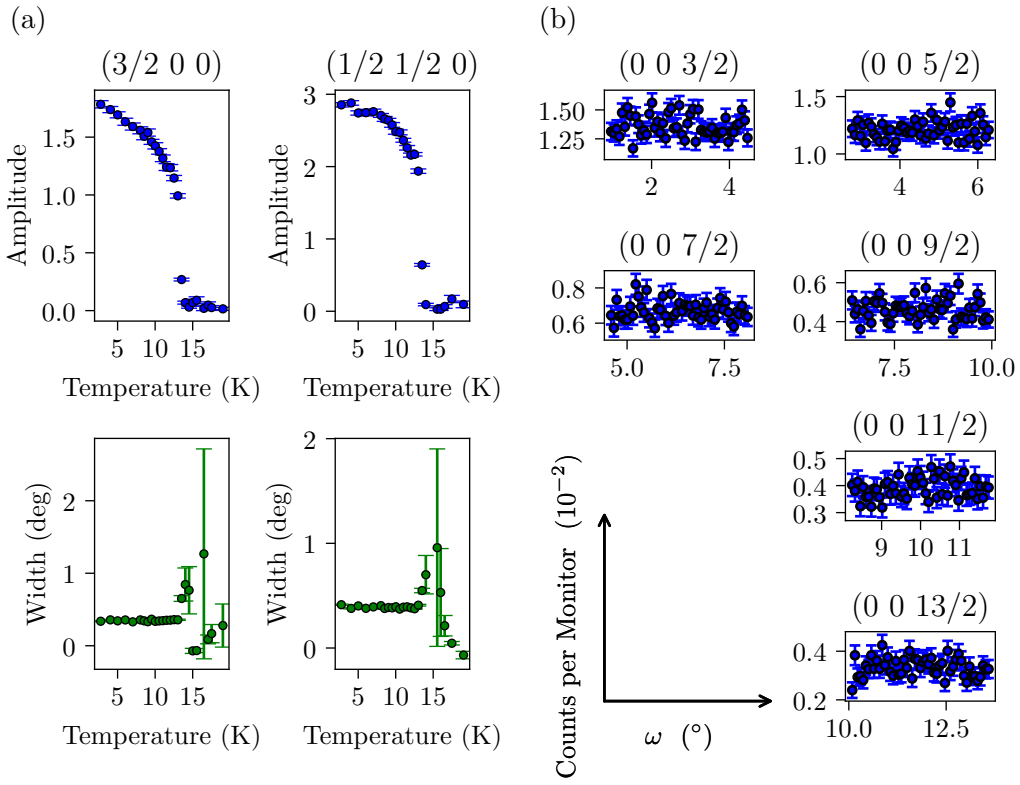

Figure 5.7: (a) Temperature dependence of the magnetic superstructure reflections $\left(\frac{3}{2}\,0\,0\right)$ and $\left(\frac{1}{2}\,\frac{1}{2}\,0\right)$. (b) There are no superstructure reflections in l direction. Consequently, the magnetic moments are aligned along the c direction. The Miller indices refer to the crystallographic cell with axes $\boldsymbol{a_0}, \boldsymbol{b_0}, \boldsymbol{c_0}$.

	Γ_2	Γ_3	Γ_6	Γ_7
R(obs)	65.50 %	9.10 %	66.82 %	75.29 %
wR(obs)	77.08 %	7.66 %	73.14 %	80.19 %
R(all)	102.33 %	32.35 %	83.70 %	169.56 %
wR(all)	77.79 %	9.10 %	73.23 %	83.08 %

Table 5.6: The refinements show clearly that the magnetic structure according to the irreducible representation Γ_3 describes the measured intensities.

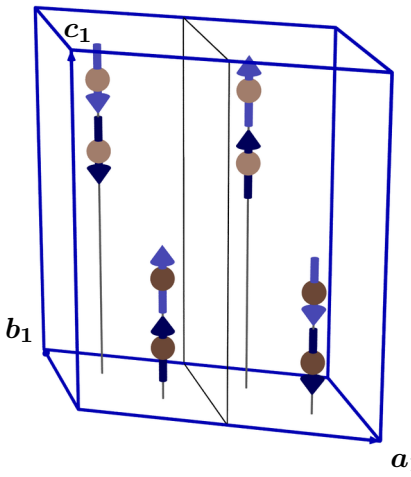

Figure 5.8: Magnetic structure according to the irreducible representation Γ_3. The figure shows one magnetic unit cell with axes $\boldsymbol{a_1}, \boldsymbol{b_1}, \boldsymbol{c_1}$.

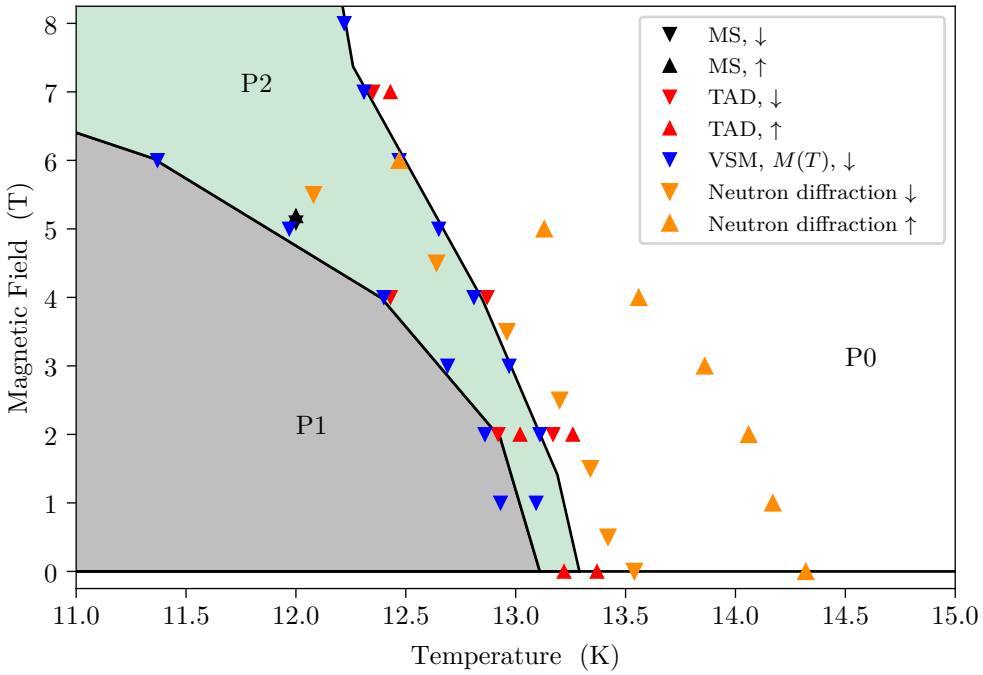

Figure 5.9: Section of the phase diagram 5.1. Additionally, the points are shown at which the $(\bar{1}\,\frac{1}{2}\,0)$ reflection disappears when heating (↑) or appears when cooling (↓). The absolute temperature cannot be determined precisely, however the shape of the phase boundary line shows that the reflection disappears when the sample enters the field phase P2.

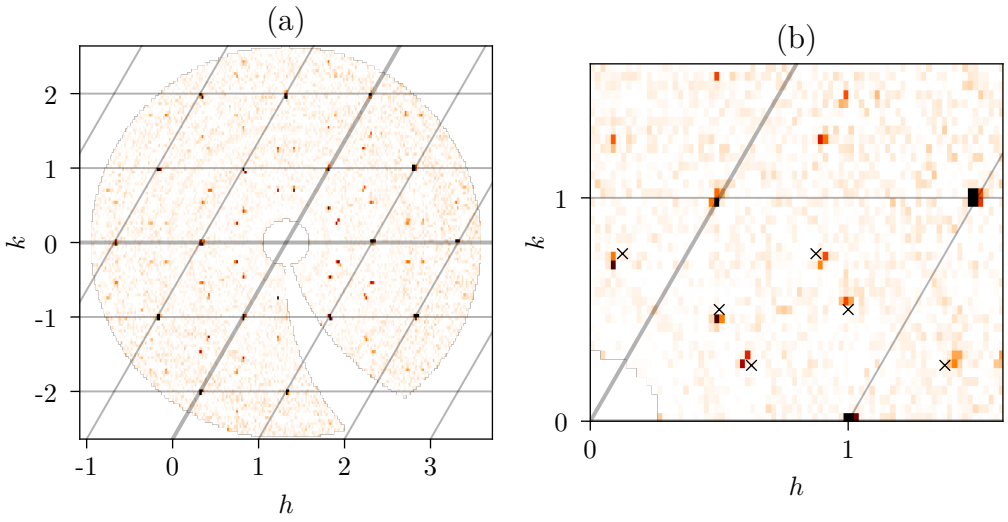

Figure 5.10: Section of the reciprocal space measured by neutron diffraction in phase P2 for $Cs_3Fe_2Br_9$ with $l = 0$ according to the axes $\boldsymbol{a_0}, \boldsymbol{b_0}, \boldsymbol{c_0}$ (cf. Figure 5.3 and Equation 5.1). There are superstructure reflections close to positions with $h, k \in \{\frac{1}{4}, \frac{1}{2}, \frac{3}{4}\}$ (marked by $\times$).

Biesenkamp [133], using a sample stick without curvature, revealed that the magnetic structure is in fact incommensurate. So the exact positions of the magnetic reflections slightly deviate from the values given above. The data quality does not allow for any further investigations of phase P2 in the scope of the present work.

5.3.2.3 Phase P3

Sections of the reciprocal space in the $(h\,k\,l)$ plane are shown in Figure 5.11. Both data were collected at a temperature of 50 mK. The left plot shows the reflections without applied magnetic field, while the data for the right plot were recorded at a magnetic field of 6 T. The reflections are not exactly at the expected positions because the sample stick was bent. It is clearly visible that in both magnetic fields, the same reflections are present. An investigation of the reciprocal space at other l values does not show any qualitative differences, either.

Since the superstructure reflections are the same in phase P1 and P3, it seems natural to use the same symmetry analysis and perform the same refinements of the magnetic structure. The irreducible representations that come into question are listed in Table 5.5. Again, the assumption is made that all magnetic moments are aligned along the axes $\boldsymbol{c_0}$, so that the set of possible irreducible representations reduces to Γ_2, Γ_3, Γ_6 and Γ_7. The R values of the refinements are listed in Table 5.7. Similar to Phase P1, the intensities are best described by the magnetic structure according to the irreducible representation Γ_3. The twins cover fractions of 51(4) %, 29(3) % and 20(3) %. Different twin fractions in phase P1 and P3 can be ascribed to the fact that different samples were used for the investigations of phases P1 and P3.

	Γ_2	Γ_3	Γ_6	Γ_7
R(obs)	72.03 %	22.06 %	61.97 %	72.09 %
wR(obs)	84.81 %	23.83 %	73.78 %	84.84 %
R(all)	78.01 %	29.14 %	65.95 %	85.65 %
wR(all)	84.89 %	24.68 %	74.00 %	85.09 %

Table 5.7: Similar to phase P1 (cf. Table 5.6), the measured intensities in phase P3 are best described by the magnetic structure according to the irreducible representation Γ_3.

We have seen that the magnetic structures of phases P1 and P3 are roughly the same. A more detailed analysis by including more parameters to the refinements is not possible due to the bad data quality. However, magnetostriction shows some signal at this phase transition, as can be seen in Figure 5.1. Thus it can be expected that there are small changes of the magnetic structure at the phase transition.

Field dependent scans of the reflections $\left(^3/_2\,0\,0\right)$ and $\left(\overline{^1/_2}\,1\,0\right)$ were carried out at a temperature of 50 mK in magnetic fields between 0 T and 7 T. Since the raw data exhibited a very bad statistic but very many data points, each 20 data points were combined. This is equivalent to the case where fewer data points at longer counting time would have been collected. The data are shown in Figure 5.12(a, b) as blue dots. At first glance it is apparent that with increasing magnetic field the intensity decreases. At low magnetic fields the slope is constant and suddenly changes to a bigger slope at a certain magnetic field. Within both intervals, the intensity seems to follow an affine function of the magnetic field and there is no jump at the junction. Thus, we can describe the number of counts in dependence on the magnetic field by the following model:

$$I(H) = \begin{cases} I_\mathrm{c} + s_1(H - H_\mathrm{c}) & \text{for } H \leq H_\mathrm{c} \\ I_\mathrm{c} + s_2(H - H_\mathrm{c}) & \text{for } H > H_\mathrm{c} \end{cases} \tag{5.2}$$

H_c denotes the magnetic field at which the slope changes from s_1 to s_2. I_c is the number of counts measured at H_c. The model has no physical justification, we will only use it in order to determine the magnetic field H_c at which the slope changes. Appropriate fits were carried out, varying the parameters H_c, I_c, s_1 and s_2. The fits are shown in Figure 5.12(a, b) as orange lines. By comparison with the phase diagram in Figure 5.1, it seems natural to identify the change of slope with the phase transition from phase P1 to phase P3, thus $H_\mathrm{c} = H_{\mathrm{P1,P3}}(50\,\mathrm{mK})$. We yield $H_{\mathrm{P1,P3}}(50\,\mathrm{mK}) = 5.38(6)\,\mathrm{T}$ resp. $5.49(4)\,\mathrm{T}$ which does not deviate too much from each other within the errors.

This result is in good agreement with measurements of the magnetization [129], shown in 5.12(c). This is one of the measurements used to determine the phase diagram shown in Figure 5.1. Though the temperatures for the neutron measurement in Figure 5.12(a, b) is not the same as for the magnetization measurement (c), the field at which the transition takes place is very similar.

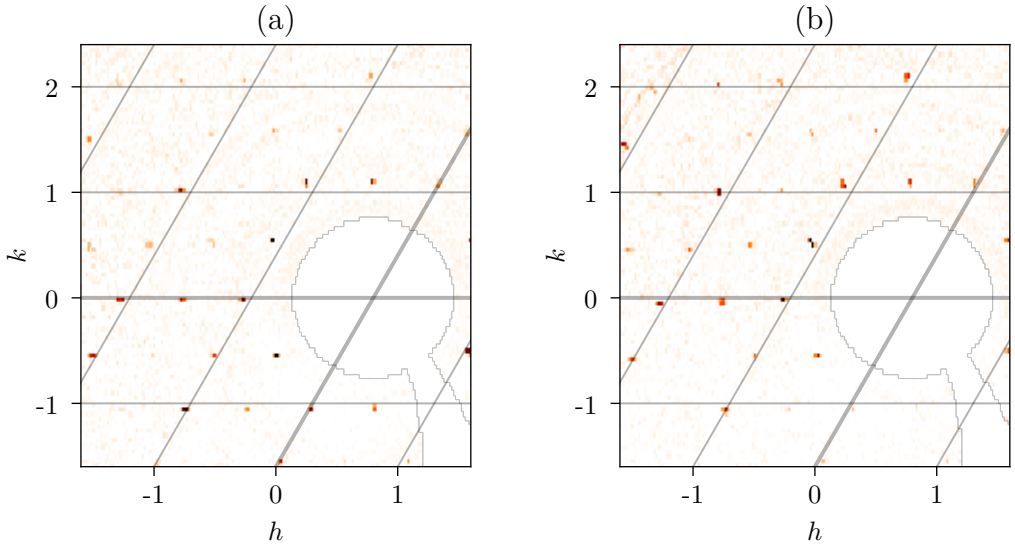

Figure 5.11: $(h\,k\,0)$ plane of the reciprocal space of $Cs_3Fe_2Br_9$ at a temperature of 50 mK in a magnetic field of (a) 0 T and (b) 6 T. The coordinates in reciprocal space refer to the axes $(\boldsymbol{a_0}, \boldsymbol{b_0}, \boldsymbol{c_0})$ in Figure 5.3.

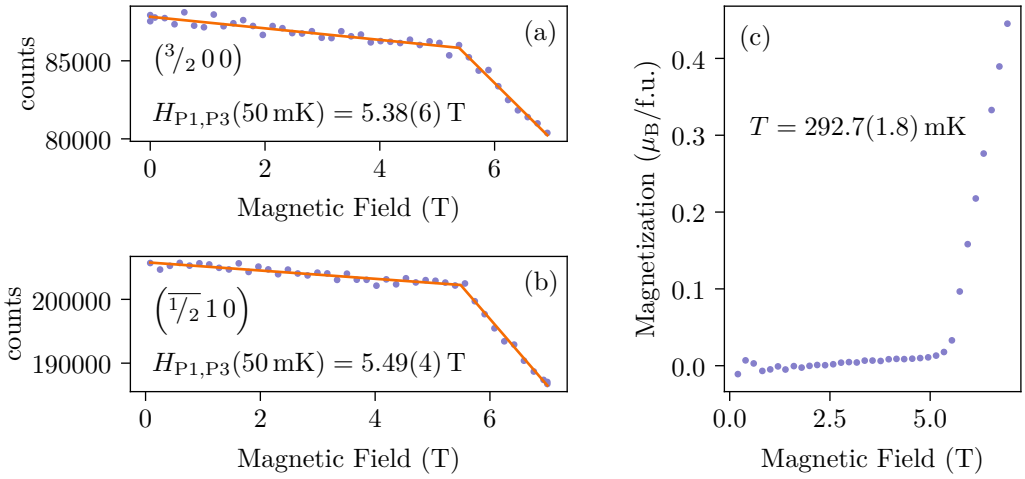

Figure 5.12: Magnetic-field dependence of the superstructure reflections $(^3/_2\,0\,0)$ (a) and $\left(\overline{^1/_2}\,1\,0\right)$ (b) at a temperature of 50 mK. The measured date (preprocessed as described in the text) is shown as blue dots. The fits according to Equation 5.2 are shown as orange lines. The phase transition takes place around 5.4 T. (c) Magnetisation (μ_B per formula unit) in dependence on the magnetic field yields a critical field of 5.6 T [129]. The temperature is higher, but the magnetic field at which the phase transition from phase P1 to phase P3 takes place is similar.

5.3.2.4 Conclusion

The magnetic structure of phase P1 breaks the three-fold axis of space group $P6_3/mmc$. However, the structural changes are small and could not be detected via single-crystal neutron-diffraction. The magnetic ordering follows the Γ_3 mode. Within the precision of the experiments, phase P3 exhibits the same magnetic structure while the intensities of magnetic reflections are decreased. The fact that the Fe atoms in a double octahedron are aligned ferromagnetically is in contrast to the prediction of Wei et al. [128], where a DFT calculation leads to the result that antiferromagnetically aligned nearest neighbors would be energetically favored. This contradiction can be explained by the fact that the DFT of Wei et al. uses different distances and angles for the $[Fe_2Br_9]$ double octahedra as shown in Section 5.3.1. However, the crystal structure used in the DFT calculation rather resembles the structure of the compound $Cs_3Cr_2Br_9$ [131] as we have seen in Section 5.3.1. Indeed, the magnetic moments inside the double-octahedrons in $Cs_3Cr_2Br_9$ couple antiferromagnetically [134]. The magnetic structure of phase P2 could not be solved because the experimental setup did not allow a precise determination of the propagation vector.

6 Compounds of the form $Ba_3XIr_2O_9$

6.1 Latest state of research

Compounds of the form $Ba_3AB_2O_9$, are structurally related to $BaTiO_3$.

Above 120°C, the compound $BaTiO_3$ crystallizes with perovskite structure in space group $Pm\overline{3}m$ with Wyckhoff positions $1b$ for Ba, $1a$ for Ti, and $3d$ for O [135][136]. At room temperature, the structure exhibits a tetragonal distortion [137]. At lower temperatures, this material becomes orthorhombic [138], and further cooling induces a transition to a rhombohedral phase [139]. A summary of the several phases is given in [140]. The crystal structures of the cubic, the tetragonal and the orthorhombic phases are separated by ferroelectric transitions [140] and differ only in slight shifts of the atomic positions. There exists also a hexagonal modification of $BaTiO_3$ [141], which however is not easy to stabilize at room temperature [140]. While the cubic, the tetragonal and the orthorhombic phases are very closely related to each other, the hexagonal modification shows stronger differences. The arrangement of the atoms within the hexagonal ab plane is substantially unaltered, but the stacking orders of these planes differ. The cubic and the hexagonal structures are shown in Figure 6.1. For sake of comparison, the cubic structure is plotted with the [1 1 1] direction vertical. All TiO_6 octahedrons in the cubic phase are corner-sharing (Figure 6.1(a)). The hexagonal phase also contains octahedrons which are connected to neighbored octahedrons only via a corner. These are labeled by I in Figure 6.1(b). The other octahedrons are arranged as face-sharing double-octahedrons $\mathrm{II}_{\mathrm{a...d}}$. Due to the three-fold axes $3^{\pm}$ $0, 0, z$ of space group $P6_3/mmc$, all octahedrons in one layer are symetrically equivalent. Also the octahedrons $\mathrm{II}_{\mathrm{a...d}}$ are equivalent with respect to this space group because of the mirror plane m $x, y, \frac{1}{4}$ and the inversion center $\overline{1}$ $0, 0, 0$. However, substituting Ti by other elements can break these symmetries, reducing the symmetry to space group $P6_3mc$. In the next paragraph, diverse related compounds will be classified with respect to the occupation of the sites I and $\mathrm{II}_{\mathrm{a...d}}$ by other elements.

There are many related compounds, where 2/3 of the Ti atoms are substituted by one element M and 1/3 by another atom X. This yields the stoichiometry $Ba_3XM_2O_9$. The most obvious possibility for arranging these two different atom types in the crystal structure is placing the X atoms on the sites I and the M atoms on sites $\mathrm{II}_{\mathrm{a...d}}$. This substitution does not break the symmetry since the sites $\mathrm{II}_{\mathrm{a...d}}$ are still symmetrically equivalent. This situation is realized for the compounds $Ba_3XIr_2O_9$ with $X \in \{$Y, Ce, Pr, Sm, Eu, Gd, Tb, Dy, Ho, Yb, Lu$\}$ [142] and with $X \in \{\mathrm{Mg, Sc, Zn, Zr, In}\}$ [143]. Indeed, these compounds exhibit space group $P6_3/mmc$. The site I is occupied by X

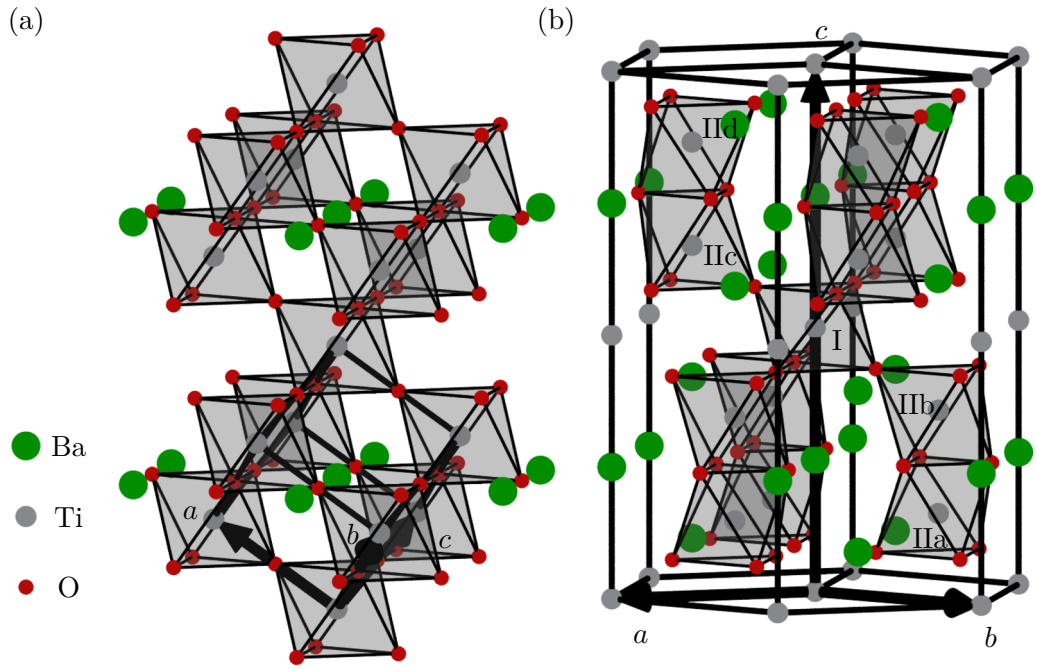

Figure 6.1: (a) Cubic configuration of $BaTiO_3$, [1 1 1] direction pointing upwards. (b) Hexagonal configuration of $BaTiO_3$. The structures differ in the stacking along the vertical axis. For references regarding structural data, see text. The Ti atoms in the octahedrons I and $II_{a...d}$ can be substituted by other elements.

and the sites $\mathrm{II}_{\mathrm{a...d}}$ are occupied by Ir, forming Ir_2O_9 double-octahedrons.

The compounds $Ba_3XIr_2O_9$ with $X \in \{\mathrm{La}, \mathrm{Nd}\}$ [142] or $X \in \{\mathrm{Ca}, \mathrm{Sr}\}$ [143] have very similar structures but exhibit a monoclinic distortion so that the space group is $C2/c$ is realized. In this work, it will turn out that the same applies for the compounds $Ba_3InIr_2O_9$, $Ba_3NbIr_2O_9$ and $Ba_3CeIr_2O_9$. The Ir_2O_9 double-octahedrons in these componds are arranged in a triangular lattice. At first glance, one would expcect the spins of the Ir^{5+} ions in the double-octahedrons to form a singlet state with $J = 0$. However, a small magnetic moment was reported to persist [39]. The explanation for this is that the spin orbit singlet state is destabilized by interdimer hopping [39]. To the knowledge of the author, there does not exist any theoretical prediction for this specific model, but it was supposed to form a quantum spin-orbit liquid similar to the compound $FeSc_2S_4$ which contains Fe^{2+} ions on a diamond lattice [36].

Another situation occurs for $Ba_3IrTi_2O_9$, $Ba_3RuTi_2O_9$ and $Ba_3CuSb_2O_9$. Since the chemical formulas are of the form $Ba_3XM_2O_9$, one could expect that they distribute like in the preceding paragraphs, preserving the $P6_3/mmc$ symmetry. However, they crystallize in space group $P6_3mc$ [10][140][9]. The sites I, II_{a} and II_{c} are occupied by Ti resp. Sb while the sites II_{b} and II_{d} are occupied by the other atom, i.e. Ir/Ru/Cu. That means the sites II_{a} and II_{b} are not symmetrically equivalent, so that the m $x, y, \frac{1}{4}$ mirror plane is broken. In the case of $Ba_3RuTi_2O_9$ the stabilization of the hexagonal perovskite modification is well understood: Due to Ti − Ti repulsion, it is energetically unfavorable to occupy both sites IIa and IIb of the double octahedron by Ti [144]. There are several further possibilities to distribute the Ru and Ti atom over the sites $\mathrm{II}_{\mathrm{a...d}}$. Considering metal-metal bonding and structural distortions, it turns out that the above mentioned configuration is the most favorable one. The most significant property of these structures is the fact that each double-octahedron is occupied by one magnetic ion and one non-magnetic ion. The magnetic ions thus form a triangular lattice, which is geometrically frustrated as discussed in section 1.2.2. The compound $Ba_3CuSb_2O_9$ used to be a spin liquid candidate with $5d$ electrons of the Cu^{2+} ions [9] and $Ba_3IrTi_2O_9$ its $5d$ analog [10].

6.2 $Ba_3InIr_2O_9$

6.2.1 Samples and experimental setup

Polycrystalline material of the compound $Ba_3InIr_2O_9$ was grown by T. Dey [145] using a $BaCl_2$ flux in air. In a second step this material was used to grow single crystals. The educts In_2O_3, $BaCO_3$ and IrO_2 were used with stoichiometric ratio.

An as-grown sample (TD065-S001) of the compound $Ba_3InIr_2O_9$, as depicted in Figure 6.2(a), was used for single-crystal X-ray diffraction on APEX (cf. Section 3.1.1) at room temperature.

For the $Ba_3InIr_2O_9$ sample PB065-S001, 69 971 reflections were collected, 877 of which

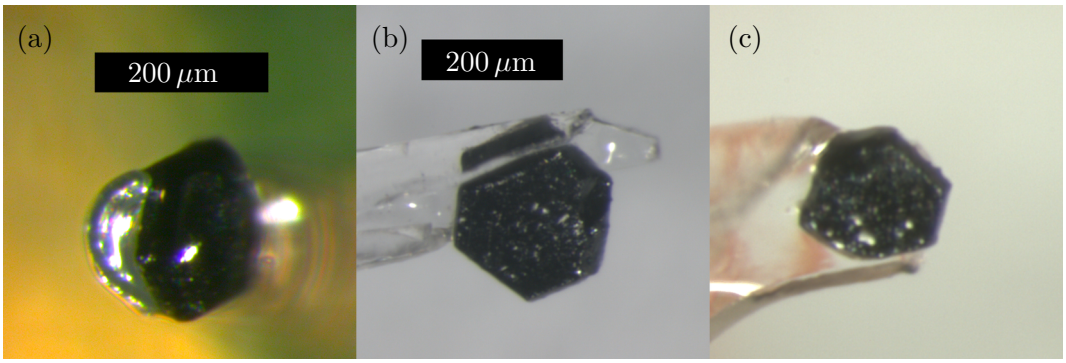

Figure 6.2: As-grown sample TD065-S001 of the compound $Ba_3InIr_2O_9$ (a) and as-grown samples TD105-S001 (b) and TD105-S002 (c) of the compound $Ba_3NbIr_2O_9$ used for single-crystal X-ray diffraction.

are unique with respect to space group $P6_3/mmc$. All unique reflections were observed. The sample exhibits the shape of a hexagonal prism, so for absorption correction a model with the eight faces (0 0 1), (1 0 0) and equivalents was used. The initial resp. overall wR^2(int) value amounts to 8.42 % resp. 6.53 %.

6.2.2 Occupation ordering and non-stoichiometry

The single-crystal X-ray diffraction data were refined using models with space group $P6_3/mmc$. The O atoms have isotropic ADPs because otherwise some tensors are not positive definite. All other atoms are refined with anisotropic ADPs. Three such refinements were carried out: For the first refinement, a fully ordered occupation of the In and Ir sites was assumed. The model of the second refinement contains total disorder. For this model it is assumed that the nominal stoichiometry with a In : Ir ratio of 1 : 2 is preserved. The third refinement deals with a partially ordered structure. The resultant R values are shown in Table 6.1. In the partially ordered model, the occupancies of atoms sharing a site are constrained to add up to full occupancy. The stoichiometry is not constrained in this case since the concerning Wyckoff positions have different multiplicities. It turns out that for all three samples, the partially ordered model yields the best R values.

The In site is nearly completely occupied by In (2.1(9) % Ir on In site) while 7.6(1.3) % In can be found on the Ir sites. The stoichiometry is $Ba_3In_{1.131(28)}Ir_{1.869(28)}O_9$ with a surplus of In.

	$Ba_3InIr_2O_9$	fully ordered	fully disordered	partially ordered
TD065-S001	wR(all)	9.14 %	19.56 %	7.44 %
	GoF	5.87	12.57	4.79
	Ir on In site	0	0.667	0.021(9)
	In on Ir site	0	0.333	0.076(13)

	$Ba_3NbIr_2O_9$	fully ordered	fully disordered	partially ordered
TD105-S001	wR(all)	7.08 %	18.87 %	5.89 %
	GoF	4.03	10.73	3.35
	Ir on Nb site	0	0.667	0.124(6)
	Nb on Ir site	0	0.333	0.046(8)
TD105-S002	wR(all)	10.01 %	21.00 %	9.51 %
	GoF	6.83	14.32	6.49
	Ir on Nb site	0	0.667	0.094(10)
	Nb on Ir site	0	0.333	0.051(13)

	$Ba_3CeIr_2O_9$	fully ordered	fully disordered	partially ordered
PB011-S001	wR(all)			5.98 %
	GoF			2.51
	Ir on Ce site			−0.010(4)
	Ce on Ir site			−0.007(5)

Table 6.1: Refinements of single-crystal X-ray diffraction data of the $Ba_3InIr_2O_9$ sample TD065-S001, the $Ba_3NbIr_2O_9$ samples TD105-S001 and TD105-S002 and the $Ba_3CeIr_2O_9$ sample PB011-S001. The R values, the goodness of fit and the occupation ratios for the In/Nb/Ce and Ir sites are given for a fully ordered, a fully disordered and a partially ordered structure. For $Ba_3CeIr_2O_9$, the refinement was carried out in space group $C2/c$, for the other samples the results of refinements in the high-symmetry space group $P6_3/mmc$ are listed.

6.2.3 Breaking of symmetries

6.2.3.1 Translation symmetries

A breaking of translation symmetries is investigated by a search for half-integer superstructure reflections.

For the $Ba_3InIr_2O_9$ sample TD065-S001, the statistic of a full collection yields for the intensities of half-integer reflections the Gaussian distribution as shown in Figure 6.3(a). The intensities of the reflections are in good agreement with zero intensity within their errors. Figure 6.3(b) shows a comparison of half-integer reflections $(^{h}/_{2}\,^{k}/_{2}\,^{l}/_{2})$ with the intensity of the reflection $(h\,k\,l)$. The latter is divided by the factor determined in Figure 7.6, so that this the plot shows the expected intensity for the $\lambda/2$ reflection. Note that most of the reflections lie approximately on a line which however has a slope different from 1. This can be explained by the fact that the effective intensity ratio of the λ and $\lambda/2$ radiation depends on the sample due to a different absorption correction. The intensities of the half-integer reflections can statistically be well explained by the $\lambda/2$ effect. In order to confirm this result, the strongest half-integer reflections of Figure 6.3(b) are scanned with a long exposure time. The acceleration voltage of the X-ray tube is reduced to 30 kV, so that no $\lambda/2$ radiation is generated. Each reflection is scanned along 0.5° for 2000 s/deg. The result is shown in Figure 6.4. Most reflections are clearly absent. The reflections $(0\,0\,^{25}/_{2})$, $(2\,\bar{1}\,^{25}/_{2})$ and equivalents show some features, which however look like artifacts from neighbored reflections. This suggestion can be proved by calculated precession images of the data collection, as shown in Figure 6.5. Since the data for Figures 6.4 and 6.5 come from different measurements, the orientation matrices might be different. This is why all equivalent reflections are shown. The blue dots in figure 6.5 mark the position of the half-integer reflection and the green dots mark a neighbored integer reflection with $l = 12$. It is clearly visible that the intensities collected for these half-integer reflections can be explained by tails of neighbored reflections. It can be concluded that, if a symmetry reduction occurs, the symmetry is lowered to a translationengleiche subgroup of space group $P6_3/mmc$.

6.2.3.2 Forbidden reflections

Space group $P6_3/mmc$ exhibits the selection rules $hh\overline{2h}l : l = 2n$ which are caused by the glide planes $c\ x, x, z$, $c\ x, 0, z$ and $c\ 0, y, z$. Figure 6.6 shows reflections violating these selection rules for the $Ba_3InIr_2O_9$ sample TD065-S001. Some of these reflections are visible although the acceleration voltage of the X-ray tube was reduced to 30 kV so that the $\lambda/2$ effect can be ruled out.

6.2.3.3 Refinements in space group *C2/c*

In [146], it is shown that $Ba_3InIr_2O_9$ exhibits space group $C2/c$ at a temperature of 3.4 K, while the room temperature crystal structure has the symmetry $P6_3/mmc$. This

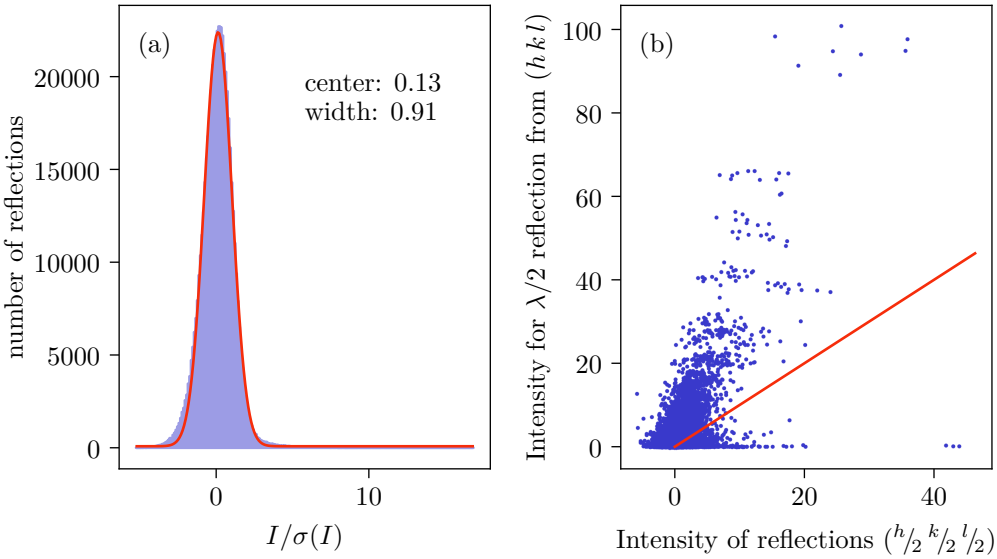

Figure 6.3: (a) Half-integer single-crystal X-ray reflections of the $Ba_3InIr_2O_9$ sample TD065-S001 lie close to zero within their errors. (b) The half-integer reflections ($^h/_2\ ^k/_2\ ^l/_2$) for which also the reflection $(h\,k\,l)$ was measured can roughly been explained by the $\lambda/2$ effect. The effective intensity ratio of the λ and $\lambda/2$ radiation was determined for the Ba_2CeIrO_6 sample AR506a, as shown in Figure 7.6. Assuming that ratio, the reflections are supposed to lie on the red line. The ratio seems to be different for this sample.

is in contradiction with the room temperature reflections visible in Figure 6.6. This is why a refinement of the collected single crystal X-ray diffraction data of the $Ba_3InIr_2O_9$ sample TD065-S001 at room temperature is carried out in space group $C2/c$. All ADPs in the model are isotropic and the O atoms are constrained to have the same ADPs. The results of the refinements in space groups $P6_3/mmc$ and $C2/c$ are shown in Tables A.9 and A.10, respectively. The occupations slightly deviate from the results above due to the isotropic ADPs used in the latter refinements. The R values drastically decrease from wR(all) = 8.41 % to wR(all) = 5.01 % when the symmetry of the model is lowered from $P6_3/mmc$ to $C2/c$. The goodness of fit is much closer to 1 for the low-symmetry structure. This clearly shows that the crystal structure exhibits the monoclinic space group already at room temperature. All atoms, except from In3/Ir3 which are fixed to Wyckoff position $4a$ $0, 0, 0$, show small but significant deviations. The intra-dimer $\mathrm{Ir}-\mathrm{Ir}$ distance hardly changes: In space group $P6_3/mmc$ it is 2.6494(9) Å while it amounts to 2.64799(26) Å in space group $C2/m$. This distance is in good agreement with 2.637(2) Å as published in [146]. Also the next-nearest $\mathrm{Ir}-\mathrm{Ir}$ distance that is measured between the closest Ir atoms of two dimers shows no significant difference. It amounts to 5.82900(10) Å in space group $P6_3/mmc$ and 5.82899(9) Å and 5.82900(10) Å in space group $C2/c$. The crystal structure of Table A.10 is plotted in Figure 6.7(c)-(d), while the coordinate shifts compared to the undistorted structure are plotted with a factor of 2 for a better visibility of the distortion. The undistorted hexagonal structure is shown in Figure 6.7(a)-(b) for comparison.

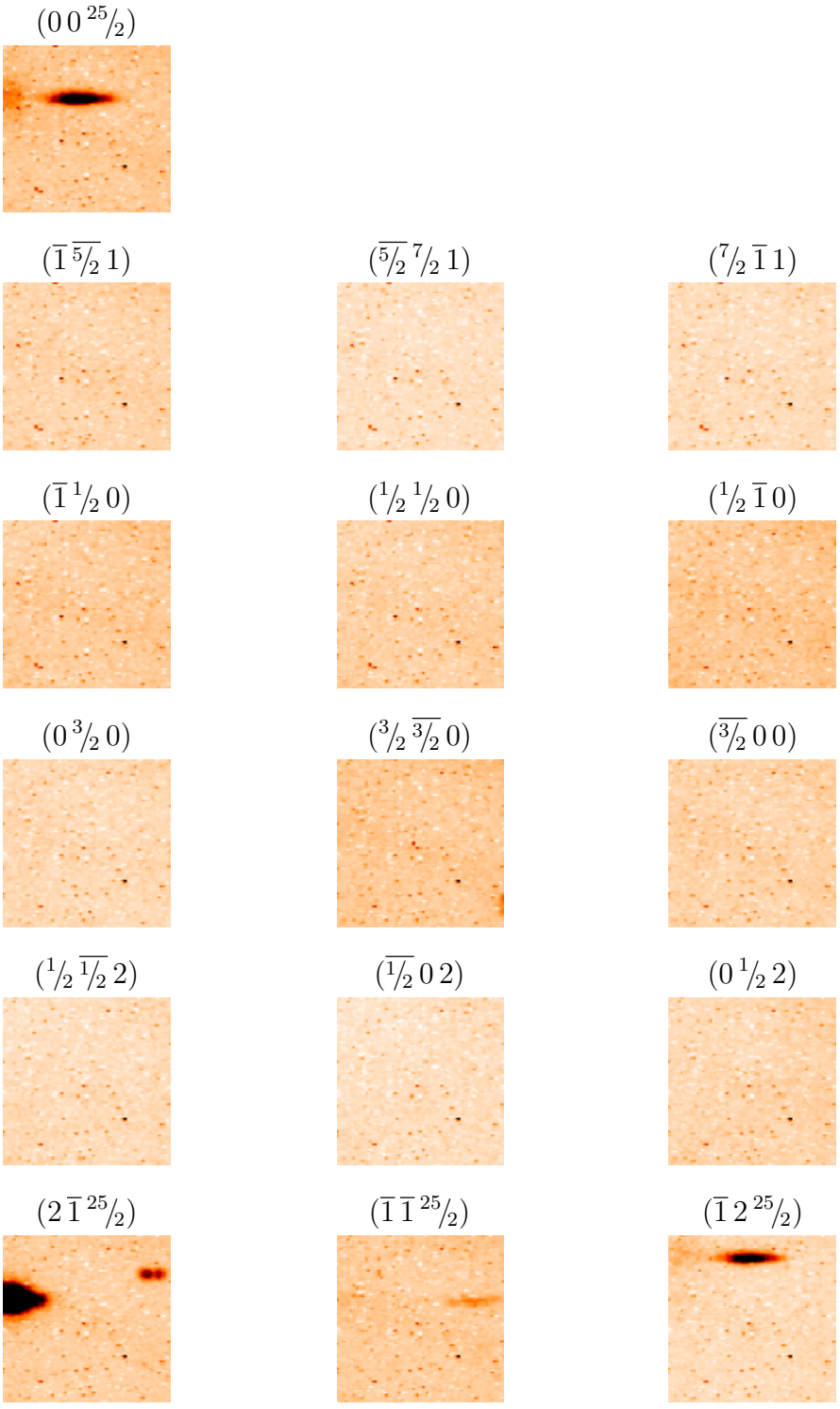

Figure 6.4: Half-integer single-crystal X-ray reflections of the $Ba_3InIr_2O_9$ sample TD065-S001. All of them were measured with an acceleration voltage of 30 kV, with a scan width of 0.5° and a scan time of 2000 s/deg. Most scans show no feature at all. There is something visible for the reflections $(0\,0\,^{25}/_2)$, $(2\,\bar{1}\,^{25}/_2)$, $(\bar{1}\,\bar{1}\,^{25}/_2)$ and $(\bar{1}\,2\,^{25}/_2)$. These reflections are investigated by looking at the calculated precession images in Figure 6.5.

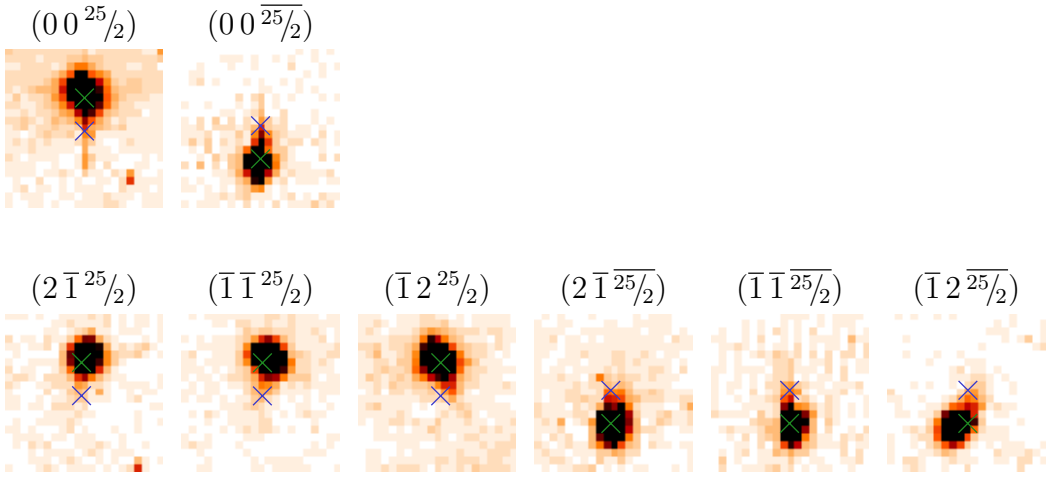

Figure 6.5: Calculated precession images of reflections of the $Ba_3InIr_2O_9$ sample TD065-S001 that show a feature in Figure 6.4, marked by a blue $\times$. All of them can be explained by the neighbored reflection with $l = 12$, marked by a green $\times$. The orientation matrix of the measurements used for the two figures might differ, so all equivalent reflections are shown.

The distortion is similar to the results in [146], where no significant splitting of the $\mathrm{Ir} - \mathrm{Ir}$ distances in the low-symmetry crystal structure is visible, neither. The refinements using the two space groups show the largest differences in the O positions. The breaking of the $P6_3/mmc$ symmetry thus can be attributed to tilts and distortions of the octahedrons. This is similar to the result of [146] but in the present work it can be shown that the hexagonal symmetry is already broken at room temperature. In Section 6.5, the structural distortions are discussed in detail for this compound and the compounds with $X \in \{\mathrm{Nb}, \mathrm{Ce}\}$.

The forbidden reflections shown in Figure 6.6 seem to show a breaking of the three-fold axis, since the reflections $(\bar{3}\,6\,\bar{3})$ and $(3\,\bar{6}\,1)$ could not be observed, while their equivalent reflections are observed. One could conclude that no twinning occurs. However, it seems that the absence of those reflections is an artifact caused by an insufficient alignment of the UB matrix, since the refinement in space group $C2/c$ shows equal volume fractions for all twins.

6.2.4 Conclusion

The compound $Ba_3InIr_2O_9$ exhibits a few percent occupation disorder of the In and Ir sites. The crystal structure has symmetry $C2/c$ already at room temperature. The structural distortion mainly affects the O atoms.

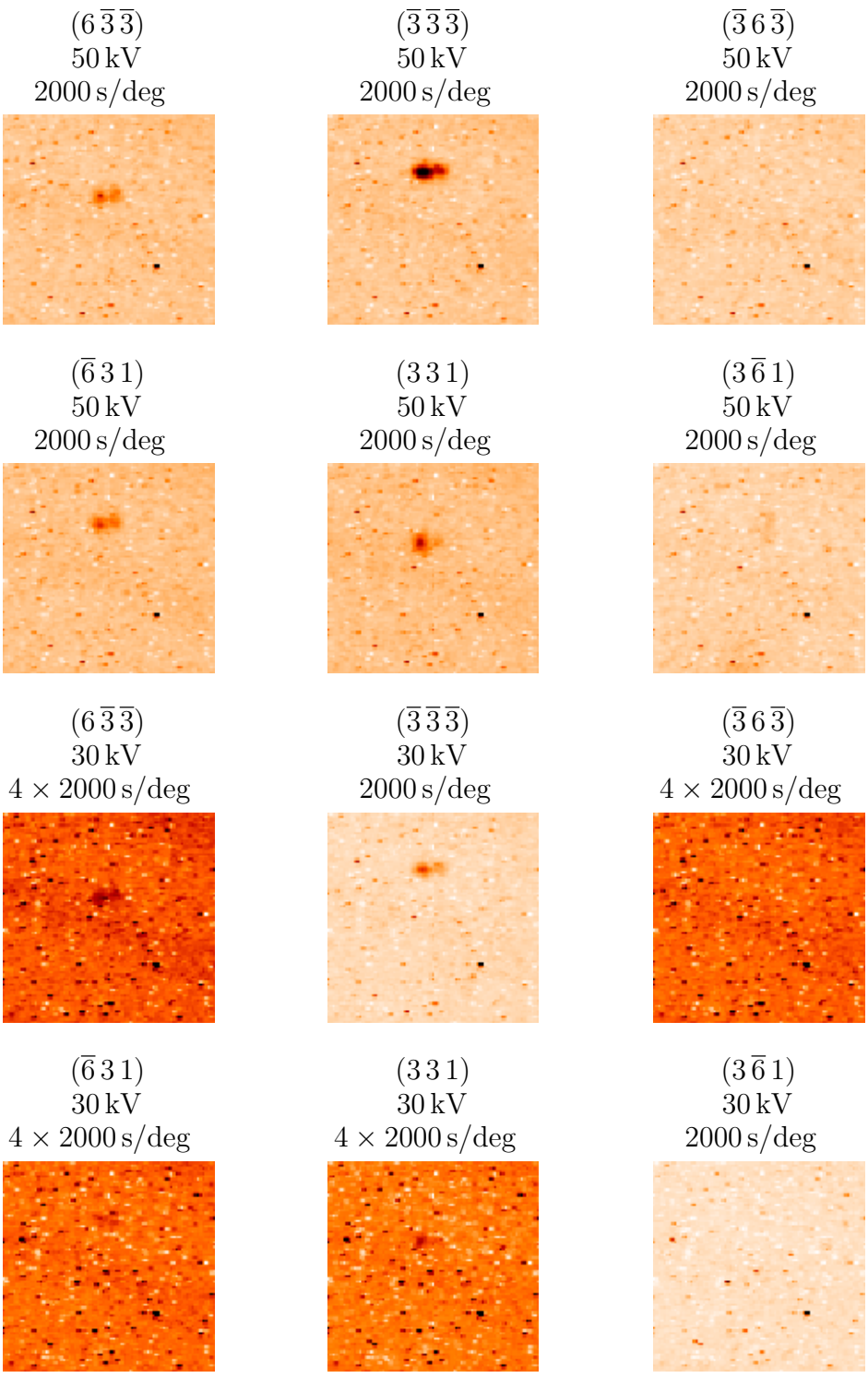

Figure 6.6: Single-crystal X-ray reflections of the $Ba_3InIr_2O_9$ sample TD065-S001 which violate the selection rule $hh\bar{2}hl : l = 2n$ of space group $P6_3/mmc$. Even at an acceleration voltage of 30 kV, some reflections are clearly visible. A scan width of 0.5° was used for all scans.

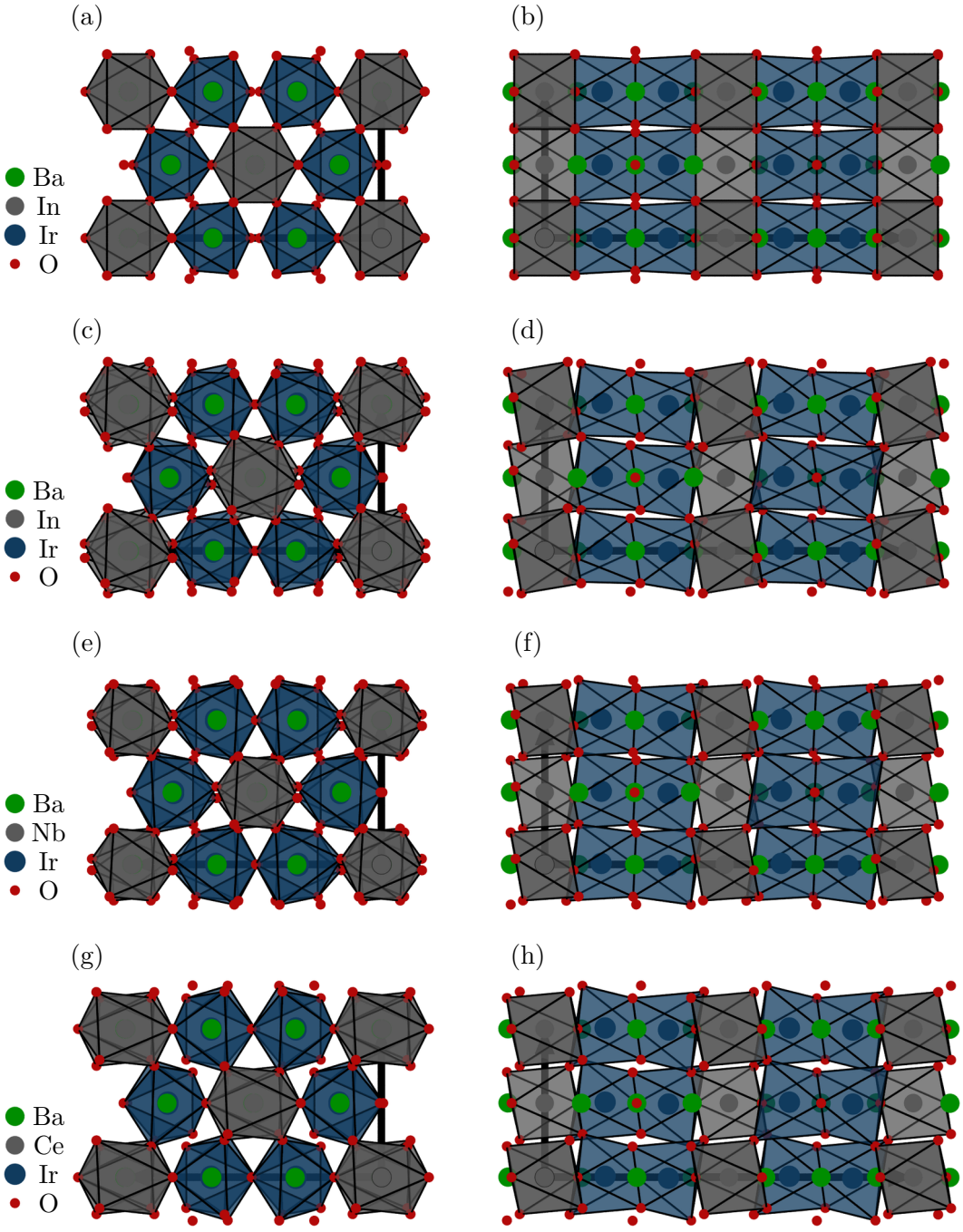

Figure 6.7: Monoclinic distortion in space group $C2/c$ of $Ba_3XIr_2O_9$. The deviations from the high symmetry structure are scaled by a factor of 2 for better visibility. (a), (b): Undistorted $Ba_3InIr_2O_9$ structure with hexagonal symmetry. (c), (d): $Ba_3InIr_2O_9$ sample TD065-S001. (e), (f): $Ba_3NbIr_2O_9$ sample TD105-S001. (g), (h): $Ba_3CeIr_2O_9$ sample PB011-S001. (a), (c), (e), (g): View along c axis. a axis up, b axis to the left. (b), (d), (f), (h): View along b axis. a axis up, c axis to the right.

6.3 $Ba_3NbIr_2O_9$

The investigation of the compound $Ba_3NbIr_2O_9$ is analogue to $Ba_3InIr_2O_9$ in Section 6.2. Many paragraphs refer to that section.

6.3.1 Samples and experimental setup

The growth of $Ba_3NbIr_2O_9$ samples was carried out by T. Dey [145] similarly to $Ba_3InIr_2O_9$ whereas Nb_2O_3 was used instead of In_2O_3.

Two as-grown samples (TD105-S001 and TD105-S002) of the compound $Ba_3NbIr_2O_9$, as depicted in Figure 6.2(b, c), were used for single-crystal X-ray diffraction on APEX (cf. Section 3.1.1) at room temperature.

For the samples PB105-S001 resp. PB105-S002, 84 806 resp. 75 601 reflections were colleted at room temperature, 914 resp. 854 of which are unique with respect to space group $P6_3/mmc$. 744 resp. 841 unique reflections are observed. Absorption correction was carried out similarly to the $Ba_3InIr_2O_9$ sample. The initial resp. overall wR^2(int) values amount to 9.17 % resp. 6.72 % for sample TD105-S001 and 10.17 % resp. 6.37 % for sample TD105-S002.

6.3.2 Occupation ordering and non-stoichiometry

Similarly to $Ba_3InIr_2O_9$, refinements were carried out in space group $P6_3/mmc$ with a fully ordered, a fully disordered, and a partially ordered model. The results are listed in Table 6.1 of Section 6.2. For details of the refinements confer ibidem.

The Nb sites contain about 12.4(6) % resp. 9.4(1.0) % Ir atoms and around 4.6(8) % resp. 5.1(1.3) % of the Ir sites are occupied by Nb for sample TD105-S001 res. TD105-S002. The stoichoimetry is nearly consistent with the nominal stoichiometry within the errors: $Ba_3Nb_{0.968(17)}Ir_{2.032(17)}O_9$ for sample TD105-S001 and $Ba_3Nb_{1.008(28)}Ir_{1.992(28)}O_9$ for sample TD105-S002.

6.3.3 Breaking of symmetries

6.3.3.1 Translation symmetries

A search for half-integer reflections was carried out for the $Ba_3NbIr_2O_9$ sample TD105-S001. Half-integer reflections are a hint for a breaking of translation symmetries. Figure 6.8 is completely analogue to the Figure 6.3 for $Ba_3InIr_2O_9$. For details confer Section 6.2. The center of the Gauss distribution shown in Figure 6.8(a) is above zero, but still below one standard deviation. Nevertheless, this could be a hint for a breaking of translational symmetries. A comparison of the superstructure reflections with the prediction due to

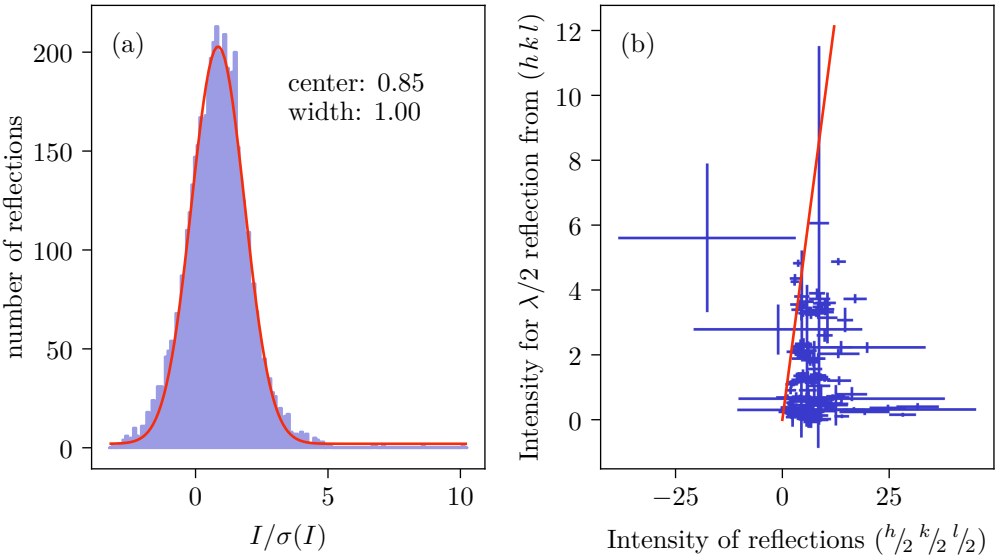

Figure 6.8: (a) Statistic of half-integer single-crystal X-ray reflections of the $Ba_3NbIr_2O_9$ sample TD105-S001. (b) The half-integer reflections $(^h/_2\,^k/_2\,^l/_2)$ for which also the reflection $(h\,k\,l)$ was measured slightly exceeds the prediction for $\lambda/2$ effect. However, the errors are quite large. The effective intensity ratio of the λ and $\lambda/2$ radiation, which corresponds to the red line, was determined for the Ba_2CeIrO_6 sample AR506a, shown in Figure 7.6.

the $\lambda/2$ effect also shows that the reflections are slightly larger than predicted as visible in Figure 6.8(b). However, the uncertainties of the intensities are quite large. We might have found a hint for a breaking of translational symmetries, but the precision of the measurement is not sufficient for structural refinements. The strongest reflections were collected with really long exposure time, as shown in Figure 6.9. Despite the fact that the acceleration voltage was set to 30 kV, the reflections $(\bar{3}\,\bar{3}\,^1/_2)$, $(\bar{3}\,6\,^1/_2)$ and $(0\,0\,^{\overline{25}}/_2)$ are visible. Figure 6.10 shows calculated precession images of these reflections. In some cases they can be explained by tails of neighbored reflections, in other cases very small features are visible. This work will focus on distortions that break the six-fold symmetry as discussed in the next paragraph. It should be kept in mind that a breaking of translational symmetries can not be excluded in the case of $Ba_3NbIr_2O_9$, but the distortions must be very small if they exist.

6.3.3.2 Forbidden reflections

Figure 6.11 shows reflections of the $Ba_3NbIr_2O_9$ sample TD105-S001, that are forbidden by the selection rules $hh\overline{2h}l : l = 2n$ in space group $P6_3/mmc$. Like in the case of the compound $Ba_3InIr_2O_9$, also for $Ba_3NbIr_2O_9$, some of those reflections are clearly visible.

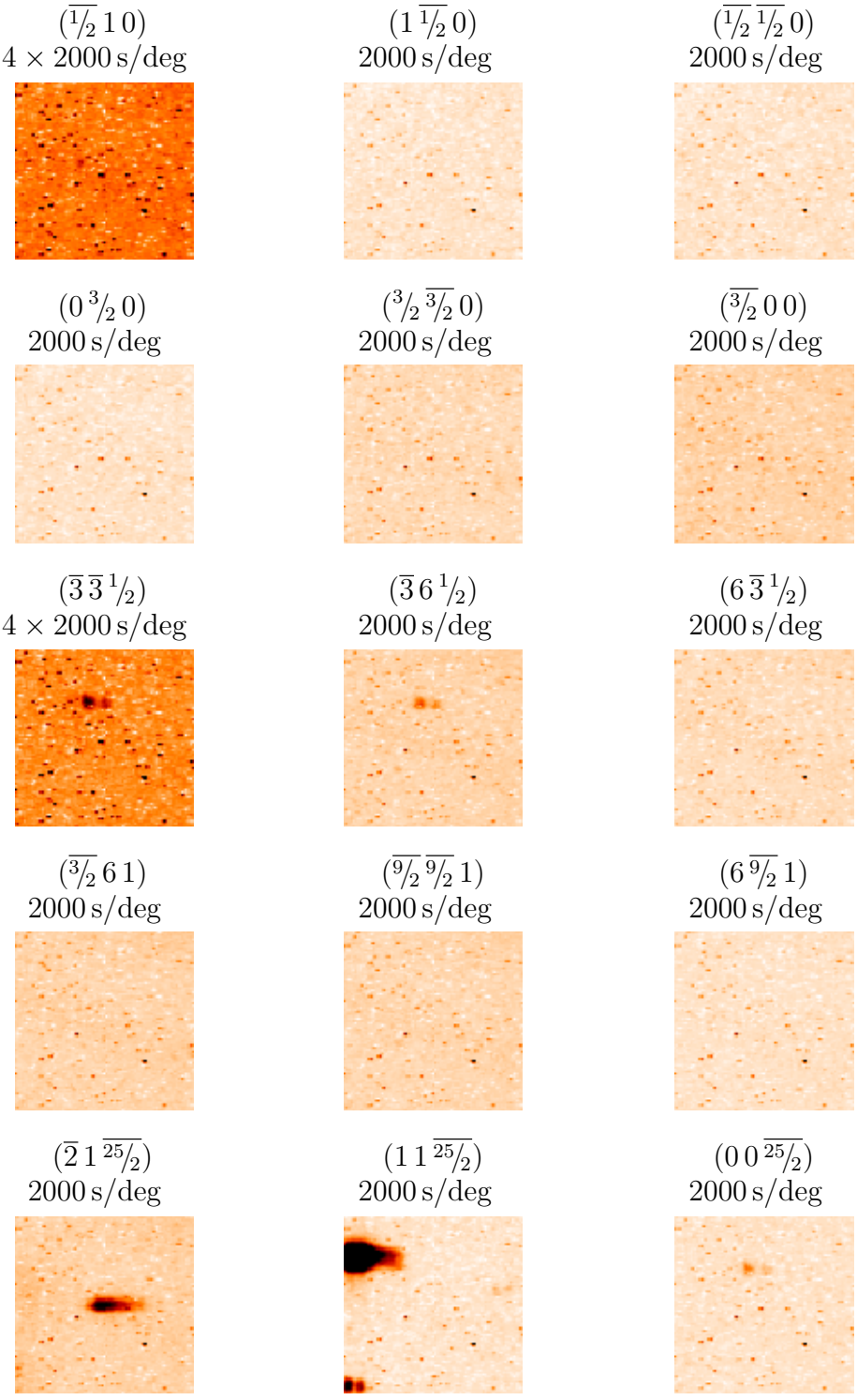

Figure 6.9: Half-integer single-crystal X-ray reflections of the $Ba_3NbIr_2O_9$ sample TD105-S001. All of them were measured with an acceleration voltage of 30 kV, with a scan width of 0.5°. The $(\overline{3}\,\overline{3}\,1/2)$ reflection seems to exist. The $(\overline{2}\,1\,\overline{25/2})$ reflection is an artifact as shown in figure 6.10.

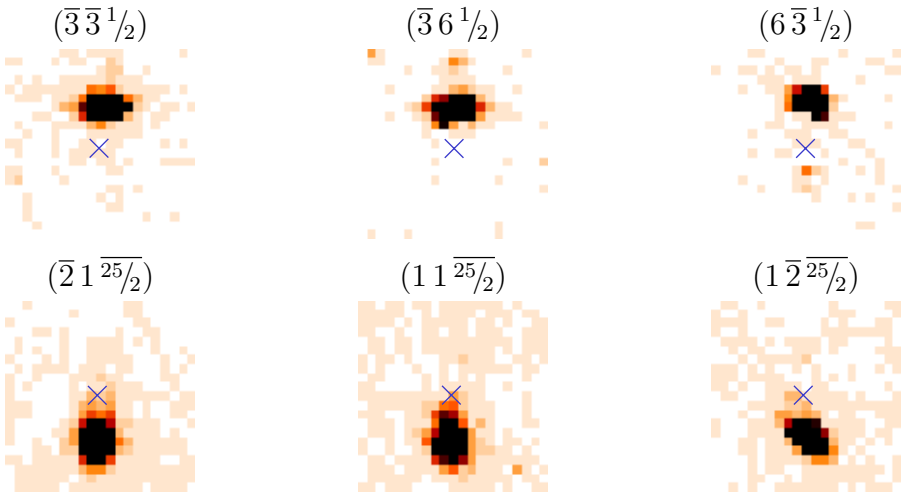

Figure 6.10: Calculated precession images of reflections of the $Ba_3NbIr_2O_9$ sample TD105-S001 that show a feature in Figure 6.9, marked by a blue $\times$. The reflection $(1\,1\,\overline{{}^{25}\!/_{2}})$ can be explained by the strong neighbored reflection. The reflection $(\overline{3}\,\overline{3}\,{}^{1}\!/_{2})$ might be real.

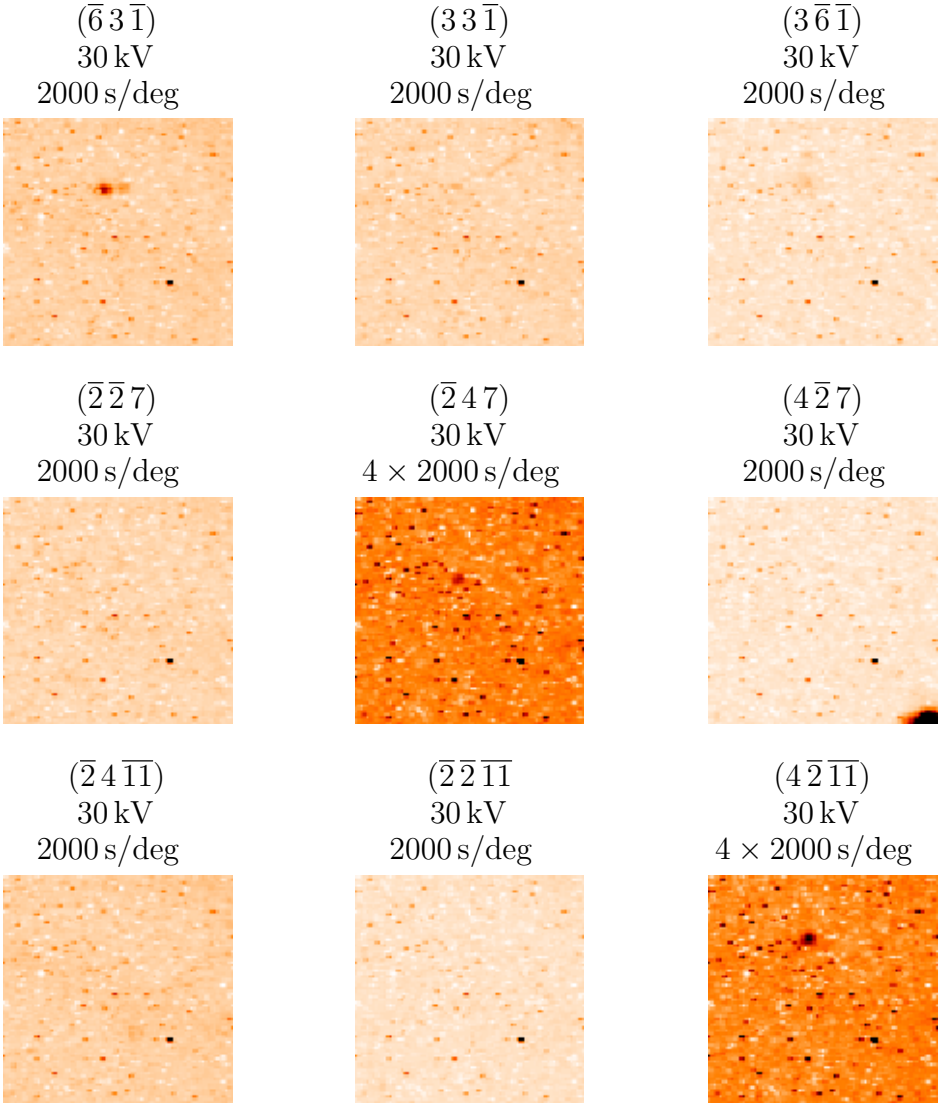

Figure 6.11: Single-crystal X-ray reflections of the $Ba_3NbIr_2O_9$ sample TD105-S001 which violate the selection rule $hh\bar{2}\bar{h}l : l = 2n$ of space group $P6_3/mmc$. Some reflections are visible. An acceleration voltage of 30 kV and a scan width of 0.5° was used.

6.3.3.3 Refinements in space group *C2/c*

Like for the $Ba_3InIr_2O_9$ sample in Section 6.2, also for the $Ba_3NbIr_2O_9$ samples TD105-S001 and TD105-S002, refinements were carried out in space group $C2/c$. The models were chosen similar to those for the In compound. Tables A.11 and A.13 show the refinements in space group $P6_3/mmc$ and Tables A.12 and A.14 those in $C2/c$. The refinement in space group $P6_3/mmc$ differs from the refinement that was carried out in order to determine the occupation disorder in the way that the latter used anisotropic ADPs for the heavy atoms. The symmetry reduction leads to an improvement of the wR(all) value from 6.19 % to 4.77 % for sample TD105-S001 and from 9.58 % to 5.45 % for sample TD105-S002. This is a huge improvement so that also for this compound, the low-symmetry space group $C2/c$ is clearly a better description of the crystal structure compared to space group $P6_3/mmc$. The refinements return negative ADPs for some O atoms. Figures 6.7(e)-(f) show that the structural distortions are very similar to those of the In compound. The structures differ in the way that the single octahedrons for $Ba_3NbIr_2O_9$ are rather sheared than tilted. A detailed discussion of the distortions of this compound and the compounds with $X \in \{\mathrm{In}, \mathrm{Ce}\}$ will be given in Section 6.5. The $\mathrm{Ir}-\mathrm{Ir}$ intra-dimer distances of 2.6712(9) Å for sample TD105-S001 resp. 2.6699(12) Å for sample TD105-S002 refined in space group $P6_3/mmc$ do not change when the symmetry is reduced to space group $C2/c$. The same applies to the $\mathrm{Ir}-\mathrm{Ir}$ inter-dimer distance of 5.7437(5) Å for sample TD105-S001 and 5.74490(30) Å for sample TD105-S002. The distortion effects mainly the O atoms.

6.3.4 Conclusion

Space group $C2/c$ describes the crystal structure of $Ba_3NbIr_2O_9$ better than $P6_3/mmc$. The structural distortion effects mainly the O atoms. There are hints for a breaking of translational symmetries but the additional distortions must be small compared to the distortions that are already visible in the refinements in space group $C2/c$.

6.4 $Ba_3CeIr_2O_9$

In the present work, a symmetry reduction of $Ba_3CeIr_2O_9$ to $C2/c$ is investigated by X-ray diffraction methods. There are structurally related compounds which exhibit this symmetry reduction, as stated in Section 6.1. We will see that subgroup $P6_3mc$, which occurs for related compounds as stated in Section 6.1, can be ruled out.

6.4.1 Samples and experimental setup

The samples PB011-S001 and PB011-S002 of the compound $Ba_3CeIr_2O_9$, which were grown by P. Becker [147], are investigated via single crystal X-ray diffraction on a Bruker

AXS Kappa APEX II four-circle X-ray diffractometer using a wavelength of 0.7 Å generated as MoK_α radiation (cf. Section 3.1.1). Sample PB011-S001 (Figure 6.13(a)) is a small crystal as grown, while sample PB011-S002 (Figure 6.13(b)) is bigger in size but prepared to exhibit a spherical shape using a Bond grinder as described in Section 3.1.1.

In order to exclude half-integer superstructure reflections, 19 such reflections of sample PB011-S002 were collected. These reflections were scanned over an ω range of 1°. During one scan, the acceleration voltage of the X-ray tube was set to 50 kV, which is the usual operating voltage. During a second scan, the voltage was reduced to 30 kV. At this lower voltage, no radiation with half of the wavelength can be generated ($\lambda/2$-effect). While it is possible that at 50 kV there are half-integer reflections due to the $\lambda/2$ effect, this can be excluded for 30 kV. In order to compensate the reduced intensity, the scan time of 20 s per degree for 50 kV was increased for 30 kV to 200 s per degree.

During the measurement of sample PB011-S001, 94 002 reflections were collected, 1 395 of which are unique and 1 241 unique reflections are observed for space group $P6_3/mmc$. The absorption correction was carried out using a model with 25 faces, which improved the internal wR^2 value from 10.75 % to 6.78 %. Structural refinements were carried out using the software JANA [69] in both space groups $P6_3/mmc$ and $C2/c$.

Since single crystal X-ray diffraction is not a good method for the determination of lattice constants, powder diffraction was carried out using a D5000matic powder diffractometer. The sample was mixed with Si powder for a correction of the offset in 2θ. A LeBail refinement is used for the determination of the lattice parameters.

6.4.2 Results and discussion

One question is whether the occupation of the Ir and Ce atoms is ordered. A refinement of the X-ray diffraction data of sample PB011-S001 is shown in Table A.15. The refinement was constrained in the way that all lattice sites are occupied by one atom in total. The refinement yields an occupation of $-0.5(1.2)$ % Ir atoms on the Ce site and $-6.2(1.5)$ % Ce atoms on the Ir site. Negative occupations are physically meaningless. However, we will later see that a refinement in a lower space group yields more reasonable occupations. This is why in Table 6.1 results in the lower space group are listed, instead.

Figure 6.12 shows that some half-integer reflections are visible with an acceleration voltage of 50 kV. However, they disappear when the voltage is reduced to 30 kV. This proves that they occur due to the wavelength $\lambda/2 = 0.35$ Å, which can be excluded at the lower acceleration voltage. It can be concluded that no half-integer superstructure reflections exist, thus the unit cell is not doubled in any direction.

In analogy to $Ba_3InIr_2O_9$ and $Ba_3NbIr_2O_9$ in Sections 6.2 and 6.3, a refinement in space group $C2/c$ is carried out. The resultant structural parameters are shown in Table A.16. Like for the high-symmetry refinement, the ADPs of all O atoms are constrained to be equal. The monoclinic structure of Table A.16 is displayed in Figure 6.7(g)-(h) where

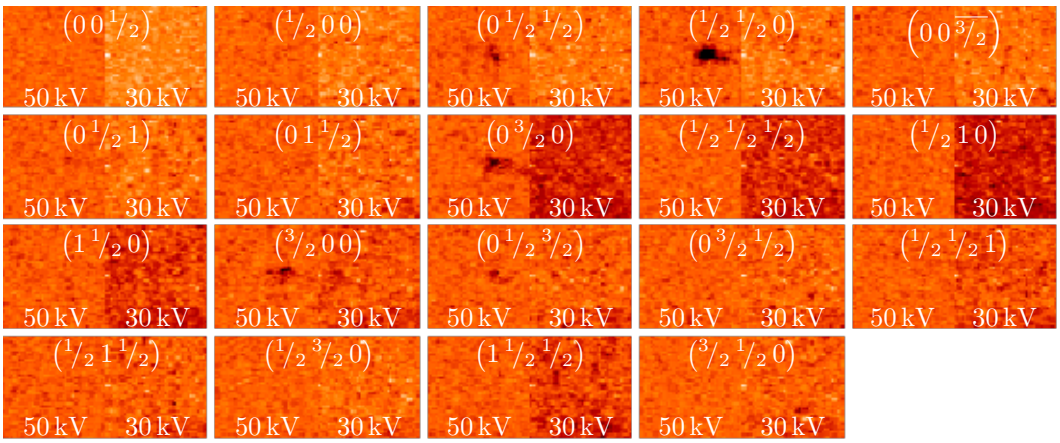

Figure 6.12: Half integer single-crystal X-ray reflections of the $Ba_3CeIr_2O_9$ sample PB011-S002 at room temperature. With an accelaration voltage of 50 kV, half integer reflections are visible. However, they disappear at an acceleration voltage of 30 kV, so they can be explained by the $\lambda/2$-effect. The reflections were scanned over an ω rangle of 1°. The scan time was 20 s per degree for 50 kV and 200 s per degree for 30 kV.

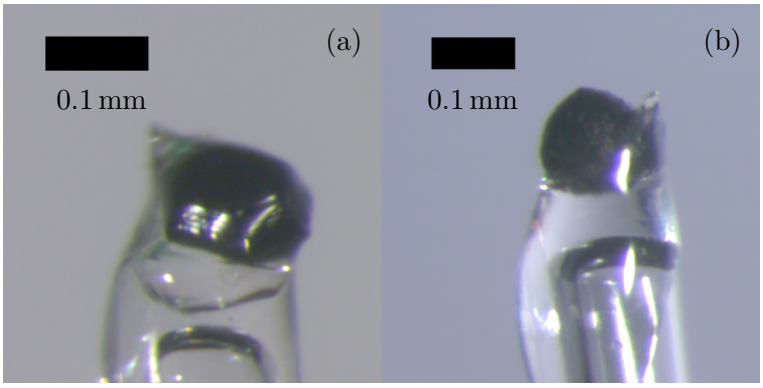

Figure 6.13: Samples of $Ba_3CeIr_2O_9$. (a) Sample PB011-S001. (b) Sample PB011-S002.

the displacements with respect to the high-symmetry structure are scaled by a factor of 2 for better visibility. The distortion is substantially the same as for the compound $Ba_3NbIr_2O_9$ shown in Figure 6.7(e)-(f). The wR(all) value improves from 7.44 % in space group $P6_3/mmc$ to 5.98 % in space group $C2/c$. The refinement in space group $C2/c$ yields still slightly negative occupations for Ir on the Ce site and vice versa, which are roughly consistent with zero within the error. This is why in Table 6.1, these values (namely 1.0(4) % Ir on the Ce site and 0.7(5) % Ce on the Ir site) are listed.

An unambiguous indication for a monoclinic distortion can be achieved by a determination of the monoclinic angle. This cannot be done using single-crystal X-ray diffraction data since they are not suitable for a precise determination of the metric. X-ray powder diffraction is the better choice for this.

The metric of $Ba_3CeIr_2O_9$ is determined by a LeBail refinement of X-ray powder diffraction data at room temperature. The sample contains powder of $Ba_3CeIr_2O_9$ together with well-investigated Si powder as reference material. In a first step, the correction parameters Zero, SySin and SyCos are determined from three isolated Si reflections. Only small regions of the diffractogram around these reflections are included in the refinement. The Si lattice constant is kept fixed at 5.43110 Å [148] with cubic space group $Fd\overline{3}m$. The Cu K_α wavelengths of $\lambda_1 = 1.54056$ Å and $\lambda_2 = 1.54439$ Å are taken from [125] with an intensity ratio of $I_2/I_1 = 0.51$ from [149]. Also the pseudo-Voigt width parameters U, V, W, X for Si are refined in this refinement. In a further step, a second refinement is carried out, including the whole diffractogram and the two phases $Ba_3CeIr_2O_9$ and Si. Only the lattice parameters a, b, c, β and the profile width parameters for $Ba_3CeIr_2O_9$ are refined. This two-step procedure ensures that Si reflections cannot be mistaken as $Ba_3CeIr_2O_9$ reflections and the calibration of Zero, SySin and SyCos is reliable. The refinement is shown in Figure 6.14. An R value of 10.32 % is obtained with a χ^2 of 1.35. The monoclinic angle of 90.322(3)° clearly deviates from 90° that would be expected in this setting for a hexagonal crystal structure. As stated in Section 6.1, the compounds $Ba_3IrTi_2O_9$, $Ba_3RuTi_2O_9$ and $Ba_3CuSb_2O_9$ crystallize in space group $P6_3mc$. This possibility can now be excluded for $Ba_3CeIr_2O_9$.

Using the lattice constants of the powder-diffraction together with the structural parameters of Table A.16 in space group $C2/c$, one yields an intra-dimer Ir − Ir distance of 2.52865(26) Å. The Ir − O − Ir angles inside the double-octahedron are not symmetrically equivalent in space group $C2/c$. Two of these angles amount to 77.49(12)° and one of them equals 74.76(20)°. The Ir − Ir distance is in good agreement with the value reported in [142], where this short distance is attributed to a strong antiferromagnetic coupling [142].

The values used for the publication [150] by A. Revelli et al**.** were calculated before the powder-diffraction experiment was carried out. This explains slight differences in the distances and angles. For the same reason, the publication [150] does not discuss a refinement in $C2/c$. In [150], a double slit experiment is carried out with resonant inelastic X-ray scattering (RIXS) in order to investigate whether the electronic structure of the Ir atoms can be explained neglecting spin-orbit coupling. This method yields an intra-dimer Ir − Ir distance of 2.530(8) Å. That distance is in very good agreement with

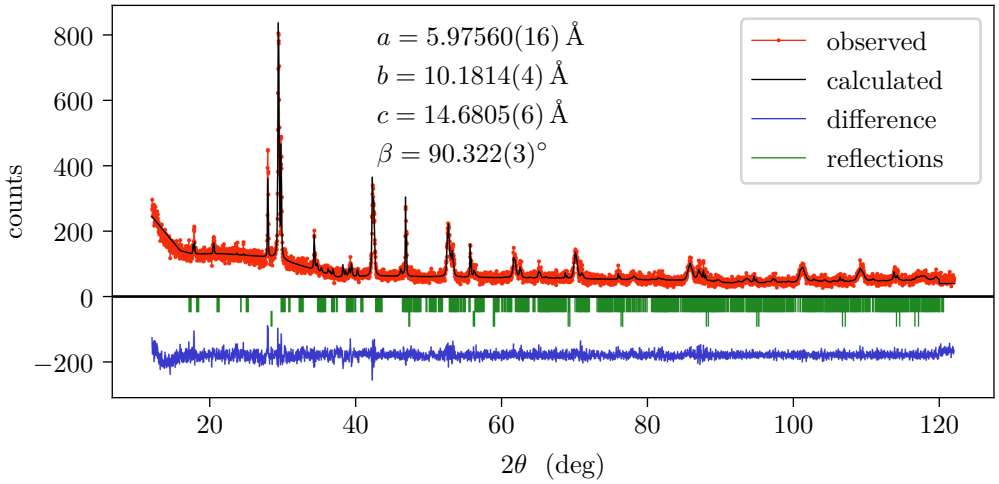

Figure 6.14: X-ray powder diffraction with a sample containing $Ba_3CeIr_2O_9$ (reflections marked by upper row green lines) and Si (lower row) for reference. The LeBail refinement is carried out in space group $C2/c$ for $Ba_3CeIr_2O_9$ while the cubic Si structure is kept fixed. The lattice parameters of the $Ba_3CeIr_2O_9$ phase are given.

the result of the elastic X-ray diffraction discussed in the present work.

6.4.3 Conclusion

The compound $Ba_3CeIr_2O_9$ was investigated via X-ray diffraction. The crystal structure exhibits space group $C2/c$ with a monoclinic angle deviating $0.322(3)°$ from a right angle. The occupation of the Ce and Ir sites is ordered. The intra-dimer $\mathrm{Ir}-\mathrm{Ir}$ distance is $2.52865(26)$ Å.

6.5 Comparison of $Ba_3XIr_2O_9$ compounds

Figure 6.15 shows the occupation disorder of different compounds of the form $Ba_3XIr_2O_9$. The compounds with $X \in \{\mathrm{Nb}, \mathrm{In}, \mathrm{Ce}\}$ were investigated in this work. Additionally, results from [143] are included in the plot for the compounds with $X \in \{\mathrm{Ti}, \mathrm{Sc}\}$. The crystal radii given in [151] are used. The valences are $Ce^{4+}(Ir^{4+})$, $In^{3+}(Ir^{4.5+})$, $Nb^{5+}(Ir^{3.5+})$, $Ti^{4+}(Ir^{4+})$ and $Sc^{3+}(Ir^{4.5+})$. A coordination number of VI is used for all cations. For non-integer valences, the mean of the crystal radii for the neighbored integer valences was taken. The refinements in this work differ from the refinements in [143] in the way that the former refinements have independent occupations for Ir on X sites and for X on Ir sites while the latter refinements are constrained in the way that the stoichiometry is conserved. It can be seen in Figure 6.15 that similar radii result in higher occupation disorder. The occupations for the compound with $X = \mathrm{Ce}$ are slightly negative, however the absolute value is small so that the crystal structure can be considered as ordered

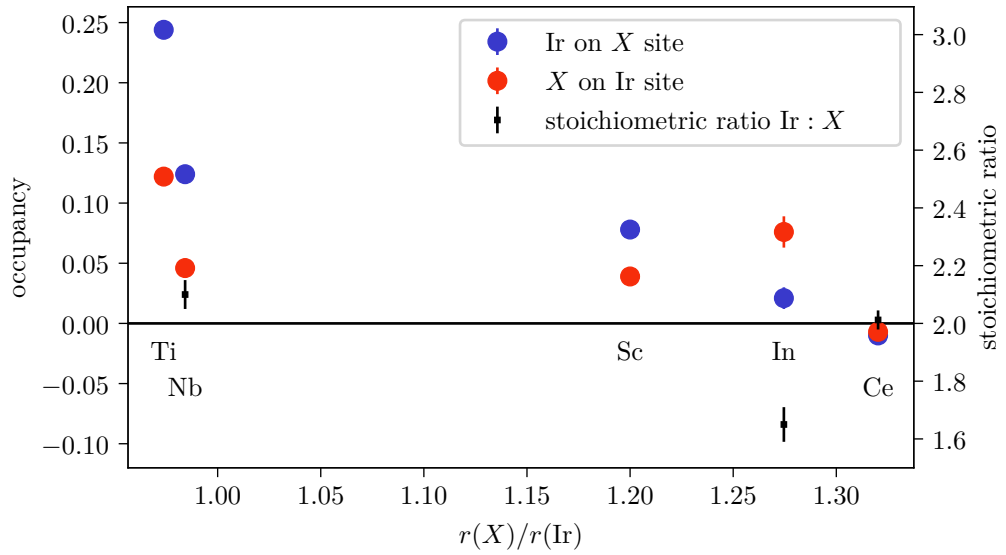

Figure 6.15: Plot of the occupation disorder (Ir atoms on X sites and vice versa) against the ratio of the atomic radii for different $Ba_3XIr_2O_9$ compounds. For the refinements in this work, where the stoichiometry is not constraint, also the stoichiometric ratio of the Ir and X atoms is given. The data for the compounds with $X \in \{\mathrm{Ti}, \mathrm{Sc}\}$ are taken from [143]. In the case $X = \mathrm{Ce}$, the refinement in space group $P6_3/mmc$ yields strongly negative occupations so that the refinement in space group $C2/c$ is taken for this plot.

like stated above. The compound with $X = \mathrm{In}$ was also investigated in [143] where no occupation disorder could be detected. For the same compound, a small site mixing of 2.8(5) % is reported in [146], but it is considered as not reliably distinguishable from the fully ordered model.

Magnetic interactions are strongly influenced by the distances between the concerning ions, in this case Ir. This is why the $\mathrm{Ir} - \mathrm{Ir}$ distances are compared in Figure 6.16. Three such distances are of interest, which are depicted in Figure 6.16(a): The intra-dimer distance $d(\mathrm{Ir}, 1)$ which is the distance in c direction between the two Ir atoms in a double-octahedron; the inter-dimer distance within the ac plane $d(\mathrm{Ir}, 2)$ that seperates two adjacent dimers from each other; and the diagonal distance $d(\mathrm{Ir}, 3)$ which is between an Ir atom and one of the three nearest Ir atoms in the adjacent dimer layer. The valence of the Ir ion depends on the compound, as stated above. The crystal radius of the Ir ion depends on the valence. Crystal radii from [151] are used for further calculations. One could expect that the intra-dimer distance $d(\mathrm{Ir}, 1)$ depends mainly on the valence state of the Ir ion. Figure 6.16(b) compares the radius of the Ir ion to this distance. The compound with $X = \mathrm{Ce}$ and Ir^{4+} has the smallest distance $d(\mathrm{Ir}, 1)$ compared to the compounds with $X \in \{\mathrm{In}, \mathrm{Nb}\}$, while the crystal radius of Ir^{4+} lies in between the radii of $\mathrm{Ir}^{3.5+}$ and $\mathrm{Ir}^{4.5+}$. The distance shows large variations for compounds with the same valence state. This means that differences in the intra-dimer distance $d(\mathrm{Ir}, 1)$ cannot be explained by the crystal radii of the Ir ion. Figure 6.16(c) compares all three distances $d(\mathrm{Ir}, 1 \ldots 3)$ to the crystal radius of the X atom. The distance $d(\mathrm{Ir}, 2)$ and

compound	X ion	V	Ir ion	V	Ba1 atom	V	Ba2 atom	V
$Ba_3InIr_2O_9$	In^{3+}	3.38	$Ir^{4.5+}$	4.85	Ba^{2+}	2.11	Ba^{2+}	2.11
$Ba_3NbIr_2O_9$	Nb^{5+}	5.17	$Ir^{3.5+}$	4.33	Ba^{2+}	2.27	Ba^{2+}	2.31
$Ba_3CeIr_2O_9$	Ce^{4+}	3.84	Ir^{4+}	4.59	Ba^{2+}	1.96	Ba^{2+}	1.90

Table 6.2: Valence sums of the X ion and of the Ir ion for the compounds $Ba_3XIr_2O_9$ with $X \in \{\mathrm{In}, \mathrm{Nb}, \mathrm{Ce}\}$ calculated from structural refinements in space group $C2/c$.

$d(\mathrm{Ir}, 3)$ split into two resp. three different distances in space group $C2/c$. However, this splitting is rather small compared to the element dependence. The comparison of the three compound reveals clear trends: The inter-dimer distances $d(\mathrm{Ir}, 2 \ldots 3)$ increase with increasing crystal radius of the X atom, while the intra-dimer distance $d(\mathrm{Ir}, 1)$ decreases. The increase of the inter-dimer distances can be explained by the fact that the $[XO_6]$ octahedrons occupy more space for larger crystal radii of the X ion. Since this octahedron is located diagonally between two dimer planes and between three dimers of the same plane, both inter-dimer distances are pushed apart when the crystal radius of the X ion increases. The influence of this crystal radius on the intra-dimer distance $d(\mathrm{Ir}, 1)$ is less trivial. Independently from the size of the $[XO_6]$ octahedron, this distance could stay the same if the lattice parameter c changed. The fact that $d(\mathrm{Ir}, 1)$ decreases with increasing crystal radius of the X ion is a hint for further couplings, e.g. between X or Ba atoms, which prefer a certain distance in c direction.

The fact that the intra-dimer $\mathrm{Ir} - \mathrm{Ir}$-distance is dependent on the radius of the X atom is in agreement with considerations about dimerization. The short distance is ascribed to the strong magnetic coupling between the Ir atoms in [142] and to large intra-dimer $\mathrm{Ir} - \mathrm{Ir}$ hopping in [150].

For all three investigated compounds $Ba_3XIr_2O_9$, valence sums were calculated for the Ce^{4+}, In^{3+}, Nb^{5+} and Ir cations. The formula, the constant b and the constants $R_{X,\mathrm{O}}$ were taken from [73]. For the Ir ion, only Ir^{5+} was found in [73], so that not the precise valence could be used in the calculation. The valence sums are shown in Table 6.2. Some valence sums, like the ones for Ba^{2+}, are very close to the nominal valence. Others, like the valence sum for $Ir^{3.5+}$, are not in good agreement.

A criterion for the distortion of an octahedron is given in [152]: The deviations of 12 angles $\theta_1, \ldots, \theta_{12}$ that equal 90° in the undistorted octahedron are taken into account. The deviations squares are summed up so that the quantity $\sigma_\theta^2 = \sum_{i=1}^{12} (\theta_i - 90°)^2/11$ is zero for the undistorted octahedron and positive for distorted ones. For the angles it is possible to use the $\mathrm{O} - \mathrm{O} - \mathrm{O}$ angles between edges of the octahedron or the $\mathrm{O} - X - \mathrm{O}$ angles between two neighbored corners and the central atom. In the present work, we call the first alternative "exterior deviation" and the second one "interior deviation" ($\sigma^2_{\theta(\mathrm{ext.})}$ and $\sigma^2_{\theta(\mathrm{int.})}$). Additionally to the distortion, also the tilting of the octahedrons are of interest. The tilting in the $C2/c$ crystal structure can be described by the angles along $X - \mathrm{O} - \mathrm{Ir}$ that connects the single-octahedron to a corner-shared $[IrO_6]$

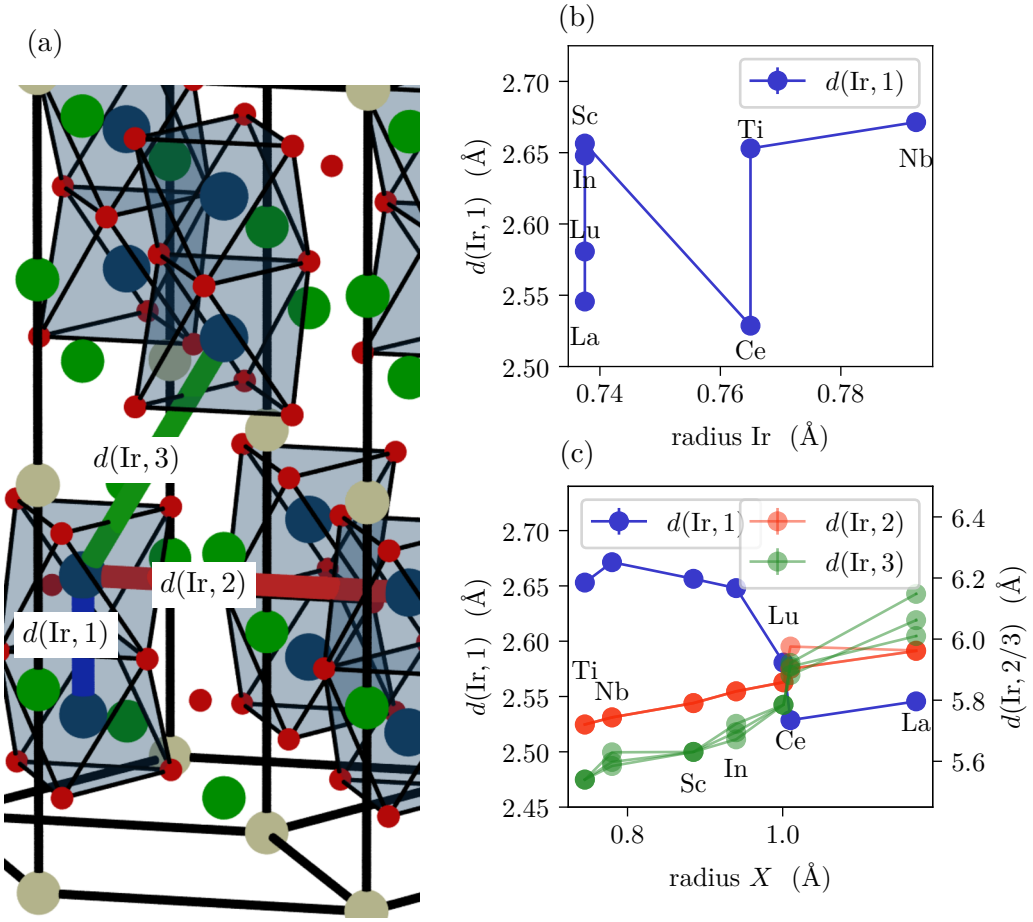

Figure 6.16: (a) The intra-dimer Ir − Ir distance $d(\mathrm{Ir},1)$, the in-plane Ir − Ir distance $d(\mathrm{Ir},2)$ and the diagonal Ir − Ir distance $d(\mathrm{Ir},3)$ are investigated for the compounds $Ba_3XIr_2O_9$ with $X \in \{\mathrm{Ce},\mathrm{In},\mathrm{Nb}\}$ from this work, $X \in \{\mathrm{Lu},\mathrm{La}\}$ from [142] and $X \in \{\mathrm{Sc},\mathrm{Ti}\}$ from [143]. (b) The intra-dimer distance $d(\mathrm{Ir},1)$ plotted against the Ir radius . The radius differs due to the valence. (c) All three Ir − Ir distances plotted against the radius of the X atom. Crystal radii from [151]. In space group $C2/c$, the distances $d(\mathrm{Ir},2)$ and $d(\mathrm{Ir},3)$ split.

compound	$Ba_3InIr_2O_9$	$Ba_3NbIr_2O_9$	$Ba_3NbIr_2O_9$	$Ba_3CeIr_2O_9$
sample	TD065-S001	TD105-S001	TD105-S002	PB011-S001
$\sigma^2_{\theta(\text{single-oct., ext.})}$	0.62(27) deg^2	7.0(9) deg^2	21.5(1.5) deg^2	3.8(5) deg^2
$\sigma^2_{\theta(\text{double-oct., ext.})}$	13.6(7) deg^2	15.4(7) deg^2	27.6(1.0) deg^2	18.0(6) deg^2
$\sigma^2_{\theta(\text{single-oct., int.})}$	13.1(1.3) deg^2	9.4(1.1) deg^2	25.3(1.6) deg^2	20.6(1.3) deg^2
$\sigma^2_{\theta(\text{double-oct., int.})}$	34.9(1.0) deg^2	32.0(8) deg^2	39.3(1.0) deg^2	24.3(6) deg^2
	171.1(5)°	172.7(4)°	173.9(5)°	179.4(6)°
tilt angles	169.81(34)°	172.03(29)°	170.31(30)°	168.58(30)°
(single octahedron)	172.21(30)°	174.76(28)°	173.47(32)°	169.99(27)°

Table 6.3: The parameter σ^2_θ according to [152] describes the distortion of the $[Ir_2O_9]$ double-octahedrons and $[XO_6]$ single-octahedrons for four samples of the compounds $Ba_3XIr_2O_9$ with $X \in \{\text{In}, \text{Nb}, \text{Ce}\}$. The tilt angles along $X - \text{O} - \text{Ir}$ show the rotation of the single-octahedrons. For the definition of $\sigma^2_{\theta(\text{ext.})}$ and $\sigma^2_{\theta(\text{int.})}$ cf. text.

octahedron that is part of an $[Ir_2O_9]$ double-octahedron. Since the X atom occupies the site $4a$ $0, 0, 0$, which is at an inversion centre in space group $C2/c$, only three of the six angles are unique. The distortions and the tiltings for the three compounds $Ba_3XIr_2O_9$ with $X \in \{\text{In}, \text{Nb}, \text{Ce}\}$ are listed in Table 6.3. For all compounds, the single-octahedrons are less distorted than the double-octahedrons. The strong distortion of the latter can be attributed to the fact that a simple rotation is not possible because the two octahedrons share a common face. For the case $X = \text{In}$, the single-octahedrons are hardly distorted if the exterior distortion $\sigma^2_{\theta(\text{single-oct., ext})}$ is considered. This can be explained by the strong covalent bonding of the In^{3+} ions that prevents a distortion. For $X \in \{\text{In}, \text{Ce}\}$, the exterior distortion of the single-octahedrons is much smaller than the interior distortion. This means that the distortion mainly effects the central atom while the O atoms are rather rotated. For $X = \text{Nb}$, the O atoms seem to have a bigger influence on the distortion because the exterior and interior distortion of the single-octahedrons are similar. The tilting angles are comparable to those for $Ba_3InIr_2O_9$ in [146] which can be calculated to 175.0(6)°, 170.7(4)° and 172.57(34)°.

6.6 Conclusion

It could be shown by X-ray diffraction that the three compounds $Ba_3InIr_2O_9$, $Ba_3NbIr_2O_9$ and $Ba_3CeIr_2O_9$ have $C2/c$ symmetry already at room temperature. For the compound $Ba_3CeIr_2O_9$ could be determined to 90.322(3)°. The distortions effect mainly the O atoms, which break the six-fold symmetry. Differences in the atomic radii of the X and the Ir cation favor an ordered occupation of these ions, while similar radii lead to higher disorder. The $\text{Ir} - \text{Ir}$ distances are not effected by the crystal radius of the Ir ion (which

appears with different valences in these compounds), but rather by the crystal radius of the X ion. The double-octahedrons are strongly distorted while the single octahedrons are rather tilted. The small distortion of the single octahedrons is substantially caused by a displacement of the central X atom for $X \in \{\mathrm{In}, \mathrm{Ce}\}$ while for $X = \mathrm{Nb}$ the O atoms play a stronger role for the distortion.

7 Double-perovskites of the form Ba_2XIrO_6

Compounds of the form ABO_3 with a perovskite structure that exhibits space group $Pm\bar{3}m$ in the undistorted case [153] are prone to structural distortions. An overview over many such related crystal structures is given in [154]. In the case of $GdFeO_3$, the structural distortion involves a tilting of the [FeO_6] octahedrons as reported in [155], where the tilting of the octahedrons reduces the cubic symmetry to the orthorhombic space group $Pbnm$. Distortions of perovskite-type structures that involve tilts of the octahedrons can be described using the notation of Glazer [156]. The tilts are assumed to be small so that tilts around perpendicular axes approximately commute with each other and the octahedrons are not distorted as long as small-angle approximation holds. A tilt about the cubic a axis has to be in opposite direction for octahedrons that are connected in b or c direction, while octahedrons that are connected in a direction can tilt in either the same or the opposite direction of rotation. This allows to write many possible distorted perovskite-type componds in the form $a^{\sigma_a}b^{\sigma_b}c^{\sigma_c}$ where $\sigma \in \{-, 0, +\}$. A superscript $-$ ($+$, 0) means a rotation in the opposite direction (a rotation in the same direction, no rotation) around this axis for octehedrons that are connected along this axis. If the rotations around two axis are of the same magnitude, the axis are named equally. E.g. the expression $a^-a^-c^0$ describes a distorted perovskite where the octahedrons are rotated around the a and b axis about the same angle and the direction of rotation alternates. A detailed description of this formalism can be found in [156].

The crystal structures of Ba_2CeIrO_6 and Ba_2PrIrO_6 are related to the cubic perovskite structure, however the site within the octahedron is alternating occupied by a Ce/Pr and Ir atom, so that the unit cell has to be chosen 8 times as large compared to the perovskite structure as shown in Figure 7.1 for the case of Ba_2CeIrO_6. The double-perovskite structure is described in space group $Fm\bar{3}m$. The same structural instabilities as for perovskites can be expected for double perovskites. The notation of Glazer, as mentioned above, can also be used for this structure type if the [Ce/PrO_6] and the [IrO_6] octahedrons are treated identically. One has to keep in mind that the size of those octahedrons may vary so that smaller octahedrons rotate about a greater angle than larger ones.

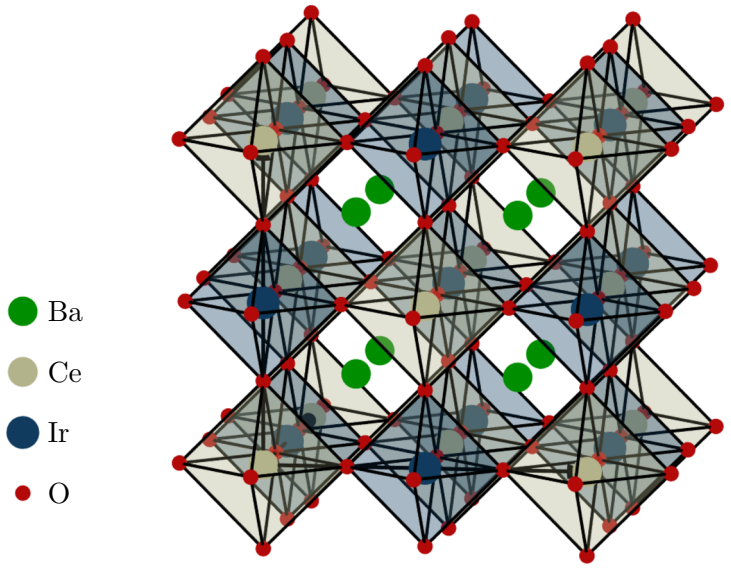

Figure 7.1: Double-perovskite crystal structure of Ba_2CeIrO_6.

7.1 Ba_2CeIrO_6

7.1.1 Latest state of research

In [157], the crystal structure of Ba_2CeIrO_6 has been found to be monoclinically distorted so that the space group is $P2_1/n$. A symmetry reduction to $P2_1/n$ is also reported for the related compound Sr_2CeIrO_6 [158].

The Ir sites are arranged in a face centered cubic lattice. This gives rise to magnetic frustration even if next-nearest neighbor Heisenberg coupling is included [159]. However, Kitaev interaction is found to stabilize long-range magnetic order [159]. This is surprising since Kitaev interaction is in other arrangements known as a mechanism that prevents long-range magnetic order (cf. 1.2.2).

The Ir^{4+} ion exhibits $5d^5$ electrons that occupy the t_{2g} orbitals that are energetically favored in the presence of O^{2-} ligands in octahedral configuration. Spin-orbit coupling furthermore splits the t_{2g} states. The configuration of the five electrons can have a total momentum of $j = 1/2$ or $j = 3/2$, where the $j = 1/2$ state is the ground state. A distortion of the crystal field, that breaks cubic symmetry, might further split the excited state. In this case, the ground state is a linear combination of the $j = 1/2$ and $j = 3/2$ states.

In RIXS experiments, two different excitation energies are visible [159]. This shows that the non-cubic distortion is not negligible. From the excitation energies, the linear combination for the ground state could be determined. It is very close to the pure $j = 1/2$ state [159].

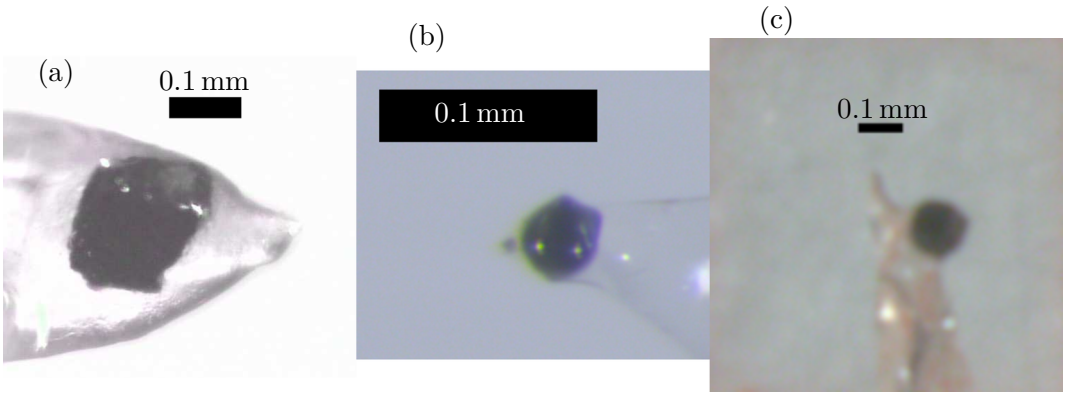

Figure 7.2: Ba_2CeIrO_6 samples for single-crystal X-ray diffraction. (a) Sample AR506a. (b) Sample PB016-S001. (c) Sample PB016-S003. Sample PB016-S002 is the same crystal as PB016-S001, but mounted differently.

7.1.2 Samples and experimental setup

The samples were grown by P. Becker [147] using melt solution growth with the melt solvent $BaCl_2$ and the educts $BaCO_3$, IrO_2 and CeO_2. The growth of crystals with a size about $1\,mm^3$ took three weeks. Details about the crystal growth can be found in [159].

Two Ba_2CeIrO_6 crystals were investigated via single-crystal X-ray diffraction on APEX (cf. Section 3.1.1). The crystals are shown in Figure 7.2. The crystal of sample AR506a (Figure 7.2(a)) is very big. Sample PB016-S001 (Figure 7.2(b)) is much smaller, which is better for single-crystal X-ray diffraction due to less absorption. These two samples were used for room temperature measurements. Sample PB016-S002 contains the same crystal as sample PB016-S001, but it is glued in a more robust way so that it can be used for low-temperature measurements. Sample PB016-S003 (Figure 7.2(c)) is used for searching superstructure reflections.

For sample AR506a, 25 770 reflections were collected at room temperature, 210 of them are unique in space group $Fm\bar{3}m$. 207 unique reflections were observed. The absorption correction was carried out using a sample shape with 12 faces.

For sample PB016-S001, 32 921 reflections were collected at room temperature, 198 of them are unique in space group $Fm\bar{3}m$. All reflections were observed. The sample has an octahedral shape with $30\,\mu m$ edge length. An appropriate model was used for absorption correction (all eight faces $(\pm 1\ \pm 1\ \pm 1)$ are $12.3\,\mu m$ away from the centre). The absorption coefficient amounts to $41.340\,mm^{-1}$.

For sample PB016-S002, 13 274 reflections were collected at 100 K, 205 of them are unique in space group $Fm\bar{3}m$. 118 of the unique reflections were observed. The "multiscan absorption correction" of the APEX2 software was used [76].

With sample PB016-S002, the temperature dependence of three equivalent reflections

was investigated by scanning these reflections at different temperatures with the single-crystal X-ray diffractometer APEX.

Some points in reciprocal space of sample PB016-S003 were scanned with long exposure time in order to exclude superstructure reflections.

7.1.3 Room temperature crystal structure

The crystal structure of Ba_2CeIrO_6 can be roughly described in the cubic space group $Fm\overline{3}m$. However, a distortion from the double-perovskite structure remains an open question, so that also the monoclinic space group $P2_1/c$ has been proposed [157][1].

Space group $Fm\overline{3}m$ exhibits 97 translationengleiche subgroups, including the two trivial subgroups and counting twins separately. Figure 7.3 shows a graph that represents the group-subgroup relations of some translationengleiche subgroups of $Fm\overline{3}m$. Only maximal translationengleiche subgroups and maximal subgroups of them are shown. Space group $P2_1/c$ is not translationengleich but a klassengleiche subgroup of $C2/m$. The Bärnighausen diagram [132] $Fm\overline{3}m > R\overline{3}m > C2/m > P2_1/c$ is shown in Figure 7.4. $Fm\overline{3}m$, $R\overline{3}m$ and $C2/m$ are translationengleich and $P2_1/c$ is a klassengleiche subgroup of $C2/m$.

In order to determine the correct space group for Ba_2CeIrO_6, it is useful to start with an investigation of the translation symmetries. Space group $Fm\overline{3}m$ is face-centered, so the selection rule $h+k, h+l, k+l \in 2\mathbb{Z}$ applies. For the two samples AR506a and PB016-S001, the intensities of reflections breaking this selection rule are investigated using statistical methods in Figure 7.5: A histogram of the quantity $I/\sigma(I)$, where I is the intensity and $\sigma(I)$ its error, shows a nearly perfect Gaussian distribution. In the case of purely statistic deviations of the intensities from zero, a Gaussian distribution of width 1 centered at 0 would be expected. The width is very close to 1 and the center deviates from 0 much less than one standard uncertainty. One might argue that the shift of the center towards a positive value is an indication for weak superstructure reflections. However, it is also possible that the intensities of these reflections can be explained by the $\lambda/2$ effect, where reflections with twice the wave vector and half the wave length are measured. Five such forbidden reflection were measured with the usual acceleration voltage of the X-ray tube 50 kV and with 30 kV, at which no radiation with wavelength $\lambda/2$ can be generated. Indeed, these reflections disappear at the lower acceleration voltage, so they are definitely caused by $\lambda/2$ radiation. These reflections $(h\,k\,l)$ were plotted against the intensities of the allowed reflections $(2h\,2k\,2l)$, as shown in Figure 7.6(a). A fit shows that the intensity of $\lambda/2$ is by a factor of 82(6) weaker compared to the nominal radiation. This factor is used together with the structural data and the scaling factor of a refinement in space group $Fm\overline{3}m$ and disordered Ce/Ir occupation for the calculation of the $\lambda/2$ reflections of the other forbidden reflections. Figure 7.6(b)

[1] In [157], the non-standard setting $P2_1/n$ is used, which can obtained from the standard setting $P2_1/c$ by the following transformation: $(\vec{a},\vec{b},\vec{c})_{P2_1/n} = (-\vec{a}-\vec{c},\vec{b},\vec{a})_{P2_1/c}$. For a comparison of Fig. 2 in [157], it is useful to realize that a shift of $\frac{1}{2}\vec{b}$ does not change the space group $P2_1/n$.

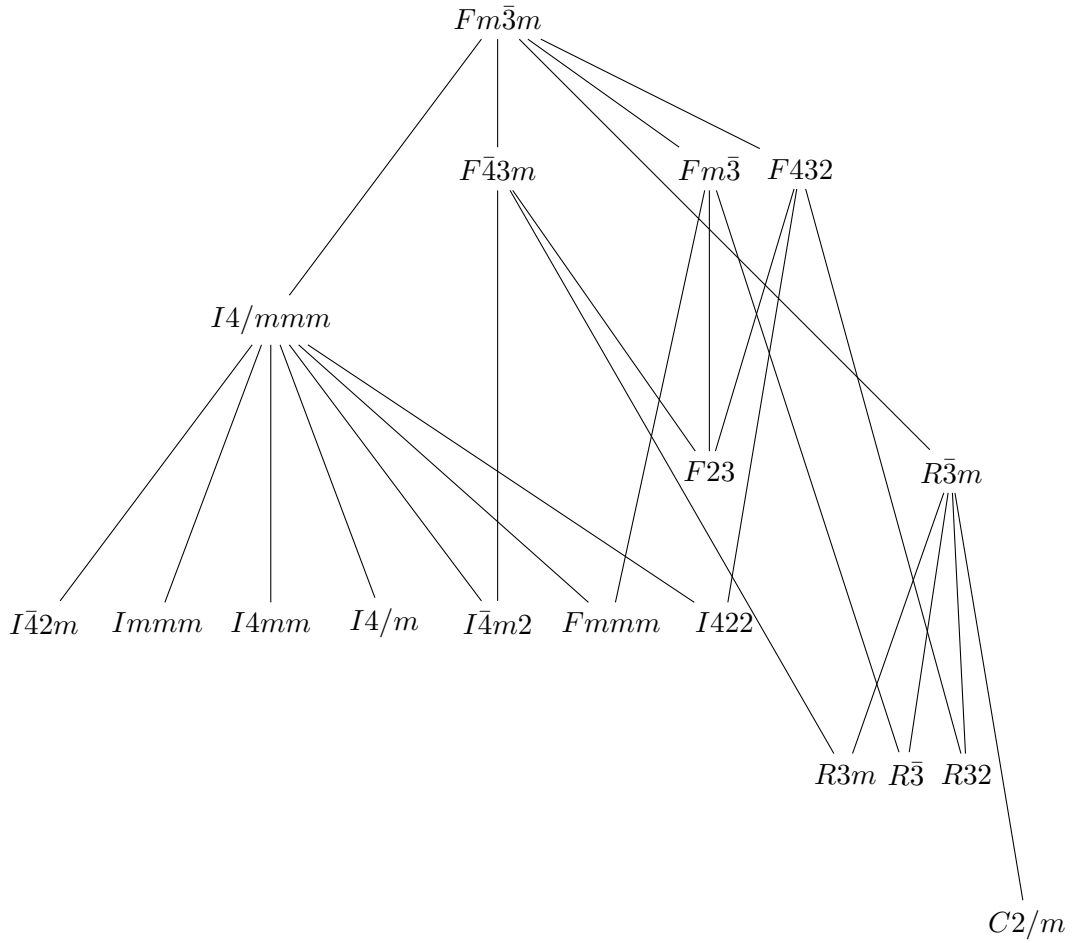

Figure 7.3: Group-subgroup relations of the maximal translationengleiche subgroups of $Fm\bar{3}m$ and maximal translationengleiche subgroups of them.

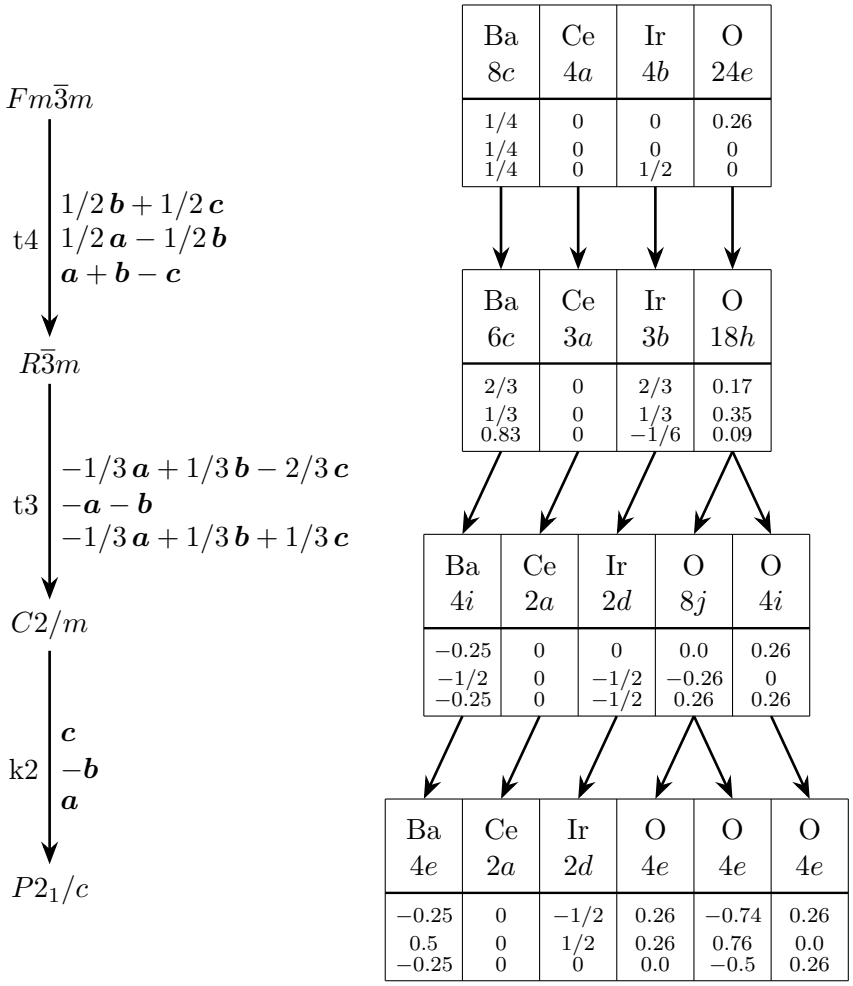

Figure 7.4: Bärnighausen diagram that displays the relationship of the cubic space group $Fm\bar{3}m$ and the monoclinic space group $P2_1/c$ that is proposed for Ba_2CeIrO_6 in [157].

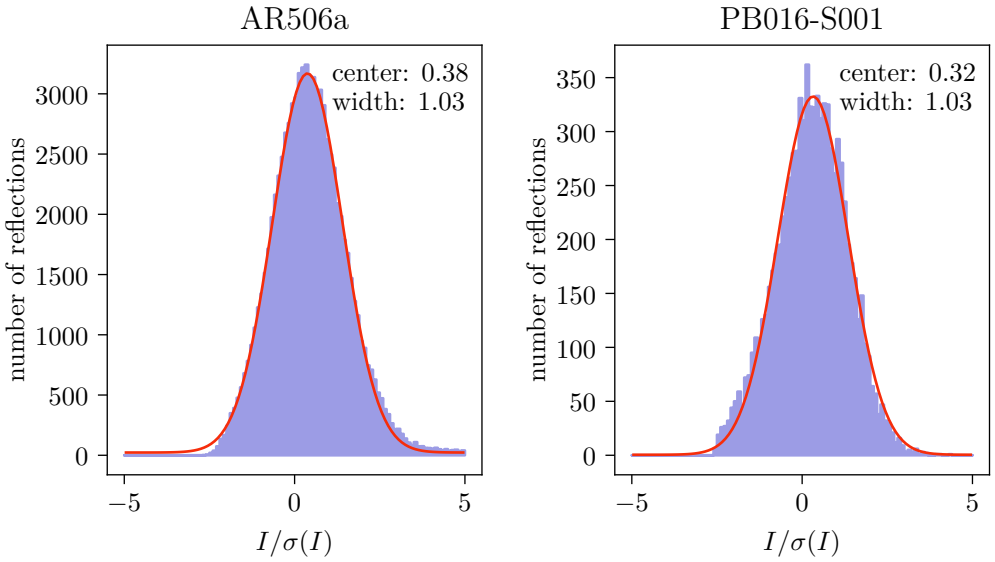

Figure 7.5: Histograms (blue) of single-crystal X-ray reflections that are forbidden by the F centering in space group $Fm\bar{3}m$. The reflections were collected at room temperature. Fits of a Gaussian function (red) show that the ratio $I/\sigma(I)$ of the intensity divided by its error is well compatible to zero intensity. Left: Sample AR506a. Right: Sample PB016-S001.

shows the comparison of the calculated and observed intensities of these reflections. The red line displays equality. The obsorved intensities can be roughly explained by the $\lambda/2$ effect.

This means especially that spacegroup $P2_1/c$ as proposed in [157] can be ruled out.

In order to settle any doubts about a missing breaking of the translation symmetry, a simulation is carried out for the case that the distortion is described as $a^+a^+a^+$ according to the Glazer notation [156]. The model assumes a tilt of the [CeO_6] octahedrons about 5° for each axis. The [IrO_6] octahedrons tilt slightly stronger because they are smaller. This distortion breaks the F centering of space group $Fm\bar{3}m$, so super structure reflections violating the selection rule $hkl : h+k, h+l, k+l = 2n$ appear in this model. The crystal structure for this simulation is based on the structural data of the refinement in $Fm\bar{3}m$ given in Table A.17. Furthermore, the intensity ratio of the radiation with wavelength λ and $\lambda/2$ determined in Figure 7.6 is used for the prediction of the intensities of $\lambda/2$ reflections. The result is shown in Figure 7.7. The intensities are given in arbitrary units which are identical for all axes. The change for the allowed reflections is at an extent that should be visible for very good refinements. Nearly all forbidden reflections are smaller than the expected $\lambda/2$ contribution.

A strong superstructure reflection is (3 5 0) which in the distorted structure has an intensity of 1146 a.u. which is comparable to the (6 10 0) reflection with half the wavelength that has an intensity of 1882 a.u. Unfortunately, some reflections which are equivalent to (3 5 0) in space group $Fm\bar{3}m$ have an intensity of only 389 a.u. for the distorted model.

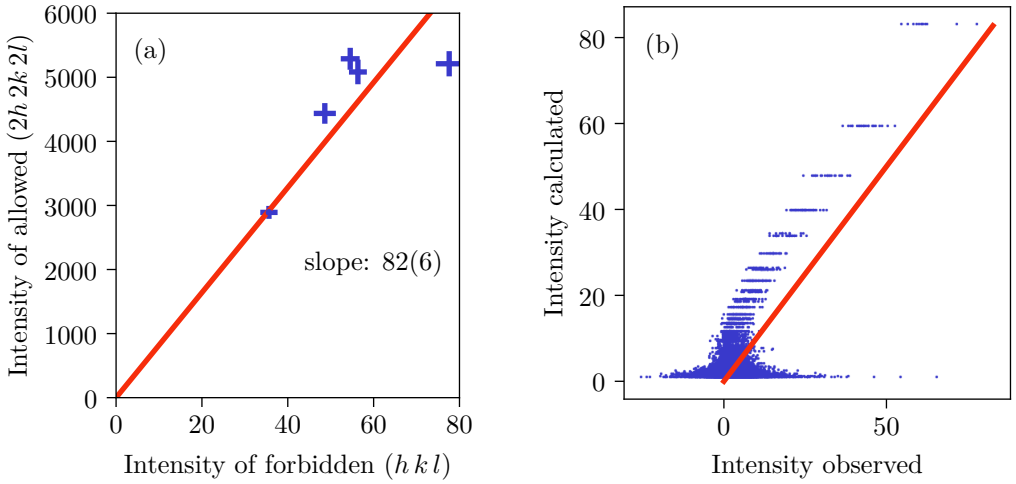

Figure 7.6: (a) The intensity ratio of reflections with the nominal wave length λ and half of the wave length $\lambda/2$ is determined from reflections $(h\,k\,l)$ which are definitely caused by $\lambda/2$ radiation. (b) The intensity of reflections $(h\,k\,l)$ that are forbidden in space group $Fm\bar{3}m$ are plotted against the intensity that is expected for reflections $(2h\,2k\,2l)$ with half of the wave length. The red line is the angle bisector.

We should keep that in mind for a worst-case consideration. In order to prove that this reflection does not appear, it is useful to compare it with a similarly strong allowed reflection. For the undistorted structure, the reflection (6 2 2) and equivalents have an intensity of 634 a.u., which however is approximately three times as large for the distorted structure. For this reason, also the reflections (2 2 2) and equivalents are taken into account, which have a specially weak intensity of 918 a.u. for the distorted structure.

Figure 7.8 shows the allowed reflections (6 2 2) and (2 2 2), which are clearly visible with an acceleration voltage of 30 kV. The exposure time was set to 1000 s/deg. At this voltage, $\lambda/2$ radiation can be ruled out. The forbidden reflection (3 5 0) is not visible with 30 kV, although the exposure time was twice as long. The $\lambda/2$ reflection is visible at 50 kV, which proves that the orientation matrix was precise enough to hit this reflection. All four measurements were carried out with a scan width of 0.5°.

The forbidden reflection was simulated to be approximately half as strong compared to the two allowed reflections in the worst case. It can be concluded that we can exclude a breaking of translational symmetries by a $a^+a^+a^+$ distortion about 5°.

As shown in Figure 7.4, the translationengleiche subgroup closest to space group $P2_1/c$ as proposed in [157] is $C2/m$. For the room temperature single-crystal X-ray diffraction measurements of both samples AR506a and PB016-S001, structural refinements were carried out in space groups $Fm\bar{3}m$ and $C2/m$. All atomic displacement parameters in the model are isotropic. The results are shown in the upper part of Table 7.1. The values left of the arrow "→" relate to refinements in the low-symmetry space group with the structural parameters fixed from refinements in the high-symmetry space group.

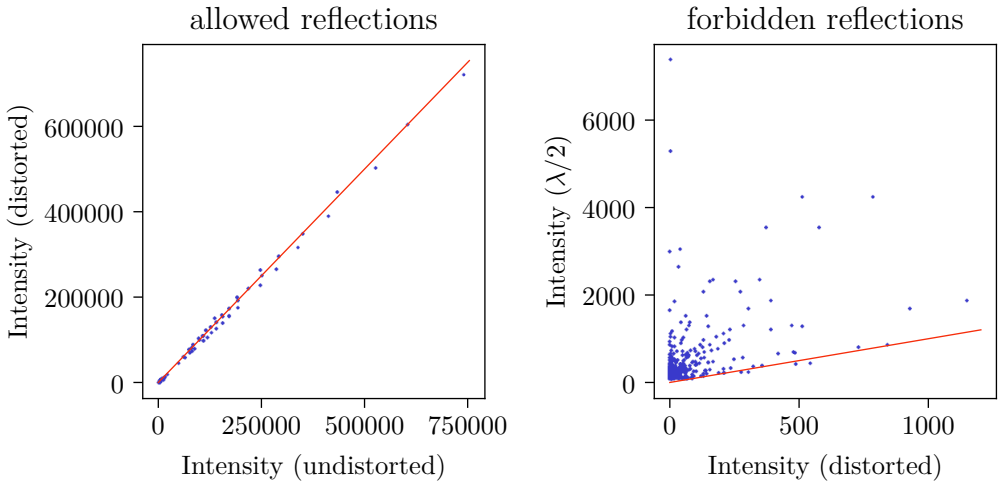

Figure 7.7: Simulation of X-ray reflections assuming a distorted double-perovskite structure for Ba_2CeIrO_6 where the [CeO_6] octahedrons are tilted about 5° following the $a^+a^+a^+$ distortion according to the Glazer notation [156]. Left: Reflections that are allowed in space group $Fm\bar{3}m$ for the undistorted and the distorted structure are compared. Right: Reflections that are forbidden in space group $Fm\bar{3}m$ are calculated for the distorted structure and compared to the $\lambda/2$ reflection with twice the reciprocal vector. The red lines are angle bisectors.

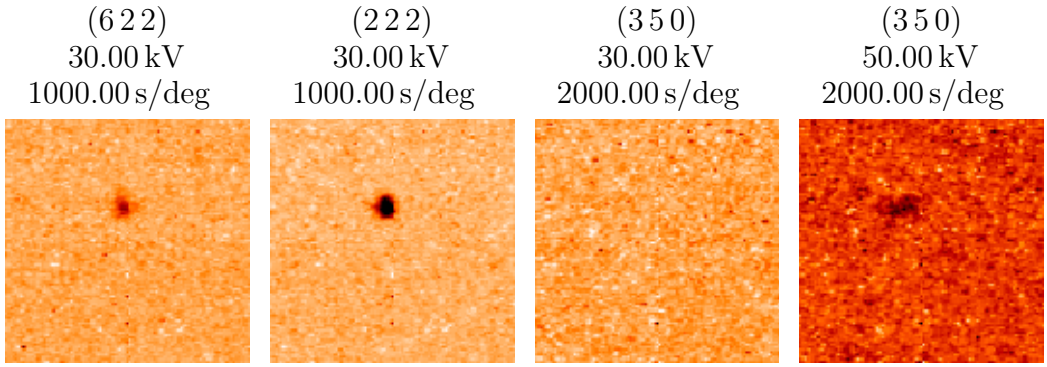

Figure 7.8: Scans of single-crystal X-ray reflections of the Ba_2CeIrO_6 sample PB016-S003. The scans have a scan-width of 0.5°. The reflections (6 2 2) and (2 2 2) are weak allowed reflections (cf. text). They are measured with an acceleration voltage of 30 kV for the X-ray tube. The reflection (3 5 0) is forbidden in space group $Fm\bar{3}m$. Measured with 30 kV, this reflection is not visible. The $\lambda/2$ reflection measured with 50 kV proves that the orientations of sample and detector were chosen correctly in order to observe it. The forbidden reflection was measured with twice the exposure time compared to the allowed reflections.

For sample AR506a, the wR(all) value in the lower symmetry space group $C2/m$ is much larger than for the high symmetry space group $Fm\overline{3}m$. This can be explained by the fact that the bad data quality due to the big size of the sample can be compensated by the data reduction in the high symmetry space group. The bigger number of parameters in $C2/m$ does not decrease the wR(all) value significantly: A refinement with parameters fixed from the high-symmetry refinement yields only a slightly higher R value compared to the refinement in space group $C2/m$.

The wR(all) value for sample PB016-S001 is decreased when the symmetry is lowered to $C2/m$. This would be a hint for a structural distortion to the monoclinic space group. However, we will see in the following that the data can be even better explained by another model.

Another possible scenario is a statistical occupation of the Ce and Ir sites by both elements. Refinements were carried out in space groups $Fm\overline{3}m$ and $C2/m$, where both sites are occupied by Ce and Ir and the occupancies on each site add up to full occupancy. Atoms sharing a site are constrained to have the same position and ADPs. The results are shown in the lower part of Table 7.1. The refinements in space group $Fm\overline{3}m$ yield much better wR(all) values compared to the refinements in space group $C2/m$ for both samples. Again, this might be due to different data reduction, so that the refinement in the low-symmetry space group is also carried out with the structural parameters of the high-symmetry space group (wR(all) value left of the arrow "$\rightarrow$" in Table 7.1). The additional degrees of freedom in space group $C2/m$ do hardly improve the R value. Thus, it can be concluded that the crystal structure can be described with space group $Fm\overline{3}m$. The Ce site is fully occupied by Ce atoms (with an uncertainty around 1 %) and the Ir site contains statistically 12 % Ce atoms for sample AR506a and 18 % for sample PB016-S001.

The structural results of the refinements of the room temperature X-ray diffraction data are given in Tables A.17 and A.18 for sample AR506a and in Tables A.19 and A.20 for sample PB016-S001.

It is also possible that the crystal structure is distorted locally, so that the average symmetry is not broken. Tables A.18 and Table A.20 suggest that the Ba atoms shift slightly. This is why a split model is tested, where the Ba atom shifts from the Wyckoff site $8c$ $(1/4, 1/4, 1/4)$ to $32f$ (x, x, x). The occupation is lowered to 1/4, so that this model describes a disordered displacement of this atom. The split model is combined with vacancies on the Ce/Ir sites or alternatively with statistically distributed Ir atoms on the Ce site and vice versa. All such combinations are shown in Table 7.2 for the samples AR506a and PB016-S001 at room temperature. The heavy atoms in these models have isotropic ADPs and the O atoms anisotropic ones. The difference between the vacancy model and the model with mixed occupations is not great. In the case of sample AR506a, the model with vacancies yields better R values, for sample PB016-S001, it is the model with mixed occupations. The refinements of sample AR506a yield negative ADPs for some atoms, so the data seem not to be precise enough for such a refinement. For sample PB016-S001, the split model slightly decreases the R values. Although this improvement is not big, one has to keep in mind that only one degree of freedom has been

ordered occupation	AR506a		PB016-S001	
	$Fm\bar{3}m$	$C2/m$	$Fm\bar{3}m$	$C2/m$
wR(all):	5.78 %	11.53 % → 11.43 %	4.35 %	4.07 % → 3.91 %
GoF:	4.31	3.99 → 3.96	2.78	1.41 → 1.35

occupation disorder	AR506a		PB016-S001	
	$Fm\bar{3}m$	$C2/m$	$Fm\bar{3}m$	$C2/m$
wR(all):	5.43 %	11.47 % → 10.87 %	2.83 %	3.30 % → 3.20 %
GoF:	4.07	3.96 → 3.77	1.82	1.14 → 1.11
occ(Ir) on Ce site:	0.002(15)	0.013(11)	−0.006(8)	0.038(4)
occ(Ce) on Ir site:	0.120(30)	0.088(16)	0.181(11)	0.197(5)

Table 7.1: Refinements of the room temperature single-crystal X-ray diffraction data of sample PB016-S001. Top: Ordered occupation of the Ce and Ir sites. Bottom: Ce and Ir atoms share sites. Left of the arrow "→", the wR(all) value for the refinement in the low-symmetry space group with fixed structural parameters from the refinement in the high-symmetry space group is given.

added compared to the unsplit model. Thus, this increase can be seen as significant. The shift of the Ba atom to position $x = y = z = 0.2543(9)$ corresponds to a shift of 0.063(13) Å. The most reliable refinement yields 16 % Ce on the Ir site and the Ce site is fully occupied by Ce.

7.1.4 Low temperature crystal structure

In order to search for a structural phase transition, the temperature dependence of three equivalent reflections of sample PB016-S002 was investigated as shown in Figure 7.9. No hint for a structural transition is visible.

A breaking of translational symmetries at 100 K is investigated by a statistic of the reflections which are forbidden in space group $Fm\bar{3}m$. Figure 7.10 shows a histogram similar to Figure 7.5. Again, the intensities of the reflections obey a perfect Gaussian distribution. It can be concluded that no translational symmetries are broken at 100 K.

Refinements of the single-crystal X-ray diffraction data measured at 100 K were carried out in space group $Fm\bar{3}m$ and $C2/m$. All ADPs in the models are isotropic. The wR(all) values of the results are shown in the upper part of Table 7.3. The R values for the refinement in space group $C2/m$ are much worse compared to $Fm\bar{3}m$.

Also at 100 K, a statistical occupation of the Ce and Ir sites is investigated. The result

		ordered	vacancies	shared sites
Sample: AR506a	unsplit	R(obs) = 3.74 %	R(obs) = 4.22 %	R(obs) = 4.16 %
		wR(obs) = 5.40 %	wR(obs) = 4.85 %	wR(obs) = 4.96 %
		R(all) = 3.85 %	R(all) = 4.33 %	R(all) = 4.27 %
		wR(all) = 5.41 %	wR(all) = 4.86 %	wR(all) = 4.96 %
			occ(Ce) = 1.000(6)	Ir on Ce: 0.015(13)
			occ(Ir) = 0.956(7)	Ce on Ir: 0.12(2)
	split		R(obs) = 4.22 %	R(obs) = 4.16 %
			wR(obs) = 4.85 %	wR(obs) = 4.96 %
			R(all) = 4.33 %	R(all) = 4.27 %
			wR(all) = 4.85 %	wR(all) = 4.96 %
			occ(Ce) = 1.001(6)	Ir on Ce: 0.015(13)
			occ(Ir) = 0.956(7)	Ce on Ir: 0.12(2)
			x(Ba) = 0.2528(19)	x(Ba) = 0.2529(18)
		ordered	vacancies	shared sites
Sample: PB016-S001	unsplit	R(obs) = 3.07 %	R(obs) = 1.91 %	R(obs) = 1.94 %
		wR(obs) = 4.10 %	wR(obs) = 2.54 %	wR(obs) = 2.47 %
		R(all) = 3.07 %	R(all) = 1.91 %	R(all) = 1.94 %
		wR(all) = 4.10 %	wR(all) = 2.54 %	wR(all) = 2.47 %
			occ(Ce) = 1.005(3)	Ir on Ce: 0.015(7)
			occ(Ir) = 0.952(3)	Ce on Ir: 0.161(10)
	split		R(obs) = 1.90 %	R(obs) = 1.93 %
			wR(obs) = 2.52 %	wR(obs) = 2.46 %
			R(all) = 1.90 %	R(all) = 1.93 %
			wR(all) = 2.52 %	wR(all) = 2.46 %
			occ(Ce) = 1.005(3)	Ir on Ce: 0.015(7)
			occ(Ir) = 0.953(3)	Ce on Ir: 0.160(10)
			x(Ba) = 0.2544(9)	x(Ba) = 0.2543(9)

Table 7.2: Refinements of single-crystal X-ray diffraction data of the samples AR506a and PB016-S001 at room temperature using models with not fully occupied Ir/Ce sites, occupation disorder and split Ba positions.

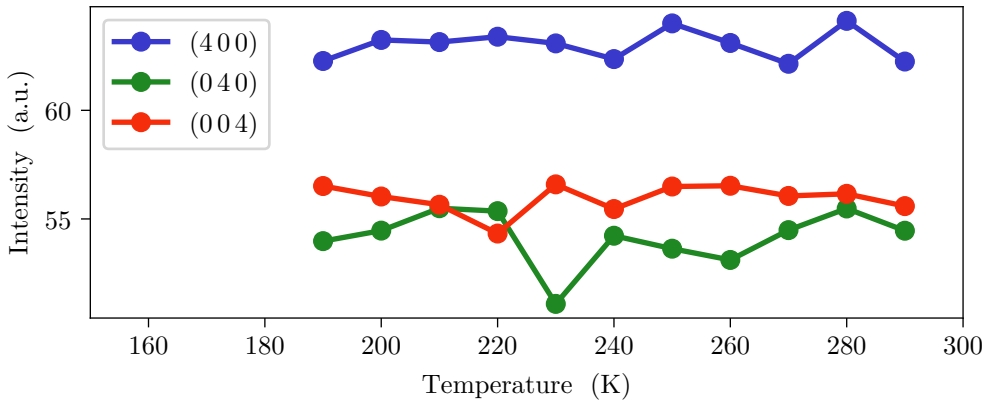

Figure 7.9: Temperature dependence of the single-crystal X-ray reflections (4 0 0), (0 4 0) and (0 0 4) (with respect to space group $Fm\bar{3}m$) of sample PB016-S002. No clear indication for a phase transition is visible.

is shown in the lower part of Table 7.3. Again, the model with space group $Fm\bar{3}m$ yields the best R values. In order to exclude the effect of different data reduction for the two space groups, a refinement in space group $C2/m$ is carried out with structural parameters fixed from the refinement in space group $Fm\bar{3}m$ (left of the arrow "$\rightarrow$"). Again, the improvement of the R values due to the larger number of degrees of freedom in space group $C2/m$ is not big. It can be concluded that the crystal structure at 100 K can also be described in space group $Fm\bar{3}m$. The Ce site is fully occupied by Ce and 16 % of the Ir sites are occupied by Ce. This is in perfect agreement with the room temperature result of sample PB016-S001 (which is the same crystal) as shown in Table 7.1. The structural data of the refinements are shown in Tables A.21 and A.22.

In order to exclude that the data can be explained by a reduction of symmetry rather than occupation disorder, refinements in all space groups shown in Figure 7.3 are carried out. All ADPs are isotropic. The R values of these refinements are shown in Table A.23. The R values left of the arrows "$\rightarrow$" in Table A.23 were obtained by carrying out a refinement in the low symmetry space group using fixed atomic positions from the refinement in $Fm\bar{3}m$. Space group $Fm\bar{3}m$ yields the best R values together with space group $Fm\bar{3}$, which yields very similar R values. In can be concluded that there is no unambiguously better suitable space group for the crystal structure at 100 K than $Fm\bar{3}m$.

In analogy to the room temperature data, for the data at 100 K, a split model was tested, where the Ba atom is located at the $32f$ (x, x, x) site. The results for combinations with vacancies resp. shared occupations of the Ce and Ir sites are shown in Table 7.4. The result is similar to the room temperature data of sample PB016-S001: The best R values are obtained by the split model with shared occupations. The $x = y = z = 0.2588(7)$ position is approximately twice as far away from the high symmetry site $8c$ $(1/4, 1/4, 1/4)$ compared to the room temperature result and corresponds to a shift of 0.129(10) Å. This model yields 14 % Ce on the Ir sites and the Ce site is fully occupied by Ce.

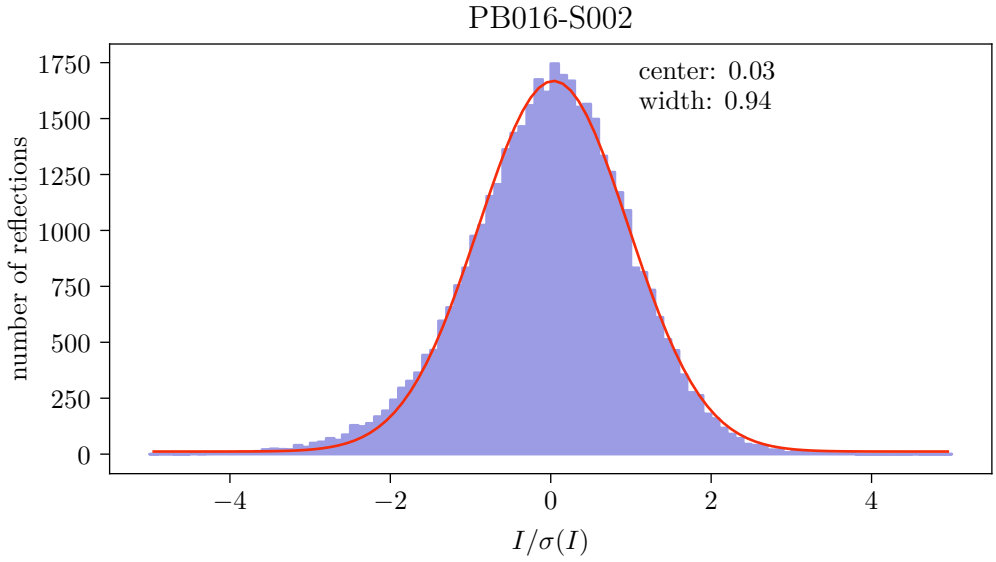

Figure 7.10: Histograms (blue) of single-crystal X-ray reflections that are forbidden by the F centering in space group $Fm\bar{3}m$. The reflections of sample PB016-S002 were collected at a temperature of 100 K. A fit of a Gaussian function (red) shows that the ratio $I/\sigma(I)$ of the intensity divided by its error is well compatible to zero intensity.

ordered occupation	$Fm\bar{3}m$	$C2/m$
wR(all):	4.02 %	5.32 % → 4.77 %

occupation disorder	$Fm\bar{3}m$	$C2/m$
wR(all):	3.26 %	5.03 % → 4.56 %
occ(Ir) on Ce site:	0.005(13)	−0.008(9)
occ(Ce) on Ir site:	0.158(17)	0.190(11)

Table 7.3: Refinements of single-crystal X-ray diffraction data of sample PB016-S002 measured at a temperature of 100 K. Top: Ordered occupation of the Ce and Ir sites. Bottom: Ce and Ir atoms share sites. Left of the arrow "→", the wR(all) value for the refinement in the low-symmetry space group with fixed structural parameters from the refinement in the high-symmetry space group is given.

Sample: PB016-S002		ordered	vacancies	shared sites
	unsplit	R(obs) = 3.61 %	R(obs) = 3.23 %	R(obs) = 3.21 %
		wR(obs) = 3.72 %	wR(obs) = 3.11 %	wR(obs) = 3.05 %
		R(all) = 7.59 %	R(all) = 7.16 %	R(all) = 7.16 %
		wR(all) = 3.94 %	wR(all) = 3.29 %	wR(all) = 3.23 %
			occ(Ce) = 1.001(5)	Ir on Ce: 0.002(13)
			occ(Ir) = 0.959(5)	Ce on Ir: 0.151(17)
	split		R(obs) = 3.15 %	R(obs) = 3.13 %
			wR(obs) = 3.00 %	wR(obs) = 2.96 %
			R(all) = 7.14 %	R(all) = 7.12 %
			wR(all) = 3.22 %	wR(all) = 3.17 %
			occ(Ce) = 1.003(5)	Ir on Ce: 0.007(13)
			occ(Ir) = 0.962(5)	Ce on Ir: 0.139(17)
			x(Ba) = 0.2590(7)	x(Ba) = 0.2588(7)

Table 7.4: Refinements of single-crystal X-ray diffraction data of the sample PB016-S002 at 100 K using models with not fully occupied Ir/Ce sites, occupation disorder and split Ba positions.

7.1.5 Conclusion

The crystal structure of Ba_2CeIrO_6 is well described as a double-perovskite structure in space group $Fm\bar{3}m$. Despite a careful search for superstructure reflections and a thorough investigation of the statistics of thousands of reflections, no breaking of translational symmetry, neither at room temperature nor at 100 K, could be detected by single-crystal X-ray diffraction. Also a breaking of other symmetries could not be unambiguously detected. The most reliable refinements were carried out with occupation disorder and a statistical shift of the Ba atom, preserving space group $Fm\bar{3}m$ in the average unit cell. The $4a$ $(0,0,0)$ position is approximately fully occupied by Ce atoms. The $4b$ $(0,0,1/2)$ position is mainly occupied by Ir atoms, but around 15 % of these sites is occupied by Ce atoms. We published similar refinements of the same samples PB016-S001 and PB016-S002 in [159]. There, the occupancies of the Ce and Ir sites were refined, allowing for vacancies. The models are similar, taking into account that Ce has a smaller electron number compared to Ir. A quantitative comparison (neglecting the different angular dependence of the form factors) shows that the vacancy concentration of about 5% for the Ir sites published in [159] corresponds to a Ce amount of about 12 % on these sites. This is slightly lower than the $14-16$ % found in this work. The R values of the refinement with site mixing are better than the R values of the refinements with vacancies, so that the $14-16$ % disorder on the Ir sites seem more reliable. The Ba atoms are shifted along the space diagonal about 0.063(13) Å at room temperature and 0.129(10) Å at 100 K without long-range order.

7.2 Ba_2PrIrO_6

7.2.1 Latest state of research

The compound Ba_2PrIrO_6 exhibits a double-perovskite structure and is isostructural to Ba_2CeIrO_6. Similar to the latter, it was claimed to exhibit a monoclinic distortion that lowers the symmetry from $Fm\bar{3}m$ to $P21/n$ [157]. However, later investigations showed that this is not the case, so the cubic symmetry is preserved [160]. In [161], the tetragonal space group $P4/mnc$ was was determined for this material. The related compound Ba_2LaIrO_6 was found to be rhombohedral with space group $R\bar{3}$ and Ba_2YIrO_6 preserves the cubic double-perovskite structure with space group $Fm\bar{3}m$ [162]. All these different structures can be described by tilting the octahedrons according to the formalism explained in [156]. In this section, single-crystal X-ray diffraction is carried out in order to clarify deviations from the cubic structure for Ba_2PrIrO_6.

7.2.2 Samples and experimental setup

Samples of the compound Ba_2PrIrO_6 were grown by P. Becker [147] using melt solution growth from $BaCl_2 \cdot 2H_2O$ flux. After the chemical reaction took place, the solution was

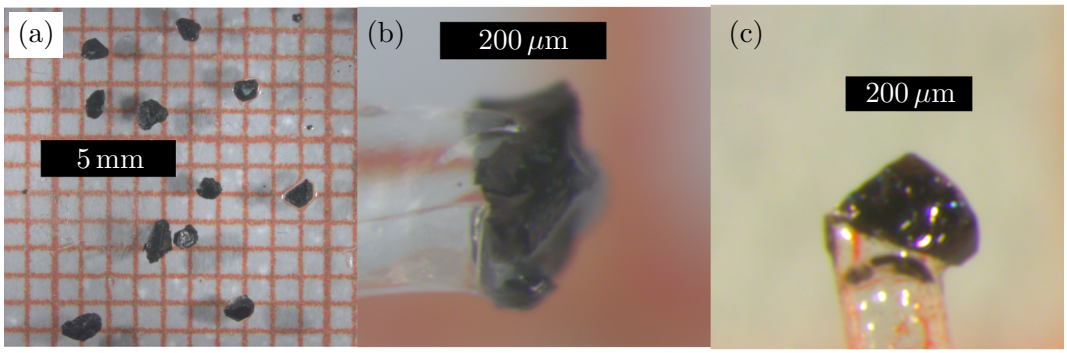

Figure 7.11: Samples of the compound Ba_2PrIrO_6 for single-crystal X-ray diffraction. (a) Batch PB019. (b) Sample PB019-S001. (c) Sample PB019-S002.

cooled down for several weeks. The crystals were dissolved out by distilled water and exhibited a size up to about 1 mm.

Crystals of the batch PB019 are shown in Figure 7.11(a). Most of the crystals are too big for single-crystal X-ray diffraction, but some of them have a proper size. Two such crystals (PB019-S001 and PB019-S002) as shown in Figure 7.11(b) and (c) were used as samples for single-crystal X-ray diffraction on the diffractometer APEX (cf. Section 3.1.1).

For sample PB019-S001, 28 712 reflections were collected at room temperature, 190 of them are unique with respect to space group $Fm\bar{3}m$. All unique reflections were observed. Absorption correction in point group $\bar{1}$ was carried out using a polytope-shaped model with 16 faces. The initial wR^2(int) value amounts to 14.56 % and the overall value to 9.95 %.

For sample PB019-S002, 29 753 reflections were collected at room temperature, 191 of them are unique with respect to space group $Fm\bar{3}m$. All unique reflections were observed. A polytope-shaped model with 21 faces was used for absorption correction in point group $\bar{1}$. The initial resp. overall wR^2(int) value amounts to 10.94 % resp. 6.76 %.

7.2.3 Breaking of translational symmetries

A possible breaking of translational symmetries was investigated by searching for superstructure reflections. Space group $Fm\bar{3}m$ exhibits the selection rule that h, k and l must be either all even or all odd. Statistics of the forbidden reflections are shown in Figure 7.12 for both samples. The figure shows histograms of the ratio $I/\sigma(I)$ of the intensity divided by its error for all forbidden reflections. The fits show that the histogram for sample PB019-S002 is very close to a Gaussian distribution of width 1 centered at 0. This means that all intensities for superstructure reflections are compatible with zero within the errors. The situation is different for sample PB019-S001: The histogram exhibits too many reflections at higher intensities so that it deviates clearly from a Gaussian distribution. These reflections might appear due to the $\lambda/2$ effect. In

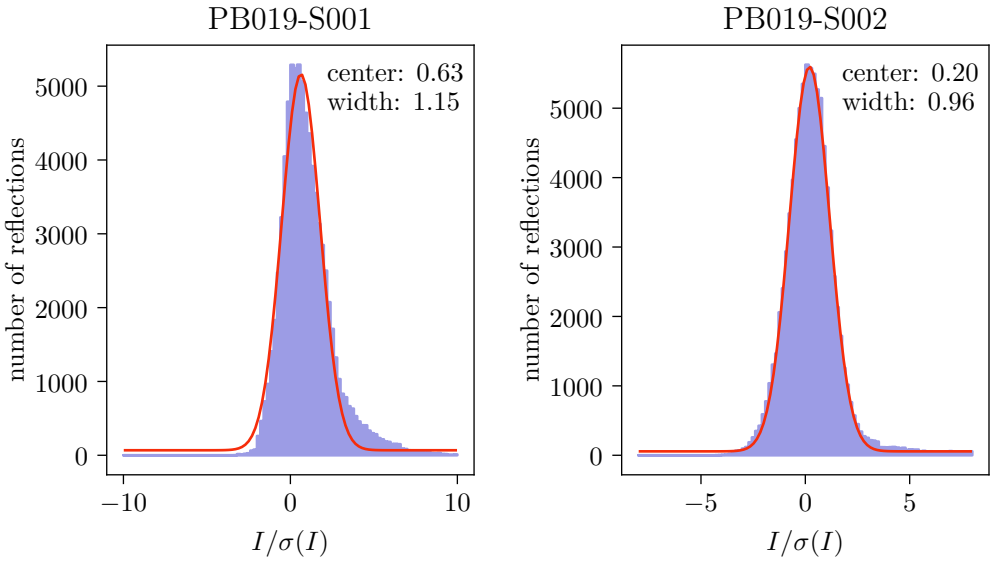

Figure 7.12: Histograms (blue) of single-crystal X-ray diffraction data at room temperature of the samples PB019-S001 (left) and PB019-S002 (right). A Gauss distribution fitted to the histogram (red) shows that for sample PB019-S002, the ratio $I/\sigma(I)$ is well compatible to zero intensity. For sample PB019-S001, the histogram clearly deviates from the Gauss distribution.

this case, a reflection recorded with indexes $(h\,k\,l)$ is actually the reflection $(2h\,2k\,2l)$ with half of the nominal wave length. In order to check this, all reflections with the same indexes were averaged and the data reduced in this way were analyzed in Figure 7.13. If for a reflection $(h\,k\,l)$ there exists also the reflection $(2h\,2k\,2l)$ in the data collection, a data point with the intensity of the reflection $(h\,k\,l)$ for the x value and the intensity of the reflection $(2h\,2k\,2l)$ for the y value is plotted. A strong correlation is visible. The slope is smaller for stronger reflections, which is expected for strong extinction. Figure 7.13 clearly shows that a forbidden reflections $(h\,k\,l)$ is strong only if the reflection $(2h\,2k\,2l)$ is strong. If the forbidden reflections were of structural origin, no such simple relation would be expected. We can conclude that the forbidden reflections arise from the $\lambda/2$ effect and thus no translational symmetries are broken.

7.2.4 Occupation disorder

A disorder of the occupations of the sites $4a$ (0, 0, 0) and $4b$ (0, 0, $\frac{1}{2}$) in space group $Fm\bar{3}m$ by the Pr and Ir atoms was investigated. For the totally ordered structure, all $4a$ (0, 0, 0) sites are occupied by Pr and all $4b$ (0, 0, $\frac{1}{2}$) sites are occupied by Ir. Refinements were carried out in space group $Fm\bar{3}m$ assuming full occupation order, yielding a wR(all) value of 4.13 % for sample PB019-S001 and 4.04 % for sample PB019-S002 as shown in Table 7.5. The model uses isotropic ADPs for all atoms. In a further step, both positions were occupied by both atoms, while the occupancy was refined. The ADPs for all atoms are isotropic and atoms sharing a site are constrained to have the

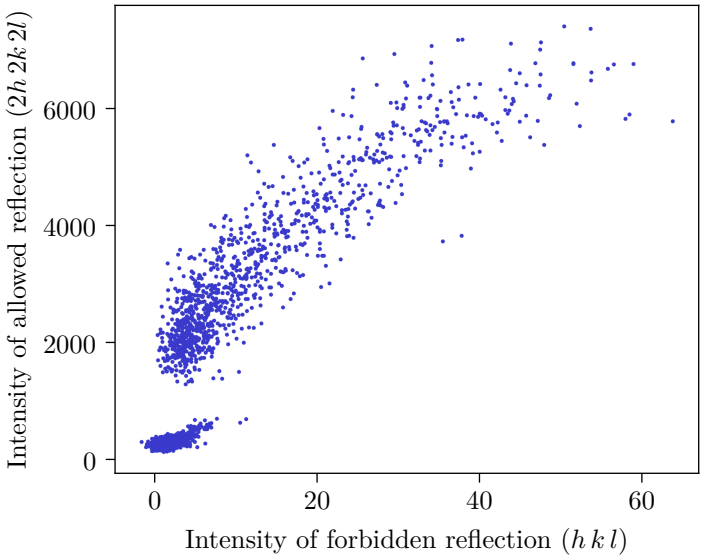

Figure 7.13: The intensities of reflections $(h\,k\,l)$ of sample PB019-S001 that are forbidden in space group $Fm\bar{3}m$ are plotted against the intensities of the allowed reflections $(2h\,2k\,2l)$. The intensities are strongly correlated, which is a hint for $\lambda/2$ effect.

same ADPs. The occupancies of atoms sharing a site are constrained to add up to full occupancy. The R values hardly change, so that the wR(all) value amounts to 4.08 % for sample PB019-S001 and 3.98 % for sample PB019-S002. The result is very close to a fully ordered structure, deviations of the occupancies amount to a few percent. The occupancy of Ir atoms on the Pr site 4*a* (0, 0, 0) is slightly negative which has no physical meaning. The occupancy of Pr atoms on the Ir site 4*b* (0, 0, $\frac{1}{2}$) is well compatible with zero. We can conclude that, assuming space group $Fm\bar{3}m$, the diffraction data can be explained best by a fully ordered model.

7.2.5 Breaking of non-translational symmetries

Perovskite structures are usually structurally unstable against a rotation of the $[MO_6]$ octahedrons where M is a metal. An example of such a structural distortion is $GdFeO_3$ [155]. It seems natural that the double-perovskite structure of Ba_2PrIrO_6 behaves similarly. Since the F centered octahedrons must tilt in the same way as the octahedron at the origin, only tilts of the form $a^{\sigma_a}b^{\sigma_b}c^{\sigma_c}$ with $\sigma_a, \sigma_b, \sigma_c \in \{0, -\}$ are possible in the formalism of [156]. Such rotations can be attributed to the four subgroups according to the Γ_4^+ mode of the parent space group $Fm\bar{3}m$ in [123]. These subgroups are listed in Table 7.6.

The simplest possibility is a rotation about only one axis, which can be written as $a^-b^0b^0$ in the Glazer notation[2] [156]. This causes a symmetry reduction to space group

[2]The distortion $a^-b^0b^0$ is equivalent to $a^0a^0c^-$. The notation depends on the setting.

sample: PB019-S001		$Fm\bar{3}m$	$C2/m$
ordered occupation	R(obs)	2.83 %	6.00 % → 5.69 %
	wR(obs)	4.13 %	6.87 % → 6.44 %
	R(all)	2.83 %	6.00 % → 5.69 %
	wR(all)	4.13 %	6.87 % → 6.44 %
	GoF	3.62	3.23 → 3.04
occupation disorder	R(obs)	2.80 %	6.00 % → 5.61 %
	wR(obs)	4.08 %	6.88 % → 6.40 %
	R(all)	2.80 %	6.00 % → 5.60 %
	wR(all)	4.08 %	6.88 % → 6.40 %
	GoF	3.60	3.23 → 3.02
	Ir on Pr site:	−0.026(12)	0.009(7)
	Pr on Ir site:	0.010(20)	−0.065(11)

sample: PB019-S002		$Fm\bar{3}m$	$C2/m$
ordered occupation	R(obs)	2.21 %	3.07 % → 2.72 %
	wR(obs)	4.04 %	4.35 % → 3.96 %
	R(all)	2.21 %	3.07 % → 2.72 %
	wR(all)	4.04 %	4.36 % → 3.96 %
	GoF	3.62	2.30 → 2.10
occupation disorder	R(obs)	2.11 %	3.03 % → 2.68 %
	wR(obs)	3.98 %	4.32 % → 3.96 %
	R(all)	2.11 %	3.03 % → 2.68 %
	wR(all)	3.98 %	4.32 % → 3.96 %
	GoF	3.60	2.29 → 2.10
	Ir on Pr site:	−0.027(12)	0.000(4)
	Pr on Ir site:	0.010(20)	−0.011(7)

Table 7.5: R values of refinements of single-crystal X-ray diffraction data of the Ba_2PrIrO_6 samples PB019-S001 and PB019-S002 measured at room temperature. The refinements were carried out with occupation order and with Pr and Ir atoms sharing the sites. Both space groups $Fm\bar{3}m$ and $C2/m$ are tested. The R values left of the arrow "→" are obtained by refinements in $C2/m$ with fixed structural parameters from the refinement in $Fm\bar{3}m$.

space group	Glazer notation	description
$I4/m$	$a^-b^0b^0$	Rotation around only one axis.
$C2/m$	$a^-a^-c^0$	Rotation around two axes about the same angle.
$R\bar{3}$	$a^-a^-a^-$	Rotation around all axes about the same angle.
$P\bar{1}$	$a^-b^-c^-$	Rotation around all axes about different angles.

Table 7.6: Subgroups according to the Γ_4^+ mode of space group $Fm\bar{3}m$ [123] and possible rotations of the [Ir/PrO_6] octahedrons described in the notation of Glazer [156].

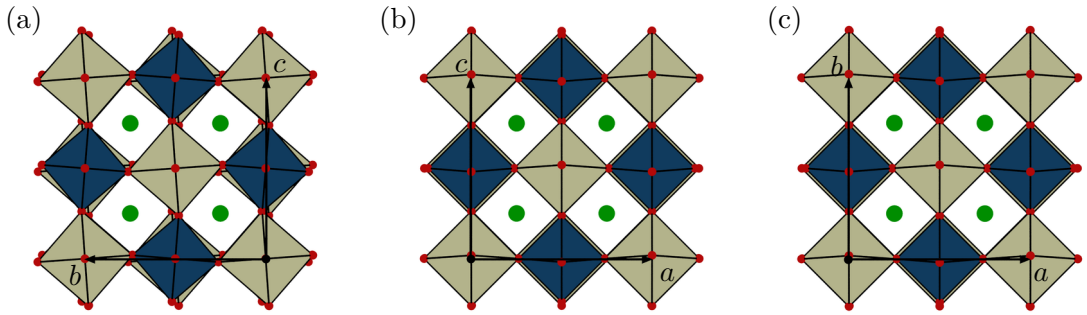

Figure 7.14: Crystal structure of the refinement shown in Table A.24. (a) View along a direction. (b) View along b direction. (c) View along c direction. The crystal structure corresponds to the distortion $a^-b^0b^0$ according to [156].

$I4/m$. Refinements were carried out in this subgroup for both samples PB019-S001 and PB019-S002. The resulting R values and the goodness of fit are listed in Table 7.7. The refinements in space group $Fm\bar{3}m$ are identical to those in Table 7.5 without occupation disorder. The position of the O atom splits in the low-symmetry space group and in the refinements the ADPs of these atoms are constrained to be identical. Values left of the arrow "$\rightarrow$" correspond to refinements in space group $I4/m$ where the structural parameters are fixed from the refinement in the parent space group. For sample PB019-S001, the refinement in subgroup $I4/m$ yields even higher R values compared to $Fm\bar{3}m$. This can be attributed to the fact that in the high-symmetry space group artifacts are better compensated by averaging during the data reduction. The bigger number of free parameters in the low-symmetry space group does not improve the quality of the refinement in this case. The situation is different for sample PB019-S002, where the low-symmetry space group clearly yields better R values and also the goodness of fit is improved. This is especially significant if one takes into account that the low-symmetry model possesses only two additional structural parameters compared to the high-symmetry model. The volumes of the six twins have nearly the same size between 15.5 % and 17.2 % of the total volume. The crystal structure in space group $I4/m$ is illustrated in Figure 7.14. The structural data are summerized in Table A.24.

Refinements in the subgroups $C2/m$, $R\bar{3}$ and $P\bar{1}$ were also carried out. They do not

sample		$Fm\bar{3}m$	$I4/m$
PB019-S001	R(obs)	2.83 %	5.96 % → 5.87 %
	wR(obs)	4.13 %	6.70 % → 6.58 %
	R(all)	2.83 %	5.96 % → 5.87 %
	wR(all)	4.13 %	6.70 % → 6.58 %
	GoF	3.62	3.15 → 3.10
PB019-S002	R(obs)	2.21 %	3.03 % → 2.76 %
	wR(obs)	4.04 %	4.06 % → 3.74 %
	R(all)	2.21 %	3.03 % → 2.76 %
	wR(all)	4.04 %	4.06 % → 3.75 %
	GoF	3.62	2.14 → 1.98

Table 7.7: R values and goodness of fit for refinements of single-crystal X-ray diffraction data of the Ba_2PrIrO_6 samples PB019-S001 and PB019-S002 in space group $Fm\bar{3}m$ and $I4/m$.

yield better R values compared to space group $I4/m$ and the refinement in space group $P\bar{1}$ does not even converge. An unambiguous evidence for a subgroup would only be possible if the crystal is not twinned. So the subgroups $C2/m$, $R\bar{3}$ and $P\bar{1}$ can not be surely ruled out because differences in the diffraction pattern would be small due to twinning.

7.2.6 Conclusion

A breaking of the F centering of space group $Fm\bar{3}m$ can be ruled out since no corresponding superstructure reflections were observed. A symmetry reduction to the translationengleiche subgroup $I4/m$ with a tilting of the octahedrons according to $a^-b^0b^0$ seems most likely.

8 Cu-intercalated Bi_2Se_3

8.1 Latest state of research

While conventional superconductivity, described by the Bardeen-Cooper-Schrieffer (BCS) theory, is characterized by a breaking of the $U(1)$ gauge symmetry, a superconductivity that breaks additional symmetries is called unconventional superconductivity [163]. One possibility for such a symmetry breaking is the loss of a rotational symmetry of the crystal structure. Two types of such symmetry breaking can be distinguished: In the first case, the phase degree of freedom breaks the symmetry. This is difficult to verify experimentally because interference effects are needed [163] In the second case, the gap-amplitude or the spin breaks the symmetry [163] This simplifies the verification, because it effects several quantities of the bulk. In this case, the superconductivity is called nematic [163]. Doping Bi_2Se_3 with Cu[8], Sr[164][165] or Nb[166] results in such a nematic superconducting phase.

The growth of Bi_2Se_3 goes back to the 1950s [167][168]. In the following decades it was investigated thoroughly because it exhibits interesting thermoelectric properties [169].

The samples in literature seem to be of differing quality with respect to the stoichiometry: In [169] the density determined via the mass is lower than it should be for stoichiometric Bi_2Se_3 (taking into account the lattice parameters). This could be explained by 6.5 % vacancies on the Se sites. In contrast to this, in [170], the stoichiometry is correct within 0.2 %.

The crystal structure of Bi_2Se_3 can be described in space group $R\bar{3}m$ as shown in Figure 8.1(a). The Bi atoms are surrounded by six Se atoms, which are arranged approximately octahedral, forming $Se - Bi - Se - Bi - Se$ quintuple layers. The binding within the quintuple layers is supposed to be covelent-ionogenic, which can be explained by atomic distances between covalent and ionic bond length [171]. In contrast to that, between the quintuple layers there is only weak van-der-Waals interaction [169]. This is why the samples are easy to cleave perpendicular to the three-fold axis.

The bulk of Bi_2Se_3 is a degenerate n-type semiconductor [170] with a band gap of 0.21 eV [172]. Some authors state a higher value like 0.35 eV [173]. Possibly, the higher value is distorted by the Burstein-Moss effect [172]. The band gap was located in reciprocal space at the Γ point [170]. The origin of the charge carriers has been a much-discussed issue. One possible explanation was given by the hypothesis that Bi atoms located at interstitial sites act as donors [172]. An alternative hypothesis states that the donors are Se vacancies [170]. The fact that the density of the samples is lower than it would

be in the stoichiometric case (see above) supports the second hypothesis. In either case, adding of Se (by Se rich melts [170] or by tempering in Se atmosphere [172]) reduces the charge carrier concentration.

Great attention was payed to doping Bi_2Se_3 with Cu. On the one hand, the Cu atoms act as acceptors and decrease the charge carrier density [174]. On the other hand, the Cu doped Bi_2Se_3 shows indications for topological superconductivity [8], as theoretically predicted in [175]. However, there is a ferocious debate about where the Cu atoms are located in the crystal lattice. One proposition is that they substitute Bi atoms [174]. Other authors rule out substitution [176]. Another – widely accepted – hypothesis is that the Cu atoms are intercalated between the quintuple layers. In [8], Cu is claimed to occupy the position $3b$ $(0, 0, 1/2)$, which they confirmed by powder X-ray diffraction. These positions are displayed in Figure 8.1(b). A greater number of possible positions is discussed in [176]: By scanning tunnel microscopy, angle dissolved photoemission spectroscopy and ab initio density functional theory, they conclude that the most probable sites for the Cu atoms are two interstitial sites whithin the quintuple layers and three intercalated sites between the quintuple layers. To the knowledge of the author, reference [176] does not explicitly state the coordinates of these atoms. However, from the caption of Fig. 4 in [176], it is possible to reconstruct these coordinates. Using the structural parameters from [171], one gets the following positions: The interstitial atom Cu(i) is located at the position $6c$ $(1/3, 2/3, 0.36127(34))$, and the other interstitial position of atom Cu(ii) is $6c$ $(0, 0, 0.34032(33))$. The coordinates of the three intercalated atoms are: $6c$ $(0, 0, 0.1321(15))$ for Cu(iii), $6c$ $(2/3, 1/3, 0.2047(15))$ for Cu(iv) and $6c$ $(1/3, 2/3, 0.1733(15))$ for Cu(v). It is worth mentioning that the related compound $Tl_xBi_2Te_3$ shows a slightly smaller c lattice parameter compared to the undoped material, which is not compatible with a model where the dopant occupies a position inside the van-der-Waals gap.

While Bi_2Se_3 without Cu doping exhibits space group $R\bar{3}m$, it was observed by Knight shift measurements at Cu doped samples, that the threefold axis is broken [177]. These Knight shift measurements also confirm spin triplet pairing: Singlet pairing would not explain the breaking of the three-fold axis even if SOC is considered, because this would have a three-fold symmetry [177].

Closely related to Cu doping of Bi_2Se_3 is doping with Sr or Nb. For these related compounds, a breaking of the three fold axis is visible by measurements of the reversible magnetization [178] (Sr doping) and superconducting hysteresis loops [179](Nb doping). The compounds with Cu, Sr or Nb doping differ in some properties: The Cu-doped samples are sensitive to air [8], while the other two compounds are not. $Cu_xBi_2Se_3$ has a higher charge density concentration than $Sr_xBi_2Se_3$ and $Nb_xBi_2Se_3$ has a more complicated Fermi surface that the other two compounds. For the case of Sr doped Bi_2Se_3, there are contradicting opinions about whether this breaking of symmetry has a structural origin: Some authors report a structural distortion by X-ray diffraction [180], others could not detect any deviation from the $R\bar{3}m$ symmetry [178].

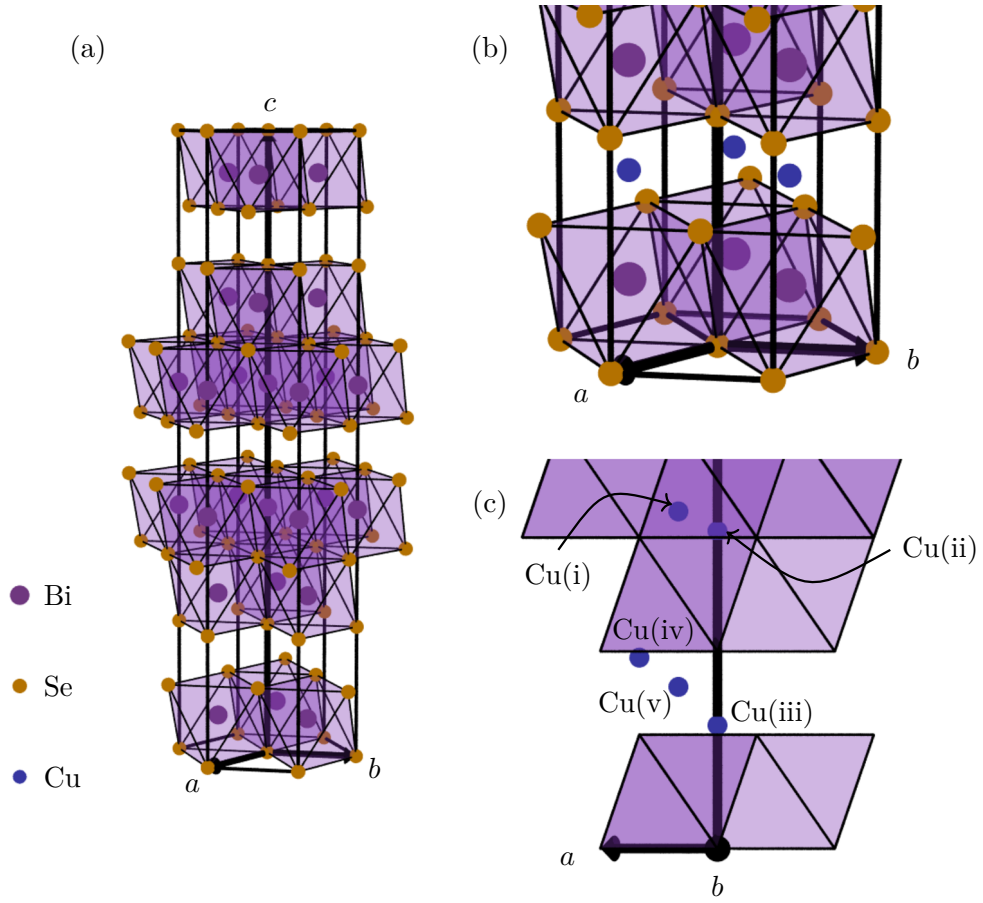

Figure 8.1: (a) Crystal structure of Bi_2Se_3. (b) Expected crystal structure of Cu-doped $Cu_xBi_2Se_3$ with Cu atoms intercalated between the quintuple layers according to [8]. Dependent on x, the Cu sites are expected to be not fully occupied. (c) Possible positions for the Cu atoms Cu(i) to Cu(v) according to [176].

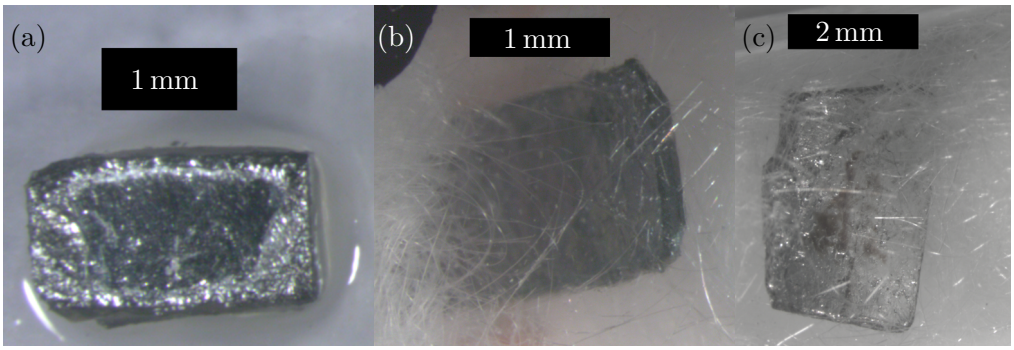

Figure 8.2: $Cu_xBi_2Se_3$ samples for neutron diffraction. (a) ZW004-S001, (b) ZW009-S001, (c) MB003-S001. Since the samples are sensitive to air, the photos of the last two samples were taken with the samples sealed in glass tubes and mechanically protected by quartz wool.

8.2 Sample characterization end experimental setup

The samples used in this work were grown by Z. Wang [181] and M. Bagchi [182] in Institute of Physics II (University of Cologne). Bi_2Se_3 single crystals were grown from a stoichiometric melt. Pieces of the single crystals were electrochemically doped by Cu using a saturated solution of CuI in CH_3CN. Typical stoichiometries for $Cu_xBi_2Se_3$ lie in the range $0.12 \leq x \leq 0.6$, and shielding fractions up to 50 % can be achieved by this technique. Details of the growth process can be found in [183].

The samples used for neutron diffraction experiments are shown in Figure 8.2. The Cu doped samples are sensitive to air, so for storage and transport they need to be sealed in glass tubes. They were cleaved to exhibit a plate-like shape and the direction of smallest extension is the c direction of the hexagonal cell. Sample ZW004-S001 exhibits a Cu amount of $x = 0.3$, for sample ZW009-S001 it is $x = 0.33$ and for sample MB003-S001 it is $x = 0.31$.

8.2.1 Single crystal neutron diffraction

Single crystal neutron diffraction was carried out with the $Cu_xBi_2Se_3$ crystals ZW004-S001, ZW009-S001 and MB003-S001 on the single-crystal neutron diffractometer D9 3.2.4. During the beam time for sample ZW004-S001, a wavelength of 0.8386 Å was used. For the other two beam times, the wavelength was set to 0.8377 Å.

The sample ZW004-S001 was measured at a temperature of 300 K, with a pinhole of 5 mm diameter. Later it turned out that the beam nose was slightly misaligned. After proper alignment, data sets were collected at temperatures of 1.9 K and 4.4 K with a pinhole of 6 mm. The data collection at 300 K is used in the evaluation, however the results are less reliable. The collections for the structural refinements cover 592 reflections (182 resp. 577 unique, 157 resp. 439 of which are observed with respect to space group $R\bar{3}m$ resp. $C2/m$) at 1.9 K, 651 reflections (203 resp. 636 unique, 178 resp. 482 of which are observed with respect to space group $R\bar{3}m$ resp. $C2/m$) at 4.4 K and 530 reflections

(157 resp. 515 unique, 124 resp. 358 of which are observed with respect to space group $R\bar{3}m$ resp. $C2/m$) at 300 K. At 1.9 K and 4.4 K, most of the reflections were collected with exposure times between 3 s and 6 s. At 300 K, most of the reflections were collected with exposure times between 5 s and 8 s. At 300 K and 1.9 K, 152 resp. 167 reflections were collected which are forbidden by the selection rules in space group $R\bar{3}m$.

Sample ZW009-S001 was measured with pinholes of 8 mm and 10 mm diameter, however only temperature scans are used in this evaluation. The beam time was only short due to an unpredictable shut down of the reactor.

In order to obtain the optimal beam size, for sample MB003-S001, several equivalent reflections and Renninger scans were carried out. A pinhole of 7 mm diameter was chosen. The collections for the structural refinements cover 860 reflections (179 resp. 745 unique, 167 resp. 632 of which are observed in space group $R\bar{3}m$ resp. $C2/m$) at 2 K and 640 reflections (139 resp. 557 unique, 129 resp. 459 of which are observed in space group $R\bar{3}m$ resp. $C2/m$) at 300 K. At 2 K, most of the reflections were collected with exposure times between 2 s and 7 s per data point. At 300 K, most of the reflections were collected with exposure times between 3 s and 5 s.

During the cooling and heating processes, we collected temperature scans of certain reflections for all three samples in order to search for a phase transition.

Before the structural refinements were carried out, the intensity data were absorption corrected using the program DATAP. For sample LB004-S001, the orientation was exactly known, and a box geometry with a length of 2.82 mm, a width of 1.55 mm and a thickness of 0.73 mm was assumed, which roughly corresponds to the real shape of the sample. The length and width was determined optically, and the thickness was calculated via the mass of 25.226 mg assuming a density of 7.90 g/cm^3 (where the Cu doping with $x = 0.3$ is taken into account). Sample MB003-S001 exhibits a more irregular, but plate-like shape and the area was determined optically to amount to 8.536 mm^2. Via the mass of 46.22 mg and the density, the thickness of 0.69 mm was determined. For the sake of simplicity and because the exact orientation is not known, the model used for absorption correction is a regular hexagonal prism, where the thickness and the area correspond to the sample geometry. For both samples, the c^* direction of the hexagonal cell is orthogonal to the area of the main extension of the plate-like shape.

Figure 8.3 shows ω scans of one reflection for each of the three samples. The reflections are sufficiently sharp. However, sample ZW009-S001 shows shoulders in ω direction and a tail in the detector area, which is an indication for bad mosaicity.

8.2.2 Polarized single crystal neutron diffraction

Since magnetic moments of the spin triplet pairs are not visible by measurements of the magnetization due to screening in the superconducting phase, a polarized neutron diffraction experiment was carried out on D3 (cf. Section 3.2.5). The $Cu_xBi_2Se_3$ sample ZW002-S001 with a volume of 5.5 mm^3 was placed in a cryostat and measured at

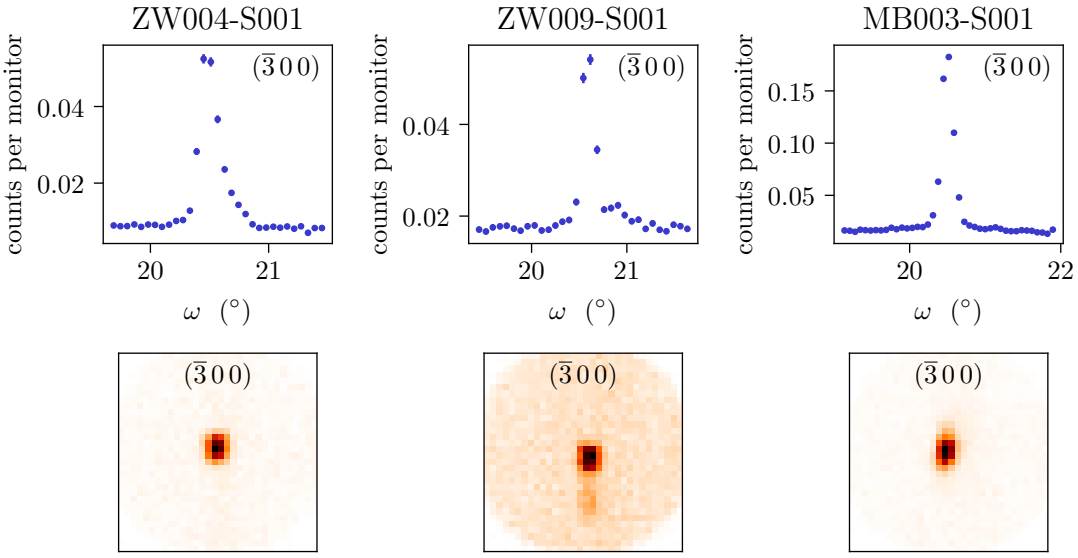

Figure 8.3: Top: ω scans, integrated over the detector area, for the reflections $(\bar{3}\,0\,0)$ of samples ZW004-S001, ZW009-S001 and MB003-S001. Bottom: The same ω scans, integrated over ω.

temperatures between 0.05 K and 2 K in magnetic fields between 2 T and 8 T. The magnetic field was applied along the b direction so that the directions a^* and c^* were in the scattering plane. The $(1\,0\,10)$ reflection and equivalent reflections were chosen for the investigation, because they showed a good intensity and peak shape. Polarized scans were carried out with the polarization parallel and antiparallel with respect to the magnetic field, wherein the efficiency of the polarization is known to be 94 %. Several scans were collected at different temperature-field pairs, respectively. The total counting time at each temperature and field adds up to several 1000 s.

8.2.3 Single-crystal X-ray diffraction

For the determination of the lattice parameter c, a powder diffractometer was used to carry out a $(0\,0\,l)$ scan. The measurement was done by M. Bagchi [182] and the evaluation was carried out in this work.

The preparation of $Cu_xBi_2Se_3$ single-crystals for X-ray diffraction was not successful: The material is too soft for cutting small pieces in the order of 100 μm from the crystal. The samples prepared in this way did not produce Bragg reflections which were possible to integrate. In some cases, however, single crystals of the proper size were obtained, which show completely different cell parameters than expected for Bi_2Se_3. Two of such samples, namely ZW006-S003 and ZW006-S005 were successfully prepared, as shown in Figure 8.4. Single-crystal X-ray diffraction was carried out on a Bruker AXS Kappa APEX II four-circle X-ray diffractometer with MoK_α radiation. For sample ZW003 resp. ZW005, 87 414 resp. 58 609 reflection were collected, 4 290 resp. 4 217 of which

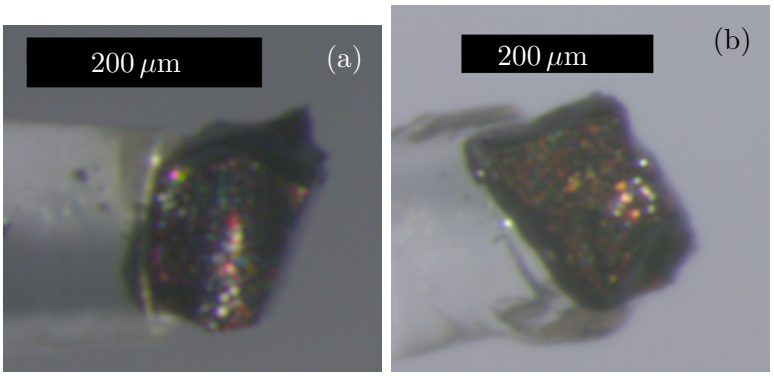

Figure 8.4: Impurity phase samples (a) ZW006-S003 and (b) ZW006-S005 for single-crystal X-ray diffraction.

were unique with respect to space group $C2/m$. 2 532 resp. 2 198 of the unique reflections were observed. The absorption correction for the measurement of sample ZW006-S003 was done using the spherical absorption correction of the Bruker software assuming point group $2/m$. The wR(int) value for sample ZW006-S003 decreases from 14.98 % to 10.55 % by the absorption correction. For ZW006-S005, a polytope-shaped model consisting of 18 faces was used for the absorption correction, and point group $\overline{1}$ was assumed. In this case, the wR(int) value decreases from 14.80 % to 10.12 %. For both measurements, the internal R values are not good, which can be explained by a bad sample quality. Since the absorption correction for sample ZW006-S005 was done in point group $\overline{1}$, the bad internal R values cannot be caused by the assumption of a wrong symmetry.

8.3 Results and discussion

8.3.1 Vacancies

As stated in section 8.1, Se vacancies are supposed to play an important role for transport properties in the case of pure Bi_2Se_3. Therefore, refinements were carried out in space group $R\overline{3}m$, where the occupations of the Se sites are refined. For sample ZW004-S001, the occupation of the Se2 site is 1.011(12) (0.995(16), 1.002(16)) and the occupation of the Se3 site is 0.999(11) (0.998(14), 0.985(16)) at a temperature of 1.9 K (4.4 K, 300 K), respectively. For sample MB003-S001, the occupation of the Se2 site is 1.008(10) (1.003(15)) and the occupation of the Se3 site is 0.989(10) (1.001(14)) at 2 K (300 K), respectively. These values are consistent with full occupation. Thus, no Se vacancies could be detected by neutron diffraction.

These refinements not only exclude Se vacancies, but also Bi vacancies: If there would be Bi vacancies, the Se occupations would be significantly greater than one.

8.3.2 The Cu doping

It seems natural that a Cu intercalation in the van-der-Waals gap shifts apart the quintuple layers and thus increases the lattice constant c [8]. For pristine Bi_2Se_3, the lattice constants $c = 28.636(20)$ Å [171] and $28.666(1)$ Å [8] were reported. Cu doping is said to increase the lattice constant to $28.736(1)$ Å [8]. LeBail refinements of the $(0\,0\,l)$ scans yield a lattice constant $c = 28.5990(8)$ Å for the undoped Bi_2Se_3 and $28.683(2)$ Å for $Cu_{0.3}Bi_2Se_3$. The R values are 1.24 % and 1.54 %, respectively. Thus, the increase in the lattice constant c could be verified.

The results for the vacancies in section 8.3.1 can be used to estimate a substitution of Bi for Cu. Cu has a smaller scattering length than Bi: $b_{\mathrm{Cu}} = 7.718$ fm and $b_{\mathrm{Bi}} = 8.532$ fm [57]. The refinements in Section 8.3.1 investigated Se vacancies. Since the scaling factor of the refinements is free, such a Se occupancy occ(Se) can also be interpreted as a Bi occupancy $\mathrm{occ}'(\mathrm{Bi}) = 1/\mathrm{occ}(\mathrm{Se})$ with full Se occupancy $\mathrm{occ}'(\mathrm{Se}) = 1$. Since Cu has a smaller neutron scattering length than Bi, these Bi vacancies can furthermore be interpreted as Cu atoms substituting Bi. The model with $\mathrm{occ}'(\mathrm{Bi}) = 1 - x$ and no Cu substitution has the same structure factor (neglecting different ADPs) as a model with $\mathrm{occ}'(\mathrm{Bi}) = 1 - y$ and $\mathrm{occ}'(\mathrm{Cu}) = y$ at the same site, if the condition

$$(1 - x)\, b_{\mathrm{Bi}} = y\, b_{\mathrm{Cu}} + (1 - y)\, b_{\mathrm{Bi}}$$

holds. This is equivalent to

$$y = x\, \frac{b_{\mathrm{Bi}}}{b_{\mathrm{Bi}} - b_{\mathrm{Cu}}} \quad .$$

Since there are two different symmetrically not equivalent Se sites, both of them can be used in order to calculate the Cu substitution y on the Bi site. Both possibilities are shown in Table 8.1 for all five measurements on the two samples at different temperatures. Note that Se occupancies smaller than 1 yield physically senseless $y < 0$. All values in Table 8.1 are compatible with 0 within the error, which is however in the order of 10 %. A Cu substitution of Se is chemically not realistic and the scattering lengths of these nuclei are very similar, so that the calculation would yield huge errors.

As stated in Section 8.1, in [8], the intercalated Cu position at $3b$ $(0, 0, 1/2)$ is proposed and [176] proposes Cu(i) to Cu(v) at different positions. Further possibilities can be found in [184] and [185]. In this section, all positions proposed in [8] and [176] are tested via structural refinements.

For testing the Cu position at $3b$ $(0, 0, 1/2)$, refinements of neutron diffraction data of two samples at different temperatures in space group $R\bar{3}m$ were carried out. In one case, only the Bi and Se atoms were used for the structural model. In the other case, a Cu atom was included at the position $3b$ $(0, 0, 1/2)$ with stoichiometric occupancy.

	calculated from	occ(Se2)	occ(Se3)
sample	temperature	Cu on Bi	Cu on Bi
ZW004-S001	1.9 K	0.11(12)	-0.01(12)
ZW004-S001	4.4 K	-0.05(17)	-0.02(15)
ZW004-S001	300 K	0.02(17)	-0.16(17)
MB003-S001	2 K	0.08(10)	-0.12(11)
MB003-S001	300 K	0.03(16)	0.01(15)

Table 8.1: Cu substition of Bi resp. Se sites. The substitution is calculated from refinements with refined occupancies of the Se2 and Se3 sites. The upper row shows the parameter which is used for the calculation.

The refinements were carried out with anisotropic ADPs for all atoms except Cu. For the Cu atom, the displacement parameter was fixed to isotropic $U = 0.005\,\text{Å}^2$ for the high temperature 300 K resp. $U = 0.0025\,\text{Å}^2$ for the low temperatures 1.9 K, 2 K and 4.4 K. The results are shown in Table 8.2: The R values are much better for the model without Cu. In further refinements, the Cu occupancy was refined, yielding very small occupation for Cu in all cases. In some cases, the occupancy is even negative.

Next, the positions for Cu(i) to Cu(v) are tested. Since we could rule out obverse/reverse twinning (see below), no twinning fractions were refined. The Bi and Se atom were refined with anisotropic ADPs. The ADPs of the Cu atoms were kept at the fixed value, because they correlate strongly with the occupancy ($U = 0.005\,\text{Å}^2$ for the high temperature 300 K and $U = 0.0025\,\text{Å}^2$ for the low temperatures 1.9 K, 2 K and 4.4 K). The positions of the Cu atoms could not be refined, since these atoms are not there. For each of the two samples ZW004-S001 and MB003-S001 at all three resp. two temperatures and for each Cu position separately, a refinement was carried out. Refining the occupations of all Cu sites with one refinement is not sensible, because some of the positions are very close so that canceling positive and negative occupancies are likely to turn out. The results of the refinements are shown in Table 8.3. Most occupancies are consistent with zero within one standard deviation and all of them within two standard deviations. Thus, there is no significant occupation on either position of Cu(i) to Cu(v).

Fourier maps were calculated for the refined models in space group $R\bar{3}m$ for sample ZW004-S001 at 1.9 K (Figure A.1) and for sample MB003-S001 at 2 K (Figure A.2), using the software JANA2006 [69]. The calculations are based on the structural parameters of the refinement and the measured intensity data. The maps show the nuclear density within the unit cell. If an atom is missing, at this position there should be an additional peak visible. All atoms of Bi_2Se_3 are clearly visible. There are no other features in the Fourier maps. Shallow peaks like the one at $(1/3, 2/3, 0.025)$ are just artifacts from the Fourier transformation, as can be seen in the vertical slices in Figure A.3. Thus, positions for Cu atoms different from the ones tested above can also be excluded.

		without Cu		with Cu		occ(Cu) refined	
sample: ZW004-S001	1.9 K	R(obs) =	3.07 %	R(obs) =	12.99 %	R(obs) =	3.07 %
		wR(obs) =	3.55 %	wR(obs) =	14.48 %	wR(obs) =	3.54 %
		R(all) =	3.71 %	R(all) =	14.09 %	R(all) =	3.69 %
		wR(all) =	3.71 %	wR(all) =	14.61 %	wR(all) =	3.70 %
						occ(Cu) =	−0.006(5)
	4.4 K	R(obs) =	5.05 %	R(obs) =	14.51 %	R(obs) =	4.98 %
		wR(obs) =	5.25 %	wR(obs) =	16.25 %	wR(obs) =	5.24 %
		R(all) =	5.71 %	R(all) =	15.36 %	R(all) =	5.74 %
		wR(all) =	5.36 %	wR(all) =	16.34 %	wR(all) =	5.38 %
						occ(Cu) =	0.000(7)
	300 K	R(obs) =	3.15 %	R(obs) =	15.32 %	R(obs) =	3.15 %
		wR(obs) =	4.83 %	wR(obs) =	17.29 %	wR(obs) =	4.83 %
		R(all) =	4.69 %	R(all) =	16.92 %	R(all) =	4.69 %
		wR(all) =	5.04 %	wR(all) =	17.40 %	wR(all) =	5.04 %
						occ(Cu) =	0.000(7)

		without Cu		with Cu		occ(Cu) refined	
sample: MB003-S001	2 K	R(obs) =	3.12 %	R(obs) =	14.49 %	R(obs) =	3.10 %
		wR(obs) =	3.97 %	wR(obs) =	18.97 %	wR(obs) =	3.96 %
		R(all) =	3.24 %	R(all) =	14.78 %	R(all) =	3.21 %
		wR(all) =	3.99 %	wR(all) =	19.02 %	wR(all) =	3.97 %
						occ(Cu) =	−0.006(5)
	300 K	R(obs) =	4.56 %	R(obs) =	14.87 %	R(obs) =	4.54 %
		wR(obs) =	5.08 %	wR(obs) =	17.31 %	wR(obs) =	5.07 %
		R(all) =	4.83 %	R(all) =	15.54 %	R(all) =	4.79 %
		wR(all) =	5.11 %	wR(all) =	17.35 %	wR(all) =	5.10 %
						occ(Cu) =	−0.005(7)

Table 8.2: Refinements of neutron diffraction data of two samples were carried out using a model without Cu, including Cu at the position $3b$ $(0, 0, 1/2)$ with full occupancy, and refining the occupancy of the Cu site. All models exhibit space group $R\bar{3}m$.

		Cu(i)	Cu(ii)	Cu(iii)	Cu(iv)	Cu(v)
ZW004-S001	1.9 K	0.4(4)	0.1(4)	0.6(4)	0.4(4)	−0.37(33)
	4.4 K	0.3(5)	0.5(5)	0.2(5)	−0.2(5)	−0.1(4)
	300 K	0.4(5)	0.3(5)	0.4(5)	0.2(5)	0.0(4)
MB003-S001	2 K	0.7(4)	0.71(33)	0.58(34)	0.44(34)	−0.43(29)
	300 K	0.6(5)	0.5(5)	0.8(5)	0.6(5)	−0.2(4)

Table 8.3: Occupancies of the possible Cu positions (i) to (v) from refinements in space group $R\bar{3}m$ in percent. There is no significant deviation from zero. Each value was determined by a separate refinement without the other Cu positions.

The refinements suggest that at the expected positions, and also on further positions, there is no Cu intercalated. This is quite surprising because Hor et al. have confirmed the crystal structure with intercalated Cu atoms by X-ray powder diffraction [8].

Rhombohedral crystals in general can exhibit two twins that differ in the way that one of the twin exhibits the obverse and the other one the reverse setting. In the refinements, these twinning fractions were refined. The refinements in space group $R\bar{3}m$ without Cu for sample ZW004-S001 yield fractions of $-0.99(1.23)$ % at 1.9 K, $-0.02(1.65)$ % at 4.4 K and $0.46(23)$ % at 300 K for the reverse setting. The corresponding refinements for sample MB003-S001 yield fractions $0.39(1.30)$ % at 2 K and $-0.82(1.99)$ % at 300 K for the reverse setting. These values are consistent with zero within the errors. Thus, the samples do not exhibit obverse/reverse twinning.

8.3.3 Structural phase transition

One could suspect that the breaking of symmetry observed by Knight shift measurements as reported in [177] is a consequence of a structural phase transition that takes place at temperatures above the super-conducting phase transition. In general, the intensity could change due to a change of the atomic positions, the peak could be broadened due to mosaicity or shift due to a change of the metric. In the next two paragraphs, temperature dependent ω scans are evaluated with respect to the overall intensity and with respect to the peak shape and position.

8.3.3.1 Intensity

The intensities of three different reflections and their equivalents in space group $R\bar{3}m$ were determined in the following way: First, a circular region of the 2D detector area around the reflection was integrated for each ω position. Then, a simplified Lehmann-Larsen algorithm [186] was applied where the peak region extends over 21 scan steps

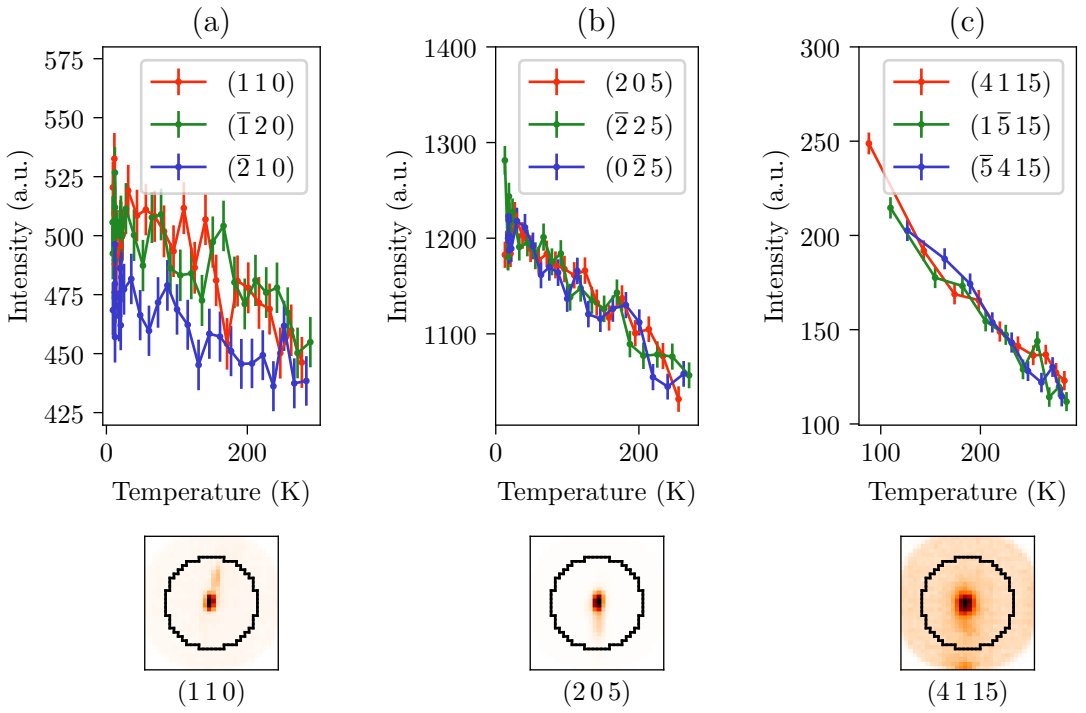

Figure 8.5: Top: Intensities of temperature dependent ω scans of (a) the (1 1 0) reflection of sample ZW009-S001, (b) the (2 0 5) reflection of sample MB003-S001, (c) the (4 1 15) reflection of sample MB003-S001 (and equivalent reflections, respectively). Bottom: Region of the 2D detector used for the integration.

around the maximum[1]. Figure 8.5 shows the integrated intensities for several reflections. In the lower part, the region of interest used for the integration is shown. Also tails of the reflections are included in the integration.

The peak intensities increase when the temperature is decreased. This can be explained by smaller atomic displacement parameters for lower temperatures. The intensities of equivalent reflections coincide within a few standard deviations. No clear indication for a structural phase transition is visible.

8.3.3.2 Shape and position

The temperature dependence of the shape and the position of the reflections is investigated by calculating correlation coefficients between the reflection images at temperatures T_1 and T_2 by the formula [187]

[1]The proper Lehman-Larsen algorithm optimizes the width of this region.

$$r(T_1, T_2) = \frac{\langle I_q(T_1) I_q(T_2)\rangle_q - \langle I_q(T_1)\rangle_q \langle I_q(T_2)\rangle_q}{\sqrt{(\langle I_q(T_1)^2\rangle_q - \langle I_q(T_1)\rangle_q^2)(\langle I_q(T_2)^2\rangle_q - \langle I_q(T_2)\rangle_q^2)}} \quad , \tag{8.1}$$

where $I_q(T)$ is the number of counts at temperature T at the point q in reciprocal space. In our experiment, q is specified by the pixel of the detector and its ω position of the ω scan. $\langle\cdot\rangle_q$ denotes the mean with respect to all pixels and ω positions.

Equation 8.1 has the property that it does not depend on the total intensity of the signal, but only on the distribution along the ω scan and the pixels. If the peak shape or position differs at two temperatures T_1 and T_2, the quantity $r(T_1, T_2)$ is small. A difference in total intensity does not effect $r(T_1, T_2)$.

It can be seen in Figure 8.6 that there is a strong tendency that the detector images are similar for similar temperatures and differ more strongly if the temperature difference is greater. This is the expected behavior that is caused by several artifacts like the temperature dependence of the length of the sample holder that can shift the position of the reflection. If the detector images changed suddenly, there would be two temperature intervals, where correlation coefficients are high for temperatures that lie in the same interval and lower correlation coefficients for temperatures in different intervals. The reflection (2 0 5) shows such a behavior slightly below 200 K, but it is very small. This effect is also visible for the $(\overline{1}\,2\,0)$ reflection, however there is also some feature above 200 K. There are further candidates for such sudden changes, but they are all very small and appear at different temperatures. It can be concluded, that also the shape and position of the reflections show no phase transition.

8.3.4 Breaking of symmetry

As mentioned in paragraph 8.1, there is a hint for a symmetry reduction regarding a breaking of the three-fold axis induced by the Cu doping. In this section, we exclude any breaking of translation symmetry and then search for subgroups which break the three-fold axis. Based on this, structural refinements are carried out.

8.3.4.1 Translation symmetry

A breaking of translation symmetry would give rise to nuclear reflections which are forbidden in space group $R\overline{3}m$. These forbidden reflections do not obey the selection rule $-h + k + l = 3n$ [188]. For excluding any breaking of translation symmetry, 152 forbidden reflections were collected at 300 K and 167 at 1.9 K by the setup described in 8.2.1. The 2D detector data were integrated using the program racer [99]. If all these reflections are absent, it is expected that approximately 68 % of them lie within one standard deviation away from 0. More specific: The quotient $I/\sigma(I)$ of the intensity divided by its error should be a Gauss distribution with mean 0 and standard deviation 1.

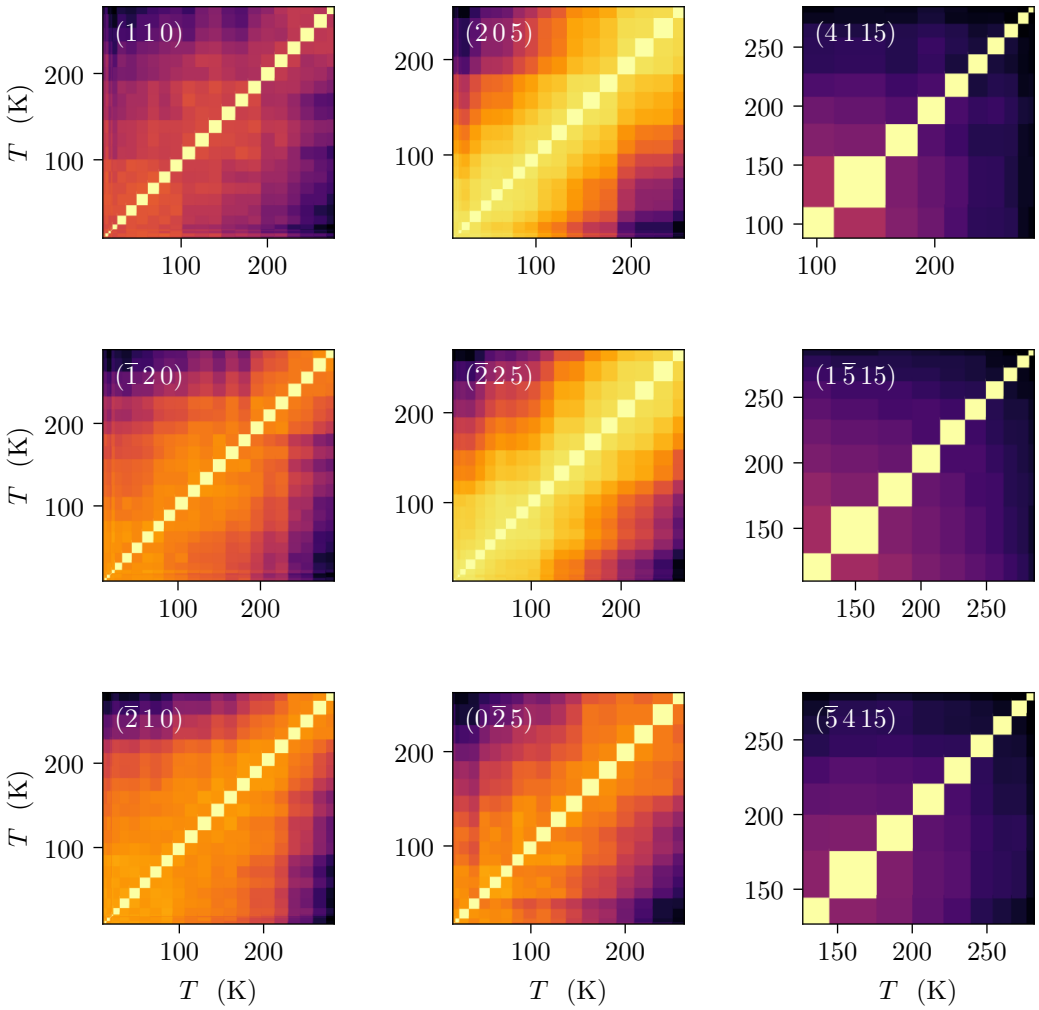

Figure 8.6: Correlations between the detector images at different temperatures of the reflections (1 1 0) and equivalents of sample ZW009-S001, (2 0 5) and equivalents of sample MB003-S001 and (4 1 15) and equivalents of sample MB003-S001. The axes denote the temperature in K, the correlation coefficient is color-coded.

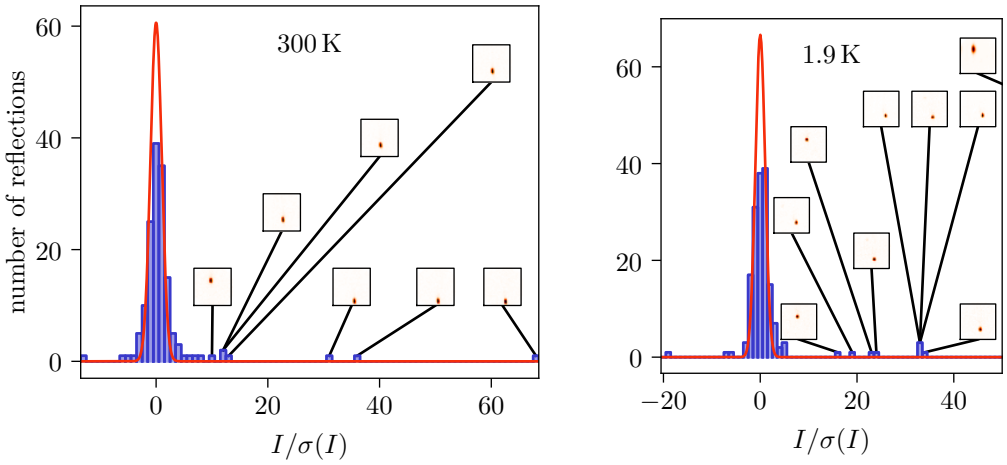

Figure 8.7: The intensity of forbidden reflections divided by its error is plotted as a histogram for the $Cu_xBi_2Se_3$ sample ZW004-S001. The red line shows a Gaussian function with $\mu = 0$ and $\sigma = 1$. The insets show the 2D detector images for reflections with $I/\sigma(I) > 10$. In these cases, neighbored strong reflections are visible. The statistic shows no hint for the appearance of reflections which are forbidden in space group $R\bar{3}m$.

Figure 8.7 shows histograms of the quantity $I/\sigma(I)$ for forbidden reflections collected at the temperatures 300 K and 1.9 K. The expected Gaussian distribution is plotted as a red line. The deviation from the expected distribution is not large. For all reflections with $I/\sigma(I) > 10$, the 2D detector images are plotted. It is conspicuous that all these 2D detector images show a neighbored reflection (the position of the investigated forbidden reflection would be in the center of the 2D detector). Thus, all deviations from a Gaussian distribution can be attributed to those artifacts and for both temperatures a breaking of the translation symmetry can be excluded.

8.3.4.2 Threefold axis

Since a breaking of translation symmetry can be excluded, the symmetry reduction can be assumed to follow a Γ mode. Since Knight shift measurements revealed a breaking of the three-fold axis [177], only the modes Γ_3^+ and Γ_3^- are possible. The investigations in the present work focus on the monoclinic space groups $C2/m$ according to Γ_3^+ and Cm according to Γ_3^-. The change of basis between the hexagonal and the monoclinic cell is not trivial and shown in Figure 8.8.

A first investigation of a breaking of the three-fold axis can be done by reducing the collected data with respect to the space groups $R\bar{3}m$ and $C2/m$, respectively. In the higher symmetry, more reflections are equivalent, and so the internal R value is expected to be higher if the three-fold axis is broken. The internal R values for data reductions

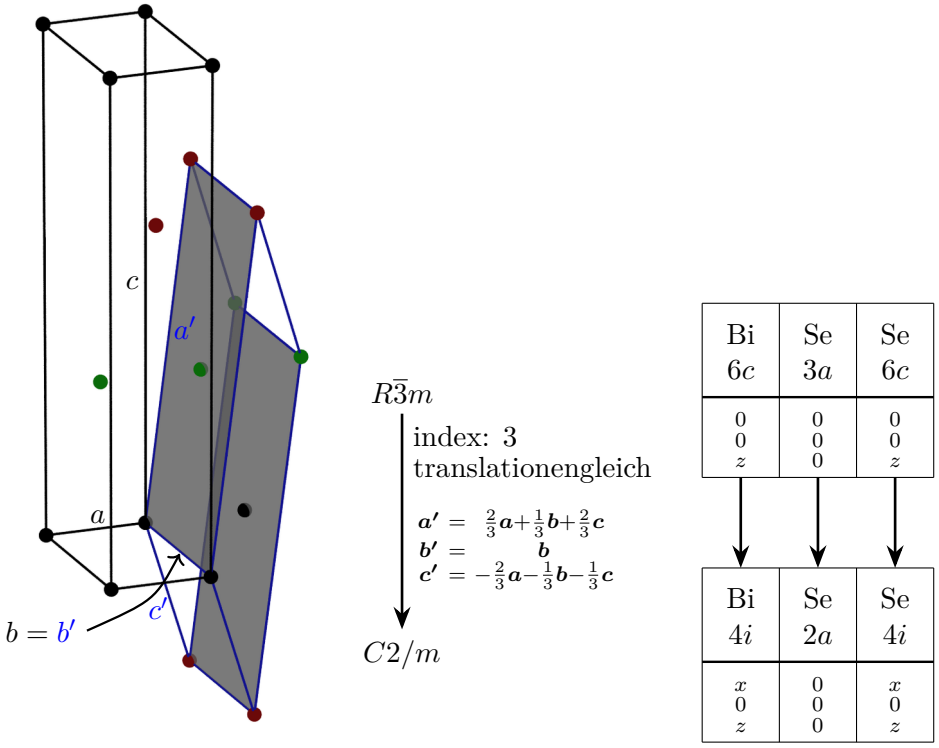

Figure 8.8: Left: The monoclinic space group $C2/m$ is the subgroup that belongs to a Γ mode and breaks the three-fold axis (cf. text). This figure shows the hexagonal cell in black and the monoclinic cell in blue, the basis vectors a, b, c belong to the hexagonal cell and a', b', c' to the monoclinic cell. The $b = b'$ axis is the same in both bases. However, the other two axes must be chosen in a more complicated way. The two different rhombohedral centering positions are shown in green resp. red. The $a'b'$ plane is shaded, so that the C centering of the monoclinic cell is visible. Right: Bärnighausen diagram of the group-subgroup relation $R\bar{3}m > C2/m$.

		$R\bar{3}m$		$C2/m$	
sample: ZW004-S001	1.9 K	reflections:	592	reflections:	592
		unique:	182	unique:	577
		R(int):	3.42 %	R(int):	1.55 %
	4.4 K	reflections:	651	reflections:	651
		unique:	203	unique:	636
		R(int):	4.04 %	R(int):	1.28 %
	300 K	reflections:	530	reflections:	530
		unique:	157	unique:	515
		R(int):	4.50 %	R(int):	1.14 %
		$R\bar{3}m$		$C2/m$	
sample: MB003-S001	2 K	reflections:	860	reflections:	860
		unique:	179	unique:	745
		R(int):	2.93 %	R(int):	1.40 %
	300 K	reflections:	640	reflections:	640
		unique:	139	unique:	557
		R(int):	3.85 %	R(int):	2.05 %

Table 8.4: Internal R values of the single crystal neutron diffraction data of two different $Cu_xBi_2Se_3$ samples at different temperatures. Reductions in the high symmetry space group $R\bar{3}m$ yield much greater internal R values compared to the reduction in the low symmetry space group $C2/m$.

with respect to both space groups are listed in Table 8.4 for different samples at different temperatures. In most cases, the reduction in the high symmetry space group $R\bar{3}m$ yields a value $R(\text{int}) > 3\,\%$ and the reduction in the low symmetry space group $C2/m$ yields a value of $R(\text{int}) < 2\,\%$. This would be a hint for a breaking of the three-fold axis. However, in space group $C2/m$, nearly all reflections are unique. So the R(int) values are not very meaningful.

Next, structural refinements in space group $C2/m$ are carried out. All atoms are refined with anisotropic ADPs. In space group $R\bar{3}m$, there are some contraints for the entries of the ADP tensors: Assume that an atom at position $(0, 0, z)^{\mathrm{T}}$ is displaced along $(\delta x, \delta y, \delta z)^{\mathrm{T}}$, so that it is located at position $(\delta x, \delta y, z + \delta z)^{\mathrm{T}}$. In space group $R\bar{3}m$, this position is equivalent to $(-\delta y, \delta x - \delta y, z + \delta z)^{\mathrm{T}}$. This means that the following equations hold for the expectation values: $\langle(\delta x)^2\rangle = \langle(-\delta y)^2\rangle$ and $\langle\delta x\delta y\rangle = \langle-\delta y(\delta x - \delta y)\rangle$. We get the constraints $\langle(\delta x)^2\rangle = \langle(\delta y)^2\rangle$ and, since the expectation value is linear,

$2\langle\delta x\delta y\rangle = \langle(\delta x)^2\rangle$. We also can derive from the equalities $\langle\delta y\delta z\rangle = \langle(\delta x - \delta y)\delta z\rangle$ and $\langle\delta x\delta z\rangle = \langle-\delta y\delta z\rangle$ the constraints $\langle\delta x\delta z\rangle = \langle\delta y\delta z\rangle = 0$. Expressed in terms of ADPs this yields the following constraints:

$$\begin{aligned} U_{11} &= U_{22} \\ U_{13} &= U_{23} = 0 \\ U_{21} &= \frac{1}{2}U_{11} \end{aligned} \tag{8.2}$$

These constraints are also used for the refinements in space group $C2/m$ for all atoms.

For a comparison of the R values, a first refinement is carried out in space group $R\bar{3}m$, a second refinement uses the same parameters as the refinement in $R\bar{3}m$, but the reduction is done in space group $C2/m$, and with a third refinement the structural parameters are refined according to the monoclinic space group. Table 8.5 shows the refinements in $R\bar{3}m$, and the refinements in $C2/m$ with the structural parameters fixed and refined (left and right of "→", respectively). It is clearly visible that the symmetry reduction improves the value wR(all) by approximately 0.5 %. Since an obverse/reverse twinning could be ruled out by the refinements in space group $R\bar{3}m$, for the refinements in space group $C2/m$ (both with parameters fixed and refined) only three twins were used that describe the breaking of the three-fold axis. In sample ZW004-S001 at 1.9 K the twins cover respectively 29.4(2.5) %, 34.1(1.8) %, 36.5(1.8) %, at 4.4 K they cover 27.8(3.8) %, 31.3(2.5) %, 40.9(2.8) % and at 300 K they cover 38.2(2.5) %, 18.9(1.9) %, 42.9(1.6) %. In sample MB003-S001 at 2 K it is 33.3(1.3) %, 32.6(0.9) %, 34.1(0.9) % and at 300 K the fractions are 33.6(1.6) %, 34.4(1.1) %, 32.0(1.2) %, respectively. Thus, all three twins cover a significant volume fraction. For sample MB003-S001, each twin covers 1/3 of the sample volume, for sample ZW004-S001 they differ in size. The twin fractions of sample ZW004-S001 at 1.9 K and 4.4 K are consistent within the errors. The twin fractions at 300 K are completely different. This can be explained by the misaligned beam nose at this temperature. Results from this measurement must be interpreted with great care. However they are shown in the present work in order to exclude large structural changes compared to the low temperature measurements.

The goodnesses of fit (GoF) are greater than 1 and decrease when the symmetry is reduced from space group $R\bar{3}m$ to $C2/m$. There are two possible reasons for the reduction of the GoF: On the one hand, it might be the case that the lower symmetry in fact allows for a better description of the crystal structure. This would decrease the GoF value when the additional parameters are refined. On the other hand, the different data reduction might affect the GoF: Data reduction reduces the statistical error which is in the denominator of χ^2 (Equation 2.16) and thus raises the GoF. This can effect the GoF also with fixed parameters. Note that the GoF is substantially reduced by reducing the symmetry, even if the structural data are kept fixed (cf. the GoF values at the left hand side of the arrows "→" in Table 8.5). A refinement of the structural parameters further improves the GoF in some cases. This means that a part of the deviation of the GoF from 1 can be attributed to the above explained artifacts, but the $C2/m$ model also

better describes the measured data.

If the crystal structure is better described in the low-symmetry space group $C2/m$, the refinement in the high-symmetry space group $R\bar{3}m$ is expected to yield too large atomic displacement parameters (ADPs). The refinements were carried out with anisotropic ADPs. Table 8.6 lists the according isotropic ADPs. As expected, the ADPs are larger for higher temperatures. The change of ADPs by the reduction of symmetry is not large. The ADPs do hardly change within one standard deviation. The room-temperature crystal structure was also investigated in [171] at room temperature by X-ray diffraction. Only an overall temperature factor $B = 1.50\,\text{Å}^2$ was determined [171], which corresponds to $U = B/(8\pi^2) = 0.0190\,\text{Å}^2$ [189]. The ADPs of our refinements of sample ZW004-S001 at room temperature lie around this value. This is a hint that the model with symmetry $R\bar{3}m$ describes the crystal structure sufficiently well. The anisotropic ADPs are listed in Table A.25. The entries of the ADP tensor increase with increasing temperature. There are hardly any changes when the symmetry is reduced from $R\bar{3}m$ to $C2/m$. The only big difference is visible for sample ZW004-S001 at 1.9 K: U_{11}, U_{22} and U_{12} (which belong to the same degree of freedom due to the constraints) for the atoms Bi1 and Se2 is significantly smaller in space group $C2/m$. In the case of Bi1, this corresponds well to the fact that a small deviation of the position is visible within the ab plane, as discussed below. However, This does not explain the decrease of the ADPs of the Se2 atom in space group $C2/m$ compared to space group $R\bar{3}m$, since this atom is still fixed to position $(0, 0, 0)^{\mathrm{T}}$ is space group $C2/m$. One should not attribute too much importance to this effect since the decrease of the ADPs is not visible for other temperatures or for the other sample.

Table 8.7 shows the positional parameters of the refinement in both space groups. The positions in space group $C2/m$ are transformed to the hexagonal axes according to Figure 8.8. The atom Se2 stays on the special position with $x = y = z = 0$. The other two atoms Bi1 and Se3 have the z coordinate that can be refined in space group $R\bar{3}m$ and additionally the x and y coordinate in space group $C2/m$. The z coordinate does not change within one standard deviation, when the symmetry is reduced. The x and y coordinates of Bi1 changes significantly. The x and y coordinates of Se3 is in some cases consistent with the position in the high symmetry space group, in some cases it moves along a few standard deviations. The deviations of the Bi atoms are displayed in Figure 8.9. The structural data are from refinements in $R\bar{3}m$ and arrows indicate the displacement in the refinements in space group $C2/m$. The arrows are scaled by a factor of 50. The structural data are averaged from the refinements of the data of sample ZW004-S001 at 1.9 K and sample MB003-S001 at 2 K. It is useful to compare the shift of the Bi positions with the ADPs. The latter are in the order of magnitude $U = 0.01\,\text{Å}^2$, which corresponds to shifts of 0.1 Å. The magnitude of the shift of the Bi atoms was calculated using an averaged crystal structure of the refinements for 1.9 K and 2 K shown in Table 8.7, lattice constant c determined by the LeBail refinement of the $(0\,0\,l)$ scan and (since we did not measure these lattice constants) the lattice constant $a = b$ for the pristine Bi_2Se_3 from [171]. The Bi atoms shift by 0.0296(9) Å in space group $C2/m$ compared to $R\bar{3}m$. This shift is smaller than the ADPs. So we expect the ADPs not to decrease when the symmetry is lowered. This also means that the fact

		$R\bar{3}m$	$C2/m$
sample: ZW004-S001	1.9 K	R(obs) = 3.07 %	R(obs) = 3.35 % → 3.07 %
		wR(obs) = 3.55 %	wR(obs) = 3.69 % → 3.46 %
		R(all) = 3.71 %	R(all) = 4.82 % → 4.68 %
		wR(all) = 3.71 %	wR(all) = 4.04 % → 3.62 %
		GoF = 2.07	GoF = 1.67 → 1.51
	4.4 K	R(obs) = 5.05 %	R(obs) = 4.90 % → 4.78 %
		wR(obs) = 5.25 %	wR(obs) = 5.33 % → 5.22 %
		R(all) = 5.71 %	R(all) = 6.57 % → 6.38 %
		wR(all) = 5.36 %	wR(all) = 5.69 % → 5.36 %
		GoF = 2.81	GoF = 2.21 → 2.10
	300 K	R(obs) = 3.15 %	R(obs) = 4.07 % → 3.97 %
		wR(obs) = 4.83 %	wR(obs) = 5.29 % → 5.22 %
		R(all) = 4.69 %	R(all) = 6.32 % → 6.29 %
		wR(all) = 5.04 %	wR(all) = 5.67 % → 5.47 %
		GoF = 2.74	GoF = 2.31 → 2.25
		$R\bar{3}m$	$C2/m$
sample: MB003-S001	2 K	R(obs) = 3.12 %	R(obs) = 3.41 % → 2.96 %
		wR(obs) = 3.97 %	wR(obs) = 3.99 % → 3.52 %
		R(all) = 3.24 %	R(all) = 4.14 % → 3.79 %
		wR(all) = 3.99 %	wR(all) = 4.14 % → 3.60 %
		GoF = 2.77	GoF = 2.16 → 1.90
	300 K	R(obs) = 4.56 %	R(obs) = 4.78 % → 4.24 %
		wR(obs) = 5.08 %	wR(obs) = 5.43 % → 4.94 %
		R(all) = 4.83 %	R(all) = 5.83 % → 5.68 %
		wR(all) = 5.11 %	wR(all) = 5.60 % → 5.03 %
		GoF = 3.26	GoF = 2.55 → 2.32

Table 8.5: Refinements in space group $R\bar{3}m$ and $C2/m$ for different samples and temperatures. The refinements in space group $C2/m$ were carried out with the same structural parameters as in $R\bar{3}m$ (left of the arrow "→") and then with the structural parameters refined according to space group $C2/m$ (right of the arrow "→"). The wR(all) values improve by approximately 0.5 %.

		$R\bar{3}m$		$C2/m$	
sample: ZW004-S001	1.9 K	Bi1	0.0067(4)	Bi1	0.0056(2)
		Se2	0.0063(5)	Se2	0.0056(4)
		Se3	0.0069(4)	Se3	0.0066(3)
	4.4 K	Bi1	0.0127(5)	Bi1	0.0111(3)
		Se2	0.0126(6)	Se2	0.0113(5)
		Se3	0.0132(5)	Se3	0.0122(4)
	300 K	Bi1	0.0215(6)	Bi1	0.0204(4)
		Se2	0.0173(8)	Se2	0.0168(7)
		Se3	0.0193(7)	Se3	0.0190(6)
		$R\bar{3}m$		$C2/m$	
sample: MB003-S001	2 K	Bi1	0.0042(3)	Bi1	0.00398(13)
		Se2	0.0031(4)	Se2	0.0034(2)
		Bi3	0.0045(4)	Bi3	0.00453(17)
	300 K	Bi1	0.0126(6)	Bi1	0.0118(3)
		Se2	0.0085(8)	Se2	0.0085(5)
		Se3	0.0104(7)	Se3	0.0105(4)

Table 8.6: Atomic displacement parameters (ADPs) of the atoms of Bi_2Se_3 of the two samples at different temperatures for refinements in the high symmetry space group $R\bar{3}m$ and the low symmetry space group $C2/m$. The ADPs do hardly change within the error. The anisotropic ADPs of these refinements are shown in table A.25.

			$R\bar{3}m$		$C2/m$	
			Bi1	Se3	Bi1	Se3
sample: ZW004-S001	1.9 K	x	0	0	−0.0095(5)	−0.0010(9)
		y	0	0	−0.0048(3)	−0.0005(4)
		z	0.40068(4)	0.21098(5)	0.40069(3)	0.21092(3)
	4.4 K	x	0	0	0.0088(7)	0.0035(11)
		y	0	0	0.0044(4)	0.0017(5)
		z	0.40064(6)	0.21076(6)	0.40064(4)	0.21072(4)
	300 K	x	0	0	−0.0103(11)	−0.0021(15)
		y	0	0	−0.0052(5)	−0.0010(7)
		z	0.40061(7)	0.21126(7)	0.40060(5)	0.21121(5)
			$R\bar{3}m$		$C2/m$	
			Bi1	Se3	Bi1	Se3
sample: MB003-S001	2 K	x	0	0	−0.0078(3)	−0.0001(5)
		y	0	0	−0.00392(17)	−0.0001(2)
		z	0.40067(4)	0.21112(4)	0.40070(2)	0.21113(2)
	300 K	x	0	0	−0.0120(7)	−0.0009(9)
		y	0	0	−0.0060(3)	−0.0004(4)
		z	0.40070(7)	0.21150(7)	0.40078(4)	0.21148(4)

Table 8.7: Positional parameters of the refinements in space groups $R\bar{3}m$ and $C2/m$. Both structures are written with respect to the hexagonal axes.

that the ADPs do not decrease when the symmetry is lowered is not an indication for an unreliable refinement. If one furthermore takes into account that the R values are obviously better in space group $C2/m$ – though the Se atoms do not move and the x and y components of the Bi atoms are coupled so that effectively only a single degree of freedom is added to the model – it can be concluded that the symmetry is broken to $C2/m$.

Also the splitting of the Bi − Se distances is calculated. The c lattice constant is used from the LeBail refinement. Since no a and b lattice constants could be determined there, these are taken from the undoped material published in [171]. In the high-symmetry space group $R\bar{3}m$, there are two different Bi − Se distances: One between the Bi atom and a Se atom at the edge of the van-der-Waals gap and another one between the same Bi atom and a Se atom in the middle of the quintuple layer. These two distances amount

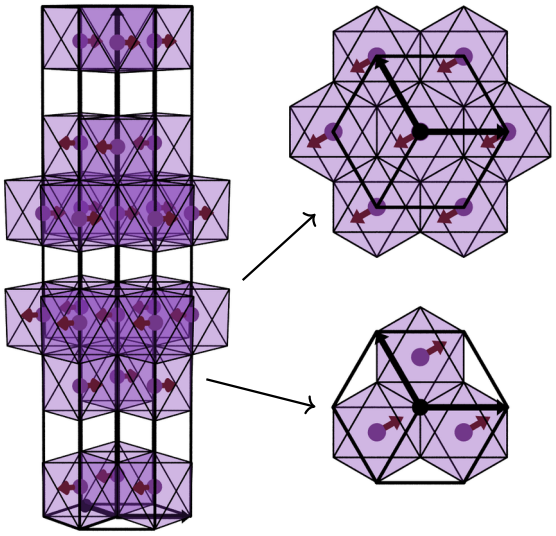

Figure 8.9: Left: The deviation of the Bi positions of the refinements in $C2/m$ compared to the positions in $R\bar{3}m$ are displayed by arrows. The arrows are 50 times as large as the actual deviations. Right: Two neighbored quintuple layers (view along the negative c axis). The deviations lie within the ab plane and the mirror plane of $C2/m$.

to 2.8642(25) Å and 3.0745(23) Å, respectively. In the low-symmetry space group $C2/m$, each of these two distances split into two different ones. The distance from the Bi atom to the "gap Se" amounts to 2.8769(26) Å or 2.8381(28) Å. The other distance splits into 3.0635(23) Å and 3.0980(24) Å. Both splittings are clearly outside the error bars, so the symmetry reduction can be described by a shift of the Bi position that breaks the three-fold symmetry.

An investigation of Se vacancies in the lower symmetry space group $C2/m$ is not necessary: From the Bärnighausen diagram in Figure 8.8, it is obvious that the occupations cannot break the symmetry since the atomic positions do not split.

Also refinements in the subgroup Cm are carried out. Again, the constraints in Equation 8.2 are used for the ADPs. The results of the refinements are listed in Tables A.26, A.27 and A.28. The mirror plane $x, -y, z$ in space group Cm transformed to the coordinate system of space group $R\bar{3}m$ reads $x, x-y, z$. This is why we obtain the constraint $x = 2y$ in space group Cm for all atoms since we use the coordinate system of space group $R\bar{3}m$. The largest displacements of atoms is visible in the x and y coordinates, that deviate in the order of magnitude 0.01 lattice constants in some cases. However, these displacements vary dependent on the sample and the temperature. For most atoms, there exists a measurement where the position hardly changes. One can notice that the two Bi atoms move in the same direction, which is not possible in space group $C2/m$ due to the inversion center. The z parameters are rather unchanged. The ADPs do not change drastically except from U_{33}, but there are exceptions where U_{33} stays rather unchanged, so no general rule can be derived.

A refinement of the occupancies in space group Cm is useful because the positions of

Bi1 and Se3 split. The refinement was carried out with the occupancy of Se2 fixed to full occupancy, and the occupancies of the other four atoms refined. This choice is rather arbitrary, so we have to keep in mind that occupancies greater than 1 can be a hint for vacancies at the Se2 position. Most refinements yield full occupancy within the error for all Se atoms. Greater deviations are visible for the occupancies of the Bi sites: The largest deviation from 1 is observed in the refinement of sample ZW004-S001 at 1.9 K: Bi1_1 has an occupancy of 0.89(2) and Bi1_2 of 1.08(2). However, for sample MB003-S001 at 2 K, both occupancies are in agreement with 1. One could argue that the occupancy for Bi that is greater than 1 is a hint for Se vacancies. However, the other Bi site has an occupation smaller than 1, which does not support this speculation. Furthermore, this is not consistent when different measurements are compared. Thus, the Bi occupation greater than 1 has probably no physical meaning and can be seen as an artifact.

Structural distortions are reported in [180] for Sr-doped Bi_2Se_3. These distortions yield a triclinic symmetry, so they are not equivalent to the monoclinic distortions investigated in this work. A comparison of the resultes in this work with the results in [180] is not possible because in [180] the lattice parameters are determined rather than structural parameters. Both studies have in common that a breaking of the three-fold axis is investigated.

8.3.5 Magnetic properties

Due to the Meissner effect, measurements of magnetic susceptibility are not possible for superconductors. Polarized neutron diffraction avoids this problem, so that information about magnetic moments inside the bulk material can be obtained by this method.

Several scans were carried out at the same temperature and in the same field, all such scans were added up. No distinction was made between the (1 0 10) reflection and equivalent reflections. By this procedure, the number of counts and of monitor counts at the peak and at two background positions is obtained with polarization parallel and antiparallel for each temperature and field, respectively. For all three positions (background – peak – background), the counts per monitor were calculated, assuming that the error of the counts is its square root and neglecting the error of the monitor. The intensity of the reflection is then obtained by subtracting the background from the peak. The flipping ratio is calculated by the formula [67]:

$$R = \frac{P^+ - \frac{1}{2}(B_1^+ + B_2^+)}{P^- - \frac{1}{2}(B_1^- + B_2^-)} \quad ,$$

where $P^\pm$ is the number of counts per monitor at the peak position and $B_1^\pm, B_2^\pm$ is the number of counts per monitor at the ω positions on either side of the peak. The superscripts + resp. − indicate that the polarization was parallel resp. antiparallel

		$R\bar{3}m$		$C2/m$	
sample: ZW004-S001	1.9 K			x(Bi) =	−0.0026(8)
		z(Bi) =	0.4012(6)	z(Bi) =	0.4012(7)
		z(Cu) =	0.392(5)	z(Cu) =	0.397(4)
		occ(Cu) =	0.07(10)	occ(Cu) =	0.15(7)
		wR(all) =	3.68 %	wR(all) =	4.02 % → 3.63 %
	4.4 K			x(Bi) =	0.0033(10)
		z(Bi) =	0.4011(9)	z(Bi) =	0.4009(6)
		z(Cu) =	0.390(9)	z(Cu) =	0.391(10)
		occ(Cu) =	0.06(12)	occ(Cu) =	0.04(10)
		wR(all) =	5.31 %	wR(all) =	5.65 % → 5.19 %
		$R\bar{3}m$		$C2/m$	
sample: MB003-S001	2 K			x(Bi) =	−0.0029(5)
		z(Bi) =	0.40175(19)	z(Bi) =	0.40176(14)
		z(Cu) =	0.3922(11)	z(Cu) =	0.3937(7)
		occ(Cu) =	0.16(3)	occ(Cu) =	0.17(3)
		wR(all) =	3.95 %	wR(all) =	4.14 % → 3.50 %
	300 K			x(Bi) =	0.0047(12)
		z(Bi) =	0.4023(4)	z(Bi) =	0.4025(3)
		z(Cu) =	0.3925(18)	z(Cu) =	0.3946(11)
		occ(Cu) =	0.21(7)	occ(Cu) =	0.26(6)
		wR(all) =	5.16 %	wR(all) =	5.61 % → 4.97 %

Table 8.8: Refinements with Cu atoms sharing the Bi sites in space group $R\bar{3}m$ and $C2/m$. The positions of Bi and Cu are independent. Cu atoms are constraint to lie at a $0, 0, z$ positions also an space group $C2/m$.

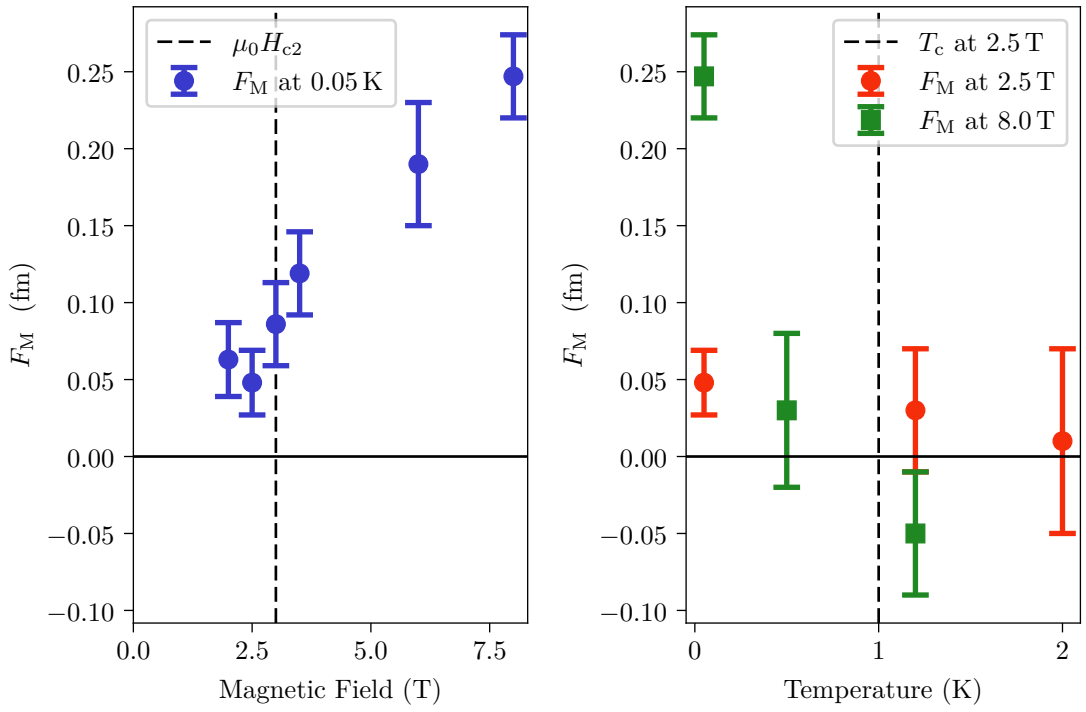

Figure 8.10: Magnetic structure factor at different temperatures and different magnetic fields calculated from flipping ratios. Left: Constant temperature of 0.05 K in different magnetic fields. The dashed line shows the critical field at very low temperatures, estimated from [191]. Right: Constant magnetic field of 2.5 K resp. 8 K at different temperatures. The dashed line shows the critical temperature at 2.5 K, estimated from [191].

to the magnetic field. Using the flipping ratio, it is possible to calculate the magnetic structure factor F_M if the nuclear structure factor F_N is known, as stated in [190]:

$$F_M = \frac{(R-1)F_N}{2(Q^+ + Q^-)}$$

The nuclear structure factor F_N for the (1 0 10) reflection was calculated using the structural data of sample ZW004-S001 at 1.9 K refined in space group $R\bar{3}m$ without Cu as shown in Table 8.7. The ADPs were neglected and the coherent bound scattering lengths of 8.532 fm for Bi and 7.97 fm for Se from [57] were used. A nuclear structure factor of 111.94 fm was obtained for the (1 0 10) reflection. Q^+ and Q^- are the efficiencies of the polarization parallel and antiparallel to the magnetic field, respectively. They both amount to 0.94. The magnetic structure factors calculated in this way for different temperatures and magnetic fields are shown in Figure 8.10. The magnetic moments persist when the superconducting phase is entered by lowering either the temperature or the magnetic field. This is in agreement with the Knight shift measurements in [177].

In principal, it would be possible that the nuclear spins align along the magnetic field

and give rise to a magnetic structure factor. Since we are at non-zero temperature, the alignment will not be perfect. Instead, the average value of the component of the nuclear magnetic moment along the direction of the magnetic field (which is the quantization axis) is expressed by the Brillouin function [192]:

$$\frac{\langle\mu\rangle}{\mu} = B_J(x) = \frac{2J+1}{2J}\coth\left(\frac{2J+1}{2J}x\right) - \frac{1}{2J}\coth\left(\frac{x}{2J}\right)$$

In this equation, J is the total angular momentum quantum number of the nucleus and $x = \mu B/(k_\mathrm{B}T)$, where μ is the total magnetic momentum of the nucleus, B is the external magnetic field, T the temperature and k_B the Boltzmann constant. The values $\mu(\mathrm{Bi}) = 2.076024 \cdot 10^{-26}\,\mathrm{J/T}$, $J(\mathrm{Bi}) = 9/2$, $\mu(\mathrm{Se}) = 0.2702382 \cdot 10^{-26}\,\mathrm{J/T}$, $J(\mathrm{Se}) = 1/2$ are taken from [193]. The structural data of sample ZW004-S001 at 1.9 K refined in space group $R\bar{3}m$ without Cu as shown in Table 8.7 are used, the ADPs and small structural distortions to space group $C2/m$ are neglected. The structure factor of the nuclear magnetic moments is calculated by

$$F_{\mathrm{M,n}}(\vec{q}, T, B) = p\sum_\alpha \mu(\alpha) B_{J(\alpha)}\left(\frac{\mu(\alpha)B}{k_\mathrm{B}T}\right) \mathrm{e}^{2\pi\mathrm{i}\vec{q}\cdot\vec{r}(\alpha)} \quad ,$$

where $\vec{q}$ is the reciprocal vector of the reflection, the sum runs over all atoms α of the unit cell, $\vec{r}(\alpha)$, $\mu(\alpha)$ and $J(\alpha)$ are the position, total magnetic moment and the total angular momentum quantum number of atom α, respectively. The factor $p = 0.2696 \cdot 10^{-14}\,\mathrm{m}/\mu_\mathrm{B}$ converts the magnetic moment into a scattering length [61], where μ_B is the Bohr magneton. Since the scattering plane is perpendicular to the magnetic field – and thus to the orientation of the magnetic moments – we can use the total structure factor and do not need to project out the component perpendicular to the magnetic moments.

The highest nuclear magnetic structure factor is expected to be at the lowest temperature and the highest magnetic field, which is in our case $T = 0.05\,\mathrm{K}$ and $B = 8\,\mathrm{T}$. For this case, we obtain $F_{\mathrm{M,n}}((1\,0\,10), 0.05\,\mathrm{K}, 8\,\mathrm{T}) = 0.0037\,\mathrm{fm}$. Most of the values in Figure 8.10 are much bigger, so they cannot be explained by nuclear magnetic moments. If Cu is taken into account, since we do not now its position inside the unit cell, all we can do is the following estimation: The structure factor would be maximal, if one Cu atom is located at the origin of the unit cell, which roughly agrees with the nominal stoichiometry. The crystal structure consisting only of Cu, then gives a nuclear magnetic structure factor of $F_{\mathrm{M,n}}((1\,0\,10), 0.05\,\mathrm{K}, 8\,\mathrm{T}) = 0.0004\,\mathrm{fm}$. In the calculation, the nuclear magnetic moment $\mu(\mathrm{Cu}) = 1.452682 \cdot 10^{-26}\,\mathrm{J/T}$ and the total angular momentum quantum number $J(\mathrm{Cu}) = 3/2$ from [193] were used. In the worst case, i.e. only constructive interference of the Cu atoms with the other atoms, the structure factors of Bi_2Se_3 and Cu are added. This gives an upper bound for the structure factor of 0.0041 fm, which still cannot explain the measured values.

The highest measured structure factor at 0.05 K in 8 T corresponds to a magnetic moment of $0.092(10)\,\mu_B$, assuming that the whole magnetic moment is concentrated at the origin of the unit cell which corresponds to a scattering vector of $\vec{Q} = \vec{0}$. In this case, a moment of $1\,\mu_B$ yields a scattering length of 2.696 fm [61].

The decrease of the structure factor when the temperature changes from 0.05 K to 0.5 K in a field of 8 K, as depicted on the right hand side of Figure 8.10, cannot be explained by the magnetic moments of isolated electrons with $S = 1/2$ and $\mu = \mu_B$ or triplets with $S = 1$ and $\mu = 2\mu_B$: In both cases, the Brillouin function shows no noteworthy deviation from 1. Even at a temperature of 2 K, the Brillouin function has decreased less then 1 % in both cases. Assuming $S = 1/2$ moments, this decrease corresponds to a magnetic moment of $0.008\,\mu_B$. Thus, the temperature-dependence of the magnetic scattering cannot be explained by single electrons or triplets.

It can be concluded that the measured data can neither be explained by nuclear nor by electronic magnetic moments.

8.3.6 Impurity phase

The lattice parameters for the impurity phase, found by single-crystal X-ray diffraction data, amount to $a = 13.6349$ Å, $b = 4.2212$ Å, $c = 15.2244$ Å, $\alpha = \gamma = 90°$, $\beta = 99.838°$ for sample ZW006-S003 and $a = 13.6411$ Å, $b = 4.2261$ Å, $c = 15.2411$ Å, $\alpha = \gamma = 90°$, $\beta = 99.785°$ for sample ZW006-S005. For this instrument, a rough estimation of the error on lattice parameters is a relative error of $5 \cdot 10^{-4}$ so that angles have errors like 0.06°. The metrices of the two measured samples are then compatible with each other within a few standard deviations.

The data were refined using the software JANA2006 [69]. The monoclinic space group C/m was suggested by the software. The Superflip algorithm yields useful results, which are similar for both samples. The structural parameters listed in the Appendix in Tables A.29 and A.30 yield wR(all) values of 8.56 % resp. 9.43 %. These R values are rather poor, which however is in agreement with the internal R values that could be explained by a bad sample quality.

The crystal structure as shown in Figure 8.11 shows similarities to Bi_2Se_3: It is a layered structure of edge-sharing $BiSe_6$ octahedrons. In contrast to Bi_2Se_3, the octahedrons do not exhibit a face perpendicular to the stacking direction. Two edges of an octahedron are aligned parallel to the b axis, whereas the rotation around the b axis appears rather arbitrary. Between these layers, there are strongly distorted $CuSe_6$ octahedrons, which share corners with the Bi_2Se_3 octahedrons in the layers above and below. The interstitial sites are occupied by further Bi atoms, which cannot be attributed to any $BiSe_6$ octahedron. These Bi atoms are surrounded by eight Se atoms, indicated by red bonds in Figure 8.11. The stoichiometry of this phase is $CuBi_6Se_9$ with two formula units per unit cell.

Bond-valence sums were calculated from the structural data as described in Section

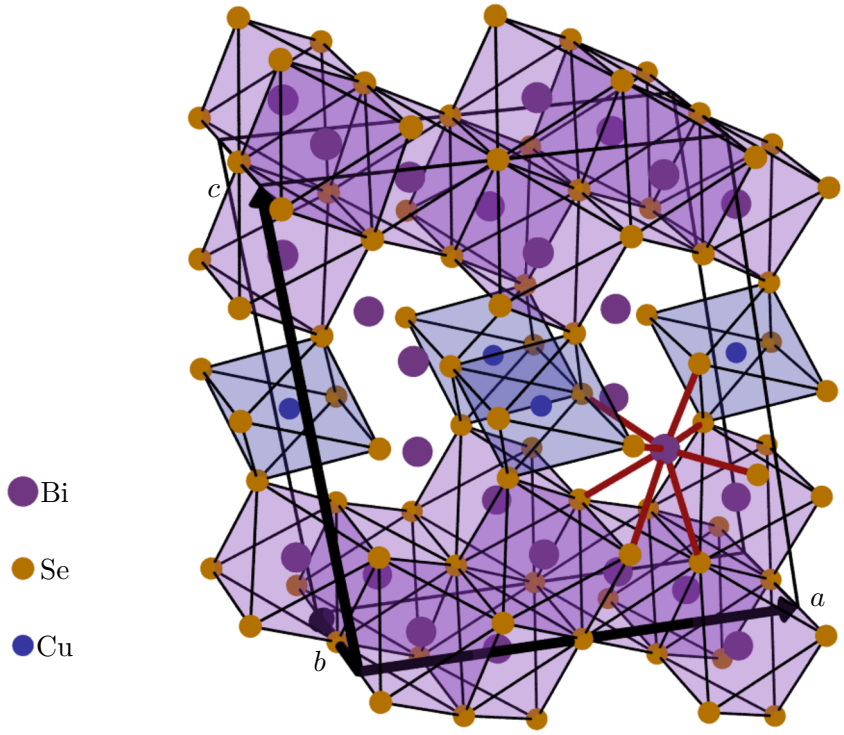

Figure 8.11: Crystal structure of the impurity phase in the Bi_2Se_3 samples. The Cu atoms and the Bi1 and Bi2 atoms are surrounded by six Se atoms which form distorted octahedrons. The Bi3 atoms are have eight neighbors which are indicated by the red bonds.

			ZW006-S003	ZW006-S005
Cu	d (Å)	equatorial	2.9898(8)	2.9903(10)
		above/below	2.3051(11)	2.3046(14)
		bond-valence sum	1.22	1.22
Bi1	d (Å)	equatorial (short)	2.9025(9)	2.9035(10)
		equatorial (long)	2.9948(4)	2.9983(4)
		above	2.7973(16)	2.7988(18)
		below	3.1607(17)	3.1617(19)
		bond-valence sum	3.29	3.27
Bi2	d (Å)	equatorial (short)	2.8713(9)	2.8744(12)
		equatorial (long)	3.0456(9)	3.0511(11)
		above	2.7779(14)	2.7819(17)
		below	3.1077(6)	3.1115(7)
		bond-valence sum	3.36	3.33
Bi3	d (Å)		2.8713(9)	2.8744(12)
			2.8713(9)	2.8744(12)
			4.8650(11)	4.8710(13)
			4.8650(11)	4.8710(13)
			4.9336(15)	4.9336(18)
			6.6082(12)	6.6161(15)
			6.6082(12)	6.6161(15)
			7.0979(12)	7.1062(14)
		bond-valence sum	3.33	3.30

Table 8.9: Distances d of the Cu and Bi atoms to the nearest Se atoms of the $CuBi_6Se_9$ impurity phase, as displayed in Figure 8.11 for the two samples ZW006-S003 and ZW006-S005. From these distances, the bond-valence sums are calculated.

2.4.3.1. The bond-valence parameters $R_{\mathrm{Bi,Se}} = 2.72\,\text{Å}$ and $R_{\mathrm{Cu,Se}} = 2.02\,\text{Å}$ from [73] were used. For both refinements, the valences for all Bi atoms are close to 3.3 and for Cu it is 1.2.

8.4 Conclusion

The most striking result about the $Cu_xBi_2Se_3$ samples is certainly the fact that no Cu atoms are visible by single crystal neutron diffraction. Several positions that were proposed in literature were tested, and none of them yields a significant occupation with Cu atoms. Also the Fourier maps show no additional peaks. The possibility for a substitution of Bi by Cu can only be ruled out with an upper bound of $x = 10\,\%$ for the stoichiometric parameter x, because the nuclear scattering lengths for Cu and Bi are unfortunately very similar. This means that not all of the Cu atoms can occupy Bi sites, since the stoichiometry of the samples was around $x \approx 0.3$.

A breaking of translation symmetry could not be detected. It is not unambiguously verified whether the three-fold axis is broken or not. There are hints for small deviations of the atomic parameters from their high-symmetry position. A structural phase transition was not observed by single crystal neutron diffraction. Structural refinements show that the symmetry might be reduced to space group $C2/c$ with an in-plane displacement of the Bi atoms by $0.0296(9)\,\text{Å}$.

The magnetic signal detected by polarized neutron diffraction can neither be attributed to nuclear magnetic moments nor to free electrons.

Single crystal X-ray diffraction revealed a monoclinic impurity phase with stoichiometry $CuBi_6Se_9$ and a layered crystal structure.

A Appendix

Space group	Cell parameters			R values	
Pnma	$a = 13.62$ Å	$\alpha = 90.00°$		$R(\text{obs}) = 4.33\,\%$	
	$b = 9.95$ Å	$\beta = 90.00°$		$\text{w}R(\text{obs}) = 5.08\,\%$	
	$c = 6.97$ Å	$\gamma = 90.00°$		$R(\text{all}) = 7.52\,\%$	
				$\text{w}R(\text{all}) = 5.25\,\%$	

	x	y	z	$U_{\text{iso/ani}}$	U_{11}	U_{22}	U_{33}	U_{12}	U_{13}	U_{23}	occupancy
Fe1	0.11800(7)	1/4	0.18982(18)	0.0070(3)	–	–	–	–	–	–	1
Cl1	0.10580(5)	0.00986(7)	0.17635(13)	0.0109(3)	0.0127(4)	0.0052(4)	0.0148(5)	-0.0003(3)	-0.0029(3)	-0.0006(3)	1
Cl2	0.00675(8)	1/4	0.45771(18)	0.0115(3)	0.0113(5)	0.0097(5)	0.0137(7)	0	0.0030(5)	0	1
Cl3	0.25070(8)	1/4	0.40035(19)	0.0096(3)	0.0091(5)	0.0103(5)	0.0093(7)	0	-0.0007(4)	0	1
Cl4	0.22549(8)	1/4	-0.07528(19)	0.0114(4)	0.0126(5)	0.0122(6)	0.0092(7)	0	0.0015(4)	0	1
O1	-0.00296(14)	1/4	0.0003(3)	0.0149(6)	0.0139(8)	0.0093(8)	0.0214(13)	0	-0.0100(8)	0	1
D1	-0.03420(10)	0.17142(13)	-0.0504(2)	0.0256(4)	0.0279(6)	0.0181(6)	0.0307(10)	-0.0047(6)	-0.0085(6)	-0.0035(6)	1
N1	0.13872(6)	0.00041(8)	0.66524(15)	0.0134(3)	0.0141(4)	0.0134(5)	0.0128(6)	0.0004(4)	-0.0004(3)	0.0020(4)	1
D2	0.1345(3)	0.0044(5)	0.8156(7)	0.0458(10)	0.0558(15)	0.0627(19)	0.0190(18)	-0.0029(14)	0.0033(12)	0.0009(14)	0.4387(16)
D3	0.1100(3)	-0.0829(4)	0.6218(8)	0.0430(10)	0.0485(15)	0.0199(11)	0.061(2)	-0.0091(12)	-0.0108(14)	-0.0089(12)	0.4387(16)
D4	0.2124(3)	0.0093(5)	0.6415(7)	0.0394(9)	0.0233(11)	0.0548(16)	0.0402(18)	-0.0028(11)	0.0030(10)	-0.0015(13)	0.4387(16)
D5	0.1041(3)	0.0821(4)	0.6092(7)	0.0402(9)	0.0358(12)	0.0239(11)	0.061(2)	0.0083(10)	-0.0093(12)	0.0091(12)	0.4387(16)
D6	0.1412(2)	-0.0094(4)	0.5180(5)	0.0458(10)	0.0558(15)	0.0627(19)	0.0190(18)	-0.0029(14)	0.0033(12)	0.0009(14)	0.5613(16)
D7	0.1713(3)	0.0818(3)	0.7076(6)	0.0430(10)	0.0485(15)	0.0199(11)	0.061(2)	-0.0091(12)	-0.0108(14)	-0.0089(12)	0.5613(16)
D8	0.0656(2)	-0.0019(3)	0.6978(5)	0.0394(9)	0.0233(11)	0.0548(16)	0.0402(18)	-0.0028(11)	0.0030(10)	-0.0015(13)	0.5613(16)
D9	0.1707(2)	-0.0835(3)	0.7174(6)	0.0402(9)	0.0358(12)	0.0239(11)	0.061(2)	0.0083(10)	-0.0093(12)	0.0091(12)	0.5613(16)

Table A.1: Refinement of single crystal neutron diffraction data of a $(ND_4)_2[FeCl_5(D_2O)]$ sample measured at 100 K in space group *Pnma*.

Space group	Cell parameters		R values
$Pnma$	$a = 13.57\,\text{Å}$	$\alpha = 90.00°$	$R(\text{obs}) = 14.45\,\%$
	$b = 9.99\,\text{Å}$	$\beta = 90.00°$	$\text{w}R(\text{obs}) = 23.51\,\%$
	$c = 6.94\,\text{Å}$	$\gamma = 90.00°$	$R(\text{all}) = 15.78\,\%$
			$\text{w}R(\text{all}) = 23.54\,\%$

	x	y	z	$U_{\text{iso/ani}}$	U_{11}	U_{22}	U_{33}	U_{12}	U_{13}	U_{23}	occupancy
Fe1	0.1193(3)	1/4	0.1868(7)	0.0039(13)	–	–	–	–	–	–	1
Cl1	0.1065(2)	0.0102(3)	0.1740(6)	0.0085(11)	0.0099(18)	0.0030(17)	0.012(2)	-0.0009(12)	-0.0038(13)	-0.0031(12)	1
Cl2	0.0063(4)	1/4	0.4573(7)	0.0071(14)	0.013(2)	0.005(2)	0.003(2)	0	0.0033(16)	0	1
Cl3	0.2502(3)	1/4	0.4010(7)	0.0046(12)	0.0010(18)	0.009(2)	0.004(2)	0	0.0015(15)	0	1
Cl4	0.2261(3)	1/4	-0.0779(8)	0.0068(14)	0.002(2)	0.006(2)	0.012(3)	0	0.0039(16)	0	1
O1	-0.0035(5)	1/4	-0.0035(14)	0.008(2)	0.006(3)	0.005(3)	0.014(4)	0	-0.001(4)	0	1
D1	-0.0352(5)	0.1714(6)	-0.0531(10)	0.0213(18)	0.025(3)	0.009(3)	0.030(4)	-0.006(2)	-0.010(3)	-0.003(2)	1
N1	0.1379(3)	0.0009(4)	0.6671(6)	0.0099(11)	0.0117(18)	0.0088(19)	0.009(2)	0.0012(14)	-0.0005(14)	-0.0001(15)	1
D2	0.1316(12)	0.0038(16)	0.814(2)	0.028(3)	0.034(5)	0.034(6)	0.016(6)	0.002(4)	0.000(4)	0.006(4)	0.501(7)
D3	0.1103(10)	-0.0806(14)	0.621(3)	0.030(3)	0.031(5)	0.014(5)	0.045(7)	-0.006(4)	0.001(5)	-0.006(5)	0.501(7)
D4	0.2136(9)	0.0076(15)	0.642(2)	0.027(3)	0.015(4)	0.033(5)	0.032(6)	0.001(4)	0.003(4)	0.010(4)	0.501(7)
D5	0.1031(10)	0.0851(14)	0.611(2)	0.025(3)	0.026(5)	0.022(5)	0.027(5)	0.011(4)	-0.010(4)	0.007(4)	0.501(7)
D6	0.1398(11)	-0.0126(15)	0.518(2)	0.028(3)	0.034(5)	0.034(6)	0.016(6)	0.002(4)	0.000(4)	0.006(4)	0.499(7)
D7	0.1687(10)	0.0850(14)	0.710(2)	0.030(3)	0.031(5)	0.014(5)	0.045(7)	-0.006(4)	0.001(5)	-0.006(5)	0.499(7)
D8	0.0648(9)	-0.0034(15)	0.702(2)	0.027(3)	0.015(4)	0.033(5)	0.032(6)	0.001(4)	0.003(4)	0.010(4)	0.499(7)
D9	0.1707(10)	-0.0827(14)	0.722(2)	0.025(3)	0.026(5)	0.022(5)	0.027(5)	0.011(4)	-0.010(4)	0.007(4)	0.499(7)

Table A.2: Refinement of single crystal neutron diffraction data of a $(ND_4)_2[FeCl_5(D_2O)]$ sample measured at 10 K in space group $Pnma$.

Space group	Cell parameters		R values	
$P2_1/a$	$a = 13.57$ Å	$\alpha = 90.00°$	R(obs) = 3.47 %	
	$b = 9.99$ Å	$\beta = 90.00°$	wR(obs) = 4.30 %	
	$c = 6.94$ Å	$\gamma = 90.00°$	R(all) = 5.45 %	
			wR(all) = 4.41 %	

	x	y	z	$U_{\mathrm{iso/ani}}$	U_{11}	U_{22}	U_{33}	U_{12}	U_{13}	U_{23}	occupancy
Fe1	0.11924(6)	0.25031(11)	0.18730(12)	0.00293(19)	–	–	–	–	–	–	1
Cl1_1	0.10304(7)	0.01047(11)	0.18253(15)	0.0051(3)	0.0054(4)	0.0029(4)	0.0069(5)	-0.0009(4)	-0.0005(3)	0.0006(4)	1
Cl1_2	0.10984(7)	0.48971(11)	0.16644(15)	0.0044(3)	0.0061(4)	0.0022(4)	0.0049(5)	-0.0002(4)	0.0002(3)	0.0012(4)	1
Cl2	0.00656(6)	0.25530(12)	0.45667(13)	0.0049(2)	0.0046(3)	0.0041(4)	0.0059(4)	-0.0006(4)	0.0011(3)	-0.0008(4)	1
Cl3	0.25160(6)	0.24854(13)	0.40007(13)	0.0047(2)	0.0049(3)	0.0042(4)	0.0050(4)	-0.0004(4)	0.0001(3)	0.0001(5)	1
Cl4	0.22698(6)	0.24562(13)	-0.07677(13)	0.0051(2)	0.0058(4)	0.0045(4)	0.0051(5)	0.0005(5)	0.0008(3)	-0.0006(4)	1
O1	-0.00163(12)	0.24958(19)	-0.0034(3)	0.0072(3)	0.0067(4)	0.0057(5)	0.0092(6)	-0.0010(8)	-0.0036(6)	-0.0017(11)	1
D1_1	-0.03495(15)	0.17039(20)	-0.0519(3)	0.0204(6)	0.0232(10)	0.0117(9)	0.0264(12)	-0.0056(7)	-0.0069(9)	-0.0029(8)	1
D1_2	-0.03518(15)	0.3278(2)	-0.0511(3)	0.0215(6)	0.0229(10)	0.0143(10)	0.0273(12)	0.0039(7)	-0.0081(9)	0.0028(8)	1
N1_1	0.13651(7)	-0.00268(13)	0.66464(16)	0.0073(3)	0.0074(4)	0.0072(5)	0.0074(6)	-0.0012(4)	-0.0004(4)	-0.0020(5)	1
N1_2	0.13979(7)	0.49493(13)	0.67016(17)	0.0080(3)	0.0093(5)	0.0059(5)	0.0087(6)	-0.0007(4)	-0.0003(4)	-0.0021(5)	1
D2_1	0.190(6)	-0.063(8)	0.701(11)	0.0251(6)	0.0317(9)	0.0325(10)	0.0111(10)	-0.0014(10)	0.0019(7)	0.0021(9)	0.045(2)
D2_2	0.1313(4)	0.4928(4)	0.8160(6)	0.0219(10)	0.0294(10)	0.026(2)	0.0105(16)	-0.0012(16)	0.0018(9)	0.0017(11)	0.953(3)
D3_1	0.998(3)	-0.184(4)	1.259(7)	0.0245(7)	0.0241(11)	0.0143(9)	0.0353(14)	-0.0077(8)	-0.0049(9)	-0.0055(9)	0.045(2)
D3_2	0.11108(17)	0.5827(2)	0.6170(3)	0.0244(6)	0.0340(12)	0.0126(9)	0.0266(12)	0.0069(8)	-0.0069(9)	0.0047(8)	0.953(3)
D4_1	0.182(3)	-0.172(4)	0.839(7)	0.0195(5)	0.0111(7)	0.0249(9)	0.0224(10)	-0.0004(8)	0.0033(6)	-0.0037(9)	0.045(2)
D4_2	0.21337(12)	0.4893(3)	0.6406(3)	0.0240(6)	0.0109(7)	0.0314(11)	0.0297(12)	0.0012(9)	0.0042(7)	-0.0037(10)	0.953(3)
D5_1	0.159(3)	0.175(4)	0.485(7)	0.0224(8)	0.0228(14)	0.0164(12)	0.0279(14)	0.0049(9)	-0.0020(10)	0.0078(9)	0.045(2)
D5_2	0.10325(15)	0.4156(2)	0.6092(3)	0.0212(6)	0.0234(10)	0.0144(9)	0.0258(12)	-0.0064(8)	-0.0057(8)	-0.0044(8)	0.953(3)
D6_1	0.14063(14)	-0.0075(3)	0.5172(3)	0.0251(6)	0.0317(9)	0.0325(10)	0.0111(10)	-0.0014(10)	0.0019(7)	0.0021(9)	0.955(2)
D6_2	0.163(3)	0.726(4)	0.528(5)	0.0219(10)	0.0294(10)	0.026(2)	0.0105(16)	-0.0012(16)	0.0018(9)	0.0017(11)	0.047(3)
D7_1	0.17019(16)	0.0828(2)	0.7138(4)	0.0245(7)	0.0241(11)	0.0143(9)	0.0353(14)	-0.0077(8)	-0.0049(9)	-0.0055(9)	0.955(2)
D7_2	0.131(10)	0.471(11)	0.835(18)	0.0244(6)	0.0340(12)	0.0126(9)	0.0266(12)	0.0069(8)	-0.0069(9)	0.0047(8)	0.047(3)
D8_1	0.06385(11)	-0.0023(2)	0.7024(3)	0.0195(5)	0.0111(7)	0.0249(9)	0.0224(10)	-0.0004(8)	0.0033(6)	-0.0037(9)	0.955(2)
D8_2	0.140(3)	1.177(4)	-0.171(7)	0.0240(6)	0.0109(7)	0.0314(11)	0.0297(12)	0.0012(9)	0.0042(7)	-0.0037(10)	0.047(3)
D9_1	0.17007(19)	-0.0850(3)	0.7239(5)	0.0224(8)	0.0228(14)	0.0164(12)	0.0279(14)	0.0049(9)	-0.0020(10)	0.0078(9)	0.955(2)
D9_2	0.194(3)	0.559(4)	0.279(6)	0.0212(6)	0.0234(10)	0.0144(9)	0.0258(12)	-0.0064(8)	-0.0057(8)	-0.0044(8)	0.047(3)

Table A.3: Refinement of single crystal neutron diffraction data of a $(ND_4)_2[FeCl_5(D_2O)]$ sample measured at 10 K in space group $P2_1/a$.

Space group	Cell parameters		R values
$P2_1/m$	$a = 13.57$ Å	$\alpha = 90.00°$	$R(\text{obs}) = 13.91$ %
	$b = 9.99$ Å	$\beta = 90.00°$	$\text{w}R(\text{obs}) = 18.11$ %
	$c = 6.94$ Å	$\gamma = 90.00°$	$R(\text{all}) = 19.39$ %
			$\text{w}R(\text{all}) = 18.30$ %

	x	y	z	$U_{\text{iso/ani}}$	U_{11}	U_{22}	U_{33}	U_{12}	U_{13}	U_{23}	occupancy
Fe1_1	0.1197(4)	1/4	0.1868(9)	0.0048(12)	–	–	–	–	–	–	1
Fe1_2	0.6200(5)	1/4	0.3143(11)	0.0081(13)	–	–	–	–	–	–	1
Cl1_1	0.1069(4)	0.0089(4)	0.1750(9)	0.0138(16)	0.018(3)	0.008(2)	0.016(3)	0.0050(18)	-0.007(3)	-0.0108(19)	1
Cl1_2	0.6057(4)	0.4907(5)	0.3262(9)	0.0133(16)	0.011(3)	0.014(3)	0.015(3)	0.0089(17)	-0.001(2)	0.016(2)	1
Cl2_1	0.0016(4)	1/4	0.4524(9)	0.0038(15)	-0.001(2)	0.018(3)	-0.005(2)	0	0.003(2)	0	1
Cl2_2	0.5118(6)	1/4	0.0395(14)	0.023(2)	0.034(5)	0.002(3)	0.033(5)	0	0.013(4)	0	1
Cl3_1	0.2496(5)	1/4	0.3928(11)	0.011(2)	0.027(4)	-0.004(3)	0.011(4)	0	0.011(3)	0	1
Cl3_2	0.7481(4)	1/4	0.0883(10)	0.0074(18)	0.003(3)	0.019(4)	0.001(3)	0	0.009(2)	0	1
Cl4_1	0.2270(5)	1/4	-0.0762(11)	0.0084(18)	0.003(3)	0.008(3)	0.014(4)	0	-0.010(3)	0	1
Cl4_2	0.7274(5)	1/4	0.5783(11)	0.012(2)	0.005(3)	0.017(4)	0.014(4)	0	-0.009(3)	0	1
O1_1	0.0071(7)	1/4	0.0176(16)	0.010(3)	0.007(4)	0.009(5)	0.013(6)	0	-0.032(4)	0	1
O1_2	0.4894(5)	1/4	0.5171(11)	-0.0080(19)	-0.0225(19)	0.005(4)	-0.007(4)	0	0.003(2)	0	1
D1_1	-0.0356(6)	0.1717(8)	-0.055(2)	0.054(4)	0.019(4)	0.021(4)	0.122(12)	-0.014(3)	-0.023(6)	-0.031(6)	1
D1_2	0.4657(5)	0.3273(6)	0.5500(10)	0.0096(17)	0.022(3)	0.005(3)	0.002(3)	0.005(3)	0.003(2)	0.004(2)	1
N1_1	0.1399(4)	0.0103(5)	0.6639(9)	0.0070(13)	0.006(2)	0.009(2)	0.006(3)	-0.0055(17)	0.0010(19)	0.0054(18)	1
N1_2	0.6340(4)	0.5101(5)	-0.1742(11)	0.0152(19)	0.015(3)	-0.0044(19)	0.035(4)	-0.0095(18)	0.004(3)	-0.007(2)	1
D2_1	0.1361(11)	0.0048(15)	0.813(2)	0.011(3)	0.020(6)	0.012(5)	0.000(6)	0.023(4)	-0.004(4)	-0.027(4)	0.463(14)
D2_2	0.611(6)	0.526(10)	-0.304(3)	0.541(6)	0.677(13)	0.985(12)	-0.039(6)	-0.817(9)	-0.049(7)	0.059(7)	0.452(16)
D3_1	0.1059(11)	-0.074(2)	0.616(3)	0.032(5)	0.007(5)	0.041(8)	0.047(10)	0.010(5)	-0.014(5)	-0.057(8)	0.463(14)
D3_2	0.619(2)	0.5829(18)	-0.115(3)	0.039(7)	0.088(15)	0.002(7)	0.028(10)	-0.035(9)	-0.043(11)	0.012(7)	0.452(16)
D4_1	0.2139(12)	0.0080(17)	0.630(2)	0.017(4)	0.016(6)	0.029(7)	0.007(7)	0.035(5)	0.003(4)	0.000(5)	0.463(14)
D4_2	0.716(2)	0.479(2)	-0.167(8)	0.123(11)	0.069(13)	0.009(7)	0.29(3)	-0.040(7)	-0.110(13)	0.045(10)	0.452(16)
D5_1	0.1084(12)	0.0797(13)	0.6161(19)	0.008(3)	0.029(7)	0.001(5)	-0.005(5)	0.007(4)	0.000(4)	-0.004(4)	0.463(14)
D5_2	0.6042(12)	0.4067(16)	-0.093(3)	0.028(6)	0.016(7)	0.009(6)	0.060(14)	-0.018(5)	0.005(7)	0.018(7)	0.452(16)
D6_1	0.1368(15)	-0.0313(15)	0.494(2)	0.033(5)	0.074(13)	0.020(7)	0.004(7)	-0.033(8)	0.002(6)	-0.001(6)	0.538(15)
...											

Table A.4: Refinement of single crystal neutron diffraction data of a $(ND_4)_2[FeCl_5(D_2O)]$ sample measured at 10 K in space group $P2_1/m$. Continued in Table A.5.

	x	y	z	$U_{\mathrm{iso/ani}}$	U_{11}	U_{22}	U_{33}	U_{12}	U_{13}	U_{23}	occupancy
...											
D6_2	0.6405(9)	0.5005(12)	-0.0239(18)	0.011(3)	0.020(6)	0.012(5)	0.000(6)	0.023(4)	-0.004(4)	-0.027(4)	0.537(14)
D7_1	0.172(4)	0.080(5)	0.707(4)	0.250(8)	0.386(16)	0.327(13)	0.037(11)	-0.378(10)	-0.104(10)	0.089(9)	0.538(15)
D7_2	0.6745(9)	0.4177(16)	-0.221(3)	0.032(5)	0.007(5)	0.041(8)	0.047(10)	0.010(5)	-0.014(5)	-0.057(8)	0.537(14)
D8_1	0.075(3)	0.0083(17)	0.711(8)	0.227(11)	0.273(16)	-0.007(6)	0.41(3)	-0.069(8)	0.308(11)	-0.090(9)	0.538(15)
D8_2	0.5657(9)	0.5131(14)	-0.2056(19)	0.017(4)	0.016(6)	0.029(7)	0.007(7)	0.035(5)	0.003(4)	0.000(5)	0.537(14)
D9_1	0.164(3)	-0.063(2)	0.755(11)	0.325(7)	0.237(10)	0.021(8)	0.716(16)	0.045(6)	-0.421(8)	-0.062(9)	0.538(15)
D9_2	0.6681(9)	0.5863(12)	-0.2222(16)	0.008(3)	0.029(7)	0.001(5)	-0.005(5)	0.007(4)	0.000(4)	-0.004(4)	0.537(14)

Table A.5: Continuation of Table A.4.

Space group	Cell parameters		R values
Pa	$a = 13.57\,\text{Å}$	$\alpha = 90.00°$	$R(\text{obs}) = 3.03\,\%$
	$b = 9.99\,\text{Å}$	$\beta = 90.00°$	$wR(\text{obs}) = 3.49\,\%$
	$c = 6.94\,\text{Å}$	$\gamma = 90.00°$	$R(\text{all}) = 4.42\,\%$
			$wR(\text{all}) = 3.59\,\%$

	x	y	z	$U_{\text{iso/ani}}$	U_{11}	U_{22}	U_{33}	U_{12}	U_{13}	U_{23}
Fe1_1	0.1159(2)	0.2538(3)	0.1874(4)	0.0041(5)	–	–	–	–	–	–
Fe1_2	-0.1223(2)	-0.2465(3)	-0.1878(4)	0.0023(5)	–	–	–	–	–	–
Cl1_1_1	0.0997(2)	0.0161(3)	0.1815(4)	0.0045(7)	0.0126(13)	-0.0019(11)	0.0028(12)	-0.0014(9)	-0.0030(10)	-0.0001(9)
Cl1_1_2	-0.10658(19)	-0.0046(3)	-0.1835(4)	0.0061(7)	0.0004(10)	0.0072(13)	0.0105(14)	-0.0012(10)	0.0023(9)	0.0007(11)
Cl1_2_1	0.1043(2)	0.4921(3)	0.1642(5)	0.0084(8)	0.0072(13)	0.0079(14)	0.0101(13)	-0.0046(11)	-0.0026(10)	-0.0041(12)
Cl1_2_2	-0.11532(19)	-0.4873(3)	-0.1687(4)	0.0013(6)	0.0035(10)	-0.0010(11)	0.0013(11)	0.0018(9)	0.0011(8)	0.0038(9)
Cl2_1	0.0038(2)	0.2584(3)	0.4568(4)	0.0042(7)	0.0062(12)	0.0049(13)	0.0015(12)	-0.0005(12)	0.0026(9)	0.0022(10)
Cl2_2	-0.0092(2)	-0.2525(3)	-0.4567(4)	0.0057(7)	0.0045(11)	0.0028(12)	0.0098(14)	0.0004(11)	-0.0014(10)	-0.0027(10)
Cl3_1	0.24696(19)	0.2547(3)	0.4017(5)	0.0040(7)	0.0016(11)	0.0041(13)	0.0063(14)	-0.0022(11)	-0.0011(9)	0.0023(11)
Cl3_2	-0.2562(2)	-0.2436(3)	-0.3988(5)	0.0060(8)	0.0093(13)	0.0046(13)	0.0041(13)	0.0008(12)	0.0005(10)	-0.0018(11)
Cl4_1	0.2233(2)	0.2505(4)	-0.0748(4)	0.0057(8)	0.0050(12)	0.0057(13)	0.0063(15)	-0.0016(11)	-0.0026(10)	-0.0024(11)
Cl4_2	-0.2307(2)	-0.2405(3)	0.0788(4)	0.0052(8)	0.0077(13)	0.0027(13)	0.0052(15)	0.0010(11)	0.0043(10)	0.0009(11)
O1_1	-0.0061(3)	0.2551(5)	0.0027(7)	0.0059(12)	0.005(2)	0.0033(18)	0.009(2)	0.0000(16)	-0.0008(17)	0.003(2)
O1_2	-0.0020(3)	-0.2448(5)	0.0094(7)	0.0078(13)	0.010(2)	0.008(2)	0.005(2)	-0.0015(19)	-0.0055(17)	-0.0062(19)
D1_1_1	-0.0364(4)	0.1734(6)	-0.0573(9)	0.0311(18)	0.028(3)	0.017(2)	0.048(4)	-0.006(2)	-0.006(2)	-0.010(2)
D1_1_2	0.0330(3)	-0.1684(5)	0.0482(7)	0.0131(12)	0.017(2)	0.011(2)	0.011(2)	-0.0039(16)	-0.0074(14)	0.0011(14)
D1_2_1	-0.0383(4)	0.3331(5)	-0.0504(9)	0.0215(16)	0.029(3)	0.009(2)	0.027(3)	0.006(2)	-0.005(2)	0.0006(19)
D1_2_2	0.0321(4)	-0.3235(5)	0.0511(9)	0.0220(16)	0.017(2)	0.016(3)	0.033(3)	0.002(2)	-0.010(2)	0.006(2)
N1_1_1	0.1295(2)	0.0010(3)	0.6645(5)	0.0074(8)	0.0127(13)	0.0036(14)	0.0060(14)	0.0052(10)	-0.0014(10)	-0.0044(11)
N1_1_2	-0.1431(2)	0.0063(3)	-0.6635(5)	0.0079(8)	0.0024(11)	0.0086(16)	0.0129(15)	-0.0074(10)	-0.0001(10)	0.0058(12)
N1_2_1	0.1347(2)	0.4969(3)	0.6734(4)	0.0090(9)	0.0187(15)	0.0071(16)	0.0011(14)	-0.0045(12)	0.0024(10)	-0.0011(11)
N1_2_2	-0.14502(19)	-0.4931(3)	-0.6660(5)	0.0066(8)	0.0021(11)	0.0046(15)	0.0132(15)	0.0016(10)	-0.0037(10)	0.0011(12)
D2_2_1	0.1297(4)	0.4966(5)	0.8165(8)	0.0259(8)	0.0358(15)	0.0219(13)	0.0201(14)	0.0012(12)	-0.0117(11)	0.0015(10)
D2_2_2	-0.1334(3)	-0.4871(6)	-0.8148(7)	0.0182(11)	0.0192(15)	0.027(2)	0.008(2)	-0.0041(15)	0.0148(14)	0.0009(17)
D3_2_1	0.1090(4)	0.5885(5)	0.6202(8)	0.0236(7)	0.0362(13)	0.0120(9)	0.0225(16)	0.0137(8)	-0.0110(11)	0.0101(9)
...										

Table A.6: Refinement of single crystal neutron diffraction data of a $(ND_4)_2[FeCl_5(D_2O)]$ sample measured at 10 K. Continued in Table A.7.

	x	y	z	$U_{\mathrm{iso/ani}}$	U_{11}	U_{22}	U_{33}	U_{12}	U_{13}	U_{23}
...										
D3_2_2	-0.1131(4)	-0.5776(6)	-0.6122(9)	0.0310(14)	0.035(3)	0.021(2)	0.037(3)	-0.006(2)	-0.0061(19)	-0.0050(18)
D4_2_1	0.2101(3)	0.4911(6)	0.6451(7)	0.0212(6)	0.0126(8)	0.0343(12)	0.0168(12)	0.0008(9)	0.0022(8)	0.0072(10)
D4_2_2	-0.2158(4)	-0.4888(6)	-0.6312(9)	0.0317(18)	0.014(2)	0.034(4)	0.047(3)	0.000(2)	0.006(2)	-0.014(3)
D5_2_1	0.0973(4)	0.4200(5)	0.6102(8)	0.0348(9)	0.0441(17)	0.0315(14)	0.0288(16)	-0.0316(13)	0.0108(12)	-0.0254(12)
D5_2_2	-0.1092(3)	-0.4118(4)	-0.6065(6)	0.0145(10)	0.0133(15)	0.0048(14)	0.025(2)	0.0108(13)	-0.0119(15)	0.0082(15)
D6_1_1	0.1357(4)	0.0027(6)	0.5172(8)	0.0412(17)	0.064(3)	0.034(3)	0.026(3)	0.010(2)	-0.024(2)	-0.004(2)
D6_1_2	-0.1453(3)	0.0157(5)	-0.5180(6)	0.0182(11)	0.0192(15)	0.027(2)	0.008(2)	-0.0041(15)	0.0148(14)	0.0009(17)
D7_1_1	0.1671(3)	0.0870(5)	0.7261(7)	0.0152(10)	0.0173(18)	0.0130(17)	0.0151(17)	-0.0080(15)	-0.0056(12)	-0.0075(13)
D7_1_2	-0.1733(4)	-0.0782(6)	-0.6956(9)	0.0310(14)	0.035(3)	0.021(2)	0.037(3)	-0.006(2)	-0.0061(19)	-0.0050(18)
D8_1_1	0.0585(3)	0.0002(5)	0.7014(6)	0.0154(13)	0.0101(18)	0.023(3)	0.013(2)	-0.0016(17)	0.0037(14)	0.0058(18)
D8_1_2	-0.0694(4)	0.0051(6)	-0.7033(9)	0.0317(18)	0.014(2)	0.034(4)	0.047(3)	0.000(2)	0.006(2)	-0.014(3)
D9_1_1	0.1645(5)	-0.0798(6)	0.7273(9)	0.0434(16)	0.055(3)	0.036(3)	0.039(3)	-0.018(2)	0.021(2)	-0.012(2)
D9_1_2	-0.1755(3)	0.0893(4)	-0.7181(6)	0.0145(10)	0.0133(15)	0.0048(14)	0.025(2)	0.0108(13)	-0.0119(15)	0.0082(15)

Table A.7: Continuation of Table A.6.

Temperature	Space group	Cell parameters		R values
room temperature	*Cmcm*	$a = 7.4288(4)$ Å	$\alpha = 90.0°$	$R(\text{obs}) = 2.57\,\%$
		$b = 17.3131(9)$ Å	$\beta = 90.0°$	$wR(\text{obs}) = 3.00\,\%$
		$c = 8.0696(4)$ Å	$\gamma = 90.0°$	$R(\text{all}) = 5.99\,\%$
				$wR(\text{all}) = 3.38\,\%$

	x	y	z	$U_{\text{iso/ani}}$	U_{11}	U_{22}	U_{33}	U_{12}	U_{13}	U_{23}
Cs1	0	0.470605(11)	1/4	0.02725(4)	0.03172(8)	0.03122(9)	0.01882(7)	0	0	0
Cs2	0	0.754766(12)	1/4	0.03297(5)	0.02977(9)	0.02664(8)	0.04251(11)	0	0	0
Fe1	0	0.121785(19)	1/4	0.01730(7)	0.01927(13)	0.01661(13)	0.01602(12)	0	0	0
Cl1	0	0.25361(4)	1/4	0.03011(17)	0.0313(3)	0.0168(2)	0.0422(4)	0	0	0
Cl2	0.22389(5)	0.11141(2)	0.45935(5)	0.03079(9)	0.02881(15)	0.03463(17)	0.02893(15)	0.00590(12)	-0.01209(12)	-0.00195(13)
O1	0	0.99580(12)	1/4	0.0314(6)	0.0576(15)	0.0169(8)	0.0197(8)	0	0	0

Temperature	Space group	Cell parameters		R values
100 K	*I*2/*c*	$a = 17.1206(14)$ Å	$\alpha = 90.0°$	$R(\text{obs}) = 3.17\,\%$
		$b = 7.3619(6)$ Å	$\beta = 90.000(14)°$	$wR(\text{obs}) = 3.94\,\%$
		$c = 16.086(4)$ Å	$\gamma = 90.0°$	$R(\text{all}) = 4.75\,\%$
				$wR(\text{all}) = 4.19\,\%$

	x	y	z	$U_{\text{iso/ani}}$	U_{11}	U_{22}	U_{33}	U_{12}	U_{13}	U_{23}
Cs1_1	-0.028711(10)	0.52178(3)	-0.125101(16)	0.00784(6)	0.00996(6)	0.00803(15)	0.00552(5)	-0.00032(4)	-0.00045(6)	0.00013(6)
Cs2_1	-0.256319(11)	0.4892(4)	0.12376(2)	0.00943(18)	0.00906(6)	0.0058(5)	0.01343(6)	0.00052(8)	0.00011(6)	0.00117(14)
Fe1_1	-0.121707(18)	-0.0056(2)	-0.37445(3)	0.00545(6)	—	—	—	—	—	—
Cl1_1	-0.25511(3)	0.0050(5)	-0.37596(5)	0.01112(12)	—	—	—	—	—	—
Cl2_1	-0.11638(11)	-0.2316(2)	-0.27473(10)	0.00900(12)	0.01055(18)	0.00818(6)	0.0083(3)	0.00035(9)	0.00069(19)	0.00220(17)
Cl2_2	-0.10840(11)	0.2196(2)	-0.26486(11)	0.00900(12)	0.01055(18)	0.00827(7)	0.0082(3)	0.00069(9)	-0.00035(19)	-0.00220(17)
Cl2_3	-0.11209(7)	0.24189(14)	-0.47235(7)	0.00900(12)	0.01055(18)	0.00818(6)	0.0083(3)	0.00035(9)	0.00069(19)	0.00220(17)
Cl2_4	-0.10908(7)	-0.21025(14)	-0.48593(7)	0.00900(12)	0.01055(18)	0.00827(7)	0.0082(3)	0.00069(9)	-0.00035(19)	-0.00220(17)
O1_1	0.00535(12)	-0.013(2)	-0.3746(2)	0.0071(15)	0.0055(6)	0.008(4)	0.0082(5)	-0.0002(8)	-0.00002(7)	0.0005(13)

Table A.8: Refinements of single-crystal X-ray diffraction data of the $Cs_2[FeCl_5(H_2O)]$ sample PB008-S003 at room temperature in space group *Cmcm* (left) and at 100 K in space group *I*2/*c*.

Temperature	Space group	Cell parameters		R values	
room temperature	$P6_3/mmc$	$a = 5.82900(10)$ Å	$\alpha = 90.0°$	$R(\text{obs}) = 5.96\,\%$	
		$b = 5.82900(10)$ Å	$\beta = 90.0°$	$\text{w}R(\text{obs}) = 8.41\,\%$	
		$c = 14.4870(6)$ Å	$\gamma = 120.0°$	$R(\text{all}) = 5.96\,\%$	
				$\text{w}R(\text{all}) = 8.41\,\%$	
				GoF = 5.39	

	x	y	z	$U_{\text{iso/ani}}$	U_{11}	U_{22}	U_{33}	U_{12}	U_{13}	U_{23}	occupancy
Ba1	0	0	1/4	0.0077(2)	–	–	–	–	–	–	1
Ba2	1/3	2/3	0.91031(6)	0.0089(2)	–	–	–	–	–	–	1
In3	0	0	0	0.0038(3)	–	–	–	–	–	–	0.985(11)
Ir3	0	0	0	0.0038(3)	–	–	–	–	–	–	0.015(11)
Ir4	1/3	2/3	0.15856(3)	0.00443(13)	–	–	–	–	–	–	0.927(14)
In4	1/3	2/3	0.15856(3)	0.00443(13)	–	–	–	–	–	–	0.073(14)
O5	0.4814(7)	0.5186(7)	1/4	0.0035(9)	–	–	–	–	–	–	1
O6	0.1702(7)	0.3405(13)	0.0837(5)	0.0144(12)	–	–	–	–	–	–	1

Table A.9: Refinement of single-crystal X-ray diffraction data of the Ba_3InIr_2O9 sample TD065-S001 at room temperature in space group $P6_3/mmc$. The In and Ir atoms share sites. The errors on the metric parameters are underestimated.

Temperature	Space group	Cell parameters			R values
room temperature	$C2/c$	$a = 5.82900(10)$ Å	$\alpha = 90.0°$		$R(\text{obs}) = 5.13\,\%$
		$b = 10.0961(2)$ Å	$\beta = 90.0°$		w$R(\text{obs}) = 5.01\,\%$
		$c = 14.4870(6)$ Å	$\gamma = 90.0°$		$R(\text{all}) = 5.13\,\%$
					w$R(\text{all}) = 5.01\,\%$
					GoF = 1.87

	x	y	z	$U_{\text{iso/ani}}$	U_{11}	U_{22}	U_{33}	U_{12}	U_{13}	U_{23}	occupancy
Ba1	0	0.00202(7)	1/4	0.00734(6)	–	–	–	–	–	–	1
Ba2	-0.00113(14)	0.33664(5)	0.089652(15)	0.00870(5)	–	–	–	–	–	–	1
In3	0	0	0	0.00389(7)	–	–	–	–	–	–	0.968(3)
Ir3	0	0	0	0.00389(7)	–	–	–	–	–	–	0.032(3)
Ir4	-0.00426(7)	0.33345(3)	0.841376(8)	0.00404(3)	–	–	–	–	–	–	0.897(3)
In4	-0.00426(7)	0.33345(3)	0.841376(8)	0.00404(3)	–	–	–	–	–	–	0.103(3)
O5_1	0	0.4880(8)	3/4	0.0038(3)	–	–	–	–	–	–	1
O5_3	0.2217(10)	0.2545(6)	0.7433(3)	0.0038(3)	–	–	–	–	–	–	1
O6_1	0.0242(15)	0.1716(5)	0.9153(4)	0.0038(3)	–	–	–	–	–	–	1
O6_2	0.2272(11)	0.4166(7)	0.9263(3)	0.0038(3)	–	–	–	–	–	–	1
O6_3	-0.2616(11)	0.4113(7)	0.9079(4)	0.0038(3)	–	–	–	–	–	–	1

Table A.10: Refinement of single-crystal X-ray diffraction data of the Ba_3InIr_2O9 sample TD065-S001 at room temperature in space group $C2/c$. The In and Ir atoms share sites. The O atoms are constrained to have the same ADPs. The errors on the metric parameters are underestimated.

Temperature	Space group	Cell parameters		R values	
room temperature	$P6_3/mmc$	$a = 5.7437(5)$ Å	$\alpha = 90.0°$	$R(\text{obs}) = 3.87\,\%$	
		$b = 5.7437$ Å	$\beta = 90.0°$	$\text{w}R(\text{obs}) = 6.03\,\%$	
		$c = 14.3767(12)$ Å	$\gamma = 120.0°$	$R(\text{all}) = 5.55\,\%$	
				$\text{w}R(\text{all}) = 6.19\,\%$	
				GoF = 3.52	

	x	y	z	$U_{\text{iso/ani}}$	U_{11}	U_{22}	U_{33}	U_{12}	U_{13}	U_{23}	occupancy
Ba1	0	0	1/4	0.00587(18)	–	–	–	–	–	–	1
Ba2	1/3	2/3	0.90485(5)	0.00673(15)	–	–	–	–	–	–	1
Nb3	0	0	0	0.0035(3)	–	–	–	–	–	–	0.883(6)
Ir3	0	0	0	0.0035(3)	–	–	–	–	–	–	0.117(6)
Ir4	1/3	2/3	0.15710(3)	0.00226(10)	–	–	–	–	–	–	0.960(8)
Nb4	1/3	2/3	0.15710(3)	0.00226(10)	–	–	–	–	–	–	0.040(8)
O5	0.4834(6)	0.5166(6)	1/4	0.0009(7)	–	–	–	–	–	–	1
O6	0.1641(5)	0.3282(10)	0.0781(3)	0.0074(7)	–	–	–	–	–	–	1

Table A.11: Refinements of single crystal X-ray diffraction data of the $Ba_3NbIr_2O_9$ sample TD105-S001 at room temperature in space group $P6_3/mmc$. The Nb and Ir atoms share sites. The errors on the metric parameters are underestimated.

Temperature	Space group	Cell parameters			R values
room temperature	$C2/c$	$a = 5.7437$ Å	$\alpha = 90.0°$		$R(\text{obs}) = 3.92\,\%$
		$b = 9.9484(12)$ Å	$\beta = 90.0°$		w$R(\text{obs}) = 4.49\,\%$
		$c = 14.3767(12)$ Å	$\gamma = 90.0°$		$R(\text{all}) = 7.57\,\%$
					w$R(\text{all}) = 4.77\,\%$
					GoF = 1.73

	x	y	z	$U_{\text{iso/ani}}$	U_{11}	U_{22}	U_{33}	U_{12}	U_{13}	U_{23}	occupancy
Ba1	0	0.00141(6)	1/4	0.00563(5)	–	–	–	–	–	–	1
Ba2	-0.00060(16)	0.33670(4)	0.095092(14)	0.00684(4)	–	–	–	–	–	–	1
Nb3	0	0	0	0.00286(8)	–	–	–	–	–	–	0.899(2)
Ir3	0	0	0	0.00286(8)	–	–	–	–	–	–	0.101(2)
Ir4	-0.00381(7)	0.33385(3)	0.842896(8)	0.00198(3)	–	–	–	–	–	–	0.934(2)
Nb4	-0.00381(7)	0.33385(3)	0.842896(8)	0.00198(3)	–	–	–	–	–	–	0.066(2)
O5_1	0	0.4937(6)	0.75	0.0010(2)	–	–	–	–	–	–	1
O5_3	0.2238(8)	0.2570(5)	0.7521(4)	0.0010(2)	–	–	–	–	–	–	1
O6_1	0.0198(14)	0.1630(4)	0.9207(4)	0.0010(2)	–	–	–	–	–	–	1
O6_2	0.2524(10)	0.4216(7)	0.9309(3)	0.0010(2)	–	–	–	–	–	–	1
O6_3	-0.2659(10)	0.4135(6)	0.9138(3)	0.0010(2)	–	–	–	–	–	–	1

Table A.12: Refinements of single crystal X-ray diffraction data of the $Ba_3NbIr_2O_9$ sample TD105-S001 at room temperature in space group $C2/c$. The Nb and Ir atoms share sites. The O atoms are constrained to have the same ADPs. The errors on the metric parameters are underestimated.

Temperature	Space group	Cell parameters		R values
room temperature	$P6_3/mmc$	$a = 5.7449(3)$ Å	$\alpha = 90.0°$	$R(\text{obs}) = 5.98\,\%$
		$b = 5.7449$ Å	$\beta = 90.0°$	w$R(\text{obs}) = 9.56\,\%$
		$c = 14.3806(9)$ Å	$\gamma = 120.0°$	$R(\text{all}) = 6.10\,\%$
				w$R(\text{all}) = 9.58\,\%$
				GoF = 6.52

	x	y	z	$U_{\text{iso/ani}}$	U_{11}	U_{22}	U_{33}	U_{12}	U_{13}	U_{23}	occupancy
Ba1	0	0	1/4	0.0055(3)	–	–	–	–	–	–	1
Ba2	1/3	2/3	0.90484(7)	0.0061(2)	–	–	–	–	–	–	1
Nb3	0	0	0	0.0025(4)	–	–	–	–	–	–	0.911(10)
Ir3	0	0	0	0.0025(4)	–	–	–	–	–	–	0.089(10)
Ir4	1/3	2/3	0.15717(4)	0.00174(15)	–	–	–	–	–	–	0.955(13)
Nb4	1/3	2/3	0.15717(4)	0.00174(15)	–	–	–	–	–	–	0.045(13)
O5	0.4828(7)	0.5172(7)	1/4	-0.0023(8)	–	–	–	–	–	–	1
O6	0.1639(7)	0.3278(14)	0.0779(5)	0.0066(10)	–	–	–	–	–	–	1

Table A.13: Refinements of single crystal X-ray diffraction data of the $Ba_3NbIr_2O_9$ sample TD105-S002 at room temperature in space group $P6_3/mmc$. The Nb and Ir atoms share sites. The errors on the metric parameters are underestimated.

Temperature	Space group	Cell parameters			R values
room temperature	$C2/c$	$a = 5.7449$ Å	$\alpha = 90.0°$		$R(\text{obs}) = 4.51\,\%$
		$b = 9.9505(7)$ Å	$\beta = 90.0°$		$\text{w}R(\text{obs}) = 5.29\,\%$
		$c = 14.3806(9)$ Å	$\gamma = 90.0°$		$R(\text{all}) = 5.73\,\%$
					$\text{w}R(\text{all}) = 5.45\,\%$
					GoF = 2.30

	x	y	z	$U_{\text{iso/ani}}$	U_{11}	U_{22}	U_{33}	U_{12}	U_{13}	U_{23}	occupancy
Ba1	0	0.00557(8)	1/4	0.00421(7)	–	–	–	–	–	–	1
Ba2	0.0003(2)	0.33479(6)	0.095080(18)	0.00629(5)	–	–	–	–	–	–	1
Nb3	0	0	0	0.00165(10)	–	–	–	–	–	–	0.928(3)
Ir3	0	0	0	0.00165(10)	–	–	–	–	–	–	0.072(3)
Ir4	-0.00348(10)	0.33268(3)	0.842840(10)	0.00150(3)	–	–	–	–	–	–	0.935(3)
Nb4	-0.00348(10)	0.33268(3)	0.842840(10)	0.00150(3)	–	–	–	–	–	–	0.065(3)
O5_1	0	0.4754(6)	0.75	-0.0028(3)	–	–	–	–	–	–	1
O5_2	0.2429(8)	0.2557(5)	0.7561(3)	-0.0028(3)	–	–	–	–	–	–	1
O6_1	0.0154(15)	0.1753(4)	0.9205(4)	-0.0028(3)	–	–	–	–	–	–	1
O6_2	0.2685(11)	0.4126(6)	0.9312(3)	-0.0028(3)	–	–	–	–	–	–	1
O6_3	-0.2767(11)	0.4155(6)	0.9145(3)	-0.0028(3)	–	–	–	–	–	–	1

Table A.14: Refinements of single crystal X-ray diffraction data of the $Ba_3NbIr_2O_9$ sample TD105-S002 at room temperature in space group $C2/c$. The Nb and Ir atoms share sites. The O atoms are constrained to have the same ADPs. The errors on the metric parameters are underestimated.

Temperature	Space group	Cell parameters		R values
room temperature	$P6_3/mmc$	$a = 5.90350(10)$ Å	$\alpha = 90.0°$	$R(\text{obs}) = 5.11\,\%$
		$b = 5.90350(10)$ Å	$\beta = 90.0°$	$\text{w}R(\text{obs}) = 7.38\,\%$
		$c = 14.7147(6)$ Å	$\gamma = 120.0°$	$R(\text{all}) = 5.78\,\%$
				$\text{w}R(\text{all}) = 7.44\,\%$
				GoF = 4.68

	x	y	z	$U_{\text{iso/ani}}$	U_{11}	U_{22}	U_{33}	U_{12}	U_{13}	U_{23}	occupancy
Ba1	0	0	1/4	0.00824(15)	–	–	–	–	–	–	1
Ba2	1/3	2/3	0.90001(5)	0.00928(14)	–	–	–	–	–	–	1
Ce3	0	0	0	0.00391(14)	–	–	–	–	–	–	1.005(12)
Ir3	0	0	0	0.00391(14)	–	–	–	–	–	–	-0.005(12)
Ir4	1/3	2/3	0.16382(2)	0.00402(8)	–	–	–	–	–	–	1.062(15)
Ce4	1/3	2/3	0.16382(2)	0.00402(8)	–	–	–	–	–	–	-0.062(15)
O5	0.4858(5)	0.5142(5)	1/4	0.0048(6)	–	–	–	–	–	–	1
O6	0.1742(4)	0.3484(8)	0.0866(4)	0.0101(6)	–	–	–	–	–	–	1

Table A.15: Refinements of single crystal X-ray diffraction data of the $Ba_3CeIr_2O_9$ sample PB011-S001 at room temperature in space group $P6_3/mmc$. The Ce and Ir atoms share sites. The errors on the metric parameters are underestimated.

Temperature	Space group	Cell parameters			R values
room temperature	$C2/c$	$a = 5.90350(10)$ Å	$\alpha = 90.0°$	$R(\text{obs}) = 5.13\,\%$	
		$b = 10.2252(2)$ Å	$\beta = 90.0°$	$wR(\text{obs}) = 5.87\,\%$	
		$c = 14.7147(6)$ Å	$\gamma = 90.0°$	$R(\text{all}) = 6.61\,\%$	
				$wR(\text{all}) = 5.98\,\%$	
				GoF = 2.51	

	x	y	z	$U_{\text{iso/ani}}$	U_{11}	U_{22}	U_{33}	U_{12}	U_{13}	U_{23}	occupancy
Ba1	0	-0.00115(10)	1/4	0.00820(5)	–	–	–	–	–	–	1
Ba2	-0.00055(17)	0.33540(6)	0.099854(18)	0.00950(5)	–	–	–	–	–	–	1
Ce3	0	0	0	0.00395(5)	–	–	–	–	–	–	1.010(4)
Ir3	0	0	0	0.00395(5)	–	–	–	–	–	–	-0.010(4)
Ir4	-0.00328(7)	0.33385(4)	0.836105(8)	0.00379(3)	–	–	–	–	–	–	1.007(5)
Ce4	-0.00328(7)	0.33385(4)	0.836105(8)	0.00379(3)	–	–	–	–	–	–	-0.007(5)
O5_1	0	0.4964(6)	0.75	0.0010(3)	–	–	–	–	–	–	1
O5_3	0.2179(6)	0.2473(3)	0.7443(3)	0.0010(3)	–	–	–	–	–	–	1
O6_1	0.000(2)	0.1792(4)	0.9119(4)	0.0010(3)	–	–	–	–	–	–	1
O6_2	0.2451(9)	0.4000(5)	0.9229(3)	0.0010(3)	–	–	–	–	–	–	1
O6_3	-0.2650(9)	0.4062(5)	0.9055(4)	0.0010(3)	–	–	–	–	–	–	1

Table A.16: Refinements of single crystal X-ray diffraction data of the $Ba_3CeIr_2O_9$ sample PB011-S001 at room temperature in space group $C2/c$. The Ce and Ir atoms share sites. The O atoms are constrained to have the same ADPs. The errors on the metric parameters are underestimated.

Temperature	Space group	Cell parameters		R values
room temperature	$Fm\bar{3}m$	$a = 8.4558(8)$ Å	$\alpha = 90.0°$	$R(\text{obs}) = 4.25\,\%$
		$b = 8.4558$ Å	$\beta = 90.0°$	$\text{w}R(\text{obs}) = 5.42\,\%$
		$c = 8.4558$ Å	$\gamma = 90.0°$	$R(\text{all}) = 4.35\,\%$
				$\text{w}R(\text{all}) = 5.43\,\%$
				GoF = 4.07

	x	y	z	$U_{\text{iso/ani}}$	U_{11}	U_{22}	U_{33}	U_{12}	U_{13}	U_{23}	occupancy
Ba1	1/4	1/4	1/4	0.0061(3)	–	–	–	–	–	–	1
Ce2	0	0	0	0.0008(3)	–	–	–	–	–	–	0.998(15)
Ir2	0	0	0	0.0008(3)	–	–	–	–	–	–	0.002(15)
Ir3	0	0	1/2	-0.0009(2)	–	–	–	–	–	–	0.88(3)
Ce3	0	0	1/2	-0.0009(2)	–	–	–	–	–	–	0.12(3)
O4	0.2607(6)	0	0	0.0100(10)	–	–	–	–	–	–	1

Table A.17: Structural refinements of single-crystal X-ray diffraction data measured at room temperature of the Ba_2CeIrO_6 sample AR506a in space group $Fm\bar{3}m$.

Temperature	Space group	Cell parameters		R values
room temperature	$C2/m$	$a = 8.4558(8)$ Å	$\alpha = 90.0°$	$R(\text{obs}) = 9.05\,\%$
		$b = 8.4558$ Å	$\beta = 90.0°$	$\text{w}R(\text{obs}) = 10.83\,\%$
		$c = 8.4558$ Å	$\gamma = 90.0°$	$R(\text{all}) = 9.32\,\%$
				$\text{w}R(\text{all}) = 10.87\,\%$
				GoF = 3.77

	x	y	z	$U_{\text{iso/ani}}$	U_{11}	U_{22}	U_{33}	U_{12}	U_{13}	U_{23}	occupancy
Ba1	0.2487(8)	0.250(5)	0.2513(8)	0.0059(2)	–	–	–	–	–	–	1
Ce2	0	0	0	0.0006(2)	–	–	–	–	–	–	0.987(11)
Ir2	0	0	0	0.0006(2)	–	–	–	–	–	–	0.013(11)
Ir3	0	0	1/2	-0.00099(12)	–	–	–	–	–	–	0.912(16)
Ce3	0	0	1/2	-0.00099(12)	–	–	–	–	–	–	0.088(16)
O4_1	0.2607(5)	-0.0002(11)	-0.0002(10)	0.0100(7)	–	–	–	–	–	–	1
O4_9	0.0000(6)	0.2605(5)	0.0000(6)	0.0102(7)	–	–	–	–	–	–	1

Table A.18: Structural refinements of single-crystal X-ray diffraction data measured at room temperature of the Ba_2CeIrO_6 sample AR506a in space group $C2/m$. The structure with space group $C2/m$ is transformed to the basis of $Fm\bar{3}m$. The standard setting of space group $C2/m$ can be obtained by the basis transformation $(\vec{a}, \vec{b}, \vec{c})_{C2/m} = \left(-\frac{1}{2}\vec{a} - \vec{b} + \frac{1}{2}\vec{c}, -\frac{1}{2}\vec{a} - \frac{1}{2}\vec{c}, \frac{1}{2}\vec{a} - \frac{1}{2}\vec{c}\right)_{Fm\bar{3}m}$.

Temperature	Space group	Cell parameters		R values
room temperature	$Fm\overline{3}m$	$a = 8.47860(10)$ Å	$\alpha = 90.0°$	$R(\text{obs}) = 2.14\,\%$
		$b = 8.47860(10)$ Å	$\beta = 90.0°$	$\text{w}R(\text{obs}) = 2.83\,\%$
		$c = 8.47860(10)$ Å	$\gamma = 90.0°$	$R(\text{all}) = 2.14\,\%$
				$\text{w}R(\text{all}) = 2.83\,\%$
				GoF = 1.82

	x	y	z	$U_{\text{iso/ani}}$	U_{11}	U_{22}	U_{33}	U_{12}	U_{13}	U_{23}	occupancy
Ba1	1/4	1/4	1/4	0.01306(16)	–	–	–	–	–	–	1
Ce2	0	0	0	0.00757(16)	–	–	–	–	–	–	1.006(8)
Ir2	0	0	0	0.00757(16)	–	–	–	–	–	–	-0.006(8)
Ir3	0	0	1/2	0.00466(11)	–	–	–	–	–	–	0.819(11)
Ce3	0	0	1/2	0.00466(11)	–	–	–	–	–	–	0.181(11)
O4	0.2591(4)	0	0	0.0203(8)	–	–	–	–	–	–	1

Table A.19: Structural refinements of single crystal X-ray diffraction data measured at room temperature of the Ba_2CeIrO_6 sample PB016-S001 in space group $Fm\overline{3}m$.

Temperature	Space group	Cell parameters		R values
room temperature	$C2/m$	$a = 8.47860(10)$ Å	$\alpha = 90.0°$	$R(\text{obs}) = 3.35\,\%$
		$b = 8.47860(10)$ Å	$\beta = 90.0°$	$wR(\text{obs}) = 2.99\,\%$
		$c = 8.47860(10)$ Å	$\gamma = 90.0°$	$R(\text{all}) = 5.09\,\%$
				$wR(\text{all}) = 3.20\,\%$
				GoF = 1.11

	x	y	z	$U_{\text{iso/ani}}$	U_{11}	U_{22}	U_{33}	U_{12}	U_{13}	U_{23}	occupancy
Ba1	0.2517(2)	0.24568(18)	0.2483(2)	0.01204(6)	–	–	–	–	–	–	1
Ce2	0	0	0	0.00472(10)	–	–	–	–	–	–	0.962(4)
Ir2	0	0	0	0.00472(10)	–	–	–	–	–	–	0.038(4)
Ir3	0	0	1/2	0.00679(9)	–	–	–	–	–	–	0.803(5)
Ce3	0	0	1/2	0.00679(9)	–	–	–	–	–	–	0.197(5)
O4_1	0.2572(5)	-0.0299(4)	0.0118(8)	0.0059(8)	–	–	–	–	–	–	1
O4_9	0.0114(3)	0.2675(3)	-0.0114(3)	-0.0150(2)	–	–	–	–	–	–	1

Table A.20: Structural refinements of single crystal X-ray diffraction data measured at room temperature of the Ba_2CeIrO_6 sample PB016-S001 in space group $C2/m$. For the choice of basis vectors, see Table A.18.

Temperature	Space group	Cell parameters		R values
100 K	$Fm\bar{3}m$	$a = 8.4700(8)$ Å	$\alpha = 90.0°$	$R(\text{obs}) = 3.16\,\%$
		$b = 8.4700(8)$ Å	$\beta = 90.0°$	$wR(\text{obs}) = 3.09\,\%$
		$c = 8.4700(8)$ Å	$\gamma = 90.0°$	$R(\text{all}) = 7.20\,\%$
				$wR(\text{all}) = 3.26\,\%$
				GoF = 1.31

	x	y	z	$U_{\text{iso/ani}}$	U_{11}	U_{22}	U_{33}	U_{12}	U_{13}	U_{23}	occupancy
Ba1	1/4	1/4	1/4	0.0108(3)	–	–	–	–	–	–	1
Ce2	0	0	0	0.0078(3)	–	–	–	–	–	–	0.995(13)
Ir2	0	0	0	0.0078(3)	–	–	–	–	–	–	0.005(13)
Ir3	0	0	1/2	0.0054	–	–	–	–	–	–	0.842(17)
Ce3	0	0	1/2	0.0054	–	–	–	–	–	–	0.158(17)
O4	0.2591(7)	0	0	0.0186(15)	0.012(3)	0.022(2)	0.022(2)	0	0	0	1

Table A.21: Structural refinements of single-crystal X-ray diffraction data of the Ba_2CeIrO_6 sample PB016-S002 measured at a temperature of 100 K in space group $Fm\bar{3}m$.

Temperature	Space group	Cell parameters		R values
100 K	$C2/m$	$a = 8.470(3)$ Å	$\alpha = 90.0°$	$R(\text{obs}) = 5.08\,\%$
		$b = 8.47$ Å	$\beta = 90.0°$	$wR(\text{obs}) = 3.83\,\%$
		$c = 8.47$ Å	$\gamma = 90.0°$	$R(\text{all}) = 24.53\,\%$
				$wR(\text{all}) = 4.56\,\%$
				GoF = 0.94

	x	y	z	$U_{\text{iso/ani}}$	U_{11}	U_{22}	U_{33}	U_{12}	U_{13}	U_{23}	occupancy
Ba1	0.2552(8)	0.2545(17)	0.2448(8)	0.00933(16)	–	–	–	–	–	–	1
Ce2	0	0	0	-0.00153(17)	–	–	–	–	–	–	1.008(9)
Ir2	0	0	0	-0.00153(17)	–	–	–	–	–	–	-0.008(9)
Ir3	0	0	1/2	0.0128(3)	–	–	–	–	–	–	0.810(11)
Ce3	0	0	1/2	0.0128(3)	–	–	–	–	–	–	0.190(11)
O4_1	0.2586(15)	0.0000(8)	0.0001(9)	0.019(2)	–	–	–	–	–	–	1
O4_9	0.0003(11)	0.260(3)	-0.0003(11)	0.021(5)	–	–	–	–	–	–	1

Table A.22: Structural refinements of single-crystal X-ray diffraction data of the Ba_2CeIrO_6 sample PB016-S002 measured at a temperature of 100 K in space group $C2/m$. For the choice of basis vectors, see Table A.18.

$Fm\bar{3}m$	R(obs) :	3.63 %	$C2/m$	R(obs) :	5.07 % → 5.23 %
	wR(obs) :	3.82 %		wR(obs) :	3.97 % → 4.01 %
	R(all) :	7.50 %		R(all) :	20.55 % → 24.09 %
	wR(all) :	4.02 %		wR(all) :	5.33 % → 4.72 %
$R3m$	R(obs) :	4.91 % → 4.86 %	$R\bar{3}$	R(obs) :	5.08 % → 5.20 %
	wR(obs) :	3.94 % → 3.76 %		wR(obs) :	3.97 % → 4.06 %
	R(all) :	22.09 % → 26.26 %		R(all) :	20.76 % → 21.96 %
	wR(all) :	5.69 % → 4.69 %		wR(all) :	5.36 % → 5.05 %
$R32$	R(obs) :	4.94 % → 5.00 %	$R\bar{3}m$	R(obs) :	5.05 % → 5.17 %
	wR(obs) :	3.97 % → 4.02 %		wR(obs) :	3.93 % → 4.03 %
	R(all) :	22.49 % → 24.21 %		R(all) :	21.55 % → 22.71 %
	wR(all) :	5.76 % → 5.27 %		wR(all) :	5.37 % → 5.05 %
$I\bar{4}2m$	R(obs) :	5.01 % → 5.06 %	$Immm$	R(obs) :	5.07 % → 5.31 %
	w5obs	3.98 % → 4.03 %		wR(obs) :	3.97 % → 4.05 %
	R(all) :	22.24 % → 23.53 %		R(all) :	20.55 % → 24.29 %
	wR(all) :	5.69 % → 5.23 %		wR(all) :	5.33 % → 4.75 %
$I4mm$	R(obs) :	4.91 % → 5.20 %	$I4/m$	R(obs) :	5.17 % → 5.26 %
	wR(obs) :	3.94 % → 4.26 %		wR(obs) :	4.05 % → 4.12 %
	R(all) :	22.09 % → 26.59 %		R(all) :	21.11 % → 22.21 %
	wR(all) :	5.69 % → 5.17 %		wR(all) :	5.45 % → 5.12 %
$I\bar{4}m2$	R(obs) :	4.56 % → 4.79 %	$Fmmm$	R(obs) :	4.26 % → 4.26 %
	w5obs	3.72 % → 3.81 %		wR(obs) :	3.70 % → 3.70 %
	R(all) :	17.26 % → 18.01 %		R(all) :	12.72 % → 12.80 %
	wR(all) :	4.68 % → 4.47 %		wR(all) :	4.25 % → 4.17 %
$I422$	R(obs) :	4.57 % → 4.62 %	$I4/mmm$	R(obs) :	4.26 % → 4.26 %
	wR(obs) :	3.73 % → 3.71 %		wR(obs) :	3.70 % → 3.71 %
	R(all) :	17.30 % → 17.79 %		R(all) :	12.72 % → 12.80 %
	wR(all) :	4.69 % → 4.47 %		wR(all) :	4.25 % → 4.18 %
$F23$	R(obs) :	3.87 % → 4.01 %	$F\bar{4}3m$	R(obs) :	3.96 % → 4.05 %
	wR(obs) :	3.63 % → 3.69 %		wR(obs) :	3.79 % → 3.82 %
	R(all) :	12.89 % → 12.94 %		R(all) :	11.13 % → 11.11 %
	wR(all) :	4.22 % → 4.13 %		wR(all) :	4.15 % → 4.10 %
$Fm\bar{3}$	R(obs) :	3.72 % → 3.73 %	$F432$	R(obs) :	3.72 % → 3.72 %
	wR(obs) :	3.71 % → 3.72 %		wR(obs) :	3.78 % → 3.72 %
	R(all) :	8.86 % → 8.86 %		R(all) :	9.57 % → 9.66 %
	wR(all) :	4.00 % → 3.99 %		wR(all) :	4.17 % → 4.11 %

Table A.23: R values of refinements of single-crystal X-ray diffraction data of sample PB016-S002 at 100 K. All ADPs are isotropic. On the left-hand side of the arrow "→", the R value of the refinement in the low symmetry space group using the result of the refinement in $Fm\bar{3}m$ is shown. The R values with the structural parameters refined according to the low symmetry space group are printed on the right-hand side of the arrow.

Temperature	Space group	Cell parameters		R values
room temperature	$Fm\bar{3}m$	$a = 8.3870(4)$ Å	$\alpha = 90.0°$	R(obs) = 2.21 %
		$b = 8.387$ Å	$\beta = 90.0°$	wR(obs) = 4.04 %
		$c = 8.387$ Å	$\gamma = 90.0°$	R(all) = 2.21 %
				wR(all) = 4.04 %
				GoF = 3.62

	x	y	z	$U_{\mathrm{iso/ani}}$	U_{11}	U_{22}	U_{33}	U_{12}	U_{13}	U_{23}
Ba1	1/4	1/4	1/4	0.00787(17)	–	–	–	–	–	–
Pr2	0	0	0	0.00368(15)	–	–	–	–	–	–
Ir3	0	0	1/2	0.00291(13)	–	–	–	–	–	–
O4	0.2616(4)	0	0	0.0096(5)	–	–	–	–	–	–

Temperature	Space group	Cell parameters		R values
room temperature	$I4/m$	$a = 8.3870(4)$ Å	$\alpha = 90.0°$	R(obs) = 2.76 %
		$b = 8.387$ Å	$\beta = 90.0°$	wR(obs) = 3.74 %
		$c = 8.387$ Å	$\gamma = 90.0°$	R(all) = 2.76 %
				wR(all) = 3.75 %
				GoF = 1.98

	x	y	z	$U_{\mathrm{iso/ani}}$	U_{11}	U_{22}	U_{33}	U_{12}	U_{13}	U_{23}
Ba1	1/4	1/4	1/4	0.00759(4)	–	–	–	–	–	–
Pr2	0	0	0	0.00330(4)	–	–	–	–	–	–
Ir3	0	0	1/2	0.00267(3)	–	–	–	–	–	–
O4_1	0.2616(12)	0	0	0.0048(3)	–	–	–	–	–	–
O4_3	0	0.2616(7)	-0.0188(4)	0.0048(3)	–	–	–	–	–	–

Table A.24: Refinement of single-crystal X-ray diffraction data of the Ba_2PrIrO_6 sample PB019-S002 at room temperature in space groups $Fm\bar{3}m$ and $I4/m$. The transformation for standard setting of $I4/m$ is $(\vec{a}, \vec{b}, \vec{c})_{I4/m} = (\frac{1}{2}\vec{b} + \frac{1}{2}\vec{c}, -\frac{1}{2}\vec{b} + \frac{1}{2}\vec{c}, \vec{a})_{Fm\bar{3}m}$ without origin shift.

ZW004-S001			U_{11}	U_{22}	U_{33}	U_{12}	U_{13}	U_{23}
$R\bar{3}m$	1.9 K	Bi1	0.0042(4)	0.0042(4)	0.0119(7)	0.00207(19)	0	0
		Se2	0.0045(5)	0.0045(5)	0.0100(10)	0.0022(2)	0	0
		Se3	0.0039(4)	0.0039(4)	0.0128(9)	0.0020(2)	0	0
	4.4 K	Bi1	0.0097(5)	0.0097(5)	0.0188(10)	0.0049(2)	0	0
		Se2	0.0095(6)	0.0095(6)	0.0188(13)	0.0047(3)	0	0
		Se3	0.0099(5)	0.0099(5)	0.0198(12)	0.0050(3)	0	0
	300 K	Bi1	0.0155(7)	0.0155(7)	0.0334(13)	0.0077(4)	0	0
		Se2	0.0132(9)	0.0132(9)	0.0255(15)	0.0066(5)	0	0
		Se3	0.0147(8)	0.0147(8)	0.0287(13)	0.0073(4)	0	0
$C2/m$	1.9 K	Bi1	0.0025(3)	0.0025(3)	0.0118(3)	0.00126(13)	0	0
		Se2	0.0027(5)	0.0027(5)	0.0112(5)	0.0014(2)	0	0
		Se3	0.0043(4)	0.0043(4)	0.0113(4)	0.00213(19)	0	0
	4.4 K	Bi1	0.0076(4)	0.0076(4)	0.0181(6)	0.0038(2)	0	0
		Se2	0.0073(6)	0.0073(6)	0.0192(9)	0.0037(3)	0	0
		Se3	0.0097(5)	0.0097(5)	0.0172(7)	0.0049(3)	0	0
	300 K	Bi1	0.0141(5)	0.0141(6)	0.0331(6)	0.0071(3)	0	0
		Se2	0.0122(9)	0.0122(9)	0.0259(9)	0.0061(5)	0	0
		Se3	0.0147(8)	0.0147(8)	0.0277(7)	0.0073(4)	0	0
MB003-S001			U_{11}	U_{22}	U_{33}	U_{12}	U_{13}	U_{23}
$R\bar{3}m$	2 K	Bi1	0.0013(4)	0.0013(4)	0.0100(6)	0.00067(19)	0	0
		Se2	0.0010(4)	0.0010(4)	0.0073(8)	0.0005(2)	0	0
		Se3	0.0016(4)	0.0016(4)	0.0103(7)	0.00081(20)	0	0
	300 K	Bi1	0.0083(7)	0.0083(7)	0.0212(12)	0.0042(4)	0	0
		Se2	0.0068(9)	0.0068(9)	0.0120(15)	0.0034(4)	0	0
		Se3	0.0077(8)	0.0077(8)	0.0159(13)	0.0038(4)	0	0
$C2/m$	2 K	Bi1	0.00141(17)	0.00141(17)	0.0091(2)	0.00071(8)	0	0
		Se2	0.0016(3)	0.0016(3)	0.0068(3)	0.00081(14)	0	0
		Se3	0.0021(2)	0.0021(2)	0.0095(2)	0.00103(11)	0	0
	300 K	Bi1	0.0078(4)	0.0078(4)	0.0197(5)	0.0039(2)	0	0
		Se2	0.0069(7)	0.0069(7)	0.0117(7)	0.0034(3)	0	0
		Se3	0.0085(5)	0.0085(5)	0.0145(5)	0.0043(3)	0	0

Table A.25: Anisotropic atomic displacement parameters of the atoms of Bi_2Se_3 of the samples ZW004-S001 and MB003-S001 at different temperatures refined in space groups $R\bar{3}m$ and $C2/m$. The constraints for the ADPs in space group $R\bar{3}m$ are also used for the refinements in space group $C2/m$.

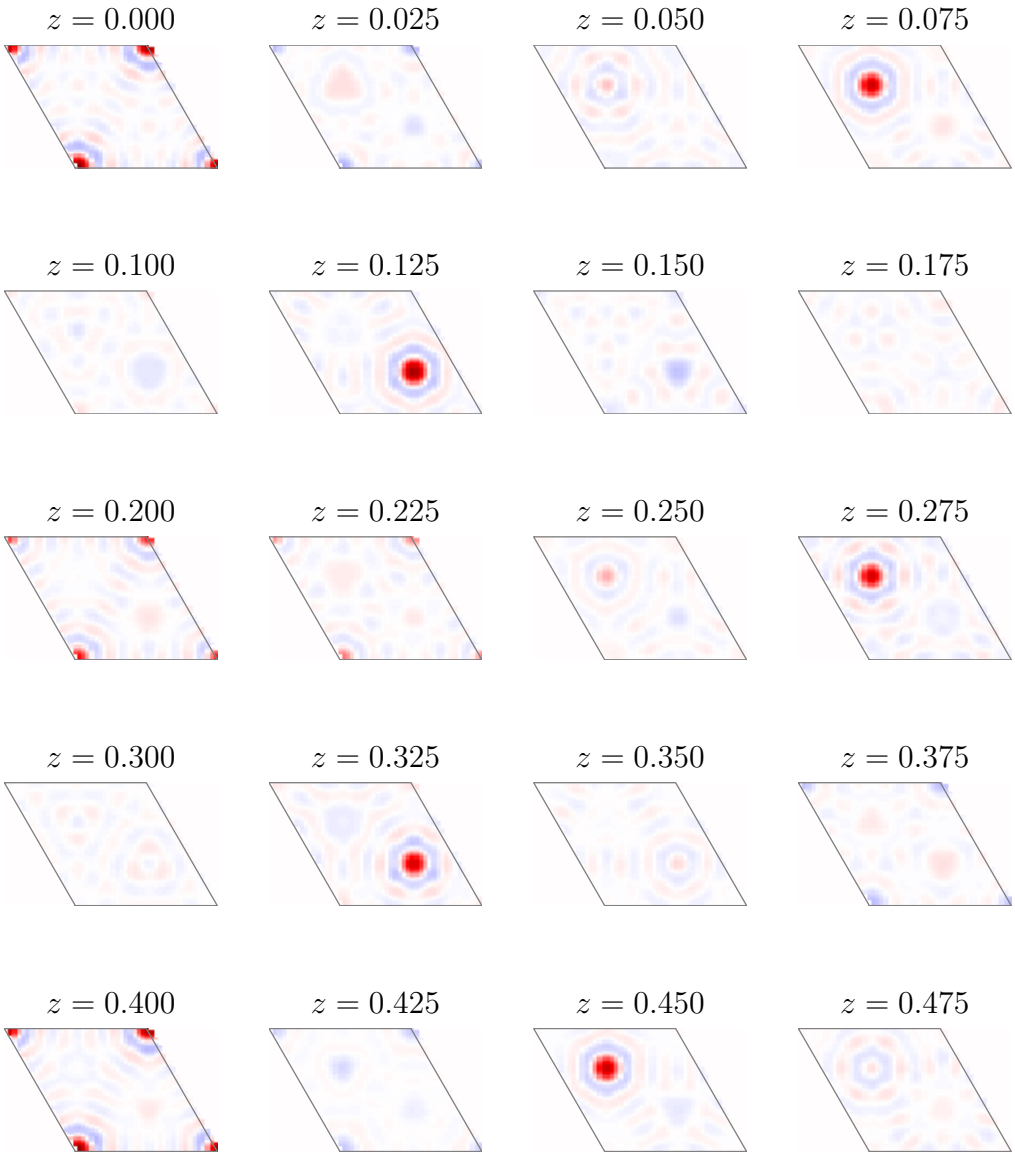

Figure A.1: Slices along the *ab* plane of a Fourier map of the density inside a unit cell at different z coordinates for the refinement in space group $R\bar{3}m$ of single crystal neutron diffraction data of sample ZW004-S001 measured at 1.9 K. No Cu atoms are included in the model. Sections of the nuclear density of the following atoms are visible according to Figure 8.8: At $z = 0$: Se2. At $z = 0.075$: Bi1. At $z = 0.125$: Se3. At $z = 0.2$: Se3. At $z = 0.275$: Bi1. At $z = 0.325$: Se2. At $z = 0.4$: Bi1. At $z = 0.45$: Se3.

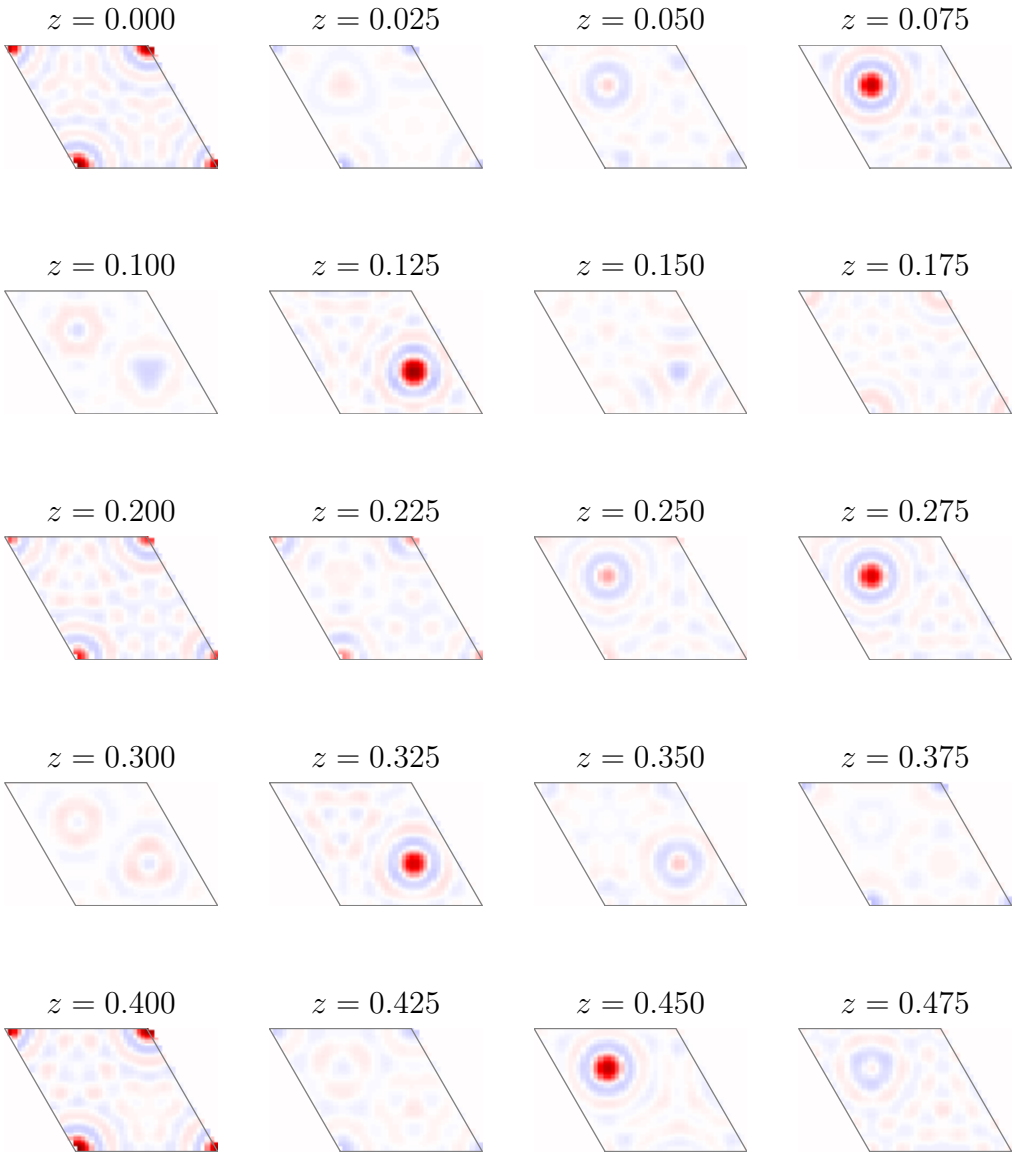

Figure A.2: Slices along the *ab* plane of a Fourier map of the density inside a unit cell at different z coordinates for the refinement in space group $R\bar{3}m$ of single crystal neutron diffraction data of sample MB003-S001 measured at 2 K. No Cu atoms are included in the model. Sections of the nuclear density of the following atoms are visible according to Figure 8.8: At $z = 0$: Se2. At $z = 0.075$: Bi1. At $z = 0.125$: Se3. At $z = 0.2$: Se3. At $z = 0.275$: Bi1. At $z = 0.325$: Se2. At $z = 0.4$: Bi1. At $z = 0.45$: Se3.

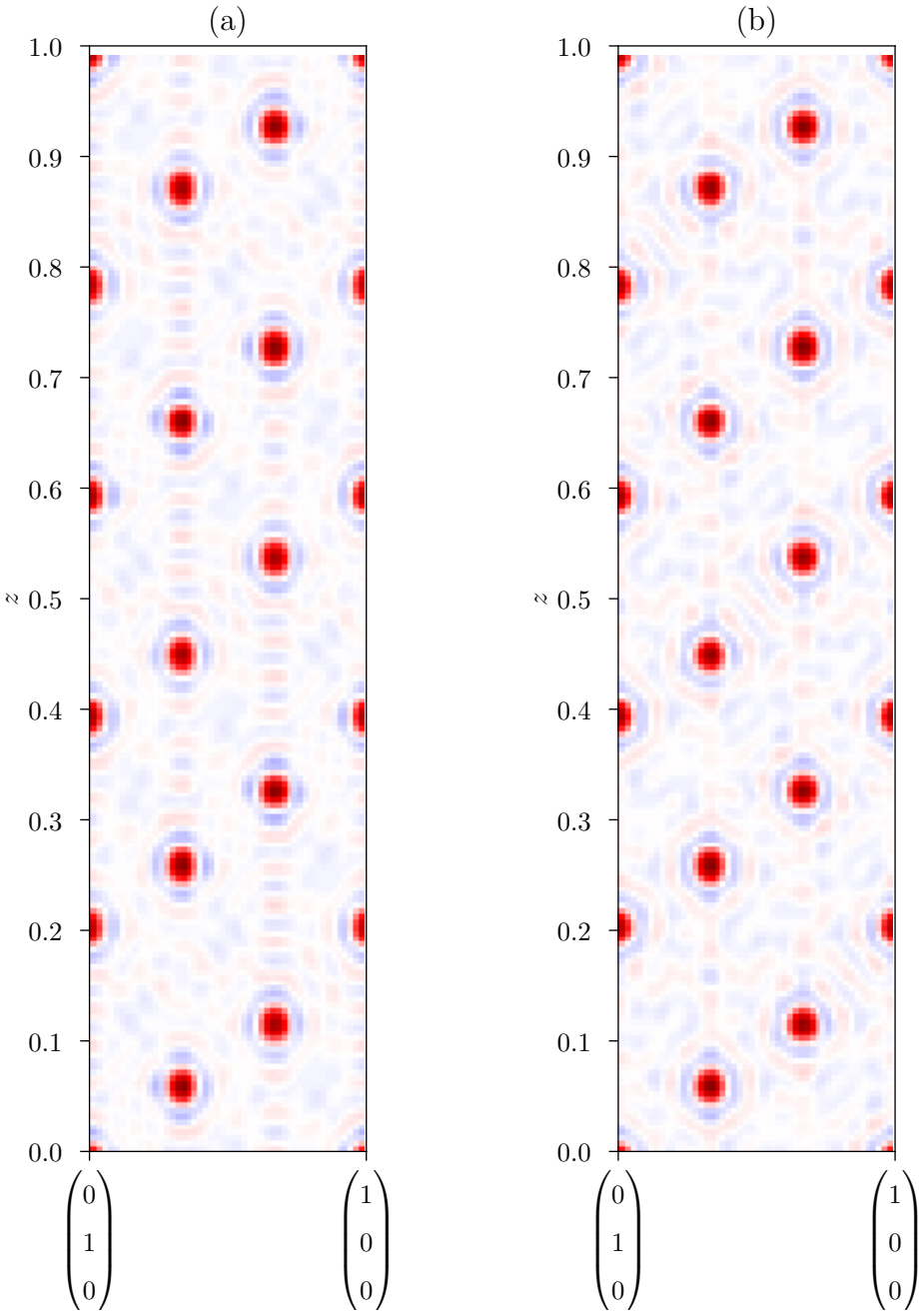

Figure A.3: Slices through the Fourier map along the plane orthogonal to the diagonal reciprocal vector (110) of refinements in space group $R\bar{3}m$ (a) of sample ZW004-S001, like Figure A.1 and (b) of sample MB003-S001, like Figure A.2. No Cu atoms were included in the models.

Temperature	Space group	Cell parameters		R values
1.9 K	Cm	$a = 4.14$ Å	$\alpha = 90.00°$	R(obs) = 2.95 %
		$b = 4.14$ Å	$\beta = 90.09°$	wR(obs) = 3.32 %
		$c = 28.61$ Å	$\gamma = 120.02°$	R(all) = 4.57 %
				wR(all) = 3.47 %
				GoF = 1.49

	x	y	z	$U_{\mathrm{iso/ani}}$	U_{11}	U_{22}	U_{33}	U_{12}	U_{13}	U_{23}	occupancy
Bi1_1	0.0073(16)	0.0037(8)	0.4012(3)	0.0084(18)	0.0004(12)	0.0004(12)	0.024(5)	0.0002(6)	0	0	1
Bi1_2	0.001(2)	0.0006(11)	-0.4000(3)	0.0041(10)	0.0056(10)	0.0056(10)	0.001(2)	0.0028(5)	0	0	1
Se2	0.0172(13)	0.0086(7)	-0.0010(5)	0.0053(5)	0.0018(6)	0.0018(6)	0.0122(10)	0.0009(3)	0	0	1
Se3_1	0.0003(11)	0.0001(6)	0.2104(3)	0.0086(15)	0.0028(15)	0.0028(15)	0.020(3)	0.0014(7)	0	0	1
Se3_2	0.0025(16)	0.0012(8)	-0.2112(3)	0.0044(12)	0.0049(14)	0.0049(14)	0.003(2)	0.0025(7)	0	0	1

Temperature	Space group	Cell parameters		R values
4.4 K	Cm	$a = 4.14$ Å	$\alpha = 90.00°$	R(obs) = 4.18 %
		$b = 4.14$ Å	$\beta = 90.09°$	wR(obs) = 4.63 %
		$c = 28.61$ Å	$\gamma = 120.02°$	R(all) = 5.94 %
				wR(all) = 4.78 %
				GoF = 1.93

	x	y	z	$U_{\mathrm{iso/ani}}$	U_{11}	U_{22}	U_{33}	U_{12}	U_{13}	U_{23}	occupancy
Bi1_1	0.0080(18)	0.0040(9)	0.4010(3)	0.0172(19)	0.0054(10)	0.0054(10)	0.041(5)	0.0027(5)	0	0	1
Bi1_2	0.0055(18)	0.0028(9)	-0.3996(3)	0.0094(10)	0.0111(11)	0.0111(11)	0.006(2)	0.0055(5)	0	0	1
Se2	0.008(2)	0.0039(12)	-0.0008(6)	0.0142(7)	0.0085(8)	0.0085(8)	0.0255(13)	0.0043(4)	0	0	1
Se3_1	-0.0048(14)	-0.0024(7)	0.2100(2)	0.0157(14)	0.0072(14)	0.0072(14)	0.033(3)	0.0036(7)	0	0	1
Se3_2	0.0001(13)	0.0001(7)	-0.2107(2)	0.0100(11)	0.0130(14)	0.0130(14)	0.004(2)	0.0065(7)	0	0	1

Table A.26: Refinements of single crystal neutron diffraction data of sample ZW004-S001, measured at 1.9 K and at 4.4 K, refined in space group Cm.

Temperature	Space group	Cell parameters		R values
300 K	Cm	$a = 4.14$ Å	$\alpha = 90.00°$	$R(\text{obs}) = 3.72\,\%$
		$b = 4.14$ Å	$\beta = 90.09°$	$wR(\text{obs}) = 4.75\,\%$
		$c = 28.61$ Å	$\gamma = 120.02°$	$R(\text{all}) = 6.10\,\%$
				$wR(\text{all}) = 4.94\,\%$
				GoF = 2.12

	x	y	z	$U_{\text{iso/ani}}$	U_{11}	U_{22}	U_{33}	U_{12}	U_{13}	U_{23}	occupancy
Bi1_1	0.0153(10)	0.0077(5)	0.3993(3)	0.017(2)	0.0135(16)	0.0135(16)	0.023(5)	0.0068(8)	0	0	1
Bi1_2	0.0149(10)	0.0075(5)	-0.4022(3)	0.027(3)	0.016(2)	0.016(2)	0.050(8)	0.0080(11)	0	0	1
Se2	0.0092(14)	0.0046(7)	0.0005(6)	0.0179(10)	0.0130(10)	0.0130(10)	0.028(2)	0.0065(5)	0	0	1
Se3_1	-0.0011(10)	-0.0005(5)	0.2098(4)	0.027(3)	0.015(2)	0.015(2)	0.049(7)	0.0077(12)	0	0	1
Se3_2	0.0005(9)	0.0003(5)	-0.2123(3)	0.015(2)	0.015(2)	0.015(2)	0.016(4)	0.0074(11)	0	0	1

Table A.27: Refinement of single crystal neutron diffraction data of sample ZW004-S001, measured at 300 K, refined in space group Cm.

Temperature	Space group	Cell parameters		R values
2 K	Cm	$a = 4.14$ Å	$\alpha = 90.00°$	R(obs) = 2.84 %
		$b = 4.14$ Å	$\beta = 90.04°$	wR(obs) = 3.32 %
		$c = 28.59$ Å	$\gamma = 119.97°$	R(all) = 4.07 %
				wR(all) = 3.44 %
				GoF = 1.77

	x	y	z	$U_{\mathrm{iso/ani}}$	U_{11}	U_{22}	U_{33}	U_{12}	U_{13}	U_{23}	occupancy
Bi1_1	-0.0044(14)	-0.0022(7)	0.40027(16)	0.0053(8)	0.0024(8)	0.0024(8)	0.0112(16)	0.0012(4)	0	0	1
Bi1_2	-0.012(2)	-0.0062(10)	-0.40095(15)	0.0054(9)	0.0020(7)	0.0020(7)	0.012(2)	0.0010(4)	0	0	1
Se2	0.0021(11)	0.0010(5)	-0.0015(3)	0.0050(5)	0.0019(5)	0.0019(5)	0.0112(9)	0.0009(3)	0	0	1
Se3_1	-0.011(2)	-0.0055(10)	0.20975(11)	-0.0018(7)	0.0003(10)	0.0003(10)	-0.0060(10)	0.0001(5)	0	0	1
Se3_2	-0.0044(16)	-0.0022(8)	-0.21260(15)	0.0143(10)	0.0049(11)	0.0049(11)	0.033(2)	0.0025(6)	0	0	1

Temperature	Space group	Cell parameters		R values
300 K	Cm	$a = 4.13$ Å	$\alpha = 90.00°$	R(obs) = 4.14 %
		$b = 4.13$ Å	$\beta = 89.79°$	wR(obs) = 4.81 %
		$c = 28.54$ Å	$\gamma = 119.98°$	R(all) = 6.06 %
				wR(all) = 4.92 %
				GoF = 2.22

	x	y	z	$U_{\mathrm{iso/ani}}$	U_{11}	U_{22}	U_{33}	U_{12}	U_{13}	U_{23}	occupancy
Bi1_1	0.016(3)	0.0079(17)	0.3995(2)	0.0076(15)	0.0090(18)	0.0090(18)	0.005(3)	0.0045(9)	0	0	1
Bi1_2	0.008(2)	0.0042(10)	-0.4020(2)	0.0119(18)	0.007(2)	0.007(2)	0.022(3)	0.0034(11)	0	0	1
Se2	0.011(4)	0.006(2)	0.0029(5)	0.0085(9)	0.0070(9)	0.0070(9)	0.012(2)	0.0035(5)	0	0	1
Se3_1	-0.0081(13)	-0.0041(6)	0.2135(3)	0.011(2)	0.007(3)	0.007(3)	0.021(3)	0.0033(14)	0	0	1
Se3_2	0.015(2)	0.0074(12)	-0.2096(2)	0.011(2)	0.007(3)	0.007(3)	0.017(4)	0.0037(13)	0	0	1

Table A.28: Refinements of single crystal neutron diffraction data of sample MB003-S001, measured at 2 K and at 300 K, refined in space group Cm.

Space group	Cell parameters		R values
$C2/m$	$a = 13.6349(7)$ Å $\quad \alpha = 90.0°$		$R(\text{obs}) = 6.69\,\%$
	$b = 4.2212(2)$ Å $\quad \beta = 99.838(3)°$		$\text{w}R(\text{obs}) = 8.18\,\%$
	$c = 15.2244(8)$ Å $\quad \gamma = 90.0°$		$R(\text{all}) = 12.05\,\%$
			$\text{w}R(\text{all}) = 8.56\,\%$
			$\text{GoF} = 2.33$

	x	y	z	$U_{\text{iso/ani}}$	U_{11}	U_{22}	U_{33}	U_{12}	U_{13}	U_{23}
Bi1	0.15087(4)	0	0.06494(4)	0.01260(12)	0.01338(20)	0.01096(19)	0.0128(2)	0	0.00048(15)	0
Bi2	0.94883(4)	0.5	0.19124(4)	0.01362(13)	0.0181(2)	0.0130(2)	0.0092(2)	0	0.00066(16)	0
Bi3	0.75496(5)	0	0.37787(4)	0.02294(16)	0.0285(3)	0.0276(3)	0.0085(2)	0	-0.0089(2)	0
Se4	0	0.5	0	0.0052(3)	0.0069(6)	0.0073(6)	0.0010(6)	0	-0.0003(5)	0
Se5	0.86161(8)	0	0.54541(8)	0.0063(3)	0.0090(4)	0.0075(4)	0.0016(4)	0	-0.0008(3)	0
Se6	0.90070(9)	0.5	0.36133(8)	0.0094(3)	0.0119(5)	0.0121(5)	0.0053(5)	0	0.0048(4)	0
Se7	0.09212(9)	0	0.23222(9)	0.0108(3)	0.0126(5)	0.0120(5)	0.0058(5)	0	-0.0038(4)	0
Se8	0.29168(9)	0.5	0.12759(10)	0.0121(3)	0.0088(5)	0.0100(5)	0.0162(6)	0	-0.0018(4)	0
Cu9	0.5	0	0.5	0.317(11)	0.044(3)	0.86(3)	0.034(4)	0	-0.030(3)	0

Table A.29: Refinement of single-crystal X-ray diffraction data of the impurity sample ZW006-S003 from the $Cu_xBi_2Se_3$ crystal ZW006 at room temperature, refined in space group $C2/m$.

Space group	Cell parameters		R values
$C2/m$	$a = 13.6411(7)$ Å	$\alpha = 90.0°$	$R(\text{obs}) = 7.57\,\%$
	$b = 4.2261(2)$ Å	$\beta = 99.785(2)°$	$\text{w}R(\text{obs}) = 9.05\,\%$
	$c = 15.2411(8)$ Å	$\gamma = 90.0°$	$R(\text{all}) = 15.45\,\%$
			$\text{w}R(\text{all}) = 9.43\,\%$
			$\text{GoF} = 2.48$

	x	y	z	$U_{\text{iso/ani}}$	U_{11}	U_{22}	U_{33}	U_{12}	U_{13}	U_{23}
Bi1	0.15093(4)	0	0.06490(4)	0.01014(16)	0.0072(3)	0.0142(3)	0.0082(3)	0	-0.00081(19)	0
Bi2	0.94886(5)	0.5	0.19133(4)	0.01094(17)	0.0116(3)	0.0163(3)	0.0042(3)	0	-0.0008(2)	0
Bi3	0.75492(5)	0	0.37790(4)	0.0196(2)	0.0220(4)	0.0297(4)	0.0032(3)	0	-0.0092(2)	0
Se4	0	0.5	0	0.0018(5)	0.0013(8)	0.0082(9)	-0.0041(7)	0	-0.0007(6)	0
Se5	0.86173(10)	0	0.54531(9)	0.0032(4)	0.0027(6)	0.0094(7)	-0.0029(5)	0	-0.0014(4)	0
Se6	0.90084(11)	0.5	0.36157(10)	0.0064(4)	0.0055(6)	0.0143(8)	0.0004(6)	0	0.0036(5)	0
Se7	0.09221(12)	0	0.23215(10)	0.0082(4)	0.0071(7)	0.0136(8)	0.0017(6)	0	-0.0052(5)	0
Se8	0.29151(11)	0.5	0.12748(11)	0.0093(4)	0.0027(6)	0.0115(8)	0.0121(8)	0	-0.0033(5)	0
Cu9	0.5	0	0.5	0.347(11)	0.025(4)	0.96(3)	0.042(4)	0	-0.033(3)	0

Table A.30: Refinement of single-crystal X-ray diffraction data of the impurity sample ZW006-S005 from the $Cu_xBi_2Se_3$ crystal ZW006 at room temperature, refined in space group $C2/m$.

List of Figures

List of Tables

Bibliography

[1] E. I. Rushba. "Spin-orbit coupling goes global". In: *J. Phys.: Condens. Matter* **28**.42 (2016), p. 421004.

[2] D. Stein and K. v. Kitzing. "Electron Spin Resonance on GaAs – $Al_xGa_{1-x}As$ Heterostructures". In: *Physical Review Letters* **51**.2 (1983), pp. 130–133.

[3] H. L. Stormer and Z. Schlesinger. "Energy Structure and Qantized Hall Effect of Two-Dimensional Holes". In: *Physical Review Letters* **51**.2 (1983), pp. 126–129.

[4] Y. A. Bychkov and E. I. Rashba. "Oscillatory effects and the magnetic susceptibility of carriers in inversion layers". In: *J. Phys. C: Solid State Phys.* **17** (1984), pp. 6039–6045.

[5] E. I. Rashba and V. I. Sheka. "Symmetry of Energy Bands in Crystals of Wurtzite Type II. Symmetry of Bands with Spin-Orbit Interaction Included". In: *New. J. Phys.* **17** (2015), p. 050202.

[6] K. I. Kugel and D. I. Khomskii. "The Jahn-Teller effect and magnetism: transition metal compounds". In: *Sov. Phys. Usp.* **25**.4 (1982), pp. 231–256.

[7] M. Sato and Y. Ando. "Topological superconductors: a review". In: *Rep. Prog. Phys.* **80** (2017), p. 076501.

[8] Y. S. Hor, A. J Williams, J. G. Checkelsky, P. Roushan, J. Seo, Q. Xu, H.W. Zandbergen, A. Yazdani, N.P. Ong, and R.J. Cava. "Superconductivity in $Cu_xBi_2Se_3$ and its Implications for Pairing in the Undoped Topological Insulator". In: *Physical Review Letters* **104** (2010), p. 057001.

[9] H. D. Zhou, E. S. Choi, G. Li, L. Balicas, C. R. Wiebe, Y. Qiu, J. R. D. Copley, and J. S. Gardner. "Spin Liquid State in the $S = 1/2$ Triangular Lattice $Ba_3CuSb_2O_9$". In: *Physical Review Letters* **106**.14 (2011), p. 147204.

[10] T. Dey, A. V. Mahajan, P. Khuntia, M. Baenitz, Koteswararao, and F. C. Chou. "Spin-liquid behavior in $J_{\text{eff}} = \frac{1}{2}$ triangular lattice compound $Ba_3IrTi_2O_9$". In: *Physical Review B* **86** (2012), p. 140405.

[11] A. Kitaev. "Anyons in an exactly solved model and beyond". In: *Annals of Physics* **321** (2006), pp. 2–111.

[12] M. Hermanns, I. Kimchi, and J. Knolle. "Physics of the Kitaev model: fractionalization, dynamical correlations, and material connections". In: *Annual Review of Condensed Matter Physics* **9** (2018), pp. 17–33.

[13] H. A. Kramers. "L'interaction Entre les Atomes Magnétogènes dans un Cristal Paramagnétique". In: *Physica* **1** (1934), pp. 182–192.

[14] P. W. Anderson. "Antiferromagnetism. Theory of Superexchange Interaction". In: *Physical Review* **79**.2 (1950), pp. 350–356.

[15] T. Moriya. “Anisotropic Superexchange Interaction and Weak Ferromagnetism”. In: *Physical Review, Volume 120, Number 1* (1960).

[16] I. Dzyaloshinsky. “A thermodynamic theory of "'weak"' ferromagnetism of antiferromagnetics”. In: *J. Phys. Chem. Solids* **4** (1958), pp. 241–255.

[17] W. C. Röntgen. “Ueber eine neue Art von Strahlen”. In: Physikalisch-Medizinische Gesellschaft zu Würzburg. 1896.

[18] M. von Laue. “Concerning the detection of X-ray interference”. In: *Nobel Lecture*. 1920.

[19] J. Chadwick. “The existence of a neutron”. In: *Proceedings of the Royal Society A* **136**.830 (1932), pp. 692–708.

[20] T. E. Mason, T. J. Gawne, S. E. Nagler, M. B. Nestor, and J. M. Carpenter. “The early development of neutron diffraction: science in the wings of the Manhattan Project”. In: *Acta Crystallographica Section A* **69** (2013), pp. 37–44.

[21] H. Ohsumi and Arima T.-h. “Novel insight into structural magnetism by polarized synchrotron X-ray scattering”. In: *Advances in Physics: X* **1**.1 (2016), pp. 128–145.

[22] Steven H. Simon. *The Oxford Solid State Basics*. Oxford Univertisy Press, 2013.

[23] Y. Ando. “Topological Insulator Materials”. In: *Journal of the Physical Society of Japan* **82** (2013), p. 102001.

[24] W. P. Su, J. R. Schrieffer, and A. J. Heeger. “Solitons in Polyacetylene”. In: *Physical Review Letters* **42**.25 (1979), pp. 1698–1701.

[25] J. K. Asbóth, L. Oroszlány, and A. Pályi. “A Short Course on Topological Insulators (lecture notes)”. In: (2015).

[26] Y. Li and Z. Xu. “Exploring Topological Superconductivity in Topological Materials”. In: *Advanced Quantum Technologies* **2** (2019), p. 1800112.

[27] L. Balents. “Spin liquids in frustrated magnets”. In: *Nature* **464** (2010), pp. 199–208.

[28] M. J. Harris, S. T. Bramwell, D. F. McMorrow, T. Zeiske, and K. W. Godfrey. “Geometrical Frustration in the Ferromagnetic Pyrochlore $Ho_2Ti_2O_7$”. In: *Physical Review Letters* **79**.13 (1997), pp. 2554–2557.

[29] J. Rehn, A. Sen, K. Damle, and R. Moessner. “Classical Spin Liquid on the Maximally Frustrated Honeycomb Lattice”. In: *Physical Review Letters* **117** (2016), pp. 167201–1.

[30] K. Kitagawa, T. Takayama, Y. Matsumoto, A. Kato, R. Takano, Y. Kishimoto, S. Bette, R. Dinnebier, G. Jackeli, and H. Takagi. “A spin-orbit-entangled quantum liquid on a honeykomb lattice”. In: *Nature* **554** (2018), pp. 341–345.

[31] H. Kageyama, K. Yoshimura, Stern. R., N. V. Mushnikov, K. Onizuka, M. Kato, K. Kosuge, C. P. Slichter, T. Goto, and Y. Ueda. “Exact Dimer Ground State and Quantized Magnetization Plateaus in the Two-Dimensional Spin System $SrCu_2(BO_3)_2$”. In: *Physical Review Letters* **82**.15 (1999), pp. 3168–3171.

[32] P. Fazekas and P. W. Anderson. “On the ground state properties of the anisotropic triangular antiferromagnet”. In: *Philosophical Magazine* **30**.2 (1974), pp. 423–440.

[33] J. A. Quilliam, F. Bert, E. Kermarrec, C. Payen, C. Guillot-Deudon, P. Bonville, C. Baines, H. Luetkens, and P. Mendels. “Single Ground State of the Quantum Antiferromagnet $Ba_3CuSb_2O_9$”. In: *Physical Review Letters* **109** (2012), p. 117203.

[34] P. Corboz, M. Lajkó, A. M. Läuchli, K. Penc, and F. Mila. “Spin-Orbit Quantum Liquid on the Honeycomb Lattice”. In: *Physical Review X* **2** (2012), p. 041013.

[35] G. Khaliullin and S. Maekawa. “Orbital Liquid in Three-Dimensional Mott Insulator: $LaTiO_3$”. In: *Physical Review Letters* **85**.18 (2000), pp. 3950–3953.

[36] G. Chen, L. Balents, and A. P. Schnyder. “Spin-Orbital Singlet and Quantum Critical Point on the Diamond Lattice: $FeCs_2S_4$”. In: *Physical Review Letters* **102**.9 (2009), p. 096406.

[37] A. A. Mozhegorov, A. E. Nikiforov, A. V. Larin, A. V. Efremov, L. É Gonchar’, and P. A. Agzamova. “Structure and the Electronic and Magnetic Properties of $LaTiO_3$”. In: *Physics of the Solid State* **50**.9 (2008), pp. 1795–1798.

[38] A. Krimmel, M. Mücksch, Tsurkan. V., M. M. Koza, H. Mutka, and A. Loidl. “Vibronic and Magnetic Excitations in the Spin-Orbit Liquid State of $FeSc_2S_4$”. In: *Physical Review Letters* **94** (2005), p. 237402.

[39] A. Nag, S. Middey, S. Bhowal, S. K. Panda, R. Mathieu, J. C. Orain, F. Bert, P. Mendels, P. G. Freeman, M. Mansson, H. M. Ronnow, M. Telling, P. K. Biswas, D. Sheptyakov, S. D. Kaushik, V. Siruguri, C. Meneghini, D. D. Sarma, I. Dasgupta, and S. Ray. “Origin of the Spin-Orbital Liquid State in a Nearly $J = 0$ Iridate $Ba_3ZnIr_2O_9$”. In: *Physical Review Letters* **116**.9 (2016), p. 097205.

[40] I.A. Sergienko and E. Dagotto. “Role of the Dzyaloshinskii-Moriya interaction in multiferroic perovskites”. In: *Phys. Rev. B* **73** (2006), p. 094434.

[41] S.-W. Cheong and M. Mostovoy. “Multiferroics: a magnetic twist for ferroelectricity”. In: *nature materials* **6** (2007), pp. 13–20.

[42] P. Hall. *The Theory of Groups*. The Macmillan Company, 1959.

[43] M. I. Aroyo, Y. Billiet, F. Gähler, V. Gramlich, A. Kirov, P. B. Konstantinov, E. B. Kroumova, U. Müller, G. Nebe, and H. Wondratschek. *International Tables for Crystallography A1, Symmetry relations between space groups*. Ed. by H. Wondratschek and U. Müller. Kluwer Academic Publishers, 2004.

[44] C. J. Bradley and A. P. Cracknell. *The mathematical theory of symmetry in solids*. Ph2-Bib: FK BRA. Clarendon Press - Oxford, 1972.

[45] T. Inui, Y. Tanabe, and Y. Onodera. *Group Theory and Its Applications in Physics*. Ed. by H. K. V. Lotsch. Springer-Verlag, 1976.

[46] Wigner E. P. *Group theory and its application to the quantum mechanics of atomic spectra*. Ed. by J. J. Griffin. Ph2-Bib: AL WIG. Palmer Physical Laboratory, Princeton University, 1959.

[47] W. K. Tung. *Group theory in physics*. Ph2-Bib: AL TUN. World Scientific Publishing Co Pte Ltd., 1985.

[48] R. Ballou and B. Ouladdiaf. "Neutron Scattering from Magnetic Materials: Representation analysis of magnetic structures". In: ed. by T. Chatterji. Elsevier B. V., 2006. Chap. 3, pp. 93–151.

[49] A. H. Clifford. "Representations Induced in an Invariant Subgroup". In: *Annals of Mathematics* **38**.3 (1937), pp. 533–550.

[50] E. P. Wigner. "Phenomenological Distinction between Unitary and Antiunitary Symmetry Operators". In: *Journal of Mathematical Physics* **1** (1960), pp. 414–416.

[51] K. S. Krane. *Introductory Nuclear Physics*. Ed. by D. Halliday. 2nd ed. John Wiley & Sons, Inc., 1988.

[52] G. E. Bacon. *X-ray and Neutron Diffraction*. Pergamon Press, 1966.

[53] A.-J. Dianoux and G. Lander. *Neutron Data Booklet*. Published by licence under the OCP Science imprint. Institut Laue-Langevin, BP 156, 38042 Grenoble Cedex 9, France, 2003.

[54] G. L. Squires. *Introduction to the Theory of Thermal Neutron Scattering*. Cambridge University Press, Dover Publications Inc., 1978, 1996, 2012.

[55] H. A. Bethe. "Theory of the Effective Range in Nuclear Scattering". In: *Physical Review* **76**.1 (1949), pp. 38–50.

[56] V. F. Sears. *Thermal-neutron scattering lengths and cross sections for condensed-matter research*. Atomic Energy of Canada Limited, 1984.

[57] A. Albinati et al. *International Tables for Crystallography*. Ed. by E. Prince. Vol. C. Kluwer Academic Publishers, 2004.

[58] M. Blume. "Polarization Effects in the Magnetic Scattering of Slow Neutrons". In: *Physical Review* **130**.5 (1963), pp. 1670–1676.

[59] F. M. Piegsa. "Novel concept for a neutron electric charge measurement using a Lalbot-Lau interferometer at a pulsed source". In: *Physical Review C* **98** (2018), p. 045503.

[60] I. A. Zaliznyak and S.-H. Lee. *Modern Techniques for Characterizing Magnetic Materials (Chapter 1)*. Ed. by Y. Zhu. Springer, 2005.

[61] J. Rossat-Mignod. *Magnetic Structures*. Academic Press, Inc, 1987.

[62] T. Chatterji, ed. *Neutron Scattering from Magnetic Materials*. Elsevier Science, 2006.

[63] C. Giacovazzo, H. L. Monaco, D. Viterbo, F. Scordari, G. Gilli, G. Zantotti, and M. Catti. *Fundamentals of Crystallography*. Ed. by C. Giacovazzo. International Union of Crystallography, Oxford University Press, 1992.

[64] R. M. Moon, T. Riste, and W. C. Koehler. "Polarization Analysis of Thermal-Neutron Scattering". In: *Physical Review* **181**.2 (1969), pp. 920–931.

[65] F. Tasset. “Zero Field Neturon Polarimetry”. In: *Physica B* **156 & 157** (1989), pp. 627–630.

[66] O. Schärpf. *The spin of the neutron as measuring probe. Application of spin polarized neutrons to measure electronic (including magnetic) properties of metals, semiconductors, superconductors.*

[67] J. R. Stewart, P. P. Deen, K. H. Andersen, H. Schober, J.-F. Bartélémy, J. M. Hillier, A. P. Murani, T. Hayes, and B. Lindenau. “Disordered materials studied using neutron polarization analysis on the multi-detector spectrometer, D7”. In: *Journal of Applied Crystallography* **42** (2009), pp. 69–84.

[68] D. Watkin. “Structure refinement: some background theory and practical strategies”. In: *Journal of Applied Crystallography* **41** (2008), pp. 491–522.

[69] V. Petříček, M. Dušek, and L. Palatinus. “Crystallographic Computing System JANA2006: General features”. In: *Z. Kristallogr.* 229(5) (2014), pp. 345–352.

[70] P. A. Karplus and K. Diederichs. “Linking crystallographic model and data quality”. In: *Science* **336** (2012), pp. 1030–1033.

[71] K. Diederichs and P. A. Karplus. “Improved R-factors for diffraction data analysis in macromolecular crystallography”. In: *Nature Structural Biology* **4**.4 (1997), pp. 269–275.

[72] *Statistische Datenanalyse – Grundlagen und Methoden für Physiker*. In der Ph2-Bibliothek unter ST-WAL. Springer Spektrum, 2015.

[73] N. E. Brese and M. O’Keeffe. “Bond-Valence Parameters for Solids”. In: *Acta Cryst.* **B47** (1991), pp. 192–197.

[74] I. D. Brown and D. Altermatt. “Bond-Valence Parameters Obtained from a Systematic Analysis of the Inorganic Crystal Structure Database”. In: *Acta Cryst.* **B41** (1985), pp. 244–247.

[75] V. M. Goldschmidt. “Die Gesetze der Krystallochemie”. In: *Die Naturwissenschaften* **21** (1926), pp. 477–485.

[76] *APEX2 Version 2 User Manual*. Bruker AXS Inc. 5465 East Cheryl Parkway, Madison, WI 53711, 2006.

[77] *Oxford Cryosystems N-Helix Operation & Instruction Guide v1.1*. Oxford Cryosystems Ltd. 3 Blenheim Office Park Lower Road Long Hanborough, 2004.

[78] *Coolstar Cryodrive 1.5 & 3.0 Operation & Instruction Guide v 1.2*. Oxford Cryosystems. 3 Blenheim Office Park Lower Road Long Hanborough, 2009.

[79] W. L. Bond. “Making Small Spheres”. In: *Review of Scientific Instruments* **22** (1951), p. 344.

[80] Cordero-Borboa. “An improved grinder for single crystal x-ray diffraction work”. In: *J. Phys. E: Sci. Instrum.* **18** (1985), pp. 393–395.

[81] O. J. Schumann. “Structural Investigations on layered Manganites and Ruthenates”. PhD thesis. Mathematisch-Naturwissenschaftliche Fakultät der Universität zu Köln, 2010.

[82] Bert H. Freitag. "Automatisierung und Optimierung einer Röntgendiffraktometrieanlage". Diploma thesis. Universität zu Köln, 1991.

[83] Christoph Huhnt. "Strukturelle Phasenübergänge in Phosphiden mit $ThCr_2Si_2$-Struktur". PhD thesis. Universität zu Köln, 1998.

[84] M. S. A. Haider. "Strukturuntersuchungen an $La_{2-x}Sr_xCo_{1-y}Ru_yO_4$ und Umbau der XPD Anlagen". Diploma thesis. Universität zu Köln, 2005.

[85] Holger Ulbrich. "Interplay between charge, orbital and magneitc ordering in manganites". PhD thesis. Mathematisch-Naturwissenschaftliche Fakultät der Universität zu Köln, 2012.

[86] L. Spieß, G. Teichert, R. Schwarzer, H. Behnken, and C. Genzel. *Moderne Röntgenbeugung*. 2nd ed. Vieweg+Teubner, GWV Fachverlage GmbH, 2009.

[87] R. E. Dinnebier, ed. *Kristallstrukturbestimmung molekularer Substanzen aus Röntgenbeugungsaufnahmen an Pulvern*. Deutsche Gesellschaft für Kristallographie. 2000.

[88] P. Thompson, D. E. Cox, and J. B. Hastings. "Rietveld Refinement of Debye-Scherrer Synchrotron X-ray Data from Al_2O_3". In: *J. Appl. Cryst.* **20** (1987), pp. 79–83.

[89] G. Caglioti, A. Paoletti, and F. P. Ricci. "Choice of collimators for a crystal spectrometer for neutron diffraction". In: *Nuclear Instruments* **3** (1958), pp. 223–228.

[90] P. Scherrer. "Bestimmung der Grösse und der inneren Struktur von Kolloidteilchen mittels Röntgenstrahlen". In: *Nachrichten von der Gesellschaft der Wissenschaften zu Göttingen* (1918), pp. 98–100.

[91] P. W. Stephens. "Phenomenological model of anisotropic peak broadening in powder diffraction". In: *J. Appl. Cryst.* **32** (1999), pp. 281–289.

[92] G. K. Wertheim, M. A. Butler, K. W. West, and D. N. E. Buchanan. "Determination of the Gaussian and Lorentzian content of experimental line shapes". In: *Rev. Sci. Instrum.* **45**.11 (1974), pp. 1369–1371.

[93] Rodríguez-Carvajal. *An Instroduction to the Program FullProf 2000*. Version July2001. Laboratoire Léon Brillouin (CEA-CNRS). CEA/Saclay, 91191 Gif sur Yvette Cedex, France, 2001.

[94] URL: http://www-llb.cea.fr/fr-en/spectros_p.php.

[95] URL: http://www-llb.cea.fr/spectros/spectro/5c2/5c2.html.

[96] Martin Meven and Andrew Sazonov. "HEiDi: Single crystal diffractometer at hot source". In: *Journal of large-scale research facilities* **1** (2015), pp. 1–4.

[97] *D9: Hot Neutron Four-Circle Diffractometer*. Institut Laue-Langevin. 71 avenue des Martyrs CS 20156, 38042 Grenoble Cedex 9, France.

[98] M. S. Lehmann, W. F. Kuhs, G. J. McIntyre, C. Wilkinson, and J. R. Allibon. "On the Use of a Small Two-Dimensional Position-Sensitive Detector in Neutron Diffraction". In: *J. Appl. Cryst.* **22** (1989), pp. 562–568.

[99] C. Wilkinson, H. W. Khamis, R. F. D. Standsfield, and G. J. McIntyre. “Integration of single-crystal reflections using area multidetectors”. In: *J. Appl. Cryst.* **21** (1988), pp. 471–478.

[100] E. Lelièvre-Berna, E. Bourgeat-Lami, Gibert, N. Kernavanois, J. Locatelli, T. Mary, G. Pastrello, A. Betukhov, S. Pujol, R. Rouques, F. Thomas, M. Thomas, and F. Tasset. “ILL polarized hot-neutron beam facility D3”. In: *Physica B* **356** (2005), pp. 141–145.

[101] A. J. Bradley and J. W. Rodgers. “The Crystal Structure of the Heusler Alloys”. In: *Proceedings of the royal society A* **144** (1934), pp. 340–359.

[102] URL: https://www.ill.eu/users/support-labs-infrastructure/sample-environment/services-for-advanced-neutron-environments/history/cryogenics/orange-cryostats/.

[103] E. Lelièvre-Berna and F. Tasset. “The D3C project: improvements and a new field of science”. In: *Physica B* **267-268** (1999), pp. 21–26.

[104] Simon Holbein. “Microscopic and macroscopic investigations of multiferroics”. Diploma thesis. Universität zu Köln, 2011.

[105] Jonas Stein. “Makroskopische und mikroskopische Untersuchungen an Multiferroika”. Diploma thesis. Universität zu Köln, 2012.

[106] C. B. Sawyer and C. H. Tower. “Rochelle Salt as dielectric”. In: *Physical Review* **35** (1930), pp. 269–273.

[107] M. Gabás, F. Palacio, J. Rodríguez-Carvajal, and D. Visser. “Magnetic structures of the three-dimensional Heisenberg antiferromagnets $K_2FeCl_5 \cdot D_2O$ and $Rb_2FeCl_5 \cdot D_2O$”. In: *J. Phys.: Condens. Matter* **7** (1995), pp. 4725–4738.

[108] R. L. Carlin, S. N. Bhatia, and C. J. O’Connor. “A New Series of Antiferromagnets”. In: *Journal of the American Chemical Society* **99**.23 (1977), pp. 7728–7729.

[109] B. N. Figgis, C. L. Raston, R. P. Sharma, and A. H. White. “Crystal Structure of Diammonium Aquapentachloroferrate(III)”. In: *Aust. J. Chem.* **31** (1978), pp. 2717–2720.

[110] M. Ackermann, D. Brüning, T Lorenz, P Becker, and L Bohatý. “Thermodynamic properties of the new multiferroic material $(NH_4)_2[FeCl_5(H_2O)]$”. In: *New Journal of Physics* **15** (2013), p. 123001.

[111] J. E. Greedan, D. C. Hewitt, R. Faggiani, and I. D. Brown. “Structure of and Hydrogen Bonding in Dicaesium Aquapentachloroferrate(III)”. In: *Acta Cryst. B* **36** (1980), pp. 1927–1929.

[112] J. Luzón, J. Campo, F. Palacio, G. J. McIntyre, and A. Millán. “Understanding magnetic interactions in the series $A_2FeX_5 \cdot H_2O$ ($A = \mathrm{K}, \mathrm{Rb}; X = \mathrm{Cl}, \mathrm{Br}$). I. Spin densities by polarized neutron diffraction and DFT calculations”. In: *Physical Review B* **78** (2008), p. 054414.

[113] J. A. Rodríguez-Velamazán, Ó Fabelo, Á Millán, J. Campo, R. D. Johnson, and L. Chapon. “Magnetically-induced ferroelectricity in the $(ND_4)_2[FeCl_5(D_2O)]$ molecular compound”. In: *Scientific Reports* **5** (2015).

[114] J. Chadwick and M. F. Thomas. "Mössbauer investigation of the crystallographic phase transition in $Cs_2FeCl_5.H_2O$". In: *J. Phys. C: Solid State Phys.* **20** (1987), pp. 3979–3983.

[115] M. Ackermann, T. Lorenz, P. Becker, and L. Bohatý. "Magnetoelectric properties of $A_2[FeCl_5(H_2O)]$ with $A = K, Rb, Cs$". In: *J. Phys.: Condens. Matter* **26** (2014), p. 506002.

[116] J. N. McElearney and S. Merchant. "Nonisomorphic antiferromagnetic behavior of two isomorphic salts: Low-Temperature Heat Capacities and Magnetic Susceptibilities of $(NH_4)_2FeCl_5 \cdot H_2O$ and $K_2FeCl_5 \cdot H_2O$". In: *Inorg. Chem.* **17**.5 (1978), p. 1207.

[117] W. Tian, H. Cao, J. Wang, F. Ye, M. Matsuda, J.-Q. Yan, Y. Liu, V. O. Garlea, H. K. Agrawal, B. C. Chakoumakos, B. C. Sales, R. S. Fishman, and J. A. Fernandez-Baca. "Spin-lattice coupling mediated multiferroicity in $(ND_4)_2FeCl_5 \cdot (D_2O)$". In: *Physical Review B* **94** (2016), p. 214405.

[118] J. A Puértolas, R. Navarro, F. Palacio, J. Bartolomé, D. González, and R. L. Carlin. "Magnetic dimensionality crossover studies on the Heisenberg antiferromagnet $Rb_2FeCl_5 \cdot H_2O$". In: *Physical Review B* **31**.1 (1985), pp. 516–526.

[119] J. Campo, J. Luzón, F. Palacio, G. J. McIntyre, A. Millán, and A. R. Wildes. "Understanding magnetic interactions in the series $A_2FeX_5 \cdot H_2O$ ($A = K, Rb; X = Cl, Br$). II. Inelastic neutron scattering and DFT studies". In: *Physical Review B* **78** (2008), p. 054415.

[120] Ladislav Bohatý. "private communication". Institut für Geologie und Mineralogie, Abteilung Kristallographie, Universität zu Köln.

[121] D. Brüning, T. Fröhlich, M. Langenbach, T. Leich, M. Meven, P. Becker, L. Bohatý, M. Grüninger, M. Braden, and T. Lorenz. "Magnetoelectric coupling in the mixed erythrosiderite $[(NH_4)_{1-x}K_x]_2[FeCl_5(H_2O)]$". In: *Phys. Rev. B* **102** (2020), 054413, arXiv:2001.11780.

[122] T. Fröhlich, J. Stein, L. Bohatý, P. Becker, A. Gukasov, and M. Braden. "Structural and magnetic phase transitions in $Cs_2[FeCl_5(H_2O)]$". In: *J. Phys.: Condens. Matter* **30** (2018), p. 295403.

[123] H. T. Stokes and D. M. Hatch. *Isotropy Subgroups of the 230 Crystallographic Space Groups*. World Scientific, Singapore, 1988.

[124] J. Stein, M. Baum, S. Holbein, T. Cronert, V. Hutanu, A. C. Komarek, and M. Braden. "Control of multiferroic domains by external electric fields in $TbMnO_3$". In: *J. Phys.: Cond. Mat.* **27** (2015), p. 446001.

[125] J. A. Bearden. "X-Ray Wavelengths". In: *Reviews of modern physics* **39**.1 (1967), pp. 78–124.

[126] O. Fabelo, J. A. Rodríguez-Velamazán, L. Canadillas-Delgado, L. Mazzuca, J. Campo, Á. Millán, L. C. Chapon, and J. Rodríguez-Carvajal. "Origin of the magnetoelectric effect in the $Cs_2FeCl_5 \cdot D_2O$ compound". In: *Physical Review B* **96** (2017), p. 104428.

[127] J. Rodriguez-Carvajal. “Recent advances in magnetic structure determination by neutron powder diffraction”. In: *Physica B.* **192** (1993), pp. 55–69.

[128] F. Wei, F. Brivio, Y. Wu, S. Sun, P. D. Bristowe, and A. K. Cheetham. “Synthesis, crystal structure, magnetic and electronic properties of the caesium-based transition metal halide $Cs_3Fe_2Br_9$”. In: *J. of Materials Chemistry C* **6** (2018), pp. 3573–3577.

[129] D. Brüning. “private comminication”. II. Physikalisches Institut, Universität zu Köln.

[130] I. Cisarova. “private communication”. Charles University in Prague, Faculty of Science, Department for Inorganic Chemistry.

[131] B. Leuenberger, H. U. Güdel, and P. Fischer. “Synthesis, Structural Characterization, and Magnetic Properties of the Dimer Compounds $Cs_3Cr_2X_F, X = \mathrm{Cl}, \mathrm{Br}, \mathrm{I}$”. In: *J. of Solid State Chemistry* **64** (1986), pp. 90–101.

[132] U. Müller. “Kristallographische Gruppe-Untergruppe-Beziehungen und ihre Anwendung in der Kristallchemie”. In: *Z. Anorg. Allg. Chem.* **630** (2004), pp. 1519–1537.

[133] Sebastian Biesenkamp. “private communication”. II. Physikalisches Institut, Universität zu Köln.

[134] B. Leuenberger, A. Stebler, H. U. Güdel, A. Furrer, R. Feile, and J. K. Kjems. “Spin dynamics of an isotropic singlet-ground-state antiferromagnet with alternating strong and weak interactions: An inelastic-neutron-scattering study of the dimer compound $Cs_3Cr_2Br_9$”. In: *Phys. Rev. B* **30**.11 (1984), pp. 3600–3607.

[135] St. v. Náray-Szabó. “Der Strukturtyp des Perowskits ($CaTiO_3$)”. In: *Die Naturwissenschaften* **16/18** (1943), p. 203.

[136] H. D. Megaw. “Temperature changes in the crystal structure of barium titanium oxide”. In: *Proc. Roy. Soc. A* **189** (1946), pp. 261–283.

[137] H. D. Megaw. “Crystal Structure of Double Oxides of the Perovskite Type”. In: *The Proceedings of the Physical Society* **58**.326 (1946), p. 10.

[138] G. Shirane, H. Danner, and R. Pepinsky. “Neutron Diffraction Study of Orthorhombic $BaTiO_3$”. In: *Physical Review* **105**.3 (1957), pp. 856–860.

[139] A. W. Hewat. “Structure of thombohedral ferroelectric barium titanate”. In: *Ferroelectrics* **6** (1974), pp. 215–218.

[140] C. Maunders, J. Etheridge, N. Wright, and H. J. Whitfield. “Structure and microstructure of hexagonal $Ba_3Ti_2RuO_9$ by electron diffraction and microscopy”. In: *Acta Crystallographica Section B* **61** (2005), pp. 154–159.

[141] R. D. Burbank and H. T. Jr. Evans. “The Crystal Structure of Hexagonal Barium Titanate”. In: *Acta Cryst.* **1** (1948), pp. 330–336.

[142] Y. Doi and Y. Hinatsu. “The structural and magnetic characterization of 6H-perovskite-type oxides $Ba_3LnIr_2O_9$ (Ln = Y, lanthanides)”. In: *Journal of Physics: Condensed Matter* **16** (2004), pp. 2849–2860.

[143] T. Sakamoto, Y. Doi, and Y. Hinatsu. "Crystal structures and magnetic properties of 6H-perovskite-type oxides $Ba_3MIr_2O_9$ (M = Mg, Ca, Sc, Ti, Zn, Sr, Zr, Cd and In)". In: *Journal of Solid State Chemistry* **179** (2006), pp. 2595–2601.

[144] R. Radtke, C. Maunders, A. Saúl, S. Lazar, H. J. Whitfield, J. Etheridge, and G. A. Bonnon. "Electronic structure and stability of hexagonal $Ba_3Ti_2RuO_9$". In: *Physical Review B* **81**.8 (2010), p. 085112.

[145] Tusharkanti Dey. "private communication". II. Physikalisches Institut, Universitat zu Koln.

[146] T. Dey, M. Majumder, J. C. Orain, A. Senyshyn, M. Prinz-Zwick, S. Bachus, Y. Tokiwa, F. Bert, P. Khuntia, N Büttgen, A. A. Tsirlin, and P. Gegenwart. "Persistent low-temperature spin dinamics in the mixed-valence iridate $Ba_3InIr_2O_9$". In: *Physical Review B* **96** (2017), p. 174411.

[147] Petra Becker. "private communication". Institut fur Geologie und Mineralogie, Abteilung Kristallographie, Universitat zu Koln.

[148] Y. Okada and Y. Tokumaru. "Precise determination of lattice parameter and thermal expansion coefficient of silicon between 300 and 1500 K". In: *J. Appl. Phys.* **56**.2 (1984), pp. 314–320.

[149] A. Thompson, D. Attwood, E. Gullikson, M. Howells, K.-J. Kim, J. Kirz, J. Kortright, I. Lindau, Y. Liu, P. Pianetta, A. Robinson, J. Scofield, J. Underwood, G. Williams, and H. Winick. *X-Ray Data Booklet*. Lawrence Berkeley National Laboratory, University of California, Berkely, CA 94720, 2009.

[150] A. Revelli, M. Moretti Sala, G. Monaco, P. Becker, L. Bohatý, M. Hermanns, T. C. Koethe, T. Fröhlich, P. Warzanowski, T. Lorenz, S. V. Streltsov, P. H. M. van Loosdrecht, D. I. Khomskii, J. van den Brink, and M. Grüninger. "Resonant inelastic x-ray incarnation of Young's double-slit experiment". In: *Science Advances* **5**.eaav4020 (2019).

[151] R. D. Shannon. "Revised Effective Ionic Radii and Systematic Studies of Interatomic Distances in Halides and Chalcogenides". In: *Acta Cryst. A* **32** (1976), p. 751.

[152] K. Robinson, G. V. Gibbs, and P. H. Ribbe. "Quadratic Elongation: A Quantitative Measure of Distortion in Coordination Polyhedra". In: *Science* 172 (1971), pp. 567–570.

[153] M. J. Mehl, D. Hicks, C. Toher, O. Levy, R. M. Hanson, G. Hart, and S. Curtarolo. "The AFLOW library of Crystallographic Prototypes: Part 1". In: *Computational Materials Science* **136** (2017), pp. 1–828.

[154] R. S. Roth. "Classification of Perovskite and Other ABO_3-Type Compounds". In: *Journal of Research of the National Bureau of Standards* **58**.2 (1957), pp. 75–88.

[155] S. Geller. "Crystal Structure of Gadolinium Orthoferrite, $GdFeO_3$". In: *J. Chem. Phys.* **24**.6 (1956), pp. 1236–1239.

[156] A. M. Glazer. "The Classification of Tilted Octahedra in Perovskites". In: *Acta Cryst.* **B28** (1972), pp. 3384–3392.

[157] M. Wakeshima, D. Harada, and Y. Hinatsu. “Crystal structures and magnetic properties of ordered perovskites Ba_2LnIrO_6 (Ln = Lanthanide)”. In: *Journal of Materials Chemistry* **10** (2000), pp. 419–422.

[158] S. Kanungo, K. Mogare, B. Yan, M. Reehuis, A. Hoser, C. Felser, and M. Jansen. “Weak orbital ordering of Ir t_{2g} states in the double perovskite Sr_2CeIrO_6”. In: *Physical Review B* **93** (2016), p. 245148.

[159] A. Revelli, C. C. Loo, D. Kiese, P. Becker, T. Fröhlich, T. Lorenz, M. Moretti Sala, G. Monaco, F. L. Buessen, J. Attig, M. Hermanns, S. V. Streltsov, D. I. Khomskii, J. van den Brink, M. Braden, P. H. M. van Loosdrecht, S. Trebst, A. Paramekanti, and M. Grüninger. “Spin-orbit entangled $j = \frac{1}{2}$ moments in Ba_2CeIrO_6: A frustrated fcc quantum magnet”. In: *Physical Review B* **100** (2019), p. 085139.

[160] W. T. Fu and D. J. W. IJdo. “On the space group of the double perovskite Ba_2PrIrO_6”. In: *Journal of Solid State Chemistry* **178** (2005), pp. 1312–1316.

[161] L. Li and B. J. Kennedy. “Valence structural transitions in the mixed $Ru - Ir$ perovskites $Ba_2PrRu_{1-x}Ir_xO_6$”. In: *Journal of Solid State Chemistry* **177** (2004), pp. 3290–3300.

[162] W. T. Fu and D. J. W. IJdo. “Re-examination of the structure of Ba_2MIrO_6 (M = La, Y: space group revised”. In: *Journal of Alloys and Combounds* **394** (2005), pp. L5–L8.

[163] S. Yonezawa, K. Tajiri, S. Nakata, Y. Nagai, Z. Wang, K. Segawa, Y. Ando, and Y. Maeno. “Thermodynamic evidence for nematic superconductivity in $Cu_xBi_2Se_3$”. In: *arXiv* 1602.08941v1 (2016).

[164] Z. Liu, X. Yao, J. Shao, M. Zuo, L. Pi, S. Tan, C. Zhang, and Y. Zhang. “Superconductivity with Topological Surface State in $Sr_xBi_2Se_3$”. In: *Journal of the Americal Chemical Society* **137** (2015), pp. 10512–10515.

[165] V. K. Shruti, P. Maurya, P. Neha, P. Srivastava, and S. Patnaik. “Superconductivity by Sr intercalation in the layered topological insulator Bi_2Se_3”. In: *Physical Review B* **92** (2015), p. 020506.

[166] Y. Qiu, K. N. Sanders, J. Dai, J. E. Medvedeva, W. Wu, P. Ghaemi, T. Vojta, and Y. S. Hor. “Time reversal symmetry breaking superconductivity in topological materials”. In: *arXiv* (2015).

[167] J. W. Earley. “Description and synthesis of the selenide minerals”. In: *The American Mineralogist* **35**.5 and 6 (1950), pp. 337–364.

[168] E. Donges. “Über Chalkogenohalogenide des dreiwertigen Antimons und Wismuts”. In: *Zeitschrift für Anorganische und Allgemeine Chemie* **263** (1950), pp. 112–132.

[169] H. Gobrecht, K.-E. Boeters, and G. Pantzer. “Über Kristallstruktur and elektrische Eigenschaften der Wismutselenide Bi_2Se_2 und Bi_2Se_3”. In: *Zeitschrift für Physik* **177** (1964), pp. 68–83.

[170] G. R. Hyde, H. A. Beale, I. L. Spain, and J. A. Woollam. “Electronic properties of Bi_2Se_3”. In: *J. Phys. Chem. Solids* **35** (1974), pp. 1719–1728.

[171] S. Nakajima. "The crystal structure of $Bi_2Te_{3-x}Se_x$". In: *J. Phys. Chem. Solids* **24** (1963), pp. 479–485.

[172] H. Gobrecht, S. Seek, and T. Klose. "Der Einfluß der freien Ladungsträger auf die optischen Konstanten des Bi_2Se_3 im Wellenlängengebiet von 2 bis 23 μm". In: *Zeitschrift für Physik* **190** (1966), pp. 427–443.

[173] J. Black, E. M. Conwell, L. Seigle, and C. W. Spencer. "Electrical and optical Properties of some $M_2{}^{V-B}N_3{}^{VI-B}$ semiconductors". In: *J. Phys. Chem. Solids* **2** (1957), pp. 240–251.

[174] A. Vaško, L. Tichý, J. Horaák, and J. Weissenstein. "Amphoteric nature of copper impurities in Bi_2Se_3 crystals". In: *Applied Physics* **5** (1974), pp. 217–221.

[175] L. Fu and E. Berg. "Odd-Parity Topological Superconductors: Theory and Application to $Cu_xBi_2Se_3$". In: *Physical Review Letters* **105** (2010), p. 097001.

[176] Y.-L. Wang, Xu Y., Y.-P. Jiang, J.-W. Liu, C.-Z. Chang, M. Chen, Z. Li, C.-L. Song, L.-L. Wang, K. He, X. Chen, W.-H. Duan, Q.-K. Xue, and X.-C. Ma. "Structural defects and electronic properties of the Cu-doped topological insulator Bi_2Se_3". In: *Physical Review B* **84** (2011), p. 075335.

[177] K. Matano, M. Kriener, K. Segawa, Y. Ando, and G. Zheng. "Spin-rotation symmetry breaking in the superconducting state of $Cu_xBi_2Se_3$". In: *Nature Physics* **12** (2016), pp. 852–855.

[178] M. P. Smylie, K. Willa, H. Claus, A. E. Koshelev, K. W. Song, W.-K. Kwok, Z. Islam, G. D. Gu, J. A. Schneeloch, Zhong, and U. Welp. "Superconducting and normal-state anisotropy of the doped topological insulator $Sr_{0.1}Bi_2Se_3$". In: *Scientific Reports* **8** (2018), p. 7666.

[179] T. Asaba, B. J. Lawson, C. Tinsman, L. Chen, P. Corbae, G. Li, Y. Qiu, Y. S. Hor, L. Fu, and L. Li. "Rotational Symmetry Breaking in a Trigonal Superconductor Nb-doped Bi_2Se_3". In: *Physical Review X* **7** (2017), p. 011009.

[180] A. Y. Kuntsevich, M. A. Bryzgalov, V. A. Prudkoglyad, V. P. Martovitskii, Y. G. Selivanov, and E. G. Chizhevskii. "Structural distortion behind the nematic superconductivity in $Sr_xBi_2Se_3$". In: *New Journal of Physics* **20** (2018), p. 103022.

[181] Zhiwei Wang. "private communication". II. Institute of Physics, University of Cologne.

[182] Mahasweta Bagchi. "private communication". II. Institute of Physics, University of Cologne.

[183] M. Kriener, K. Segawa, Zhi Ren, S. Sasaki, S. Wada, S. Kuwabatu, and Y. Ando. "Electrochemical synthesis and superconducting phase diagram of $Cu_xBi_2Se_3$". In: *Physical Review B* **84** (2011), p. 054513.

[184] K. Sobczak, P. Strak, P. Kempisty, A. Wolos, A. Hruban, A. Materna, and J. Borysiuk. "Electronic and structural properties of Bi_2Se_3 : Cu". In: *Physical Review Materials* **2** (2018), p. 044203.

[185] Z. Li, M. Wang, D. Zhang, N. Feng, W. Jiang, C. Han, W. Chen, M. Ye, C. Gao, J. Jia, J. Li, S. Qiao, D. Qian, B. Xu, H. Tian, and B. Gao. "Possible structural origin of superconductivity in Sr-doped Bi_2Se_3". In: *Physcal Review Materials* **2** (2018), p. 014201.

[186] M. S. Lehmann and F. K. Larsen. "A method for location of the peaks in step-scan-measured Bragg reflexions". In: *Acta Cryst.* **A30** (1974), pp. 580–584.

[187] O. Bikondoa. "On the use of two-time correlation functions for X-ray photon correlation spectroscopy data analysis". In: *Journal of Applied Crystallography* **50** (2017), pp. 357–368.

[188] H. Arnold, M. I. Aroyo, E. F. Bertraut, Y. Billiet, M. J. Buerger, H. Burzlaff, J. D. H. Donnay, W. Fischer, D. S. Fokkema, B. Gruber, Th. Hahn, H. Klapper, E. Koch, P. B. Konstantinov, G. A. Langlet, A. Looijenga-Vos, U. Müller, P. M. de Wolff, H. Wondratschek, and H. Zimmermann. *International Tables for Crystallography*. Ed. by Th. Hahn. Vol. A. Springer, 2005.

[189] K. N. Trueblood, H.-B. Bürgi, H. Burzlaff, J. D. Dunitz, C. M. Gramaccioli, H. H. Schulz, U. Shmueli, and S. C. Abrahams. "Atomic displacement parameter nomenclature". In: *Acta Cryst. A**52**, 770-781* (1996).

[190] P.J. Brown, T. Chatterji, A. Stunault, Y. Su, Y. Xiao, R. Mittal, T. Brückel, T. Wolf, and P. Adelmann. "Magnetization distribution in the tetragonal phase of $BaFe_2As_2$". In: *Physical Review* **82** (2010), p. 024421.

[191] M. Kriener, ¡. Segawa, Z. Ren, S. Sasaki, and Y. Ando. "Bulk superconducting phase with a full energy gap in the doped topological insulator $Cu_xBi_2Se_3$". In: *Phys. Rev. Let.* **106** (2011), p. 127004.

[192] S. Blundell. *Magnetism in Condensed Matter*. Oxford University Press, 2001.

[193] N. J. Stone. "Table of nuclear magnetic dipole and electric quadrupole moments". In: *Atomic Data and Nuclear Data Tables* **90** (2005), pp. 75–176.

[194] J. Engelmayer, X. Lin, C. P. Grams, R. German, T. Fröhlich, J. Hemberger, K. Behnia, and T. Lorenz. "Charge transport in oxygen-deficient $EuTiO_3$: The emerging picture of dilute metallicity in quantum-paraelectric perovskite oxides". In: *Physical Review Materials* **3** (2019), p. 051401.

[195] J. Stein, M. Baum, S. Holbein, T. Finger, T. Cronert, C. Tölzer, T. Fröhlich, S. Biesenkamp, K. Schmalzl, P. Steffens, C. H. Lee, and M. Braden. "Control of Chiral Magnetism Through Electric Fields in Multiferroic Compounds above the Long-Range Multiferroic Transition". In: *Physical Review Letters* **119** (2017), p. 177201.

Danksagung

Ich bedanke mich bei Prof. Dr. Markus Braden für die Möglichkeit einer Promotion in seiner Arbeitsgruppe. Durch die Kombination der experimentellen Arbeit in den institutseigenen Laboren mit zahlreichen Messreisen zu verschiedenen Forschungsreaktoren konnte ich einen breitgefächerten Einblick in das Gebiet der elastischen Beugungsexperimente gewinnen. Für die Hilfe bei technischen Problemen und besonders bei der Interpretation der Messdaten möchte ich mich bedanken.

Prof. Dr. Thomas Lorenz danke ich für die Bereitschaft, meine Arbeit zu begutachten. Auch danke ich Prof. Dr. Petra Becker dafür, den Vorsitz der Prüfungskommision bei meiner Disputation zu übernehmen. Bei Christoph Grams bedanke ich mich für die Bereitschaft zum Beisitz.

Ich möchte mich bei allen bedanken, die die vielfältigen Kristalle gezüchtet haben, die in dieser Arbeit untersucht wurden: Bei Prof. Dr. Ladislav Bohatý bedanke ich mich für alle Materialien dieser Arbeit, die Fe enthalten. I thank Tusharkanti Dey for the growth of the compounds of the form $Ba_3XIr_2O_9$ and for the time we shared the office. Prof. Dr. Petra Becker danke ich für die Darstellung der Doppelperowskit-Verbindungen. I thank Zhiwei Wang and Mahasweta Bagchi for the growth of copper doped Bi_2Se_3. Ich danke auch Daniel Brüning, dessen Messungen an $Cs_3Fe_2Br_9$ für die Interpretation meiner Daten eine wichtige Rolle gespielt haben.

Ich danke Lisa Weber für die Einführung in die Bedienung des Einkristall-Diffraktometers APEX zu Beginn meiner Arbeit, sowie Florian Waßer und Stefan Kunkemöller für die Unterstützung an den Pulver-Diffraktometern D5000 und D5000-matic. Jonas Stein danke ich für die pyroelektrischen Messungen am Instrument DiMoS, die Hilfe beim Textsatz mit LaTeX und die gemeinsame Zeit im Büro. Auch bei Alexandre Bertin bedanke ich mich für die leider nur kurze Zeit, in der wir uns das Büro geteilt haben.

Neutronen-Beugung wäre ohne die unermüdliche Arbeit der Instrumentenverantwortlichen nicht möglich. La diffraction de neutrons n'était pas possible sans le travail acharné des responsables d'intruments. Daher gilt mein besonderer Dank Martin Meven (MLZ, Garching bei München) für die technische und wissenschaftliche Unterstützung, en particullier je veux remercier Arsen Gukasov, Alexandre Bataille et Xavier Fabrège (LLB, Saclay), Anne Stunault, Oscar Fabelo et Bachir Ouladdiaf (ILL, Grenoble) pour le soutien technique et scientifique. Ich bedanke mich auch bei allen technischen Mitarbeitern an den Forschungsreaktoren, deren technische Kompetenz die Hard- und Software der Neutronendiffraktion ermöglicht. Je remercie aussi tous les collaborateurs technique dans les réacteurs de recherche, qui mettent le matériel et le logiciel de contrôle pour la diffraction de neutrons à disposition.

Ich bedanke mich auch bei allen Mitarbeitern der Werkstätten des II. Physikalischen Instituts. Mein besonderer Dank richtet sich an Christian Honerlage, Klaus Lehmann und Siegurt Skoda, die bei technischen Problemen des Pulverdiffraktometers eine große Hilfe waren.

Ich bedanke mich bei Sebastian Biesenkamp fürs Korrekturlesen und die Diskussionen über Methoden der Neutronenbeugung, wofür ich auch Simon Holbein und Kevin Jenni danke.

Auch bei Johannes Engelmayer bedanke ich mich fürs Korrekturlesen, Hilfe bei Problemen mit BibLaTeX sowie für interessante Diskussionen über Themen der Kristallographie und Festkörperphysik. Bei Lionel Andersen bedanke ich mich für Hinweise zur Präparation des schwer handabbaren Wismut-Selenits.

Ich danke Alessandro Revelli, Christian Dickel und Jens Brede für die geduldige Beantwortung meiner Fragen zur Spin-Bahn-Kopplung in Iridaten, zu topologischen Supraleitern und zur Topologie von Bandstrukturen im Allgemeinen.

Abstract

In the present work, a variety of compounds with spin-orbit coupling is investigated using elastic X-ray and neutron diffraction techniques. The multiferroic compound ammonium pentachloroaquaferrate(III) shows Dzyaloshinsky-Moriya interaction. This is a superexchange interaction which includes spin-orbit coupling so that magnetic and ferroelectric orders interact. A related caesium-based transition-metal halide is also investigated, which exhibits several anisotropic magnetic phases. Again, this anisotropy indicates strong spin-orbit coupling. Furthermore, this work deals with 6H-perovskite-type iridates, which are related to spin-liquid candidates. The physics behind such compounds is based on the Kitaev model, which applies when spin interactions are direction dependent due to spin-orbit coupling. In iridates of double-perovskite type, spin-orbit coupling leads to the formation of $j = 1/2$ moments, which give rise to rich physics. A further topic of this work is copper doped bismuth selenite, which is a topological superconductor. The superconductivity of this compound stems from the band structure of pristine bismuth selenite that exhibits a spin-textured Fermi surface due to spin-orbit coupling.

Ammonium pentachloroaquaferrate(III) $(ND_4)_2[FeCl_5(D_2O)]$ was investigated addressing a structural phase transition with a symmetry reduction that can be attributed to an ordering of the $[ND_4]$ molecules which are disordered at higher temperatures. Refinements in space group Pa yield values for the polarization that are not consistent with other measurements so that this breaking of symmetry could not be detected within the experimental precision.

A structural phase transition of the erythrosiderite-type compound $Cs_2[FeCl_5(H_2O)]$, that lowers the symmetry to a monoclinic space group, was clarified. A reduction to a polar subgroup can be ruled out by pyroelectric measurements. The magnetic structure at low temperature exhibits Shubnikov group $Cmcm'$.

The magnetic structure of the low-temperature zero-field phase of $Cs_3Fe_2Br_9$ was determined. It breaks the $P6_3/mmc$ symmetry according to the Γ_3 mode. The accompanied structural distortions are below the experimental precision. The phase at 50 mK in a magnetic field of 7 T was found to be qualitatively identical but yields weaker magnetic reflections.

The compounds $Ba_3XIr_2O_9$ with $X = \mathrm{In}, \mathrm{Nb}, \mathrm{Ce}$ turn out to exhibit space group $C2/c$ already at room temperature in contrast to former findings. The structural deviations from $P6_3/mmc$ symmetry mainly effect the O atoms and lead to tilts and distortions of $[XO_6]$ octahedrons and $[Ir_2O_9]$ double-octahedrons. The occupation disorder on the X and Ir sites turns out to have a strong negative correlation with the difference of the radii of the X and Ir cations. The $\mathrm{Ir} - \mathrm{Ir}$ distances depend on the radius of the X ion.

Neither at room temperature nor at 100 K, the $Fm\bar{3}m$ symmetry of the double-perovskite Ba_2CeIrO_6 is broken. Refinements indicate a shift of the Ba atoms without long-range order at both temperatures. The Ce sites are roughly fully occupied by Ce atoms and the Ir sites show occupation disorder.

Also the F centering of space group $Fm\bar{3}m$ is not broken for the compound Ba_2PrIrO_6. However, structural refinements indicate that tilts of the $[(X/\mathrm{Ir})O_6]$ octahedrons reduce its symmetry to space group $I4/m$.

The Cu doping of the compound $Cu_xBi_2Se_3$ is not detectable by means of neutron diffraction. A substitution of Bi by Cu of up to $x \approx 10\,\%$ cannot be ruled out. Several further proposed sites for the Cu atoms can be discarded by the results of the present work. There are hints for a small structural distortion to space group $C2/c$ where the Bi atoms are slightly displaced. A magnetic signal was detected which however cannot be explained by free electrons or by nuclear magnetic moments. An impurity phase of this compound could be characterized as $CuBi_6Se_9$ with a layered crystal structure and monoclinic symmetry.

Kurzzusammenfassung

In der vorliegenden Arbeit wurden mehrere Verbindungen, bei denen Spin-Bahn-Kopplung eine Rolle spielt, mittels elastischer Röntgen- und Neutronenstreuverfahren untersucht. Die multiferroische Verbindung Ammonium-Pentachloraquaferrat(III) zeigt Dzyaloshinsky-Moriya-Wechselwirkung. Diese ist eine Superaustausch-Wechselwirkung mit Spin-Bahn-Kopplung, so dass sich magnetische und ferroelastische Ordnungen gegenseitig beeinflussen. Ein verwandtes cäsiumbasiertes Übergangsmetallhalogenid, das mehrere anisotrope magnetische Phasen aufweist, wurde untersucht. Auch diese Anisotropie deutet auf starke Spin-Bahn-Kopplung hin. Desweiteren behandelt diese Arbeit Iridate vom 6H-Perowskit-Typ, die verwandt mit Materialien sind, die als mögliche Spin-Flüssigkeiten diskutiert worden sind. Die Physik solcher Verbindungen basiert auf dem Kitaev-Modell, bei dem durch Spin-Bahn-Kopplung richtungsabhängige Spin-Wechselwirkungen auftreten. In Iridaten des Doppelperowskit-Typs bewirkt Spin-Bahn-Kopplung $j = 1/2$-Momente, auf denen eine reichhaltige Physik beruht. Ein weiteres Thema dieser Arbeit ist kupferdotiertes Wismut-Selenit, ein topologischer Supraleiter. Die Supraleitung dieser Verbindung lässt sich auf die Bandstruktur des reinen Wismut-Selenits zurückführen, auf dessen Fermi-Fäche die Spin-Bahn-Kopplung eine Spinstrukturierung bewirkt.

Die deuterierte Verbindung $(ND_4)_2[FeCl_5(D_2O)]$ wurde im Hinblick auf eine strukturelle Phasenumwandlung untersucht, welche die Symmetrie durch Ordnung von $[ND_4]$-Molekülen bricht, die bei höherer Temperatur ungeordnet sind. Verfeinerungen in Raumgruppe Pa liefern Werte für die Polarisierung, die nicht mit anderen Messungen übereinstimmen, so dass diese Symmetriebrechung innerhalb der experimentellen Genauigkeit nicht nachgewiesen werden konnte.

Es wird festgestellt, dass eine strukturelle Phasenumwandlung in $Cs_2[FeCl_5(H_2O)]$ die Symmetrie hin zu einer monoklinen Raumgruppe verringert. Eine Symmetrieverringerung zu einer polaren Raumgruppe konnte durch pyroelektrische Messungen ausgeschlossen werden. Die Magnetstruktur bei tiefer Temperatur weist die Shubnikovgruppe $Cmcm'$ auf.

Die Magnetstruktur der Verbindung Cs_3Fe2Br_9 bei tiefer Temperatur im Nullfeld wurde ermittelt. Sie bricht die $P6_3/mmc$-Symmetrie gemäß der Γ_3-Mode. Die damit zusammenhängenden strukturellen Verzerrungen liegen unterhalb der experimentellen Genauigkeit. Es wurde festgestellt, dass die Phase bei 50 mK in einem Magnetfeld von 7 T qualitativ identisch ist, aber schwächere magnetische Reflexe aufweist.

Für die Verbindungen $Ba_3XIr_2O_9$ mit $X = \mathrm{In, Nb, Ce}$ wird die Raumgruppe $C2/c$ bereits bei Raumtemperatur festgestellt, was im Widerspruch zu früheren Ergebnissen steht.

Die strukturellen Abweichungen von der $P6_3/mmc$-Symmetrie betreffen hauptsächlich die O Atome und bewirken Verkippungen und Verzerrungen der $[X\mathrm{O}_6]$-Oktaeder und $[\mathrm{Ir}_2\mathrm{O}_9]$-Doppeloktaeder. Es stellt sich heraus, dass die Besetzungsunordnung der X- und Ir-Gitterplätze eine starke negative Korrelation mit der Differenz der Radien der X- und Ir-Kationen aufweist. Die Ir − Ir-Abstände hängen vom Radius des X-Ions ab.

Die $Fm\bar{3}m$-Symmetrie des Doppelperowskits $\mathrm{Ba_2CeIrO_6}$ wird weder bei Raumtemperatur, noch bei 100 K gebrochen. Verfeinerungen deuten für beide Temperaturen auf eine Verschiebung der Ba-Atome ohne langreichweitige Ordnung hin. Die Ce-Gitterplätze sind ungefähr voll besetzt und die Ir-Gitterplätze zeigen Besetzungsunordnung.

Auch bei der Verbindung $\mathrm{Ba_2PrIrO_6}$ wird die Flächenzentrierung der Raumgruppe $Fm\bar{3}m$ nicht gebrochen. Jedoch weisen Strukturverfeinerungen auf Verkippungen der $[(X/\mathrm{Ir})\mathrm{O}_6]$-Oktaeder hin, die die Symmetrie hin zu Raumgruppe $I4/m$ verringern.

Die Cu-Dotierung der Verbindung $\mathrm{Cu}_x\mathrm{Bi_2Se_3}$ ist mittels Neutronenbeugung nicht feststellbar. Eine Substitution von Bi durch Cu von bis zu $x \approx 10\,\%$ kann nicht ausgeschlossen werden. Einige weitere Positionen, die für die Cu-Atome vorgeschlagen wurden, können durch die Ergebnisse dieser Arbeit verworfen werden. Es gibt Hinweise auf eine kleine strukturelle Verzerrung entsprechend der Raumgruppe $C2/c$, bei der die Bi-Atome leicht verschoben sind. Es konnte ein magnetisches Signal aufgezeichnet werden, dass sich jedoch weder durch freie Elektronen noch durch nukleare magnetische Momente erklären lässt. Eine Fremdphase dieser Verbindung konnte als $\mathrm{CuBi_6Se_9}$ mit einer geschichteten Kristallstruktur und monokliner Symmetrie charakterisiert werden.

Offizielle Erklärung

Ich versichere, dass ich die von mir vorgelegte Dissertation selbständig angefertigt, die benutzten Quellen und Hilfsmittel vollständig angegeben und die Stellen der Arbeit – einschließlich Tabellen, Karten und Abbildungen –, die anderen Werken im Wortlaut oder dem Sinn nach entnommen sind, in jedem Einzelfall als Entlehnung kenntlich gemacht habe; dass diese Dissertation noch keiner anderen Fakultät oder Universität zur Prüfung vorgelegen hat; dass sie – abgesehen von unten angegebenen Teilpublikationen – noch nicht veröffentlicht worden ist, sowie, dass ich eine solche Veröffentlichung vor Abschluss des Promotionsverfahrens nicht vornehmen werde. Die Bestimmungen der Promotionsordnung sind mir bekannt. Die von mir vorgelegte Dissertation ist von Prof. Dr. Markus Braden betreut worden.

Tobias Fröhlich

Teilpublikationen

- T. Fröhlich, J. Stein, L. Bohatý, P. Becker, A. Gukasov, and M. Braden. "Structural and magnetic phase transitions in $Cs_2[FeCl_5(H_2O)]$". In: *J. Phys.: Condens. Matter* **30** (2018), p. 295403
- A. Revelli, M. Moretti Sala, G. Monaco, P. Becker, L. Bohatý, M. Hermanns, T. C. Koethe, T. Fröhlich, P. Warzanowski, T. Lorenz, S. V. Streltsov, P. H. M. van Loosdrecht, D. I. Khomskii, J. van den Brink, and M. Grüninger. "Resonant inelastic x-ray incarnation of Young's double-slit experiment". In: *Science Advances* **5**.eaav4020 (2019)
- A. Revelli, C. C. Loo, D. Kiese, P. Becker, T. Fröhlich, T. Lorenz, M. Moretti Sala, G. Monaco, F. L. Buessen, J. Attig, M. Hermanns, S. V. Streltsov, D. I. Khomskii, J. van den Brink, M. Braden, P. H. M. van Loosdrecht, S. Trebst, A. Paramekanti, and M. Grüninger. "Spin-orbit entangled $j = \frac{1}{2}$ moments in Ba_2CeIrO_6: A frustrated fcc quantum magnet". In: *Physical Review B* **100** (2019), p. 085139

Weitere Publikationen

Die aufgelisteten Publikationen sind nicht Bestandteil meiner Dissertation.

- J. Engelmayer, X. Lin, C. P. Grams, R. German, T. Fröhlich, J. Hemberger, K. Behnia, and T. Lorenz. "Charge transport in oxygen-deficient $EuTiO_3$: The emerging picture of dilute metallicity in quantum-paraelectric perovskite oxides". In: *Physical Review Materials* **3** (2019), p. 051401
- J. Stein, M. Baum, S. Holbein, T. Finger, T. Cronert, C. Tölzer, T. Fröhlich, S. Biesenkamp, K. Schmalzl, P. Steffens, C. H. Lee, and M. Braden. "Control of Chiral Magnetism Through Electric Fields in Multiferroic Compounds above the Long-Range Multiferroic Transition". In: *Physical Review Letters* **119** (2017), p. 177201